Experimental investigations of internal air–water flows

by

Hassan Shaban

Thesis submitted to the
Faculty of Graduate and Postdoctoral Studies
In partial fulfillment of the requirements
For the Ph.D. degree in
Mechanical Engineering

Ottawa-Carleton Institute for Mechanical and Aerospace Engineering
Faculty of Engineering
University of Ottawa

Abstract

The objective of the present thesis research is to apply state-of-the-art experimental and data analysis techniques to the study of gas-liquid pipe flows, with a focus on conditions occurring in header–feeder systems of nuclear reactors under different accident scenarios. Novel experimental techniques have been proposed for the identification of the flow regime and measurement of the flow rates of both phases in gas-liquid flows. These techniques were automated, non-intrusive and economical, which ensured that their use would be feasible in industrial as well as laboratory settings. Measurements of differential pressure and the gas and liquid flow rates were collected in vertical upwards air–water flow at near–atmospheric pressure. It was demonstrated that the probability density function of the normalized differential pressure was indicative of the flow regime and using non-linear dimensionality reduction (the Elastic Maps Algorithm), it was possible to automate the process of identifying the flow regime from the differential pressure signal. The relationship between the probability density function and the power spectral density of normalized differential pressure with the gas and liquid flow rates in air-water pipe flow was also established and a machine learning algorithm (using Independent Component Analysis and Artificial Neural Networks) was proposed for the estimation of the phase flow rates from these properties. The proposed methods were adapted for use with single and dual conductivity wire–mesh sensors in vertical upwards and downwards air–water flows. A thorough evaluation of the performance and measurement uncertainty of wire–mesh sensors in gas–liquid flows was also performed. Lastly, measurements of the flow distribution in feeder tubes supplied with air-water mixtures by a simplified header model were collected and correlated to the observed flow patterns in the header.

Acknowledgements

I would like to express my sincere gratitude to my supervisor, Professor Stavros Tavoularis, who has been the ideal mentor and teacher throughout my doctoral studies, and has helped mold me into a capable and effective researcher. I am thankful to all of my colleagues who have offered their assistance, especially Dr. Dongil Chang and Mr. Étienne Lessard for their help with the computational and experimental aspects of my research, respectively. I am eternally grateful to my parents, Mahmoud and Nessrin; without their continued support and encouragement, this work would not have been possible. Finally, I wish to thank all of my family and friends who have helped make my experience in Canada a very enjoyable one.

Table of Contents

List of Figures

List of Tables

Nomenclature

A	cross-sectional area of a channel
D	channel hydraulic diameter
f_s	sampling frequency
G	mass flux
g	acceleration due to gravity
j	superficial velocity
L	channel length
$\dot{m}$	mass flow rate
P	pressure
ΔP^*	normalized differential pressure parameter
Q	volumetric flow rate
R	channel radius, feeder mass flow rate ratio
t	time
U	velocity
u	uncertainty
V	volume

Greek symbols

α	void fraction
ϵ	relative error
μ	dynamic viscosity
ν	kinematic viscosity
ρ	density
σ	surface tension coefficient
ϕ_{fo}^2	two–phase friction multiplier

Subscripts and superscripts

$*$	normalized
atm	atmospheric
b	bias
CS	cross-section
F	feeder
g	gas
H	header
IN	inlet
i	row index
$inst$	instantaneous
int	interfacial
j	column index
k	frame index in WMS analysis
L	lower
l	liquid
l, s	static liquid
OUT	outlet
p	precision, predicted
R	regulator
TM	turbine meter
tot	total
U	upper
V	volumetric
xc	cross–correlation–based

Mathematical symbols

$\overline{X}$	time average of X
$\|X\|$	magnitude of X
ΔX	difference in quantity X

Acronyms

AECL	Atomic Energy of Canada Limited
ANN	artificial neural networks
CANDU	CANada Deuterium Uranium
CCF	cross correlation function
CFD	computational fluid dynamics
ECT	electrical capacitance tomography
ERT	electrical resistance tomography
GWMT	global wire–mesh tomograph
ICA	independent component analysis
I.D.	inner diameter
LOCA	loss of coolant accident
LS	level swell method
MFM	multiphase flow meter
PCA	principal component analysis
PDF	probability density function
PGM	pressure gradient method
PSD	power spectral density
RF	relative frequencies
QCV	quick closing valve method
SOM	self–organizing map
SVM	support vector machine
WMS	wire-mesh sensor
WMT	wire-mesh tomograph

Chapter 1

Introduction

1.1 Gas–liquid flow in header–feeder systems

A multiphase flow is defined as the flow of a mixture of two or more distinct phases of the same or different fluids, separated by a recognizable interface (Collier & Thome, 1994). Many environmental and industrial flows are multiphase; examples include oceanic waves, bubble columns in chemical reactors, fluidized beds in power plants and oil-gas flows in petroleum pipelines. Because there are many kinds of multiphase flows, and they are considerably more difficult to study than single-phase flows, much of the research in this area has been specific to particular applications (Balachandar & Eaton, 2010).

Multiphase flows can be classified into four categories: gas-solid, liquid-solid, gas-liquid and immiscible liquid-liquid flows. Gas-liquid flows are of particular interest to safety analysis of nuclear power plants, which is the topic of concern in the present work. Gas-liquid flows may be encountered in different parts of the primary heat transport system of the CANDU (CANada Deuterium Uranium) reactor during several types of accidents, for example accidents resulting from loss of pressure or loss of coolant (LOCA).

The core of the CANDU reactor (Figure 1.1) consists of a large number of high-pressure tubes, called the *fuel channels*, which contain rod bundles of fuel elements containing pellets of nuclear fuel. The fuel channels are surrounded by a large low-pressure vessel called the *calandria*, containing the *control rods*, which control the nuclear reaction by absorbing neutrons that result from fission, and most of the *moderator*, which also controls the nuclear reaction by slowing down the neutrons. The fuel elements are cooled by heavy water flowing in the fuel channels under high pressure, which transfers the generated heat to light water under low pressure in the *steam generator*. The *headers* in a CANDU reactor are

horizontal cylindrical tanks connected to the fuel channels by pipes called *feeders*. During normal reactor operation, headers ensure a steady coolant flow through all fuel channels. In an inlet header, liquid coolant enters from the *coolant pump* through one or more inlet *turrets* and is distributed among the fuel channels by different feeders. After being heated in the fuel channels, the coolant is collected into an outlet header, and from there it flows to the steam generator through one or more outlet turrets. The feeder pipes are arranged in axially equidistant groups called *feeder banks* and, in each bank, the feeders leave the header at different angles of inclination.

The operation of nuclear power plants is licensed by a designated regulatory body, which requires regular safety analyses. Different jurisdictions specify different laws and regulations that explicitly state the allowable radioactive contamination levels in case of different accident scenarios. It is the duty of nuclear safety analysts to simulate accident scenarios and estimate the resulting contamination levels using system codes, which are composed of different modules with idealized models of the components in the nuclear power plant. The contamination level resulting from a nuclear accident depends on whether or not the integrity of the reactor core is maintained: meltdown of a particular fuel channel would occur if its sheath temperature exceeded a certain threshold, which, in turn, would occur if the flow rate of liquid coolant flowing through it dropped below a certain level.

Under normal operating conditions, the fluid in the headers and feeders is single-phase heavy water. In case of a LOCA, the reactor is shut down and the Emergency Coolant Injection System (ECIS) is activated. This system injects light water at high pressure into the inlet headers to enhance the core cooling. Boiling is expected to occur in this case, and the flow would change from a single-phase water flow to a two-phase steam-water flow. The distribution of the two phases is found to be non-uniform among the different feeder pipes. As a result, some fuel channels may receive little or no liquid coolant, which would lead to overheating of the fuel channel and eventually to fuel meltdown. A concern of nuclear safety analysts is to devise methods that ensure that liquid flow distribution in the feeders can be measured or predicted accurately. This will allow them to improve the header–feeder sub-modules in thermalhydraulics codes, leading to a better overall accuracy of the predictions of these codes.

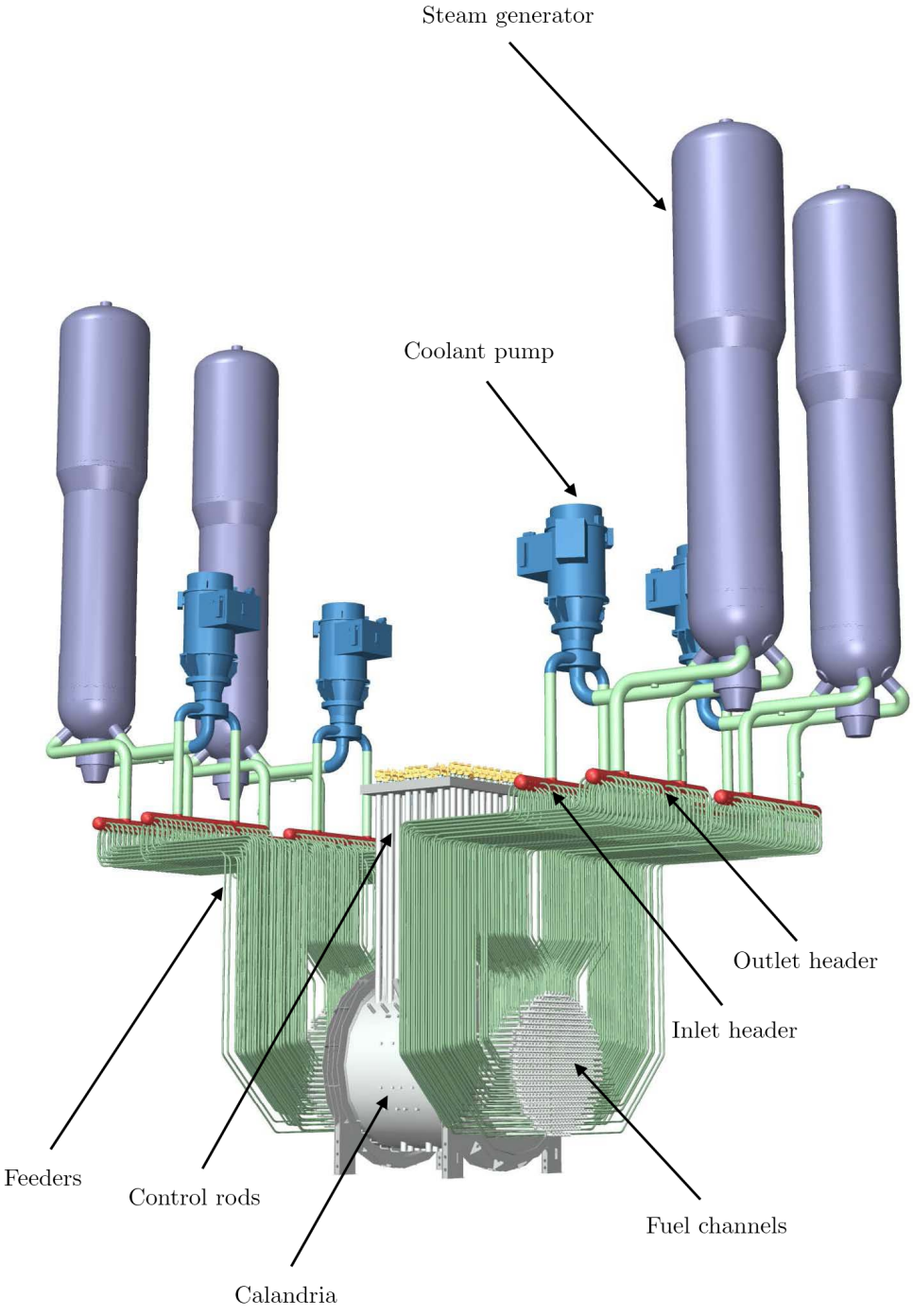

Figure 1.1: Overview of a CANDU reactor (adapted from *canteach.candu.org*).

A new header test facility has recently been built and commissioned at the Atomic Energy of Canada Limited (AECL) Chalk River Laboratories. This facility has been designed for investigations of two-phase flow characteristics in the headers and flow distribution in the feeders during postulated accident scenarios. The facility (Figure 1.2) consists of one inlet header and one outlet header, connected by 72 feeders. The feeders are arranged in 12 banks of 6 tubes each and leave the headers at different degrees of inclination. Measurements of void fraction and gas velocity can be made using wire-mesh sensors (to be described in Chapter 6). Part of the present work is in direct support of the AECL header–feeder research, with the aim of complementing the wire-mesh sensor measurements by evaluating the performance of these sensors and developing new methods for predicting the flow regime and the gas and liquid flow rates in the feeders from their measurements.

1.2 Objectives

The general objective of this thesis was the development of techniques for the measurement of primary two-phase flow parameters and their use in a header–feeder facility. The present work consisted of five distinct tasks, summarized in the following list.

1. Development of new gas-liquid flow regime identification methods using simple instrumentation.

2. Development of online, non–intrusive and cost-effective two-phase flow rate measurement methods.

3. Assessment of the performance and measurement uncertainty of wire-mesh sensors in gas-liquid flows.

4. Measurements of air-water flow characteristics using wire-mesh sensors and development of methods to predict the flow regime and phase flow rates from wire-mesh sensor signals.

5. Collection of measurements of the gas and liquid flow distribution in small numbers of active feeders connected to a header in a newly constructed and instrumented modular header–feeder facility.

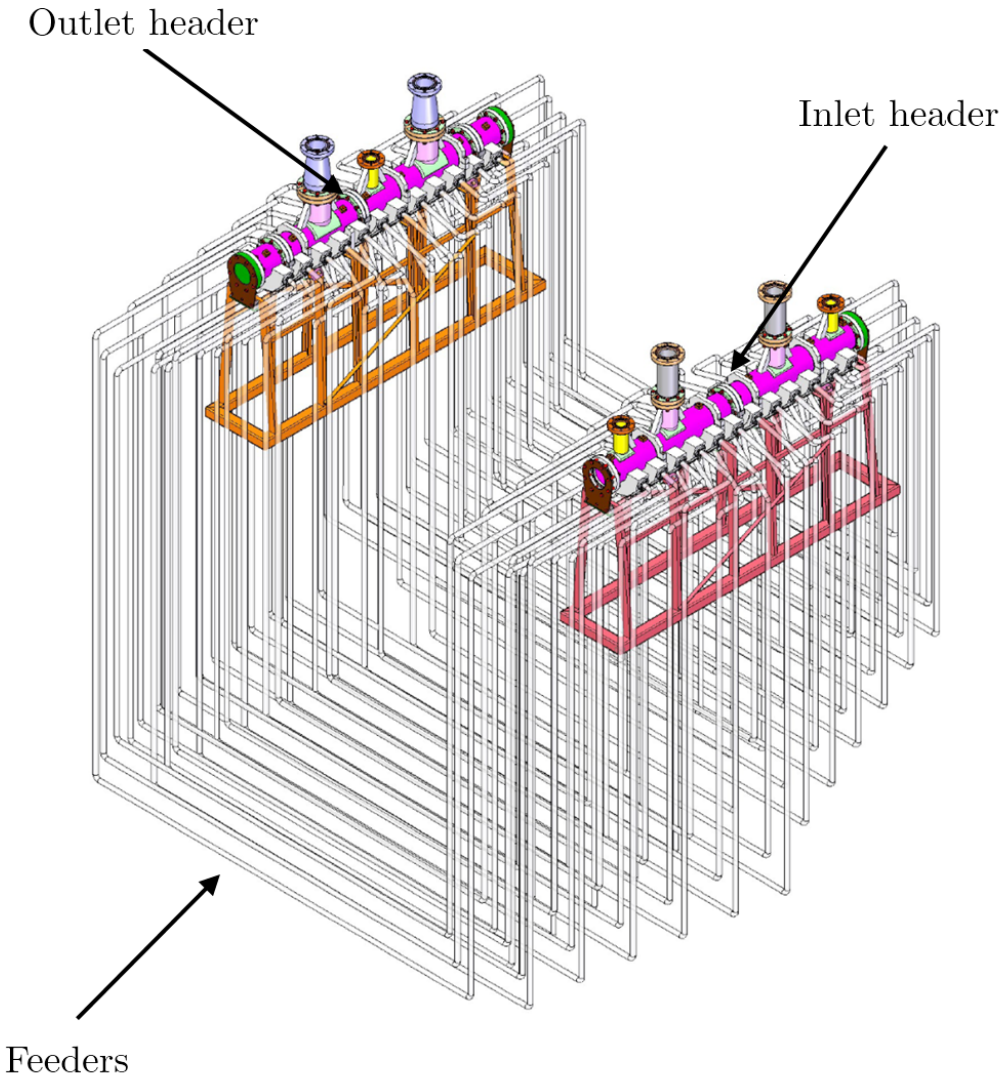

Figure 1.2: AECL Header Test Facility (Yang, 2013).

The findings of this work are expected to be used by future researchers for collecting flow measurements in gas–liquid flow applications in an efficient and cost-effective manner. In addition,it is hoped that this work will contribute to the understanding of the problem of non–uniform flow distribution in header–feeder systems. Finally, the collected data would be suited for validation of system, thermalhydraulics and CFD codes.

1.3 Thesis organization

This thesis is manuscript-based. Following this Introduction in Chapter 1, Chapter 2 presents a general background about gas–liquid flows. This is followed by Chapter 3 which describes the experimental facilities used in the present work. The next five chapters present the main results in the form of four articles and one manuscript, each of which addresses a thesis research objective, as outlined in the previous section:

- Chapter 4: Shaban, H. and Tavoularis, S. 2014. Identification of flow regime in vertical upward air–water flow using differential pressure signals and elastic maps. *Int. J. Multiphase Flow* **61**, 62-72.

- Chapter 5: Shaban, H. and Tavoularis, S. 2014. Measurement of gas and liquid flow rates in two–phase pipe flows by the application of machine learning techniques to differential pressure signals. *Int. J. Multiphase Flow* **67**, 106-117.

- Chapter 6: Shaban, H. and Tavoularis, S. 2015. Wire-mesh tomography: areas of application, performance evaluation and measurement uncertainty. (under review)

- Chapter 7: Shaban, H. and Tavoularis, S. 2015. The wire–mesh sensor as a two–phase flow meter. *Meas. Sci. Tech.* **26**, 015306 (16 pp.).

- Chapter 8: Shaban, H. and Tavoularis, S. 2015. Distribution of downward air–water flow in vertical tubes connected to a horizontal cylindrical header. *Nuc. Eng. Des.* **291**, 91-100.

Finally, the main conclusions and novel contributions of the present work are summarized in Chapter 9.

Chapter 2

Background and Literature Review

2.1 Fundamentals of gas-liquid flow

This section explains some of the terminology that is particular to the study of gas–liquid flows and is not encountered other fluid mechanics research. In the following, the subscript g refers to a property of the gas phase, whereas the subscript l refers to a property of the liquid phase.

- **Flow regimes:** Depending on the flow conditions, a gas–liquid flow exhibits one of several different patterns (Figure 2.1). Depending on which pattern is prevalent, the gas–liquid flow is said to be in a corresponding *flow regime*. The rates of momentum, heat and mass transfer between the two phases within each flow regime differ from those in another. There is no universal agreement on the names used to describe different regimes, neither on the description of flow patterns within each regime. To avoid confusion when comparing the results of the present work with those from the literature, definitions of flow regimes observed in the present studies will be presented in Chapter 4.

- **Interfacial forces:** The gas and liquid phases are separated by a thin *interface*, which may be approximated as a discontinuity in fluid properties. Momentum, heat and mass transfer take place between the two phases at the interface. In adiabatic flows, interest is limited to momentum transfer, which is the result of the action of *interfacial forces* between the phases. The magnitudes of these forces are directly related to the relative velocity between the phases, termed the *slip velocity*.

- **Void fraction:** Consider a volume V_{tot} of a flowing gas–liquid mixture (Figure 2.2

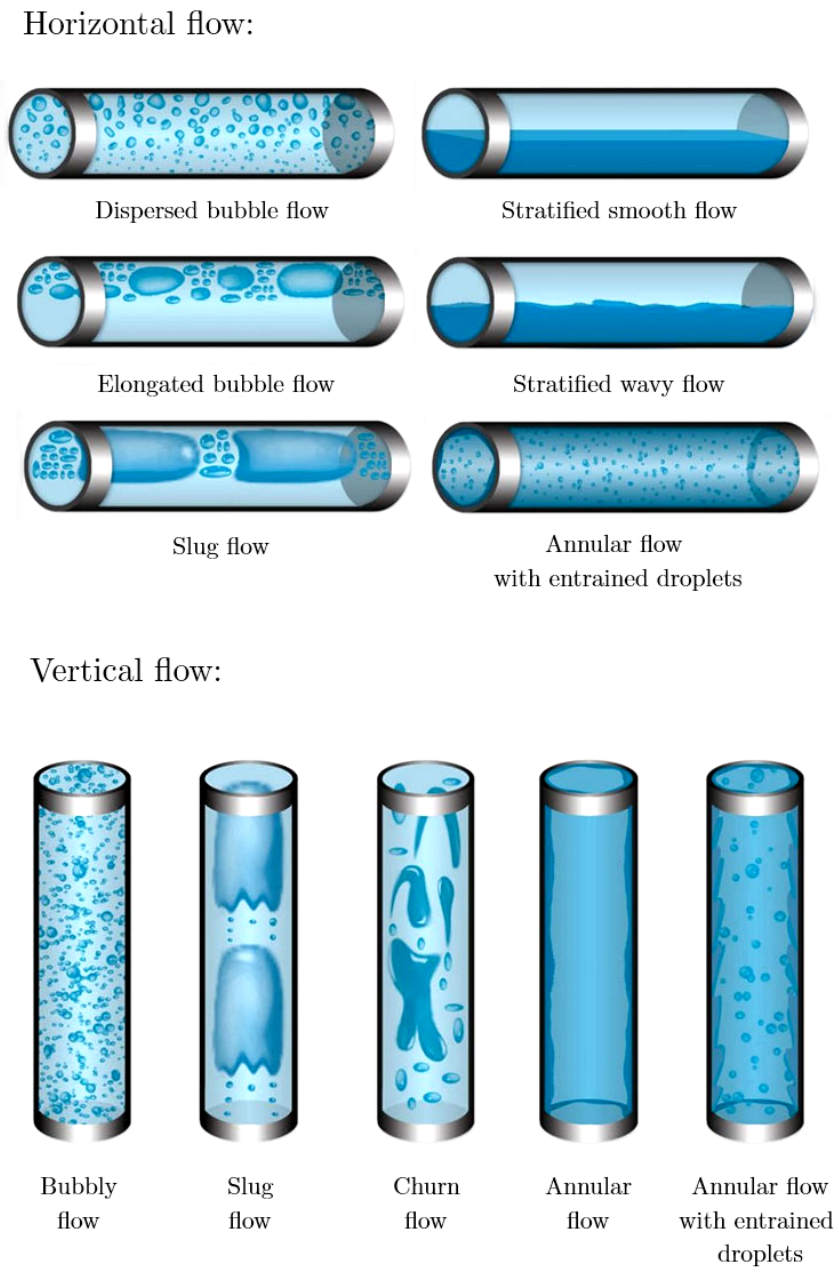

Figure 2.1: Illustration of different flow regimes in vertical and horizontal gas-liquid pipe flows (adapted from www.drbratland.com, with permission from Dr. Ove Bratland).

a). The ratio α_V of the volume V_g occupied by the gas phase and the total volume of the mixture is called the *volume-averaged void fraction*, *i.e.*,

$$\alpha_V = \frac{V_g}{V_{tot}}. \tag{2.1}$$

Now consider the cross–sectional area A of a channel in which the gas-liquid mixture flows (Figure 2.2 b). The ratio $\alpha_{CS,inst}$ of the area A_g occupied by the gas phase and the total cross–sectional area at a certain time instant is called the *instantaneous cross–section void fraction*, *i.e.*,

$$\alpha_{CS,inst} = \frac{A_g}{A}. \tag{2.2}$$

The average α_{CS} of this quantity over a sufficiently long time interval (Figure 2.2 c) is called the *time–and area–averaged void fraction*,

$$\alpha_{CS} = \frac{\overline{A_g}}{A}. \tag{2.3}$$

Momentum, heat and mass transfer are expressed in terms of the cross-section and time-averaged void fraction α_{CS}. However, if the gas and liquid flow rates are constant, the sampling time is not too short, the slip velocity and measurement volume for α_V are not excessive and the axial variations of α_{CS} are negligible, one may assume that $\alpha_{CS} \approx \alpha_V$, which allows the use of volumetric measurements in calculations. Henceforth, the time–and area–averaged void fraction will be denoted by α and referred to simply as the *void fraction*.

- **Superficial velocities:** The phase velocities U_g and U_l of the gas and the liquid flowing in a channel are difficult to measure in practice. The phase volumetric flow rates Q_g and Q_l are, however, easier to measure. From these, one can calculate the gas and liquid *superficial velocities* j_g and j_l, respectively, as the velocities of the corresponding phase if it were flowing alone in the channel, *i.e.*, as

$$j_g = \frac{Q_g}{A}. \tag{2.4}$$

and

$$j_l = \frac{Q_l}{A}. \tag{2.5}$$

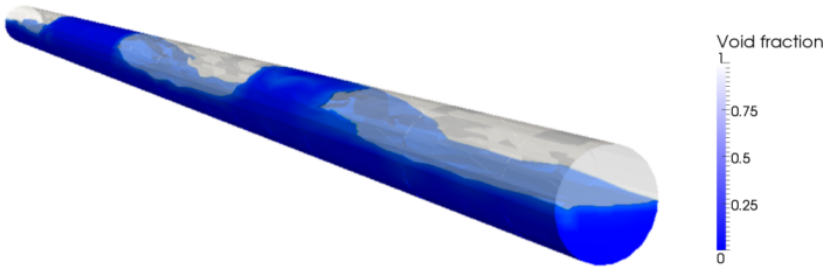

(a) Example of a gas-liquid pipe flow pattern
Volume-averaged void fraction = 0.437

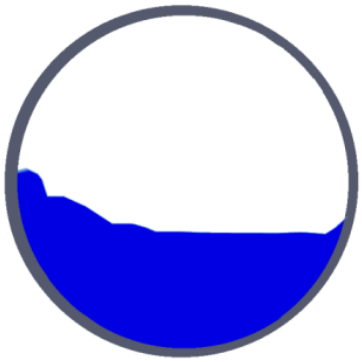

(b) Instantaneous void fraction map
Instantaneous cross-section void fraction = 0.682

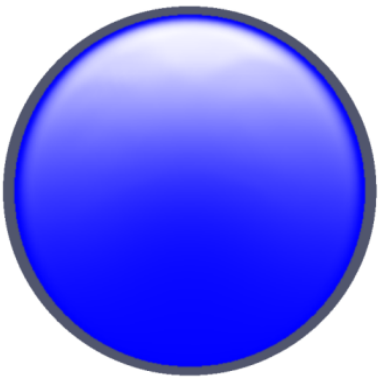

(c) Time-averaged void fraction map
Time-averaged cross-section void fraction = 0.437

Figure 2.2: Void fraction terminology.

The *total* or *mixture superficial velocity* j_{tot} is defined as

$$j_{tot} = j_g + j_l = \frac{Q_g + Q_l}{A}. \tag{2.6}$$

Note that the superficial velocities shown above are time–averaged quantities. The instantaneous superficial velocities are related to the instantaneous phase velocities as

$$U_g(t) = \frac{j_g(t)}{\alpha(t)}. \tag{2.7}$$

and

$$U_l(t) = \frac{j_l(t)}{1 - \alpha(t)}. \tag{2.8}$$

Another velocity that will be referred to in this study, is the *interfacial velocity* U_{int}. This is equivalent to the gas velocity at the gas–liquid interface, and it is not a continuous function in time.

2.2 Flow regime identification

Early flow regime studies were carried out to enable engineers to choose the most effective flow regime for certain applications. For example, bubbly flow is desirable in some chemical reactors to enhance reaction rates. Slug flow is usually avoided in industrial applications due to the possibility of pressure or thermal cycle damage caused by flow pulsations inherent to slug flow. In the petroleum industry, different flow regimes may be desirable at different stages of petroleum extraction. If petroleum is being extracted by the gas–lift method, it is desirable to choose the flow regime that can hold the most liquid in order to maximize petroleum extraction. During petroleum transport, there is a mixture of oil and gas flowing in the pipeline and it is desirable to operate with the flow regime that minimizes pressure drop in order to reduce the required pumping power. More recently, it has also been realized that the flow regime would need to be taken into consideration in any effort to model gas–liquid flows (Rouhani & Sohal, 1983). Experimental quantities of interest in gas–liquid flows, including void fraction and phase velocities, are highly dependent on the prevalent flow regime. The forms of constitutive equations for mass, momentum and energy exchanges also depend on the flow regime. For these reasons, flow regime identification

is an important and critical first step before any further analysis can be performed. One challenge when comparing the works of different researchers is that flow regime classification is highly subjective. For example, Simpson (1975) reported that, at the time, 84 different flow pattern labels had been suggested in literature. Consequently, it is very important to clearly define and describe what is meant by the flow pattern labels being used in each study.

A semi-quantitative analysis of flow regimes is usually presented in the form of flow regime maps, which attempt to predict the prevalent flow regime based on a set of flow parameters. Rouhani & Sohal (1983) presented a review of several such maps based on different coordinate systems and came to the conclusion that a simple two–dimensional flow regime map could be sufficient to predict flow regimes for a certain fluid flowing in a specified geometry but it could not be used to draw conclusions about flows of different fluids in other geometries. This is significant because it means that flow regime maps published by different authors can only be used to give a general idea of the flow regime transitions but, ideally, new flow regime maps would be developed for each new experiment.

Several flow regime detection techniques have been devised over the years and they can be classified into the following general categories (Shaikh & Al-Dahhan, 2007):

- **Visual observation:** This is the most common flow regime identification method but can only be used in pipes with transparent walls. It is unsuitable for higher flow rates and is highly subjective.

- **Measurement of global parameters:** The most common global parameter used to predict flow regimes is the void fraction (Shaikh & Al-Dahhan, 2005). This is done by plotting the void fraction *vs.* the gas superficial velocity. The flow regime transitions are identified as the flow conditions at which a sudden change occurs in the slope of this curve. The main disadvantage of this method is that it does not allow for gradual transitions in the flow regime, *i.e.*, it could be misleading if the changes in the slope of void fraction are gradual.

- **Optical and radiation techniques:** Optical methods for flow regime identification include Particle Image Velocimetry (PIV) (Chen *et al.*, 1994; Lin *et al.*, 1996) and

Laser Doppler Anemometry (LDA) (Olmos *et al.*, 2003), whereas radiation techniques include X-ray (Jones & Zuber, 1975) and gamma-ray computed tomography (CT) (Shaikh & Al-Dahhan, 2005). None of these methods have been considered in this study because they are not suited to simultaneous measurements in a large number of tubes, making them unsuitable for header–feeder studies.

- **Temporal signatures of hydrodynamic parameters:** The presence of a gas–liquid flow in a pipe introduces fluctuations in certain measured properties, due to the significant variation of physical properties of the two phases. These fluctuations have been used for flow regime identification by several authors. For example, Nishikawa *et al.* (1969) carried out a statistical analysis of static pressure pulsations in vertical upward air-water flow in a circular tube. These authors calculated the standard deviation, frequency function and spectral density of the pressure pulsations and they found a correlation between the flow regime and these statistical properties. Matsui (1984) attempted to identify flow regime through the fluctuations of the differential pressure between two axially–separated points. These authors concluded that it was possible to identify the flow regime from the probability density function, the variance and the mean of the normalized differential pressure. Jones & Zuber (1975) used the probability density function of the centre-line void fraction measured using X-rays to characterize the regimes in air-water flow. Other authors have used fluctuations of temperature (Thimmapuram *et al.*, 1992), conductivity (Zhang *et al.*, 1997) and sound (Al-Masry *et al.*, 2005) to identify the flow regime. The use of differential pressure fluctuations and void fraction fluctuations were deemed to be the most suitable in the present research.

2.3 Measurement of void fraction distribution and the phase flow rates

All the experimental methods mentioned in the previous section can be used to carry out measurements of void fraction in gas-liquid flows, in addition to detecting the flow regime. Jones (1983) presented a review of gas-liquid flow measurement techniques, most of which

are now considered industry standards (*e.g.*, optical probes, conductivity probes, gamma densitometers). Oddie & Pearson (2004), Tavoularis (2005) and Rahman *et al.* (2009), gave more up to date reviews on the state-of-the-art in two-phase flow measurement. Reviews of flow rate measurement methods in gas–liquid flows were presented by Falcone *et al.* (2002) and Thorn *et al.* (2013). From previous studies, it was noted that several challenges are associated with experimentation in gas-liquid flows, including the following ones.

- The unsteady nature of two-phase flow introduces fluctuations in all measured quantities. Therefore, an effort must be made to choose instrumentation that has a fast response and good resolution.
- Optical methods have limited application in gas-liquid flows, because the presence of the two phases prevents light from crossing the flow in a predictable manner.
- In-flow probes significantly disturb the interface of the flowing gas-liquid mixture, which may lead to large inaccuracies under certain conditions.
- Wall pressure measurements must be made with minimum flow disturbance and by ensuring that all pressure lines are filled with a single phase, usually the liquid.

Because of the importance of this type of flow in many industrial applications, and despite the previously mentioned difficulties, there have been many experimental studies of gas-liquid pipe flows. It is noted that a literature search with those keywords produced about 2300 results. More detailed discussions of studies relevant to the present thesis are presented in the appropriate chapters.

2.4 Experimental study of gas-liquid flows in header–feeder systems

A detailed literature review on this topic is presented in Chapter 8. In summary, gas–liquid flow from a header to feeders is affected by several case-specific conditions, such as, operating pressure, inlet mass flow rates of the gas and liquid and header–feeder geometry. Several researchers have attempted to link these flow conditions to gas–liquid flow

rates in the feeders or to phenomena that affect the gas–liquid distribution. For example, fundamental studies of the mechanisms that affect the distribution of gas and liquid in feeders connected to a header or manifold have been presented by Saba & Lahey Jr. (1983) and Smoglie & Reimann (1986). These works investigated the mechanisms that govern the flow pattern and phase distribution in very simple models consisting of a single header and one to three feeders. Studies in more complicated header–feeder geometries were performed by Kowalski *et al.* (1989) in the Full-Scale Header Test Facility at Stern Laboratories Inc., in a half-length model of the CANDU header–feeder system consisting of an inlet and an outlet header connected by 30 feeders at different orientations and by Teclemariam *et al.* (2003) who used a scaled down version of the header test facility used by Kowalski *et al.* (1989). Other studies have been performed on gas-liquid flow in similar geometries such as heat exchanger manifolds (Horiki *et al.*, 2004; Marchitto *et al.*, 2009) and tee-junctions in pipes (Saba & Lahey Jr., 1983). The main drawback of these studies is the limited experimental data collected due to the requirement for gas–liquid flow rate measurement in a large number of feeders. The study presented in Chapter 8 utilized a machine–learning approach for flow rate measurement which allowed a much larger database of measurements to be efficiently collected under different flow conditions and in different experimental configurations.

Chapter 3

Experimental facilities and instrumentation

3.1 Air-water flow loop

An air–water flow loop was used for the present studies that required experimental measurements in gas–liquid pipe flow. The facility mainly comprised 32.5 mm I.D. clear polyvinyl chloride (PVC) tubing, however, PVC tubing of different sizes could be used when required. Air could be injected at any of three different locations, such that measurements could be collected in one of three flow orientations, namely, vertical upwards, vertical downwards and horizontal. Water was supplied by a 0.75 hp centrifugal pump, while air was supplied from the regulated laboratory compressed air line. Details of the other relevant instrumentation and experimental configurations used with this flow loop are presented in the appropriate chapters (Chapters 4 to 7).

3.2 Modular header facility

As part of this thesis, a modular header facility was constructed at the University of Ottawa Fluid Mechanics Laboratory. The main component of the facility was a 203 mm I.D. horizontal cylindrical header with twenty feeders leaving at different angles of orientation. The header was designed to be *modular*, *i.e.* only a few feeders could be used for experiments with the other feeders plugged up to the inside diameter of the header using specially machined plugs. Experiments to be performed with one up to twenty active feeders, allowing flow pattern observation and flow rate measurement in both simple and complex flow conditions. More details about this facility are presented in Chapter 8.

3.3 Measurement uncertainty

According to the current international standards, the uncertainty u_X of a measured property X is defined as

$$u_X = \sqrt{u_{Xb}^2 + u_{Xp}^2} \quad , \tag{3.1}$$

where u_{Xb} is the bias limit and u_{Xp} is the precision limit of the measured property (Tavoularis, 2005). The precision limit is estimated as twice the standard deviation of measurements repeated under the same nominal conditions; this implies that, at a 95% confidence level and under the assumption that X is normally distributed, the precision error would be in the range $\pm u_{Xp}$. It is noted that previous authors have often estimated uncertainties as one standard deviation of repeated measurements, which is one half the precision limit according to the standard definition and disregards the bias limit. In the following discussion, we will adhere to standard definitions whenever possible, but in some cases the reported uncertainties may be defined otherwise or will remain undefined; this will be unavoidable when values are cited from manufacturer specifications or previous literature that provide no uncertainty definitions.

With the exception of the water flow meter and differential pressure sensor, all instruments used in the present study were purchased less than one year before the start of the tests and all instrumentation was found to be in good condition. The manufacturers of presently used pressure transducers, thermometers and air rotameters have provided values of $\pm 1\%$, $\pm 2\%$ and $\pm 6\%$, respectively, for the overall uncertainties of these instruments, sometimes referred to as "accuracy" (*sic*), without specifying the precise definition of either term. The water flow meter was calibrated *in situ* by timing the volumetric discharge of the pump; assuming no bias, its uncertainty was determined as $u_{Q_l} = 2\%$. The differential pressure sensor used in Chapters 4 and 5 was also calibrated *in situ* using a static liquid column and its uncertainty was determined as $u_{\Delta P} = 1\%$.

Chapter 4

Identification of flow regime in vertical upward air–water pipe flow using differential pressure signals and elastic maps

In this chapter, a novel method for identification of flow regime in vertical upward air–water flow is proposed based on the analysis of the probability density function (PDF) of the normalized differential pressure. The chapter is presented in the form of the article

> "Shaban, H. and Tavoularis, S. 2014 Identification of flow regime in vertical upward air–water flow using differential pressure signals and elastic maps. *Int. J. Multiphase Flow* **61**, 62-72"

which was submitted to the *International Journal of Multiphase Flow* on 18 November 2013 and accepted for publication on 27 January, 2014.

Identification of flow regime in vertical upward air-water pipe flow using differential pressure signals and elastic maps

H. Shaban, S. Tavoularis*

Department of Mechanical Engineering, University of Ottawa, 161 Louis Pasteur, Ottawa, ON K1N 6N5, Canada

Abstract

A new method for the identification of flow regime in vertical upward gas-liquid flows has been proposed. It consists of an application of the elastic maps algorithm, which is a machine learning method, to the probability density function of differential pressure measurements in pipes. The proposed method was found to be insensitive to axial location of the measurements, pipe diameter within the range 13.9 - 49.2 mm and absolute pressure within the range 100 - 240 kPa; it is therefore amenable to relatively simple calibration in a calibration rig. Compared to three previously suggested machine learning algorithms, the present one had a superior performance in identifying the gas-liquid flow regime.

Keywords: two-phase flow, flow regime, differential pressure, elastic maps

1. Introduction

Gas-liquid flows are commonly encountered in many engineering systems, as, for example, chemical reactors, petroleum transport pipelines, refrigeration systems and heat exchangers of thermal power plants. Depending on the flow conditions, each gas-liquid flow may exhibit one of several different patterns, based on which it may be classified as being in a corresponding

gas-liquid flow regime. Gas-liquid flows are particularly important in safety analysis of nuclear power plants, which is the area of concern in the present work. For example, the safety analysis of nuclear reactors under hypothetical accident conditions requires knowledge of the flow regimes and liquid flow rates in a large number of feeder pipes supplied with water-steam mixtures by a header vessel. The rates of momentum, heat and mass transfer between the two phases within each flow regime differ from those in another and, therefore, accurate identification of flow regime is an essential first step in gas-liquid flow analysis. Different flow regimes have been assigned names by previous authors, but there is no universal agreement either on these names or on the description of flow patterns within each regime. The simplest and most common method used to identify the flow regime is visual observation. This approach is, however, subjective and unsuitable for relatively high gas and liquid flow rates, for which the patterns exhibited by the flow become undistinguishable, unclear or ambiguous. Moreover, visual observation requires optical access to the flow, which is not possible for many applications. Alternative regime identification techniques have been suggested, which are based on the analysis of the time history of a suitable measured local property of the flow. Examples of such properties include void fraction measured by X-rays (Jones and Zuber, 1975), gauge pressure (Nishikawa et al., 1969), differential pressure (Matsui, 1984), electrical impedance (Mi et al., 1998), conductivity (Julia et al., 2008) and capacitance (Wang and Zhang, 2009).

Results of flow regime identification studies have sometimes been presented as flow regime maps, plotted *vs.* a pair of independent parameters, such as gas and liquid superficial velocities. These maps have failed to gain universal acceptance because, although they apply to the experimental configuration for which they were developed, they may not be accurate for different configurations. Several recent studies have attempted to classify two-phase flows into flow regimes using machine learning methods. Mi et al. (1998) used the output signal of an impedance void meter to train a multi-layer back-propagation neural network as well as a self-organizing neural network and tested the trained network's performance in identifying flow regimes associated with a different set of impedance signal inputs. Other authors have used neural networks to process signals of vortex flowmeters (Sun and Zhang, 2008) and conductivity probes (Julia et al., 2008), as well as images of coolant flow obtained by neutron radiography (Tambouratzis and Pazsit, 2009). Trafalis et al. (2005) identified flow regimes with the use of the support vector machine (SVM) method, having the superficial veloci-

ties and pipe diameter as inputs, whereas Wang and Zhang (2009) used the same method but with capacitance signals from an Electrical Capacitance Tomography (ECT) system as inputs. In general, all of these methods gave good predictions of the flow regime but some had difficulty in predicting certain flow regime transitions. Some of these methods are intrusive and may cause a change in the flow regime triggered by the presence of a sensor in the flow. Methods that require a radiation source also necessitate special safety measures, whereas tomographic systems would be excessively costly for simultaneous identification of flow regimes in multiple pipes, such as the feeders of a nuclear reactor header/feeder system. The use of differential pressure signals is an attractive alternative to other methods. This approach is simple, inexpensive and non-intrusive and also requires minor modification to existing piping systems, so that it would be suitable not only for laboratory models, but also for actual industrial settings.

The use of pressure measurements in two-phase flows is challenging because pressure fluctuations are sensitive to many different influences, so that a particular pattern in a pressure signal may not correspond to a unique flow regime (Mi et al., 2001). Matsui (1984) was the first to observe that the shape of the probability density function (PDF) of the differential pressure between two locations along the pipe was distinct for each flow regime. The advantage of using differential rather than static pressure to identify flow regimes is that, unlike local static pressure fluctuations, differential ones would be essentially free of disturbances caused by events in other parts of the flow loop, away from the measurement section. Consequently, the interpretation of differential pressure signals would be relatively free of ambiguity. When applying the differential pressure method, one must ensure that the the pressure lines are completely filled with liquid, as the presence of gas in these lines would introduce errors in the differential pressure measurement; this can be avoided by proper design of the pressure-sensing assembly.

The objective of the present study is to develop a method that can identify accurately, simultaneously and economically the flow regimes in a large number of pipes. As much as possible, it should also be non-intrusive and use relatively simple instrumentation. The differential pressure method was deemed to be the best candidate for a sensing method that meets all of these requirements and the elastic maps method was selected as the best flow regime identification method. In the following sections, we will summarize the main steps of the proposed method and discuss its application to flow regime identification in vertical upward air-water flows. The performance of

the method will then be evaluated in flows with wide ranges of operating conditions.

2. Background

2.1. Flow regimes in vertical upward air-water flow

In view of the lack of agreement in past literature concerning the nomenclature of gas-liquid flow regimes, it is instructive to list the regime names that will be used in this work and to summarize the flow patterns that were observed within each regime. The present interest is focussed on vertical upward air-water flows. Depending on the combination of gas and liquid superficial velocities, any of several flow regimes may occur in such flows, but we are primarily interested in four clearly distinguishable flow regimes, namely, bubbly, slug, churn and annular flows, which will be referred to as *distinct regimes*. To these, we have also added three other regimes that share some of the features of at least two of the distinct regimes: bubbly-slug, slug-churn and churn-annular flows. In past literature, such regimes have sometimes been referred to as *transitional regimes*, because, if the water flow rate in a pipe were kept constant while the air flow rate were increased, they would be observed at the transition between two distinct regimes. It must be noted, however, that these intermediate regimes do not necessarily represent any transition that takes place and can be reproduced independently by setting up the appropriate phase flow rates, without having to produce any of the distinct regimes first. The visual appearances of these seven flow regimes are described in the following paragraphs.

Bubbly flow: This flow regime occurs at relatively low gas flow rates, for which the gas phase appears in the form of small bubbles, often referred to in the literature as *deformable bubbles*. For *dispersed bubbly flows*, inter-bubble spacing is large enough for bubble collisions to be rare, while, for *dense bubbly flows*, bubble collision is the dominant mechanism that affects the flow through breakup and coalescence. For relatively high liquid flow rates, bubbly flow appears frothy and individual bubbles cannot be identified by the naked eye.

Bubbly-slug flow: Bubbly-slug flow is characterized by the presence of relatively large cap-shaped bubbles, which occupy nearly the entire pipe cross-section and flow alongside smaller, deformable bubbles.

Slug flow: In this regime, the gas phase appears mostly in the form of relatively large *Taylor bubbles*, which have characteristic bullet-like shapes

and occupy most of the cross-section of the pipe. These bubbles are separated by liquid slugs, which may contain smaller bubbles. The net liquid flow is always upwards, but liquid may be falling downwards in the annular sections that surround the Taylor bubbles.

Slug-churn flow: The liquid that falls down the sides of a Taylor bubble comes from the liquid slug ahead of it. Under certain conditions, the Taylor bubble may become so long that the liquid in the slug ahead of it is nearly depleted. Then, the liquid slug may become really thin and the gas bubble could penetrate it. When this happens, the remaining liquid falls and accumulates within the next slug. This new slug may or may not be penetrated, depending on the flow conditions. So, this regime is characterized by the existence of long Taylor bubbles and much shorter liquid slugs that occasionally break, with their liquid content falling to the lower slug.

Churn flow: The frequency of the liquid slug breakdowns in slug-churn flow depends on the flow conditions. At higher gas flow rates, the liquid slugs may be able to bridge the pipe diameter but are continually penetrated by the gas. When a liquid slug is broken, its liquid content falls. This slug is then lifted again by the gas and this process is repeated in a quasi-periodic manner. The flow appears to be highly chaotic and frothy and may seem to move upwards at some instants and downwards at other instants.

Churn-annular flow: In this regime, one may notice the existence of a gas core and a relatively uniform annular liquid film on the pipe wall as well as liquid slugs. The annular film mostly moves upwards but occasionally may seem to pause. This pause occurs when a liquid slug fills the local cross-section of the pipe, thus blocking the flow of gas in the core. Shortly afterwards, however, the liquid slug gets penetrated by gas and the upward annular-type flow is resumed.

Annular flow: This regime is observed for very high gas volume fractions, for which the gas and liquid flow as separate continuous phases, with gas in the core and liquid forming a film along the wall. The interface could be smooth or wavy and the flow appears to be less unsteady than churn-annular flow.

2.2. Dependence of flow regime on various effects

Numerous authors have confirmed the importance of the diameter effect on flow regime (Rouhani and Sohal, 1983; Spedding et al., 1998). In fact, some flow regimes may only appear in pipes with a certain range of diameters. For example, under certain conditions, bubbly flows may not appear in pipes

with diameters smaller than a critical value, although they would appear in larger pipes (Taitel et al., 1980); similarly, slug flows cannot be sustained in pipes with diameters larger than some limit (Hibiki and Ishii, 2003). Fluid density, surface tension and viscosity also have an important effect on the flow regime in a pipe. System pressure greatly affects the gas density and, to a lesser extent, other fluid properties. Brown et al. (1960), for example, found a strong effect of the gas phase density on the flow regime transitions. Certain flow regimes may even be encountered exclusively at higher pressures but not at lower ones.

Some authors have found that, under certain conditions, the flow regime may change along a pipe (Taitel et al., 1980). For instance, a flow may be bubbly close to the location of air injection but may develop into slug flow further downstream, whereas slug flows are usually accompanied by some churn flow close to the air injection location. Air injection affects the inlet bubble size, but may also have an effect on the flow regime further along the pipe. Bubble breakup and coalescence, which depend mainly on the bubble size and the turbulence level, may result in regime change of bubbly and slug flows, whereas pressure changes may induce changes of all flow regimes. In vertical upward flows, pressure decreases with increasing elevation, but also drops due to viscous friction; this implies a decrease in gas density and a commensurate increase in the gas superficial velocity with increasing elevation. Consequently, the flow pattern at a certain location in the pipe would not only depend on inlet conditions, but also on the coupled actions of bubble breakup/coalescence and pressure drop. For some conditions, gas-liquid flows may not reach full development even for very long axial pipe lengths (Liu, 1993; Lucas et al., 2005).

2.3. Elastic maps

Elastic maps (Gorban and Zinovyev, 2005, 2007, 2009) are a tool for non-linear dimensionality reduction and allow multi-dimensional data to be visualized on a two-dimensional map. This is achieved by building a non-linear principal manifold in a multi-dimensional space. The projections of the data points on this principal manifold can then be viewed in the two-dimensional internal coordinates of the manifold. The proximity of the projections of the data points on the manifold would depend on the values of the multi-dimensional co-ordinates of the data points; data points with comparable values of the multi-dimensional co-ordinates, *i.e.* those that have some features in common, would have projections on this manifold that would be

closer to each other and *vice-versa*. The method of elastic maps has been applied extensively in the field of bioinformatics, but it has also been applied for general visualization of multi-dimensional data in various other fields of science and in economics. For example, Zinovyev and Gorban (2003) used elastic maps to differentiate between coding and non-coding (junk) regions in a DNA sequence, whereas Gorban and Zinovyev (2008) used elastic maps to visualize micro-array genetic data of different types of breast and bladder cancer and found the elastic map projections to cluster together according to the type of cancer. Elastic maps have also been applied for the recovery of missing data in radiocarbon time series for geophysical analysis (Dergachev et al., 2001) and as a support tool for the optimization of stock market portfolios (Resta, 2007). Other applications include the 3D modeling of molecular surfaces and contour extraction in digital images (Gorban and Zinovyev, 2001).

Principal objects or manifolds can be points, lines or surfaces that represent a best-fit to a number of data points. Consider a set of points, scattered on a plane. Their best-fit could be represented in two ways. One way would be to use a line that is obtained by minimizing the mean squared distances. This line could then be considered to be a linear principal manifold for these points. On the other hand, one could fit these points by an unstructured set of k mean points, each of which is the mean of a certain subset of the original set. This is the well-known k-means algorithm. Both of these methods have disadvantages; the linear principal manifold is inflexible and does not fit well to non-linear data and the lack of structure of the k-means method may make its results hard to interpret. Elastic maps combine some of the features of these two special cases by introducing links between the mean points.

Consider a data set with n dimensions. The method of elastic maps first introduces a set of nodes in n-dimensional space that have a regular topology in two dimensions (for example, a rectangular map). Some pairs of nodes form edges and some pairs of edges form ribs (Figure 1). The goal of the elastic map algorithm is to construct a principal manifold by minimizing the elastic energy of the map U, which is composed of three components, the node energy $U^{(Y)}$, the edge energy $U^{(E)}$ and the rib energy $U^{(R)}$. Two user-defined coefficients λ_i and μ_i determine how much the map can stretch or bend, respectively. Minimization of the total elastic energy of the map is then performed until an error indicator drops below a specified threshold. Various optimization and adaptation strategies can be applied to further improve the approximation of the principal manifold. The next step is to

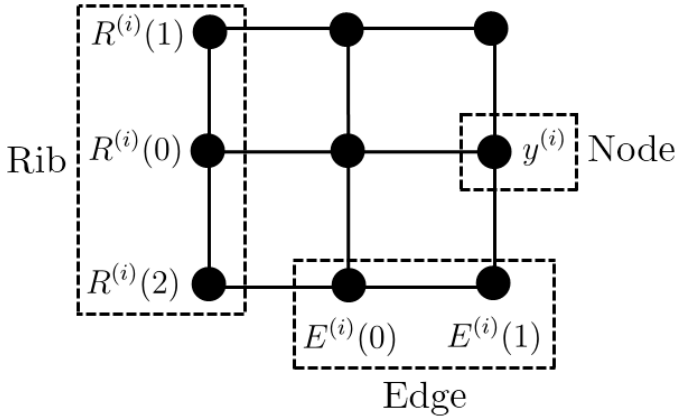

Figure 1: Nomenclature used with reference to elastic maps.

project the data points onto the manifold so that they can be visualized in a two-dimensional space. A set of simplices is introduced onto the grid; for the case of a two-dimensional grid, these simplices are triangles. For each data point, the closest node is first determined. Then the point is orthogonally projected onto the closest one of the simplices that contain this node. More specific details about the algorithm can be found in the references that were cited in the beginning of this section. The algorithm is fast and had a run time of less than 1 min on a desktop computer when used with the datasets in the present study.

3. Experimental facility

A schematic diagram of the air-water flow facility at the University of Ottawa is shown in Figure 2. Water was pumped directly from the main tank into the settling tank, from which it entered the horizontal section. At the exit of the horizontal section, valves directed the fluid either to a bypass branch, which lead to the main tank through the return pipe, or to the vertical upward-flow section and then to the vertical downward-flow section, from which it returned to the main tank. Measurements could be taken in horizontal, vertical upward and vertical downward air-water flows. The flow loop was made mainly of clear polyvinyl chloride (PVC) tubing with an inner diameter of 32.5 mm, which permitted visual observation of the flow. Each of

the two vertical sections of the flow loop is 2.44 m high and could be replaced by tube sections of the same length but different diameters.

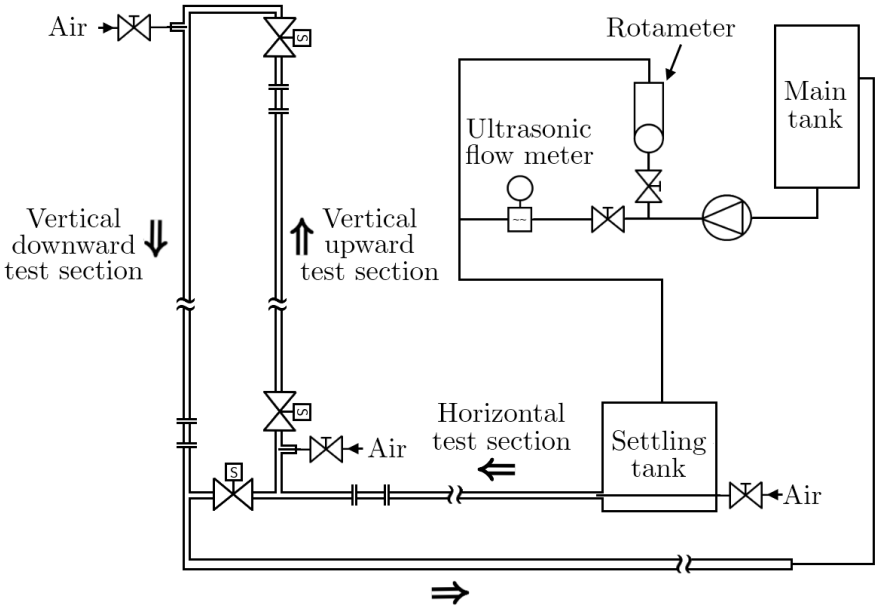

Figure 2: Schematic diagram of the air-water flow loop.

Air could be injected at any one of three ports, which are located, respectively, near the inlets of the horizontal, vertical upward and vertical downward branches. Pressurized air from the laboratory compressed air supply was injected near the inlet of the corresponding vertical section through two plugs threaded on a *cross* fitting. Air mufflers (ALWITCO Model 0579038, North Royalton, Ohio, USA), made of porous stainless steel with a pore size of 50 microns, were mounted to the ends of two branches of the air line, dispersing the air stream into bubbles, which were mixed with the water and transported downstream.

The water and air flow rates were measured by calibrated flow meters and controlled separately to allow the generation of different two-phase flow regimes. The water flow rate was measured using a transit-time ultrasonic flow meter (Omega FDT-30, Laval, Quebec, Canada) and was controlled using a butterfly valve at the exit of the pump. Lower water flow rates were measured using one of three rotameters (King Instruments Series 7510, Gar-

den Grove, California, USA), having different ranges. A rotameter, selected among four devices with different ranges, was used to measure the air flow rate (King Instruments Series 7510, Garden Grove, California, USA).

Three test sections were used, with inner diameters $D = 32.5, 49.2$ and 13.9 mm, respectively. Two pressure taps, 3 mm in diameter and separated axially by a distance equal to the corresponding $D/2$ were drilled on each of the test sections, such that the mid-point between them was located 2.275 m downstream of the air injection location; this corresponded to $L/D = 46.2, 70.0$ and 136.7, for the three sections. The two taps were connected by 6.35 mm I.D. tubing of length 152.4 mm to the two ports of a differential pressure transducer (Validyne DP103, Northridge, California, USA). According to Matsui (1984), the present spacing between the two taps, which is half the tube diameter, would allow the transducer to resolve the passage of a hemispherical cap bubble with a length that is half its diameter. In the present tests, cap bubbles were almost never found to be perfectly hemispherical, so some tests were carried out at the beginning of the study to test the effect of pressure tap distance. It was found that the use of distances much larger than $D/2$ would lead to excessive smoothing of the fluctuations, which would make the flow regimes indistinguishable by the present method. When this distance was reduced to a value that was much lower than $D/2$, it was found that the pressure transducer did not have a temporal response that was adequate for resolving the flow regimes over the entire range of conditions of present interest. This axial separation distance was thus chosen as a compromise between these two factors. To ensure that the pressure lines are always filled with water and free of air bubbles and pockets which would introduce measurement errors, two purge lines were installed. Purging is a well-known technique for ensuring the presence of a single phase in pressure lines (Shearer and Nedderman, 1965). The purge lines diverted high pressure water from the outlet of the pump and into the pressure lines. The flow rates in each of the two purge lines were monitored closely using two rotameters and were always kept equal to each other and at or below 1% of the main water flow rate. This ensured that purging did not cause a drift in the readings of the transducer. In addition, the corresponding pairs of pressure lines and purge lines had the same lengths, which ensured that frictional pressure drops were the same in the two lines. Some measurements were taken under the same flow conditions, with and without purging. During the measurements that were performed without purging, the pressure lines were closely monitored and the measurement was repeated

if any air bubbles were found to have entered the pressure line. From these measurements, it was confirmed that purging has no effect on the differential pressure signal when the pressure lines are free of air bubbles. The presence of bubbles, however, introduced large distortions and non-repeatability to the differential pressure signal.

For each test, first the air and water flow rates were adjusted to the required values using the appropriate flow control valves. To perform density corrections for the air flow rate, atmospheric pressure was measured using a barometer; the air temperature just downstream of the rotameters and the water temperature at the exit of the flow loop were recorded using dial thermometers. The gauge pressure was calculated as the average of the gauge pressures measured by two pressure transducers, located 160 mm upstream and downstream of the measurement location. Measurements of the differential pressure and the gauge pressure were recorded at a rate of 200 samples/s for a time period of 60 s. During this time, the flow regime was observed visually and noted down. This was then repeated for every desired flow rate combination.

During data processing, the air and water superficial velocities were calculated from the corresponding flow rates, taking into account density corrections for air. The differential pressure ΔP was calculated from the differential pressure transducer voltage output and a dimensionless differential pressure parameter was determined as

$$\Delta P^* = 1 - \frac{\Delta P}{\Delta P_{l,s}}, \tag{1}$$

where $\Delta P_{l,s}$ is the pressure difference between the same taps, but with the tube containing still water. According to Matsui (1984), for flows with negligible frictional losses, ΔP^* would be approximately equal to the void fraction in the measurement section. The PDF of ΔP^* was then calculated by a standard algorithm. All data processing was carried out using the open-source computational software package SCILAB 5.4 (Scilab Enterprises, 2013).

4. The PDF of differential pressure in different flow regimes

The differential pressure fluctuations contain three types of contributions: i) "noise", consisting of the combined electronic noise of all devices involved in the measurements and the discretisation noise introduced by the finite resolutions of the data acquisition system and the PDF calculation program;

ii) turbulent pressure fluctuations within each phase; and iii) pressure changes across gas-liquid interfaces.

For an overall comparison of the magnitudes of the three contributions, Table 1 lists the ranges of the variance of the differential pressure parameter in different flow regimes, including still water and air, single-phase water and air flows, and four distinct air-water flow regimes. The values in still fluids represent entirely noise, as the other contributions would be absent in such cases. Because noise may be assumed to be statistically independent of the other two contributions, the noise variance may be subtracted from the variances in the other cases to produce noise-free estimates. It may be seen that noise was likely responsible for a measurable part of pressure fluctuations in single phase flows. In contrast, the noise variance was one to two orders of magnitude smaller than the variance in bubbly flows and entirely negligible by comparison to the variances in slug, churn and annular flows. With the possible exception of the low-variance range of bubbly flows, single-phase pressure fluctuations were also found to be negligible by comparison to two-phase flow fluctuations. At any rate, pressure fluctuations associated with single-phase turbulence and interface passage would be coupled together and cannot be separated in two-phase flows. Hence, the following analysis takes into account both the effects of turbulence and those of the air-water interfaces.

Table 1: Ranges of variances of the differential pressure parameter fluctuations for different flow regimes.

Flow regime	**Variance** ($\times 10^3$)
Still water	0.010 - 0.012
Still air	0.015 - 0.018
Water flow	0.033 - 0.083
Air flow	0.044 - 0.063
Bubbly flow	0.19 - 1.7
Slug flow	2.4 - 250
Churn flow	27 - 64
Annular flow	2.6 - 34

Representative time histories and PDF $f(\Delta P^*)$ of the dimensionless differential pressure parameter ΔP^* in different flow regimes are shown in figure 3. Besides the significant differences in the variances of this parameter from one regime to another, there are differences in the time history waveforms

as well as the shapes of the PDF. These will be discussed in the following paragraphs.

Single phase water or air flows: As indicated in Table 1, the differential pressure fluctuations in single phase water or air flow were very weak, compared to those in air-water flows. The PDF $f(\Delta P^*)$ shows a sharp single peak at $\Delta P^* = 0$ for water flow and $\Delta P^* = 1$ for air flow, which is consistent with the previous assertion that ΔP^* is essentially void fraction.

Bubbly flow: In this regime, pressure fluctuations were relatively weak, compared to those in other air-water flow regimes, but much stronger than those in single-phase flows. $f(\Delta P^*)$ was nearly Gaussian with a peak at a slightly positive ΔP^*. It is noted that, for the flow ranges that were achievable in the present study, fully developed bubbly flow could not be generated in a 32.5 mm I.D. pipe at atmospheric pressure, as required for the calibration (or "training") of the elastic map method. This is in agreement with the observations of several authors (Taitel et al., 1980; Liu, 1993). The flow close to the air injection location was, however, found to be bubbly for certain flow conditions. All bubbly and bubbly-slug measurements for calibration of the elastic map were thus collected at $L/D = 10$.

Bubbly-slug flow: In bubbly-slug flow, the differential pressure fluctuated more than in bubbly flow, as a result of the passage of cap-bubbles. This led to a $f(\Delta P^*)$ that was also nearly Gaussian but with a peak that was two to three times smaller than that in bubbly flow.

Slug flow: In this regime, the flow pattern alternated between bubbly flow in the liquid slugs and annular flow in the Taylor bubbles. Thus, the pressure PDF was double-peaked, with one of the peaks located close to $\Delta P^* = 0$ and the other one close to $\Delta P^* = 1$. The relative heights of the two peaks depended on the relative lengths of the liquid slugs and the Taylor bubbles. The PDF shapes in slug flow filled the shape range between the PDF of bubbly-slug flow, which had a single peak at low ΔP^*, and the PDF of slug-churn flow, which had a single peak at high ΔP^*.

Slug-churn flow: The differential pressure parameter in slug-churn flow had mostly high values, with occasional drops, corresponding to liquid slugs that remained intact long enough to cross the sensor location. Its PDF was single-peaked and negatively skewed.

Churn flow: Churn flow, in which liquid slugs get penetrated by gas bubbles, was the most agitated flow regime. The differential pressure fluctuated strongly and with a relatively high frequency and its PDF was negatively skewed with a peak at high ΔP^*.

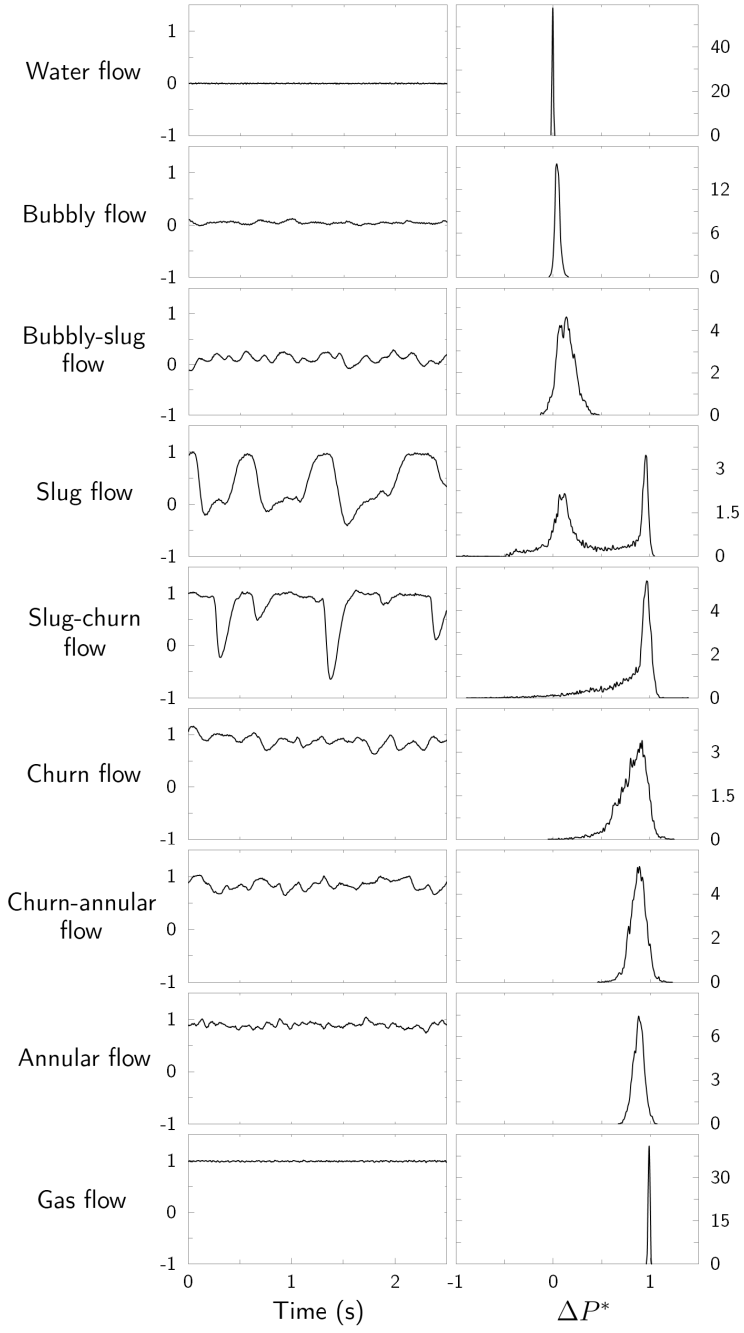

Figure 3: Representative time histories (left) and PDF $f(\Delta P^*)$ (right) of the dimensionless differential pressure parameter in different flow regimes.

Churn-annular flow: Churn-annular flow was less agitated than churn flow, as a result of less frequent formation of liquid slugs. The time histories for both flow regimes looked similar but churn-annular flow had a distinct PDF, which was nearly Gaussian, as opposed to the negatively skewed PDF in churn flow.

Annular flow: Annular flow had small pressure fluctuations compared to churn-annular flow and its PDF was nearly Gaussian. As liquid flow rate increased, the location of the peak moved to smaller values of ΔP^*. This trend may be explained by consideration of frictional pressure losses. Momentum analysis in fully developed, vertical upwards, adiabatic, annular air-water flows indicates that the rate of change of momentum would vanish (by the full development assumption) and that the pressure drop due to increase of elevation would be negligible (as it would be equal to the hydrostatic pressure change in the air core), which leaves frictional pressure loss as the only contributor to axial pressure differences. This pressure loss increases with increasing liquid flow rate, which would reduce ΔP^*, thus causing its PDF peak to move towards lower values.

Flow regime transition surface: Figure 3 clearly shows that each distinct flow regime has a particular and easily identifiable differential pressure PDF. However, it does not illustrate how this PDF changes as flow conditions are varied gradually and continuously so that one regime is succeeded by another. This can be achieved by introducing an additional variable, which we chose to be the gas flow rate under constant liquid flow rate, and plotting the PDF as a three dimensional surface, termed as *transition surface*. Albrecht et al. (1982) presented a similar transition surface, albeit only for the transition from bubbly to slug flow, based on the PDF of neutronic flux signals. Figure 4 shows a transition surface plotted *vs.* the gas superficial velocity in semi-logarithmic axes. This transition surface is continuous and provides a more global view of flow regime transitions than inspection of the individual PDF. Three peaks were identified in all transition surfaces, regardless of the water superficial velocity. The first peak was at the lowest gas superficial velocity possible in the flow loop and corresponded to either a bubbly flow or a slug flow, depending on the pipe diameter and the pressure in the flow loop. The second peak always occurred at the slug to churn flow transition, whereas the third one occurred at the maximum air flow rate that could be achieved in the flow loop and corresponded to the annular flow regime. Visualizing the PDF in this way proves that flow regimes undergo transition in a continuous manner.

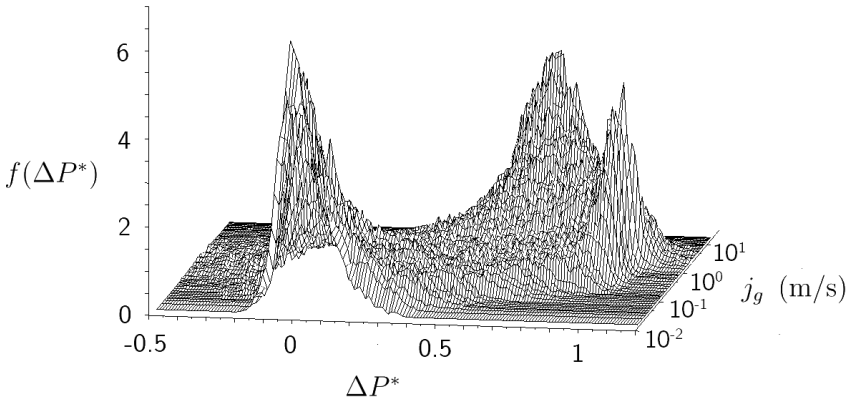

Figure 4: Three-dimensional view of the flow regime transition surface, showing the PDF of the dimensionless differential pressure parameter at different gas superficial velocities and at a constant water superficial velocity ($j_l = 0.35$ m/s).

5. Elastic map construction

In the present work, we used the elastic maps algorithm as implemented by Gorban and Zinovyev (2003) in the C++ package *elmap*, which we accessed on line.

5.1. Calibration database and selection of input parameters

To construct an elastic map of air-water flow regimes, we applied the elastic maps algorithm to differential pressure data collected during a calibration process. The calibration database consisted of 700 calibration measurements of $f(\Delta P^*)$ in a 32.5 mm I.D. pipe at near-atmospheric pressure (100 kPa $\leq P \leq$ 140 kPa). Most measurements were made at an axial location of $L/D = 70$, but the bubbly and bubbly-slug flow measurements were made at $L/D = 10$. Although the latter two flow regimes could not be observed in the downstream part of the pipe used for calibration in the range of calibration pressures, they appeared in the larger pipe, whose diameter was nearly equal to the critical diameter for the existence of bubbly flow (Taitel et al., 1980). They also appeared in the calibration pipe at a higher pressure, as a result of the increased gas density and surface tension, which resulted in smaller bubble sizes. The water superficial velocity was varied in the range from 0.04 to 0.4 m/s and the air superficial velocity was varied in the range from 0.014 to 22 m/s.

An important step in the implementation of elastic maps is the selection of parameters that define each input data point. Like any machine learning algorithm, the elastic maps algorithm can take any number of input parameters per data point and process these parameters to give a corresponding output, which, in this case is the flow regime. The number of input parameters is called the *dimension* of the input. The performance of any of these algorithms is influenced by the number and choice of input parameters. Choosing an insufficiently large number of input parameters or parameters that are not well-correlated to the output would result in a very poor prediction performance of the algorithm, because the output would not be uniquely defined by the input. On the other hand, choosing an excessively large number of input parameters would result in the, so-called, *curse of dimensionality*, namely the algorithm would require an extremely large number of data points to produce statistically reliable results; moreover, organization of the data points in distinct groups would be more challenging, unless a huge number of data points were used.

We have so far demonstrated that the shape of the PDF of the differential pressure parameter alone is a strong indicator of flow regime. An accurate representation of each PDF would require the separation of the ΔP^* axis into a large number of bins. In the previous presentation of PDF, the bin width was 0.01, which produced PDFs that were approximated by 171 discrete values in the considered range $-0.5 \leq \Delta P^* \leq 1.2$. The "dimension" 171 was unacceptably large for the present problem, and so we reduced it to 35, which corresponds to a bin width of 0.05; this dimension was sufficiently low not to introduce the curse of dimensionality, yet it represented sufficiently accurate approximations of all measured PDF. In order to keep the values of the input parameters within known bounds, we have converted the PDF to relative frequencies of data points within each bin. A representative plot of such relative frequencies, with a comparison to corresponding PDF values, is shown in Figure 5.

Several user-defined inputs are required for the construction of an elastic map, including the following ones: i) the map topology, namely whether the map is two or three-dimensional and the map size and shape; ii) stretching/bending penalties and softening strategy; iii) adaptation options; and iv) extrapolation options. We repeated the calculations using different combinations of these map parameters and selected values (see appendix) that ensured sufficient separation between the projections of data points belonging to different flow regimes. It should be noted that the data points are not

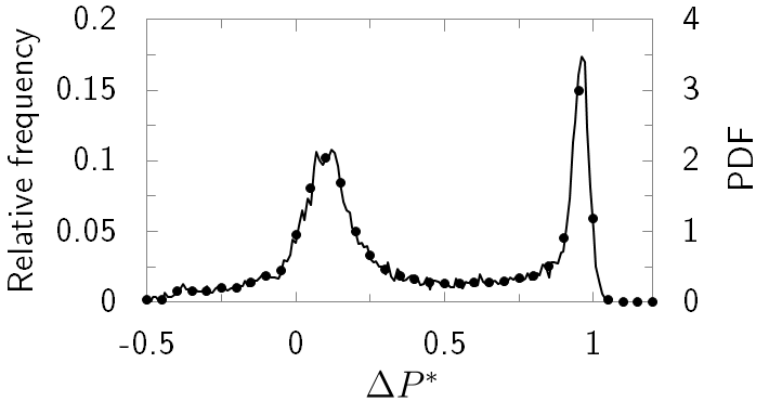

Figure 5: A representative PDF of ΔP^* (solid line) and the relative frequencies (points) that were used in its stead for elastic map construction.

affected by changes in the map parameters, but the map is modified to give the best "viewing perspective".

5.2. Map construction

The *elmap* package produces as output the co-ordinates of the elastic map nodes in multi-dimensional space, as well as the connectivity between the nodes, namely, it identifies nodes that form edges, ribs and triangles. With the knowledge of the map nodal co-ordinates and nodal connectivity, it is possible to project any arbitrary $f(\Delta P^*)$ to this map. The portion of the *elmap* program responsible for projection was implemented separately in an in-house code using the open source mathematical package SCILAB for more versatility in testing new data points. The projections of the calibration data points on the final map are shown in Figure 6. The contour of each *map zone* that is occupied by data points belonging to a particular flow regime was drawn manually, as shown in the figure. Note that parts of the zones shown in Figure 6 are bounded by dotted lines, which indicate the extent of each zone as identified by the present calibration data; some zones were extended, as will be described in the next section.

It is noted that every point on the map corresponds to a particular PDF shape, so that unoccupied regions of the map correspond to PDF shapes that were not encountered in the calibration. It was observed that the area occupied by each flow regime map zone generally increased with an increasing diversity of shape of the PDF corresponding to that flow regime. The two

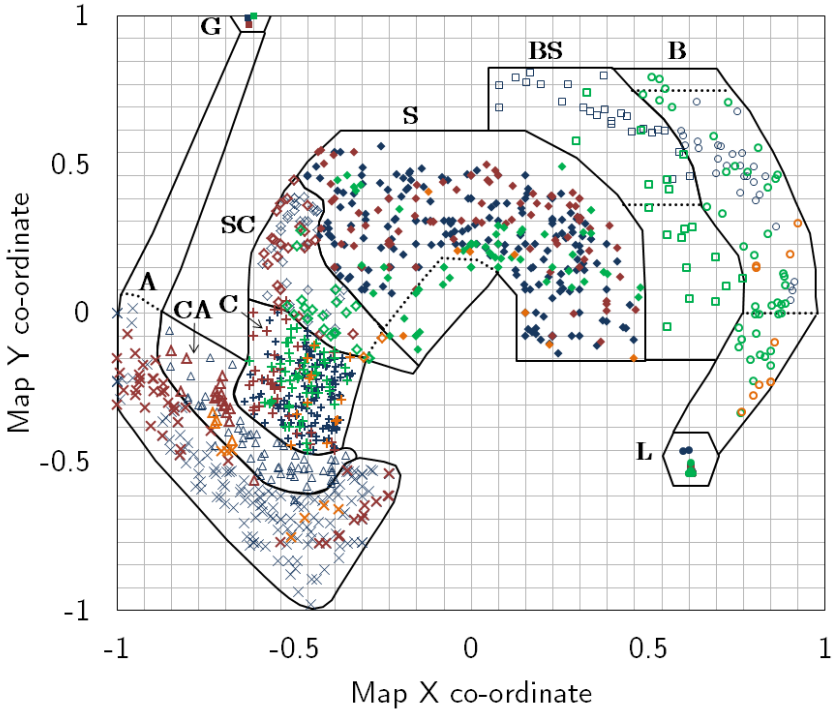

Flow regime	Data points	Map zone
Liquid	●	***L***
Bubbly	○	***B***
Bubbly-slug	□	***BS***
Slug	◆	***S***
Slug-churn	◇	***SC***
Churn	+	***C***
Churn-annular	△	***CA***
Annular	×	***A***
Gas	■	***G***

Dataset	Marker colour
Calibration (D=32.5 mm, P=100 - 140 kPa)	
Testing (D=32.5 mm, P=100 - 140 kPa)	
Larger diameter (D=49.2 mm, P=100 - 140 kPa)	
Higher pressure (D=32.5 mm, P=200 - 240 kPa)	

Figure 6: Elastic map with demarcated map zones for different flow regimes. Calibration map zone boundaries that were modified are shown as dotted lines.

single-phase (liquid and gas) regime map zones occupied very small areas, essentially areas around a point; this is consistent with the fact that the variation of single-phase pressure difference PDF was extremely small and was entirely the result of noise and turbulence. All two-phase flow regime map zones occupied significant areas. The slug flow regime map zone was the most extensive, which is consistent with the fact that slug flow occurs over most of the working range of void fractions (Jones and Zuber, 1975). The sizes of the transitional regime map zones were smaller than those of the adjacent map zones, indicating that each transitional regime occurred over a relatively narrow range of flow conditions and had a relatively small variety of PDF shapes. Even so, the data points in a transitional regime did not collapse on the boundary line between two distinct regimes, which justifies the assignment of zones to transitional as well as distinct regimes.

5.3. Map sensitivity to training dataset size

In an effort to determine the minimum training dataset size required for accurate flow regime identification, we calculated the sensitivity of map accuracy to the number of calibration data used for algorithm training. Seven different elastic maps were constructed, each using a number of calibration points from 100 to 700 in steps of 100. These maps were then tested for regime identification of 223 test cases at calibration conditions. Two error metrics were used to quantify the performance of these maps: i) the percentage of test cases for which the flow regime was identified incorrectly and ii) the percentage of test cases that lay outside the calibrated map zones. As can be seen in Figure 7, both error metrics generally decreased with increasing size of the calibration dataset. Significant drops in both errors occurred as the number of calibration data was increased from 100 to 200, but for further increases of the calibration data number the error decrease was very moderate, if any at all. So, if 2-4% errors can be tolerated in a particular application, it would be possible to train the algorithm with only 200 points. For higher accuracy, more calibration points would be required, but it appears that accuracy would be unaffected by an increase of this number beyond about 500-600, which may be deemed to be an optimal training dataset size. To achieve the highest possible identification accuracy, we presently used the slightly larger size of 700 calibration points.

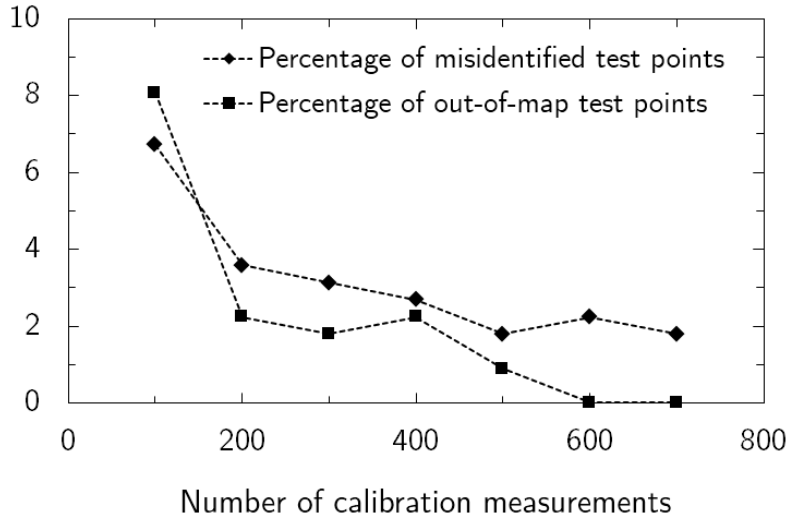

Figure 7: Effect of the number of calibration measurements on the flow regime identification accuracy by the elastic map method.

6. Elastic map testing and expansion

6.1. Testing and expansion procedures

The prediction performance of the newly constructed map was tested using "new" data that were not used for the *training* of the elastic maps algorithm, namely the map construction described in the previous section. New data were first taken at the same conditions as the calibration data, to serve for validation of the algorithm. Additional data were taken in pipes of different sizes and at different pressures, so that the effects of pipe size and pressure, if any existed, could be investigated. The identification of the flow regime of a new data point by the algorithm was deemed to be correct, if the projection of its $f(\Delta P^*)$ was found by inspection to lie within a calibrated map zone and if that zone corresponded to the visually identified flow regime. For convenience, we automated this process using a simple point-in-polygon algorithm programmed in SCILAB. The boundary of each map zone was approximated by a polygon and the algorithm iteratively identified the polygon that enclosed the projection of each data point, if such existed. If the projected point was found to be in the unoccupied map area, its regime was designated to be the one of the nearest map zone and the point was flagged for the user to confirm its status by inspection.

Even before attempting to identify the regimes of new results, we anticipated that some of their projections would lie outside the map zones constructed from calibration data. The reason for this is not that the algorithm fails, but that some ranges of PDF shapes achieved under the new tests were not possible to achieve in our facility during the calibration tests. In some cases, even entire flow regimes were unattainable for some pipe sizes, although they could be attained for others. Consequently, we expected that some of the map zone boundaries would need to be expanded in order to accommodate out-of-range new measurements. This zone boundary expansion is equivalent to an extended calibration of the elastic map and in fact helps resolve some apparent discontinuities of the original map. In particular, the isolation of the two single-phase zones from all two-phase zones contradicts physical intuition: if one gradually introduced air into a liquid flow, one would expect a continuous transition from liquid to bubbly regime, which means that the bubbly zone should share a boundary with the liquid zone; one may use similar arguments to demonstrate that the annular zone should share a boundary with the gas zone. Although not predictable quantitatively, the extension of some or all calibration map zones into unoccupied map areas seems to be very plausible. Whether or not the extended zones would be populated by any new points in the present experiments is specific to our experimental facility and could be resolved to some degree by future tests in a modified setup.

6.2. Flow regime identification for same pipe and pressure

This test was applied to 223 measurements in the 32.5 mm I.D. pipe, at near-atmospheric pressure (100 kPa $\leq P \leq$ 140 kPa) and at a measurement location with $L/D = 70$. The projections of the test points on the elastic map are shown in Figure 6. The elastic map showed an outstanding performance with the test dataset with only four out of 223 test points (1.8%) misclassified. All misclassifications happened for points that were very close to the map zone boundaries between two flow regimes. Inspection of the individual PDF of these data points indicates that they are compatible with those in the flow regime into which they were classified by the elastic map algorithm. Therefore, these discrepancies could possibly be attributed to ambiguity in the visual observation of flow regime.

6.3. Flow regime identification for different pipe sizes

To test the applicability of the constructed elastic map to air-water flows in a larger pipe, 215 differential pressure measurements were collected in the 49.2 mm I.D. pipe at near-atmospheric pressure and at different air and water superficial velocities ($0.09 \leq j_l \leq 0.44$ m/s; $0.006 \leq j_g \leq 7.9$ m/s), which spanned as many flow regimes as possible. In contrast to the smaller calibration pipe, this pipe permitted the generation of bubbly and bubbly-slug flows at low gas superficial velocities. However, due to the limited capacity of our compressed air supply system, we were unable to produce any churn-annular or annular flows in this pipe. The projections of these test points on the elastic map are shown in Figure 6. 49 out of 215 points (22.8%) lay outside any of the calibrated map zones but were correctly classified using the extended map.

Differential pressure measurements were also collected in the smaller pipe, which had a diameter of 13.9 mm. The pressure taps were placed at a distance of $D/2 =$ 6.95 mm apart, for which the differential pressure transducer dynamic response reached its limitations. Consequently, only 15 measurements were taken, all of which were in slug, churn and annular flows at the lowest liquid flow rate possible in the present facility, which was $Q_l = 2.94 \times 10^{-5}\text{m}^3/\text{s}$ ($j_l = 0.194$ m/s). The flow regimes for all these cases were successfully identified by the elastic map. These results are not presented in the figure to avoid clutter.

6.4. Flow regime identification at a different pressure

The predictions of the elastic map were also tested for flow in the 32.5 mm I.D. pipe in the absolute pressure range from 200 to 240 kPa, which was roughly twice the calibration pressure. Two air-water flows with the same superficial velocities but at different pressures may be in different flow regimes, due to differences in air density. The elastic map, however, is intended to identify the regime irrespectively of external flow conditions. Therefore, the objective of this test is to reveal whether the shape of the pressure difference PDF depends significantly on absolute pressure or not, or, in other words, whether the same elastic map applies to flows at different absolute pressures. It was found that bubbly flow could be produced in the test section at $L/D = 70$ at the higher pressures, whereas this was not possible at near-atmospheric pressures. A total of 44 measurements were made under these conditions and the projections of the measurement points onto the elastic map are shown in Figure 6. The projections of all test points were found to

lie within the extended map zones that corresponded to the visually identified regimes.

7. Comparison to previous work

This section presents comparisons of the elastic map method with three other machine learning algorithms that have been used by other authors for flow regime identification. These include the following ones: i) artificial neural networks (ANNs), used by Mi et al. (1998), Sun and Zhang (2008), Julia et al. (2008) and Tambouratzis and Pazsit (2009) with a variety of input signals; ii) the method of support vector machines (SVM), used by Trafalis et al. (2005) with superficial velocities and pipe diameter as inputs; and iii) self-organizing maps (SOM), used by Mi et al. (1998) to reduce the dimensionality of features derived from an impedance void meter; in the latter method, map nodes that corresponded to each flow regime were identified using a training dataset and test points were classified into different flow regimes depending on the closest map node. As there is no general rule for the appropriate size of a self-organizing map, SOM with two different sizes were tested. The small SOM was composed of 12×12 nodes while the large one was composed of 26×26 nodes.

The results of this comparison are presented in Table 2. In each case, the same dataset consisting of the relative frequency vectors of 700 training points was used to train the algorithm. The algorithm parameters for the ANN and SVM were chosen so as to minimize the ten-fold cross-validation error*. The trained algorithm was then tested on the same three test sets presented previously, namely sets of measurements at the training conditions, in a larger diameter pipe and at a higher pressure, respectively. The accuracy of each algorithm in predicting the flow regime for each of the datasets was then calculated as the percentage of correctly classified measurements in the corresponding dataset. Table 2 shows that all of the algorithms, except for the small SOM, performed very well with the training dataset.

*This procedure can be summarized as follows. The training dataset was partitioned into ten parts of equal size. The algorithm was trained using nine parts and the tenth part was used for testing purposes, namely for calculating the identification error. This process was repeated ten times using each of the ten parts for testing and the corresponding ten identification errors were averaged to give the ten-fold cross-validation error.

Table 2: Flow regime identification accuracy (%) of different machine learning algorithms.

	Dataset			
	Calibration	Testing	Larger diameter	Higher pressure
Elastic map	100	98.2	100	100
ANN	99.1	89.2	76.2	70.5
SVM	100	88.5	61.7	70.5
SOM (small)	94.9	94.2	83.6	88.6
SOM (large)	100	94.6	82.1	84.1

The ANN and SVM had accuracies of about 89% with the test set. Learning curves were plotted for both of these cases and they showed that the algorithms suffered from high bias, which implies that an increase in the number of training measurements would likely improve their performance with the test dataset. However, both of these algorithms performed very poorly with the datasets at experimental conditions that differed from those of the training set. This is not surprising, because these methods are known to perform well only within the range of conditions for which they were trained.

The smaller SOM was found to have a better generalization performance than the larger one, whereas the larger SOM provided a more detailed view of the data (Figure 8). In both cases, the performance for conditions outside the training ranges was inferior to that at the calibration conditions. Although the SOM method appears to be fairly similar to the present one, it also has several key differences that lead to a much poorer performance with the present differential pressure data. In SOM, as in elastic maps, nodes belonging to the same flow regime usually lie in the same region of the map; nevertheless, SOM do not have the gradual progression of the flow regime zones from single phase liquid flow to single phase gas flow that was observed in the elastic map. The SOM tends to conform to the data very well, however, this leaves no room on the map for points outside the calibration range. Such points may appear anywhere on the map, *i.e.*, they are not necessarily classified in a "similar" flow regime. SOM use piecewise constant projecting, whereby each point is projected to the closest map node. This is in contrast to the piecewise linear projection used in elastic maps, as explained earlier. Piecewise linear projection provides a much more detailed view of the data because projected points can lie anywhere on the map, not just at the node

locations. Theoretically, both methods of projection would be equivalent if an infinite number of nodes were used for their construction, however, this is not computationally feasible.

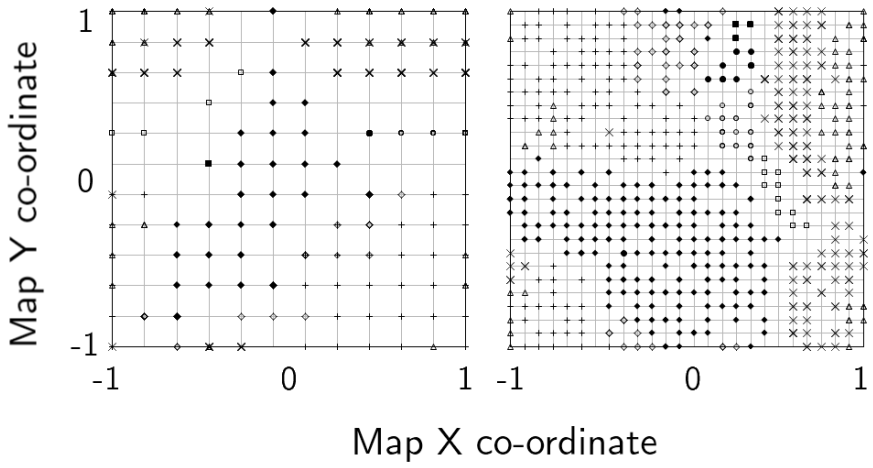

Figure 8: Small (left) and large (right) self-organizing maps, showing projections of the training points used in calibration (symbols as in Figure 6).

It is clear from the previous discussion that the present method offers some key advantages over existing ones. It is more accurate than other methods in identifying the flow regime of points within the calibration range of flow conditions. The possibility of using physical intuition to extend the map zone boundaries also makes this method much better at identifying the flow regime of points outside the calibration range of flow conditions. Unlike previous algorithms, elastic maps illustrate continuously and progressively flow regime transition and provide insight into the state of gas-liquid flow in a pipe, rather than merely labelling flow regime.

8. Summary and concluding remarks

A new method for the identification of the flow regime of a gas-liquid flow in a pipe has been developed and validated within different ranges of pipe diameter and absolute pressure. This method identifies different regimes using as criterion the shape of the PDF of the dimensionless differential pressure parameter. The elastic maps algorithm projects discretised versions of

these PDF onto a two-dimensional map and it was found that the projections of the PDF measured in all flows that belonged to the same regime were clustered within bounded zones that were clearly separated from zones that corresponded to other regimes. Transitional regimes appear on the elastic map as zones rather than lines, which indicates that transition from one distinct regime to another is not abrupt, but occurs gradually as flow conditions are changed within a finite range.

A calibration map was first constructed from tests in a particular pipe within a narrow range of absolute pressure. The algorithm accuracy was then tested against previously unused test results in the same pipe and within the same range of pressure and was found to be excellent. The calibration map was also tested against experimental data collected in pipes of two different diameters and in the calibration pipe but at a higher pressure. Most of the PDF projections for these tests fell within the appropriate calibration zones, but some cases, which had PDF shapes that were not encountered during calibration, had projections that fell outside any of the calibration zones. The zones were then expanded in a physically consistent manner to accommodate all data.

The present approach for gas-liquid regime identification is the successful combination of two distinct and novel elements: the differential pressure PDF and the elastic map algorithm. Compared to other measurable properties, the use of differential pressure as a criterion for identifying flow regime offers significant advantages, as it is relatively inexpensive and easy to implement, it is non-intrusive, it requires no optical access to the flow, and it poses no radiation hazards or other health and safety concerns. As long as a pressure transducer with adequate frequency response is used and the connecting lines are purged of gas bubbles and pockets, differential pressure PDF is a strong and reliable indicator of flow regime, and it is also insensitive to pipe size and absolute pressure, within common ranges of interest. Another advantage of this approach is that one does not need to monitor flow conditions or other properties, as the dimensionless differential pressure parameter is self-normalized and does not require any corrections or adjustments of any sort. Calibration and use of the method can be done in separate facilities; for example, one may collect calibration data in a laboratory and use the technique for regime identification in a hard-to-access industrial environment. Of course, the requirement of performing calibration tests with the same instrumentation and the same transducer connection setup as those in the main tests remains a necessity.

In this article, the method of elastic maps has been applied for the first time for flow regime identification. This method is generic, versatile, and accurate, it can be automated, and it can be implemented using essentially any signal that discriminates between flow regimes. In fact, we intend to apply the elastic map method to other types of signals, as these may be more convenient for some applications. Like the long-standing classical flow regime map approaches, the elastic map method provides a visual output, in which each flow case is represented by a point that lies within a particular flow regime zone in a map. This offers an advantage over some other machine learning techniques, which merely assign a regime label to a particular input. With the use of an elastic map, one can identify cases within a regime that are close to each other and distinguish cases which may be prone to transition to another regime, should any of the flow conditions change by a relatively small amount. Compared to three previously suggested machine learning algorithms, the elastic maps algorithm had a superior performance in identifying the gas-liquid flow regime.

Potential users of the present method may contact the authors for obtaining the scripts written to supplement the *elmap* C++ code.

Acknowledgements

Financial support for this study was provided by the Natural Sciences and Engineering Research Council of Canada (NSERC), Atomic Energy of Canada Limited (AECL) and the University Network of Excellence in Nuclear Engineering (UNENE).

Appendix

Elastic map parameters used in present study
Grid type: Rectangular
Initial grid size: 15×15
Number of epochs: 2
Epoch settings
Epoch 1 : Edge penalty: 0.1, Rib penalty: 200
Epoch 2 : Edge penalty: 0.001, Rib penalty: 30
Adaptation
Type: Break
Edge penalty: 0.001, Rib penalty: 1

Number of adaptation steps: 20
Extrapolation steps: 6 (Final grid size: 27×27)

References

Albrecht, R., Crowe, R., Dailey, D., Damborg, M., Kosaly, G., 1982. Measurement of two phase flow properties using the nuclear reactor instrument. Prog. Nucl. Energy 9, 37–50.

Brown, R., Sullivan, G., Govier, G., 1960. The upward vertical flow of air-water mixtures III: Effect of gas phase density on flow pattern, holdup and pressure drop. Can. J. Chem. Eng. 38 (2), 62–66.

Dergachev, V., Gorban, A., Rossiev, A., Karimova, L., Kuandykov, E., Makarenko, N., Steier, P., 2001. The filling of gaps in geophysical time series by artificial neural networks. Radiocarbon 43 (2A), 365–371.

Gorban, A., Zinovyev, A., 2001. Visualization of data by method of elastic maps and its applications in genomics, economics and sociology. Preprint of Institut des Hautes Etudes Scientifiques M/01/36.

Gorban, A., Zinovyev, A., 2003. *elmap*: C++ package. Available online: http://bioinfo-out.curie.fr/projects/elmap/. Last accessed: 17 November 2013.

Gorban, A., Zinovyev, A., 2005. Elastic principal manifolds and their practical applications. Computing 75 (4), 359–379.

Gorban, A., Zinovyev, A., 2007. Principal Manifolds for Data Visualisation and Dimension Reduction. Springer: Berlin-Heidelberg-New York, Ch. Elastic Maps and Nets for Approximating Principal Manifolds and Their Application to Microarray Data Visualization, pp. 97–131.

Gorban, A., Zinovyev, A., 2009. Handbook of Research on Machine Learning Applications and Trends: Algorithms, Methods and Techniques. IGI Global: Hershey, PA, USA, Ch. Principal Graphs and Manifolds, pp. 28–59.

Gorban, A. N., Zinovyev, A. Y., 2008. Principal Manifolds for Data Visualization and Dimension Reduction. Springer Berlin Heidelberg, Ch. Elastic maps and nets for approximating principal manifolds and their application to microarray data visualization, pp. 96–130.

Hibiki, T., Ishii, M., 2003. One-dimensional drift-flux model for two-phase flow in a large diameter pipe. Int. J. Heat Mass Tran. 46, 1773–1790.

Jones, O., Zuber, N., 1975. The interrelation between void fraction fluctuations and flow patterns in two-phase flow. Int. J. Multiphase Flow 2, 273–306.

Julia, J., Liu, Y., Paranjape, S., Ishii, M., 2008. Upward vertical two-phase flow local flow regime identification using neural network techniques. Nucl. Eng. Des. 238, 156–169.

Liu, T., 1993. Bubble size and entrance length effects on void development in a vertical channel. Int. J. Multiphase Flow 19 (1), 99–113.

Lucas, D., Krepper, E., Prasser, H.-M., 2005. Development of co-current air-water flow in a vertical pipe. Int. J. Multiphase Flow 31, 1304–1328.

Matsui, G., 1984. Identification of flow regimes in vertical gas-liquid two-phase flow using differential pressure fluctuations. Int. J. Multiphase Flow 10, 711–720.

Mi, Y., Ishii, M., Tsoukalas, L., 1998. Two-phase flow identification using advanced instrumentation and neural networks. Nucl. Eng. Des. 184, 409–420.

Mi, Y., Ishii, M., Tsoukalas, L., 2001. Flow regime identification methodology with neural networks and two-phase flow models. Nucl. Eng. Des. 204, 87–100.

Nishikawa, K., Segokuchi, K., Fukano, T., 1969. On the pulsation phenomena in gas-liquid two-phase flow. B. JSME 12, 1410–1416.

Resta, M., 2007. Portfolio optimization through elastic maps: Some evidence from the italian stock exchange. LECT NOTES COMPUT SC 4693, 635–641.

Rouhani, S., Sohal, M., 1983. Two phase flow patterns: A review of research results. Prog. Nucl. Energy 11, 219–259.

Scilab Enterprises, 2013. Scilab 5.4: Free and open source software for numerical computation. Available online: http://www.scilab.org. Last accessed: 17 November, 2013.

Shearer, C., Nedderman, R., 1965. Pressure gradient and liquid film thickness in co-current uupward flow of gas/liquid mixtures: Application to film-cooler design. Chem. Eng. Sci. 20, 671–683.

Spedding, P., Woods, G., Ragunathan, R., Watterson, J., 1998. Vertical two-phase flow, Part I: Flow regimes. Trans. IChemE 76, 612–619.

Sun, Z., Zhang, H., 2008. Neural networks approach for prediction of gas-liquid two-phase flow pattern based on frequency domain analysis of vortex flowmeter signals. Meas. Sci. Tech. 19, doi:10.1088/0957–0233/19/1/015401.

Taitel, Y., Bornea, D., Dukler, A., 1980. Modelling flow pattern transitions for steady upward gas-liquid flow in vertical tubes. AIChE J. 26 (3), 345–354.

Tambouratzis, T., Pazsit, I., 2009. Non-invasive on-line two-phase flow regime identification employing artificial neural networks. Ann. Nucl. Energy 36, 464–469.

Trafalis, T., Oladunni, O., Papavassiliou, D., 2005. Two-phase flow regime identification with a multiclassification support vector machine (SVM) model. Ind. Eng. Chem. Res. 44, 4414–4426.

Wang, H., Zhang, L., 2009. Identification of two-phase flow regimes based on support vector machine and electrical capacitance tomography. Meas. Sci. Tech. 20, doi:10.1088/0957–0233/20/11/114007.

Zinovyev, A., Gorban, A., 2003. Self-organizing approach for automated gene identification. OPEN SYST INF DYN 10 (4), 321–333.

Chapter 5

Measurement of gas and liquid flow rates in two-phase pipe flows by the application of machine learning techniques to differential pressure signals

In this chapter, a machine–learning procedure for the measurement of the flow rates of both phases in vertical upward air–water flow is proposed. The procedure involves calculation of the PDF and power spectral density of normalized differential pressure. This is followed by reduction of these properties to a small number of independent features, then using neural networks to correlate these features to the phase flow rates. The chapter is presented in the form of the article

> "Shaban, H. and Tavoularis, S. 2014 Measurement of gas and liquid flow rates in two-phase pipe flows by the application of machine learning techniques to differential pressure signals. *Int. J. Multiphase Flow* **67**, 106-117"

which was submitted to the *International Journal of Multiphase Flow* on 26 May 2014 and accepted for publication on 27 August 2014.

Measurement of gas and liquid flow rates in two-phase pipe flows by the application of machine learning techniques to differential pressure signals

H. Shaban, S. Tavoularis*

Department of Mechanical Engineering, University of Ottawa, 161 Louis Pasteur, Ottawa, ON K1N 6N5, Canada

Abstract

A new method for the determination of gas and liquid flow rates in vertical upward gas-liquid pipe flows has been proposed. This method consists of an application of machine learning techniques on the probability density function (PDF) and the power spectral density (PSD) of the normalized output of a differential pressure transducer connected to two axially separated wall pressure taps in the pipe. The two-phase flow regime was first identified by the application of the elastic maps method on the differential pressure PDF. The transducer signal was then pre–processed using Principal Component Analysis, and independent features were extracted using Independent Component Analysis. The extracted features were used as inputs to multi–layer back–propagation neural networks, which gave the phase flow rates as output. The present method was used to calibrate a differential pressure sensor to estimate the flow rates of both phases in air–water flow in a vertical pipe of diameter 32.5 mm and in the pressure range from 100 to 140 kPa. Predictions of the present method were in good agreement with direct flow rate measurements. Compared to previously used methods of feature extraction from differential pressure signals, the present method was the only one to have a good, consistent performance over all flow regimes and for all flow conditions encountered in this study.

Keywords: two–phase, flow rates, differential pressure, independent component analysis, principal component analysis, neural networks

1. Introduction

The present research was motivated by the need to measure simultaneously and economically the liquid flow rates in a large number of pipes containing air-water mixtures. This situation arises in laboratory models of nuclear reactor header-feeder systems under conditions simulating hypothetical nuclear accidents, such as loss-of-coolant accidents. In these cases, the feeder tubes would supply emergency coolant to the fuel channels of the reactor core and it is paramount that each feeder provides sufficient liquid flow to adequately cool the corresponding fuel channel.

A thorough review of multiphase flow rate measurement methods was presented by Falcone et al. (2002) and Thorn et al. (2013). A classical method of measuring the gas-liquid flow rates is the separation of the flow into gas and liquid streams and then measuring the flow rate of each stream using single phase flow meters. This method is accurate and reliable, but it is also highly intrusive and requires the use of expensive and bulky separators.

Methods that do not require phase separation, commonly referred to as Multiphase Flow Meters (MFMs), have also been developed. Ideally, MFMs would measure the void fraction and both phase velocities directly. Numerous options exist for relatively accurate measurements of void fraction, however, direct measurement of either phase velocity is very hard for practical reasons. The cross–correlation method is a common indirect approach for estimating the interfacial velocity from the average time of flight of the gas–liquid interfaces between two axially spaced signal detectors (for example, Dong et al. (2005); Tan and Dong (2006)). This method can only be used when there is a clearly defined interface normal to the streamwise direction, as in bubbly and slug flows, so it would not be suitable for annular flows, for example; moreover, the relationship between the interfacial velocity calculated using the cross–correlation method and the velocity of either phase may be unknown or even non-unique under some flow conditions (Falcone et al., 2002). For example, calculation of the gas flow rate by integrating the product of void fraction and gas velocity requires knowledge of the temporal and spatial distribution of these properties. The cross–correlation method cannot provide a time history of gas velocity, because its output is a single–valued

estimate of the average interfacial velocity, under the assumption that the temporal fluctuations of gas velocity would be negligible. We have discussed this issue in detail in a separate manuscript (Shaban and Tavoularis, 2014b), in which we proved that neglecting the temporal or spatial fluctuations of the gas velocity would introduce errors in the predictions of gas flow rate, especially at relatively large gas and liquid flow rates. A main conclusion of that work is that the cross–correlation method is capable of estimating fairly accurate the phase flow rates only within very narrow ranges of flow conditions.

Some MFMs are based on differential pressure measurement across obstructions, including Venturi tubes (for example, Meng et al. (2010)) and orifice plates (for example, Lin (1982); Zhang et al. (1992)), along with estimates of mass quality at the measurement location. Venturi tubes and orifice plates can be calibrated to measure the mass flow rate of the two–phase mixture from the pressure drop across the device. Empirical correlations are typically used to obtain the mass quality of the flow from the void fraction, measured using a void fraction meter. The mass flow rate of each phase can then be calculated separately by using the mixture mass flow rate and the mass quality. It is required, when using these devices, for the flow to be homogenized upstream of the measurement device to avoid dependence of the results on the flow regime and to ensure reproducibility. Another general limitation of these methods is that they rely on empirical models and so become specific to a particular flow set–up, in which they need to be calibrated.

Another type of MFMs is based on the application of machine learning regression techniques, such as neural networks or support vector regression, on some features of a measured parameter (pressure, conductivity and radiation attenuation, among others), whose fluctuations correspond to fluctuations in the phase composition of the flow. For example, Beg and Toral (1993) presented a method based on pattern recognition of features derived from the time histories of differential and absolute pressure signals across an orifice plate in horizontal air–water pipe flow with a homogenizing device. Cai and Toral (1993) expanded on this study and used first a Kohonen self–organizing map to classify the flows into different regimes and then neural networks to estimate the gas and liquid flow rates. Minemura et al. (1998) used a correlative mapping method to calculate the phase flow rates from stochastic features derived from the differential pressure signal across a Venturi tube, preceded by an eccentric elbow, which homogenized the flow. In another study, Meribout et al. (2010) used neural networks along with features ex-

tracted from the signals of five different types of sensors (including acoustic, impedance and pressure signals) to estimate the phase flow rates with a 5% uncertainty. Most recently, Fan and Yan (2013) used neural networks to estimate the gas and liquid flow rates for measurements in the slug flow regime, from mechanistic features extracted from the conductance signals of two probes. MFMs of this type also need to be calibrated before use, but they may potentially utilize, as an input, any flow property that varies with phase composition, thus introducing the possibility of a non-intrusive measurement. When the flow property, that is used as an input, can be measured by relatively inexpensive means, such methods can be quite economical.

The present study is aimed at developing an accurate two–phase flow metering method that would be suitable for simultaneous and cost–effective flow rate measurements in vertical upward gas–liquid flows in a large number of pipes. Such a method should, ideally, be free of complicated or expensive instrumentation and be non–intrusive. It should operate effectively in all flow regimes, without prior knowledge of the regime or the need for homogenizers. Previous experimental studies in facilities with large numbers of pipes have been performed by either limiting the number of pipes in which measurements were collected (Kowalski and Hanna, 1989) or by utilizing a single set of instruments for successive measurements in all of the pipes (Teclemariam et al., 2003), which required an excessive amount of time for measurements at each set of flow conditions. Following evaluation of various options, we chose the following approach: a) differential pressure transducers connected to taps in a straight pipe were used as sensing devices; b) principal component analysis and independent component analysis were used to extract independent features from the differential pressure signals; and c) neural networks models were used to correlate these features to the gas and liquid flow rates. The flow regime was identified from the same differential pressure signals by the use of the method of elastic maps, which has been developed by Shaban and Tavoularis (2014a); for brevity, this article will be henceforth referred to as ST1. The present method of flow regime identification may also be applied to signals provided by other instruments, such as impedance void meters (Mi et al., 1998), electrical capacitance tomographs (Jeanmeure et al., 2002) and conductivity probes (Julia et al., 2008). In the following sections, the data analysis and machine–learning techniques that were used in this study will be introduced, then the proposed method will be outlined and, finally, some representative results will be presented and compared to those obtained with the use of approaches introduced by previous authors.

2. Background

2.1. Terminology

Standard terminology, as established in machine–learning analysis, will be used in the following sections; some of these terms will be defined here for clarity. A *dataset* is a collection of data points, called *examples*, each of which can be represented as a vector of several values, called *features*. The number of features is called the *dimension* of the dataset. For instance, in the present study, the input dataset comprises differential pressure measurements, each of which is an input example composed of 12000 input features, which are discrete values recorded at a rate of 200 samples/s over a time interval of 60 s; therefore, this dataset has a dimension equal to 12000. Machine learning algorithms can be used for *classification*, which is a process providing, as output, a class selected among a set of classes. They can also be used for *regression*, which is a process providing, as output, a real number. An algorithm is first used to *train* a model on a certain portion of the entire dataset, called the *training set*. The objective of the training process is to calculate the unknown coefficients/weights in the model. The process of determining the optimal values of the user–specified parameters in the models is called *validation*. Finally, the trained algorithm is tested against a *test set*, which was not used for the calculation of the model coefficients or the selection of the model parameters. A trained algorithm that performs equally well on both the training and the test datasets is said to have good *generalization* performance. In some cases, a trained algorithm performs very well with the training dataset but very poorly for test examples, even if they are within the calibration (training) range, a situation referred to as *overfitting*.

2.2. Independent Component Analysis (ICA)

Independent Component Analysis (ICA) is a signal processing method for representing a measured signal as a linear summation of several independent components (Hyvarinën and Oja, 2000). Besides its use to decompose a signal into additive components, ICA can also be used for feature extraction and dimensionality reduction. In this study, ICA will be used to reduce the dimension of a dataset, so that each example would have a relatively small number of independent features.

A statistical measure of independence used in information theory is the *mutual information* between random variables, which is always non–negative, being equal to zero only if the variables are statistically independent. Finding

the most independent features from a given dataset is equivalent to the minimization of the mutual information between these features. It can be proved mathematically that, for standardized, uncorrelated features, minimization of mutual information is equivalent to maximization of non–Gaussianity, expressed by the statistical measure of negentropy (Hyvarinën and Oja, 2000). The purpose of ICA algorithms is to determine a linear transformation that maximizes the negentropy of the dataset, thus transforming the original features into a number of independent features. Unfortunately, negentropy is very difficult to compute exactly, because this would require estimating the probability density functions of the unknown independent features. Instead of determining the exact value of negentropy, most ICA algorithms use numerically computed approximations of this property.

2.3. Principal Component Analysis (PCA)

Past experience has shown that the performance of ICA algorithms can be improved by suitable pre–processing of the data (Hyvarinën and Oja, 2000). A procedure that helps reduce the number of coefficients to be calculated in the ICA transformation matrices is called *whitening* of the data; this procedure applies an orthogonal transformation to the original features to generate a set of new features that would be uncorrelated. Along with whitening, it is recommended to reduce the dimension of the data. These pre–processing tasks can be accomplished by using the statistical technique of Principal Component Analysis (PCA) (Hastie et al., 2009).

The goal of PCA is to transform the data into a form that permits the total information that was contained in all features to be concentrated in a few principal components. PCA begins by building the covariance matrix of the input features. This is a symmetric square matrix of order equal to the number of features, each term of which is equal to the covariance between two features. The eigenvalues and eigenvectors of this matrix are then determined. Each (single–valued) principal component of an example is calculated as the product of one example (a row vector whose number of columns is equal to the number of features) and an eigenvector (a column vector whose number of rows is equal to the number of features). The numerical value of each eigenvalue represents the amount of variance ("information") that would be contained in the corresponding principal component and the total variance of all principal components, *i.e.*, the sum of all eigenvalues, is equal to the sum of the variances of all the features. Only the principal components that account for a sufficiently large portion of the total variance need to be

calculated. This has the effect of representing the total information in the original dataset with a smaller number of features.

2.4. Artificial Neural Networks

Artificial neural networks (ANN) are mathematical models that mimic networks of neurons in the nervous systems of animals and are capable of fitting very complicated non–linear functions to data (Hastie et al., 2009). Each ANN is composed of computational nodes that apply a mathematical function, called the *activation* function, on the node input and give a corresponding output. A typical ANN (Figure 1) has one input layer, with a number of nodes that is equal to the number of features of the input dataset plus a bias term, one output layer, with as many nodes as outputs, and one or more hidden layers, with a user–selected number of nodes in addition to a bias term. Except for the nodes of the input layer, a node input is basically a weighted sum of the outputs of other nodes. The goal of training a neural network algorithm is to find the weights that best correlate the input features to the outputs. After training, the neural network uses these weights to predict an output from a given input.

3. Experimental facility and procedures

All experiments were conducted in the air–water flow facility at the University of Ottawa (Figure 2), which has been previously described by ST1. This facility was mainly composed of clear polyvinyl chloride (PVC) tubing with an inner diameter of $D = 32.5$ mm, which permitted visual observation of the flow. The water and air volumetric flow rates were controlled separately by butterfly and needle valves, respectively, and they were measured by rotameters (King Instruments Series 7510, Garden Grove, California, USA). The readings of the air rotameter were corrected for changes in air density, based on gauge pressure and temperature values that were measured just downstream of the rotameter and at the measurement location.

In the present study, measurements were made in the vertical upward section of the flow loop, at an axial distance of 2,275 mm from the air injection location, corresponding to $L/D = 70$. The differential pressure between two axial locations separated by a distance of $D/2$ was measured using a differential pressure transducer (Validyne DP103, Northridge, California, USA). The gauge pressure at the measurement location was calculated as the average of the gauge pressures indicated by two pressure transducers, located at

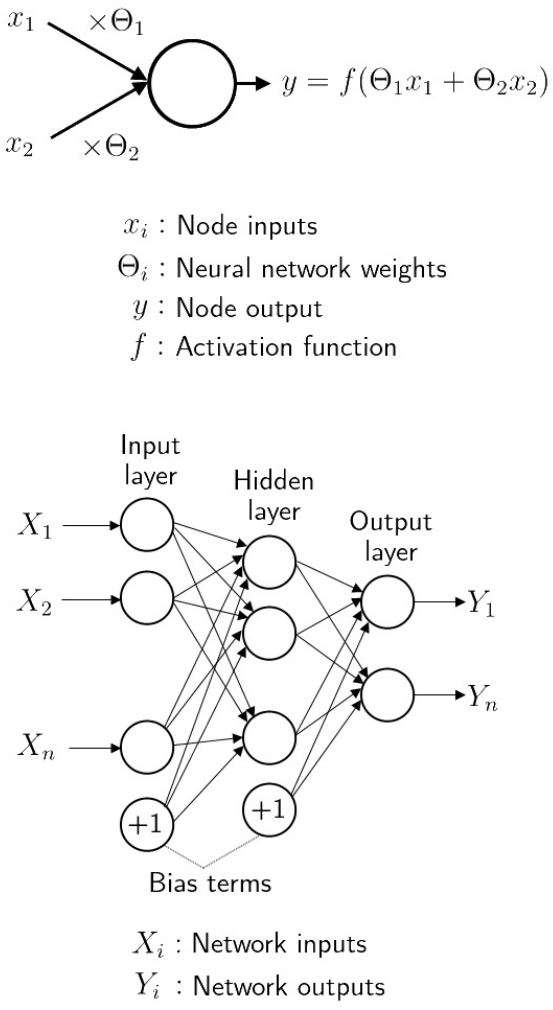

Figure 1: Neural network nomenclature for a single computational node (top) and for a representative network (bottom).

an axial distance of $L/D = 5$ upstream and downstream of the measurement location. A liquid purge system was used to keep the pressure lines free of air bubbles.

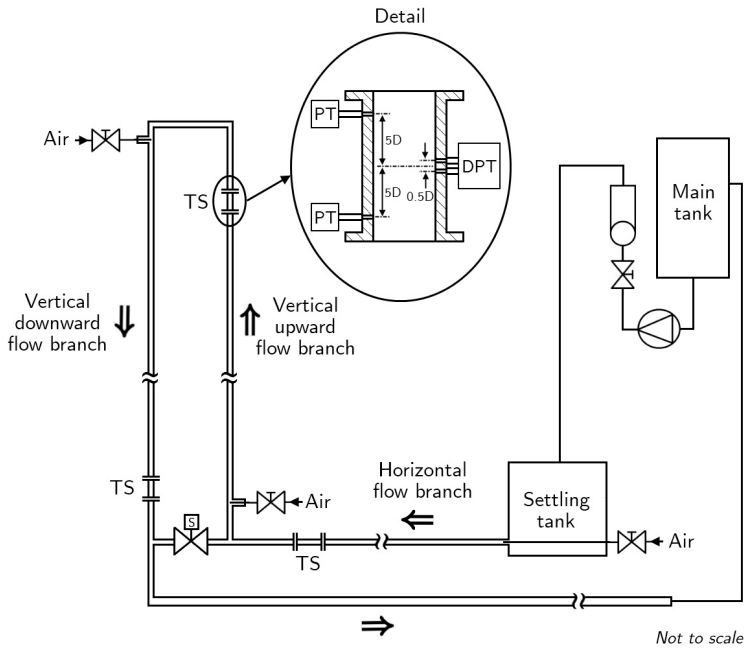

Figure 2: Schematic diagram of the air-water flow loop. PT: pressure transducer, DPT: differential pressure transducer, TS: test section.

The experiments were performed as follows. First the air and water flow rates were adjusted to the desired values, following which, the readings of the flowmeters and the flow regime were noted down. The superficial velocities of air j_g and water j_l were then calculated from the corresponding volumetric flow rates. In total, 570 tests were performed for various combinations of air and water superficial velocities in the ranges 0.014 m/s $\leq j_g \leq$ 22 m/s and 0.04 m/s $\leq j_l \leq$ 0.4 m/s. The upper limit of air flow rate corresponded to the maximum capacity of the compressed air supply system, while the upper limit of the liquid flow rate corresponded to the highest value for which pressure fluctuations could be resolved temporally by the differential pressure transducer used in this study. Three distinct flow regimes, namely slug, churn and annular flow, as well as two transitional regimes, namely, slug–churn and churn–annular flow, were encountered in this test section for

these ranges of flow conditions. The visual appearances of these flow regimes were described by ST1. The bubbly flow regime was not encountered under any flow conditions (flow rates, axial location, pressure and pipe diameter) within the ranges used in this study; this conforms with the observations of other authors (Taitel et al., 1980; Liu, 1993).

For each test, the differential pressure ΔP was recorded at a sampling rate of 200 samples/s for a duration of 60 s. A reference differential pressure $\Delta P_{l,s}$ between the same taps, but with the tube containing still water, was also recorded. For each set of conditions, the time history of the dimensionless differential pressure parameter ΔP^* was determined as

$$\Delta P^* = 1 - \frac{\Delta P}{\Delta P_{l,s}}. \tag{1}$$

Matsui (1984) noted that, if friction and acceleration pressure losses between the two pressure taps were negligible, ΔP^* would be indicative of the phase in the measurement section. This implies that the value of this parameter would be close to either 0 or 1 if the measurement volume between the two pressure taps were occupied by the liquid phase or gas phase, respectively.

4. Dependence of differential pressure properties on phase flow rates

Following consideration of various properties of the dimensionless differential pressure parameter and preliminary evaluations of them as potential indicators of phase flow rates, we decided to use the following two: the probability density function (PDF) and the power spectral density (PSD). ST1 noted that altering the individual phase flow rates affected the measured differential pressure signal in a predictable manner. The most obvious effect was the one due to the flow regime in the pipe, which was manifested in the shape of the PDF of ΔP^*. However, the PDFs of measurements, within the same flow regime, changed with the gas and liquid flow rates. The PSD was also found to change with the phase flow rates. Vince and Lahey (1982) considered the PSD among other methods as an indicator of flow regime but did not recommend it because of its sensitivity to the phase flow rates. In this study, however, the dependence of the PSD on the phase flow rates will be exploited for obtaining estimates of the phase flow rates. All calculations related to this part of the analysis were carried out using the open–source computational software package SCILAB 5.4 (Scilab Enterprises, 2013).

4.1. Calculation of the PDF, relative frequencies and PSD of ΔP^*

The range of ΔP^* that was relevant to this work was $-0.525 \leq \Delta P^* \leq 1.225$. The PDF was calculated by separating the values of ΔP^* into 35 bins, each having a width of 0.05, which corresponded to a vector of 35 representative features. As explained by ST1, this dimension was judged to be sufficiently small to avoid the curse of dimensionality, yet it accurately approximated all measured PDFs. Furthermore, to constrain the values of the input features within known bounds, the PDFs were converted to relative frequencies (RF) of the data points within each bin. The PSD of the fluctuations of ΔP^* was calculated using Welch's average periodogram method, with a Hamming window. It was found that nearly all of the signal power in all of the measurements was contained in the 0 to 5 Hz interval. In consideration of this observation, the PSD that was used for subsequent analysis was represented by an array of 25 evenly–spaced features between 0.2 and 5 Hz. Because the PSD value at zero frequency vanishes by definition of the PSD, this value was not used as a feature. The effects of the liquid and gas flow rates on RF(ΔP^*) and PSD(ΔP^*) will be discussed in the following sections.

4.2. Flow rate effects on ΔP^* in slug flow

ST1 noted that, in the slug flow regime, RF(ΔP^*) was bimodal with one peak at small ΔP^* and another at large ΔP^*. As mentioned earlier, if friction were negligible, ΔP^* would be indicative of void fraction, *i.e.*, $\Delta P^* \approx 0$ in the liquid slugs and $\Delta P^* \approx 1$ in the Taylor bubbles (Figure 3). Thus, RF(ΔP^*) would depend on the residence time of the two different flow structures at the measurement location. The amplitude of the small–ΔP^* peak would depend on the frequency and length of the liquid slugs, while its location would depend on the void fraction inside the liquid slugs. Similarly, the amplitude of the large–ΔP^* peak would depend on the frequency and length of the Taylor bubbles. In the present study, it was found that PSD(ΔP^*) in slug flow was continuous and had a sharp peak. The frequency at which this peak occurred probably represented the passage frequency of liquid slugs. This postulate is consistent with the suggestion of Jones and Zuber (1975) that the dominant frequencies in the PSD of void fraction fluctuations are related to the slug passage frequency.

Figure 4a shows the variations of the RF and PSD of ΔP^* for flows at a constant gas flow rate and three different liquid flow rates in the slug flow regime. As the liquid flow rate was increased, the shapes of both

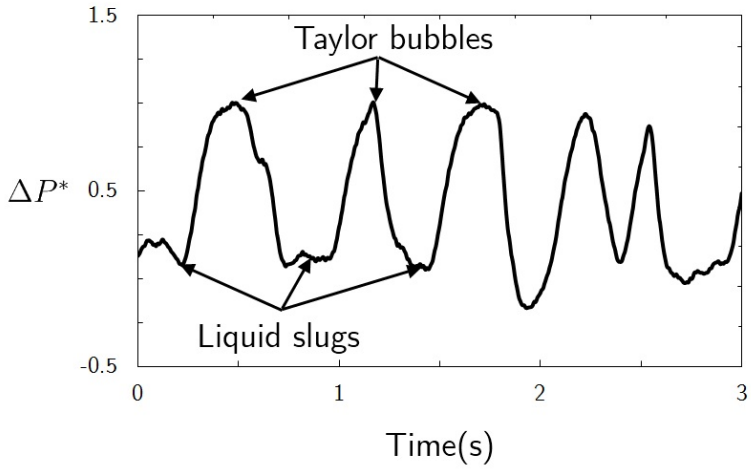

Figure 3: Time history of the differential pressure parameter in slug flow for $j_g = 0.2$ m/s and $j_l = 0.2$ m/s.

functions changed: the amplitude of the small–ΔP^* peak in RF(ΔP^*) increased, whereas that of the large-ΔP^* peak decreased; moreover, the peak in PSD(ΔP^*) decreased in amplitude and was shifted towards higher frequencies. These changes imply that the Taylor bubble length decreased, while the liquid slug length and frequency increased with increasing liquid flow rate, in conformity with our visual observations.

The effect of gas flow rate on the RF(ΔP^*) and PSD(ΔP^*) under constant liquid flow rate is illustrated in Figure 4b. With increasing gas flow rate, the small–ΔP^* peak decreased in amplitude and was shifted to slightly larger ΔP^*, while the large–ΔP^* peak increased in amplitude. This was a consequence of the increase in Taylor bubble length but also indicated that the liquid slugs contained more gas in the form of bubbles, as the gas flow rate was increased. The location of the peak in PSD(ΔP^*) was relatively insensitive to gas flow rate, but its amplitude clearly increased with gas flow rate. This indicated that the fluctuations of ΔP^* became stronger with increasing gas flow rate.

4.3. Flow rate effects on ΔP^* in churn flow

ST1 noted that RF(ΔP^*) in churn flow was unimodal and negatively skewed. As the liquid flow rate was increased while the gas flow rate was held constant, RF(ΔP^*) became slightly wider while the location of its peak

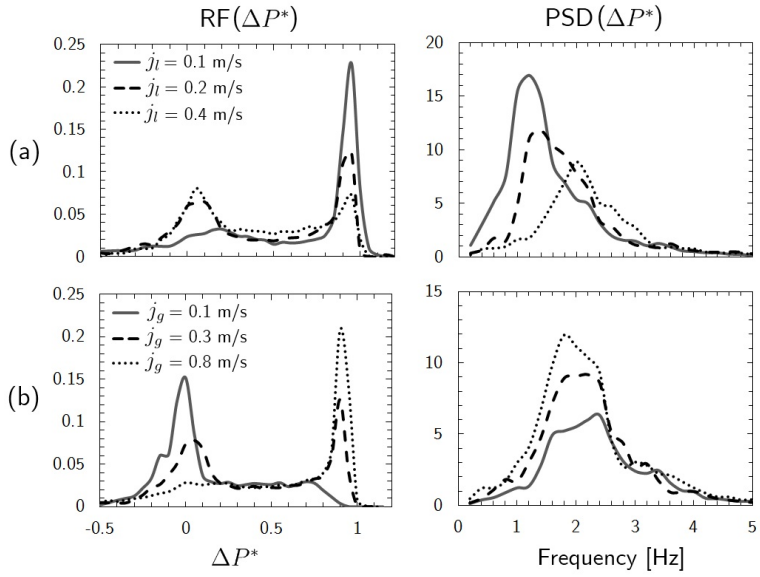

Figure 4: Relative frequencies (left) and PSD (right) of the differential pressure parameter at (a) constant gas superficial velocity ($j_g = 0.4$ m/s) and (b) constant liquid superficial velocity ($j_l = 0.2$ m/s). All these measurements are in the slug flow regime.

was shifted to slightly smaller ΔP^* (Figure 5a). This can be explained by the contribution of frictional pressure drop to the total measured differential pressure, which would tend to move RF(ΔP^*) to smaller values and which becomes increasingly significant in churn flow with increasing liquid or gas flow rate. The liquid flow rate did not appear to have a clear effect on the power spectrum at frequencies lower than 2 Hz, but the power density for all frequencies higher than 2 Hz generally increased with increasing liquid flow rate. In particular, a peak in PSD(ΔP^*) appeared between 2 and 3 Hz at higher liquid flow rates. This peak probably corresponded to the passage frequency of penetrated liquid slugs, which are the most significant cause of ΔP^* fluctuations in the churn flow regime.

With increasing gas flow rate, at a constant liquid flow rate, RF(ΔP^*) became less skewed and its peak was shifted to smaller ΔP^*, as a result of increasing frictional pressure drop (Figure 5b). The power density at all frequencies tended to decrease with increasing gas flow rate, as the fluctuations of ΔP^* became weaker.

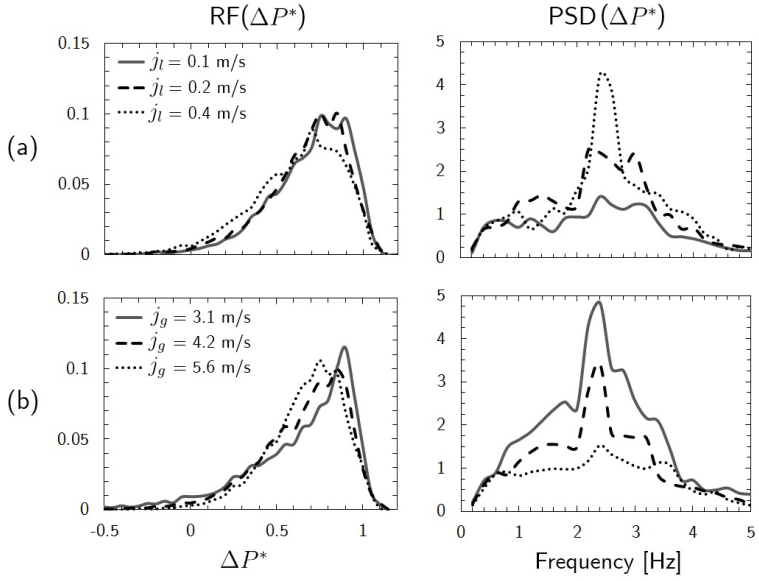

Figure 5: Relative frequencies (left) and PSD (right) of the differential pressure parameter at (a) constant gas superficial velocity (j_g = 4.8 m/s) and (b) constant liquid superficial velocity (j_l = 0.2 m/s). All these measurements are in the churn flow regime.

4.4. Flow rate effects on ΔP^* in annular flow

RF(ΔP^*) in annular flow appeared to be unimodal and had a nearly Gaussian shape. An increase in the liquid flow rate shifted the peak of the RF(ΔP^*) to smaller ΔP^* and increased the variance of the signal (Figure 6a). The power density increased for all frequencies, with increasing liquid flow rate. While PSD(ΔP^*) appeared almost flat at low liquid flow rates, a peak appeared between 2 and 3 Hz at higher ones. All of these changes suggested that the surface of the liquid film became more agitated with increasing liquid flow rate.

When the gas flow rate was increased, with the liquid flow rate held constant, the peak in RF(ΔP^*) became sharper, increased in amplitude and was shifted to smaller ΔP^* (Figure 6b). By examining PSD(ΔP^*), we noted that the power density of the signal decreased for all frequencies with increasing gas flow rate. Zabaras et al. (1986) observed that the fluctuations of the liquid film thickness tended to decrease with increasing gas flow rate, which could explain the reduction in the variance of the ΔP^* signal with increasing gas flow rate and the corresponding changes in RF(ΔP^*) and PSD(ΔP^*).

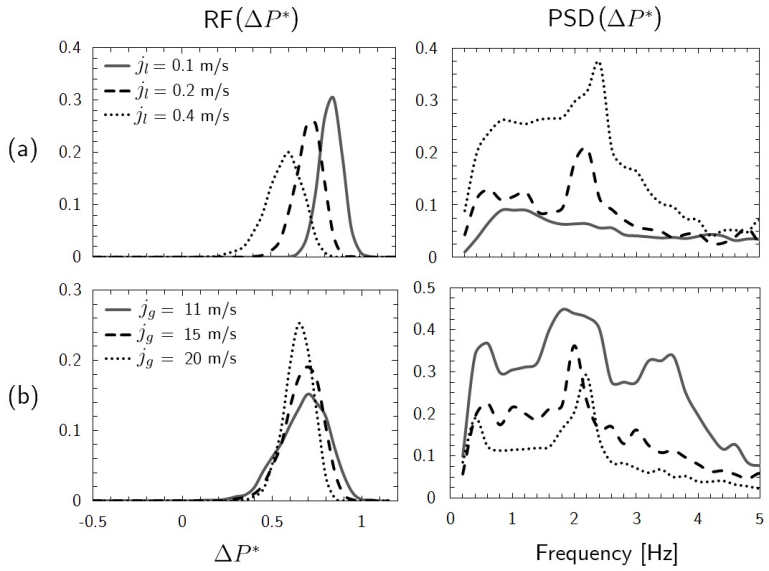

Figure 6: Relative frequencies (left) and PSD (right) of the differential pressure parameter at (a) constant gas superficial velocity ($j_g = 17$ m/s) and (b) constant liquid superficial velocity ($j_l = 0.2$ m/s). All these measurements are in the annular flow regime.

In summary, we have demonstrated that the shapes of RF(ΔP^*) and PSD(ΔP^*) depend consistently on the gas and liquid flow rates for the present ranges of flow conditions. It is fortuitous that the RF and PSD are not equally sensitive to the gas and liquid superficial velocities in different flow regimes, because this implies that, for each gas and liquid flow rate combination, the two-phase flow would have a unique signature expressed by these two properties. The purpose of the algorithm described in the next section is to identify the relationship between this signature and the two flow rates during calibration; once established, this relationship can then be reversed to estimate unknown flow rates from the signatures of measured differential pressure signals.

5. Description of the algorithm

5.1. Overview

A flowchart illustrating the main steps of the proposed flow rate measurement method is shown in Figure 7. The flowchart identifies the specific techniques employed presently in each step, but the same procedure can be

applied to alternative choices; for example, instead of the differential pressure, other flow properties that depend on the phase composition at the measurement location may be used as an input signal. Furthermore, the proposed algorithm is modular, making it possible to replace any particular technique used in each of the steps by a more suitable one, if such becomes available in the future, without changing the other steps.

The proposed method comprises two distinct algorithms: one to identify the flow regime and a second one to compute the phase flow rates, taking into consideration the particular flow regime that the flow is deemed to belong to. Both algorithms have as input the measured differential pressure time history. The elastic maps method, presented by ST1, serves as the flow regime identification algorithm. For the flow rate prediction, the PDF and PSD are first calculated from the input signal, appropriate features are extracted by using PCA followed by ICA, and regression is performed using artificial neural networks. The pre–processing steps employ methods that preserve as much of the information contained in the differential pressure signal as possible, albeit extracting features with a relatively small dimension. Moreover, preliminary work demonstrated that the use of specific regression models for each flow regime resulted in higher sensitivity and accuracy than the use of a single regression model for all regimes.

In the previous section, it was shown that the PDF and PSD of the differential pressure followed certain systematic trends as the gas and liquid flow rates were changed. In the following analysis, these two measured flow properties will be correlated to the superficial velocities of the gas j_g and the liquid j_l, which are the properties that need to be estimated, namely the output of the algorithm. The input dataset to the algorithm was a group of measured differential pressure time histories (input examples), consisting of a set of 12000 discrete values (input features) collected over an interval of 60 s. These input examples were subsequently converted into "representative" examples of 60 representative features each; those consisted of 35 features of the RF and 25 features of the PSD. The dimension of the representative dataset was still too large for a practical calculation of all required neural network weights. Therefore, it was further reduced to a much smaller value, which served as the input to the ANN regression algorithm. Details of the steps in the application of the proposed method are explained in the following subsections. All procedures were carried out using the open source data mining software RapidMiner 5 (RapidMiner, 2013).

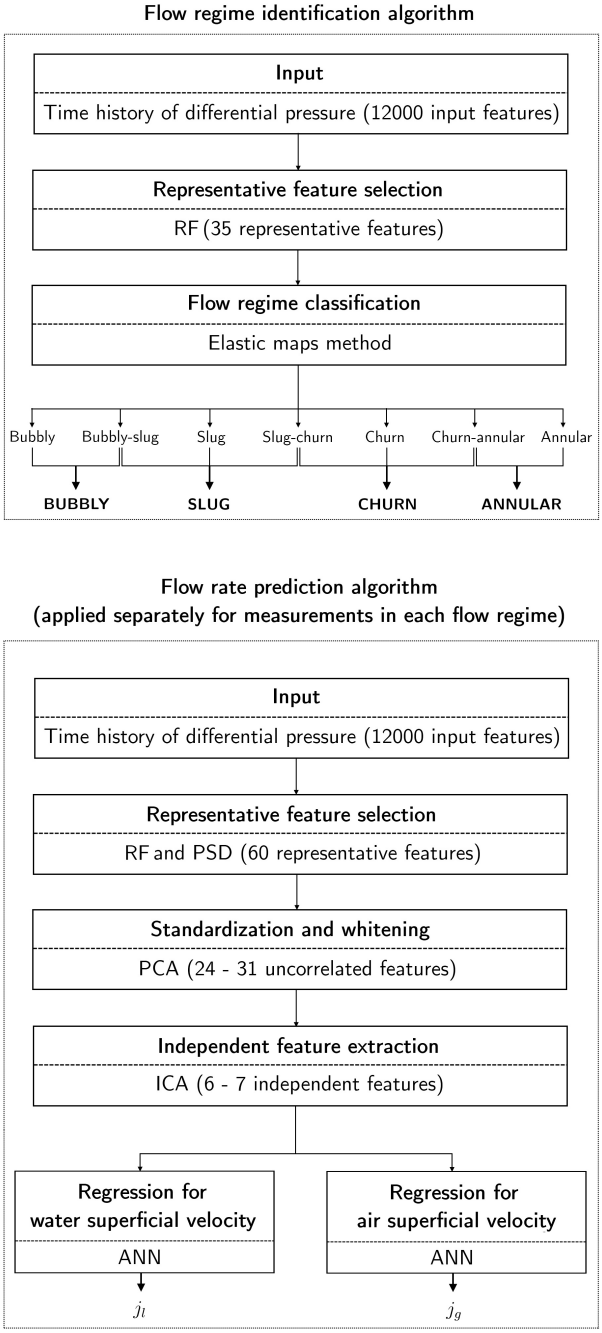

Figure 7: Flowchart of the present flow rate measurement method.

5.2. Flow regime identification

Each input example was classified into one of several flow regimes with the use of the elastic maps method presented by ST1. This method is an application of the elastics maps algorithm developed by Gorban and Zinovyev (2005), as implemented in the C++ code *elmap* (Gorban and Zinovyev, 2003). To identify the flow regime, 35 relative frequency features of a representative example were projected onto a trained two–dimensional elastic map. For convenience, the present algorithm incorporated the elastic map that was trained in ST1. The algorithm presented by ST1 identifies both distinct and transitional flow regimes. Nevertheless, the numbers of measurements in transitional regimes were not sufficiently large for the purpose of training dedicated neural networks. For this reason, for each example belonging to a transitional regime, the nearest distinct regime on the elastic map was identified and the transitional point was re-classified as belonging to that distinct flow regime. The following procedure was then followed separately for the examples in each flow regime. Each flow regime dataset was split into a training dataset, containing 80% of the examples and used to train the ANN regression model, and a test dataset, containing the remaining 20% of the examples and used for evaluating the performance of the procedure. The distributions of examples in different flow regime datasets are listed in Table 1.

Table 1: Numbers of examples in the different flow regime datasets.

Flow regime	Training dataset	Test dataset	Total
Slug	167	42	209
Churn	156	39	195
Annular	133	33	166
Total	456	114	570

5.3. Standardization and whitening

Following common practices in the field, the representative examples in each training dataset were pre-processed as follows. First, the mean of each feature over all examples was subtracted from the corresponding representative feature and the difference was divided by the standard deviation of the feature variations over all examples, so that all features were standardized.

PCA was performed next using the procedure outlined in Section 2.3. The eigenvectors accounting for a total of 98% of the variance of the training set were retained and multiplied by the standardized representative features to calculate the corresponding principal components. These were used as the uncorrelated features of the whitened examples. The dimension of the whitened dataset was nearly half that of the representative dataset.

5.4. Independent feature extraction

The extraction of "independent" features from the set of uncorrelated features obtained so far was accomplished with the use of the FastICA algorithm (Hyvarinën and Oja, 2000). In this procedure, the negentropy $J(y)$ of a random variable y was approximated as

$$J(y) = [E\{G(y)\} - E\{G(\nu)\}]^2 \ , \tag{2}$$

where E denotes the expected value (mean) of a random variable, ν is a Gaussian variable with zero mean and unit variance and

$$G(u) = -\exp\left(-u^2/2\right) \ . \tag{3}$$

The FastICA algorithm was used to calculate all of the independent components but only 6 or 7 independent features were used as inputs for training the neural networks; these were chosen by using the ICA dimensionality reduction procedure suggested by Wang and Chang (2006).

5.5. Neural network regression

Separate ANN were used for the calculation of the gas and liquid superficial velocities in each of the three flow regimes, so that a total of six ANN were trained. Each of these ANN consisted of one input layer, having a number of nodes equal to the number of independent features, one hidden layer with a user–specified number of nodes and one output layer with one output node, consisting of either the gas or the liquid superficial velocity. The backpropagation algorithm with momentum was used to train the neural network. Sigmoid activation functions were used in the hidden layer and linear activation functions were used in the output layer (Hastie et al., 2009).

5.6. Determination of user–defined parameters

The ANN training process required specification of the following user–defined parameters: (i) number of independent features, (ii) number of nodes in the hidden layer, (iii) ANN learning rate, (iv) ANN momentum parameter, and (v) ANN number of training iterations. The number of ANN training iterations was set to 2000, as we found that this value allowed ANN training to be completed within a fairly short computational time and that using a larger number of training iterations did not affect significantly the values of the ANN coefficients. The other parameters were determined by an evolutionary search algorithm available in RapidMiner. This algorithm started with several random sets of parameters within a defined range, then evaluated the performance of the ANN when each of these parameter sets was used. It then discarded the worst–performing parameter sets and tested other parameter combinations in subsequent iterations, until there was no further improvement in performance. We compared this method to a grid search method, which considered all possible combinations of the required parameters, and found that the evolutionary search algorithm was more computationally efficient, while also providing the same values for the optimum parameters. The performance measure that was minimized in the selection of the optimum parameters was the ten–fold cross–validation error. To calculate this error metric, the training dataset was divided into ten equal parts, then, the examples in nine of these parts were used to train a neural network and the tenth part was used to test its performance. This was repeated over all parts, such that each of the ten parts was used to test the network performance exactly once, with the other nine parts used for training. These ten performances were then averaged to give the ten–fold cross–validation error of the neural network.

6. Results and discussion

6.1. Performance testing approach

The performance of the proposed procedure was tested against the test datasets, which contained test input examples that had not been used for ANN training. Each input example was first classified into the appropriate flow regime. Then, its features were standardized using the same means and standard deviations as those used for the standardization of the training dataset. PCA and ICA were subsequently performed using the transformation matrices that were calculated for the training dataset. The resulting

independent features were then used as inputs to the appropriate trained neural network, which provided a prediction of the liquid or gas superficial velocity.

6.2. Performance indicators

Let j_g be a measured value of gas superficial velocity and j_{gp} be the corresponding value predicted by the appropriate neural network. The relative prediction error for each measurement is defined as

$$\epsilon = \frac{j_{gp} - j_g}{j_g} \times 100\% \ . \tag{4}$$

A similar definition can be made for the relative prediction error of the liquid superficial velocity j_l. The average relative error $\langle \epsilon \rangle$ for each of the six ANN used presently represents its bias in the flow rate prediction. The ability of the procedure to predict fairly accurately the bulk of the measurements or not may be measured by the percentages of predictions with $|\epsilon| < 10\%$, to be denoted as ϵ_{10}, and $|\epsilon| < 20\%$, to be denoted as ϵ_{20}. Finally, the generalization performance of the models may be evaluated by comparing the average absolute relative error $\langle |\epsilon| \rangle_{train}$ for the training dataset and the corresponding value $\langle |\epsilon| \rangle_{test}$ for the appropriate test dataset.

6.3. Accuracy of the present method

Figure 8 presents the ratio of predicted and measured superficial velocities for the six ANN. In general, the vast majority of predictions were within $\pm 20\%$ of the measured values. A notable exception was the very low gas superficial velocity region in the slug flow regime, in which relative errors reached values as large as 60%. It must be noted, however, that, even in this case, the actual errors were not very large, whereas the relative errors were amplified by the normalization process, which in this case divided the error by the very small measured values.

Table 2 lists the values of several performance indicators for each of the six ANN and on the average. Overall, the present method predicted fairly well the reference liquid superficial velocity measurements and it exhibited a negligible bias in all three flow regimes. 95% of these predictions had an absolute relative error that was lower than 20% and 77% of the same predictions were within $\pm 10\%$ of the measured values; the average absolute relative error was less than 9%. In view of the fact that, in nuclear safety analysis,

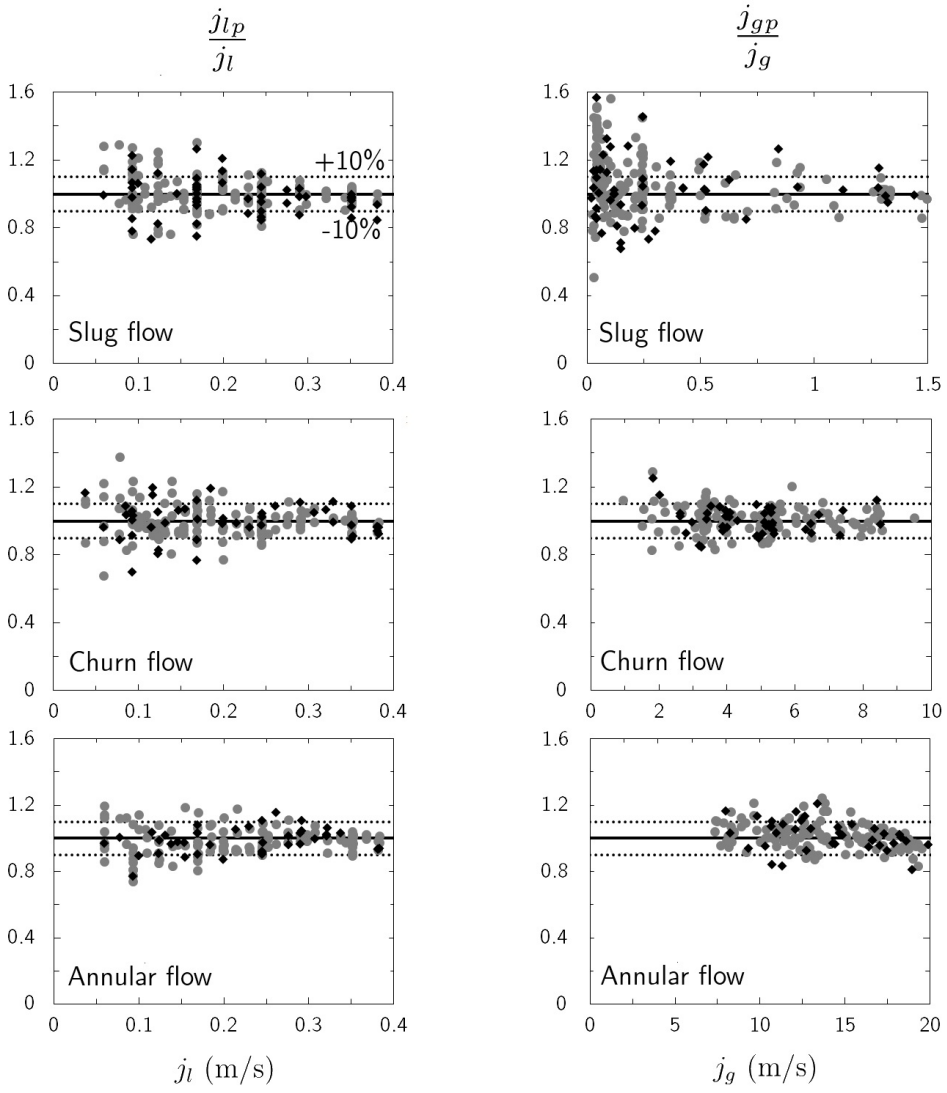

Figure 8: Ratio of predicted to measured flow rates using the present method *vs.* measured flow rates from the training dataset (●) and the test dataset (◆).

Table 2: Performance indicators of the present method.

Flow regime	Flow variable	$\langle\epsilon\rangle$ [%]	ϵ_{10} [%]	ϵ_{20} [%]	$\langle\|\epsilon\|\rangle_{train}$ [%]	$\langle\|\epsilon\|\rangle_{test}$ [%]
Slug	j_l	-0.3	72	92	9.0	8.7
	j_g	5.5	48	75	16	16
Churn	j_l	-0.1	77	96	8.9	8.0
	j_g	0.5	85	99	8.3	6.2
Annular	j_l	-0.4	81	98	8.2	6.1
	j_g	0.6	80	98	8.7	7.5
All	j_l	-0.3	77	95	8.7	7.7
	j_g	2.4	70	90	11	10

it is the liquid flow rate that is of main interest, the presence of relatively large relative errors in the very low gas flow range is not very disconcerting. Another positive observation is that the average relative differences for the training and test sets were almost identical, which demonstrates that the present method has a very good generalization performance, *i.e.*, it predicts flow rates for conditions that were not used for ANN training with the same accuracy as for those that were used for training.

It may be noted here that the present flow rate prediction is based on the assumption that the flow regime was identified correctly by the elastic maps method. In ST1, it was demonstrated that the elastic maps method predicted the correct flow regime for 98.2% of the test measurements, whereas the few misclassified measurements were found to be in the transitional zone between two distinct regimes. To test the effect of an erroneous flow regime identification on the accuracy of the present method, 60 measurements in transitional regimes were reassigned flow regime from a correctly identified one to the adjacent one. The phase flow rates in these measurements were then calculated by the ANN that correspopnded to the incorrect (but neighbouring) flow regime. For example, a slug–churn regime measurement that was classified under the churn flow regime was tested with the ANN that was trained with slug flow measurements. The average absolute values of the relative errors $\langle|\epsilon|\rangle$ of j_l and j_g predictions were 8% and 9%, respectively, in the churn–annular transitional zone and 9% and 21%, respectively, in the slug–churn transitional zone. The value of $\langle|\epsilon|\rangle$ was approximately

7% for both j_l and j_g predictions in the two transitional zones, when the correct ANN was used to predict the flow rates for the same set of measurements. It is clear that misclassification of flow regime leads to a slight decrease in prediction accuracy in most cases and a large decrease in the prediction accuracy of gas superficial velocity in the slug–churn regime. In this transitional regime, RF(ΔP^*) switches from having two peaks to having a single peak, which would strongly affect the gas superficial velocity prediction (see Section 4). In addition, misclassification of flow regime is expected to lead to less accurate flow rate predictions, simply because misclassified measurements would be outside the training range of the ANN. Measurements that were the farthest from the flow regime map zone boundaries had the least accurate predictions; this is not necessarily disconcerting, because it is highly unlikely that such measurements would be misclassified by a properly calibrated elastic map.

6.4. Accuracy of the present method using simpler feature extraction and regression algorithms

To justify the use of sophisticated machine learning algorithms in this study, the accuracy of the present method was compared to those of simpler techniques. For example, linear regression was tested as a potential substitute for artificial neural networks in the regression step of the present algorithm. As shown in Table 3, the absolute value of the relative errors of superficial velocity predictions for the test datasets $\langle|\epsilon|\rangle_{test}$ was in most cases 2–3 times larger than the errors using ANN and led to unacceptable results, especially in the slug flow regime. These tests have demonstrated that the relationship between the input features and the superficial velocities is non–linear and cannot be represented accurately by simple linear regression.

To assess the proposed feature selection methodology, a simple feature selection algorithm based on correlation was implemented in lieu of PCA–ICA feature selection. Instead of using PCA and ICA to reduce the 60 representative features to 6 or 7 independent features, the correlation coefficients between each of the 60 representative features and the output superficial velocity were calculated and the features that corresponded to the 7 largest correlation coefficients were retained and used as inputs to the neural networks. The resulting $\langle|\epsilon|\rangle_{test}$ using this approach, presented in Table 3, demonstrate that this approach is much more inaccurate than the use of PCA–ICA feature selection. Using this method, 53 of the 60 representative features were simply discarded, leading to loss of information. Additionally,

it was found that the features that were best correlated to the output were also strongly correlated to each other, as for example, adjacent points on RF(ΔP^*) or PSD(ΔP^*), and hence these features contained largely redundant information. This redundancy could potentially be mitigated in two ways: (i) choosing a larger number of features, which would require a larger number of training measurements to avoid overfitting the neural networks or (ii) discretizing the RF(ΔP^*) or PSD(ΔP^*) into a smaller number of bins, which would lead to reduced sensitivity to the phase flow rates and effectively reduce the resolution of the method. Clearly, both of these options are inferior to the PCA–ICA approach, which offers good resolution and accuracy using a relatively small number of training measurements.

Table 3: Comparison of the performance indicator $\langle|\epsilon|\rangle_{test}$ for the present method using different feature extraction and regression algorithms; LIN: Linear regression algorithm, COR: Feature selection by correlation, BEG: Feature selection by the Beg and Toral (1993) method, MIN: Feature selection by the Minemura et al. (1998) method.

Flow regime	Flow variable	Present method	LIN	COR	BEG	MIN
Slug	j_l	9	16	25	15	20
	j_g	16	57	27	28	23
Churn	j_l	8	18	31	19	8
	j_g	6	14	12	8	6
Annular	j_l	6	8	13	28	7
	j_g	7	14	12	10	7

6.5. Accuracy of the present method using previous approaches for feature extraction from differential pressure signals

The performance of the present method with respect to previous methods of two–phase flow rate measurement would ideally be evaluated by comparing results of tests with each method on flows with the same geometry and conditions. Only methods that meet the previously stated requirements of employing simple instrumentation and very low intrusiveness, thus being suitable for simultaneous use in a large number of pipes, need to be considered. Unfortunately, none of the available methods of two–phase flow rate measurement based on machine learning satisfied both of these conditions and so

a proper comparison of them with the present method was not possible. Nevertheless, rather than comparing the entire methods, it is possible to compare different aspects of the present signal processing algorithm to previous ones using the database of differential pressure time histories that were collected in the present experimental set–up. In particular, the present pre–processing approach, which is a major component of this study, will be compared in this section to two other approaches used by previous authors. In order to isolate the effect of pre–processing procedure on the method performance, we will apply all methods using the same flow regime identification and neural network regression procedures, outlined in Section 5. This comparison should demonstrate whether the use of PCA and ICA to represent the differential pressure time history by a number of independent features would lead to more accurate flow rate predictions than the use of other methods of feature extraction from differential pressure time histories.

Besides those used in the present method, two other sets of representative statistical and dynamical features were extracted from the present differential pressure signal database for comparison against the present pre–processing approach. The first set was the one used by Beg and Toral (1993), which comprised eight representative features, namely, the standard deviation, the skewness, the kurtosis, four linear prediction coefficients and the linear prediction residual of the differential pressure signal. Beg and Toral (1993) extracted these features from differential pressure measurements across an orifice plate, with and without upstream homogenization, whereas we calculated them from the time histories of ΔP. The second set was the one proposed by Minemura et al. (1998), which comprised five features extracted from differential pressure signals measured across a Venturi tube following flow homogenization, namely, the mean, the standard deviation, the skewness, the kurtosis, the peak frequency in the power spectral density of the differential pressure; it also included a sixth feature, namely, the correlation coefficient between the pressure fluctuations measured closely upstream of the Venturi tube and those measured at the throat. We calculated the first five features from the time histories of ΔP and took the last feature to be the correlation coefficient of the pressure fluctuations measured by the two pressure transducers in the test section. The representative examples of both feature sets were directly used to train neural networks, as both had sufficiently low dimensions.

The performance indicator $\langle|\epsilon|\rangle_{test}$ obtained by using these alternative representative features as inputs to neural networks are shown in Table 3.

The Beg and Toral (1993) feature set resulted in fair predictions of j_g for churn and annular flows, but poor predictions of j_g in slug flow and of j_l in all flow regimes. This may imply that the use of linear prediction coefficients to represent the dynamic characteristics of the flow is not sensitive enough for measurements in a bare pipe. The Minemura et al. (1998) feature set produced predictions of j_l in churn and annular flows that had comparable uncertainties as the predictions of the present method, but the performance of the former in slug flow was much worse. The poor performance of both these alternatives in slug flow is possibly due to the fact that aggregate statistics do not capture the bimodal nature of slug flow and hence may not be unique to a particular set of flow conditions. It must be reiterated that the authors who introduced these two feature sets used pressure differences across pressure drop producing devices (orifice plate and Venturi tube, respectively), and not along a bare pipe, as presently done. The intrusiveness of these devices as well as upstream flow homogenization must have eliminated the bimodal nature of slug flow. Considering that slug flow is a very common flow regime in vertical upward flow (Jones and Zuber, 1975), these feature extraction methods would not produce accurate flow rate predictions if used in bare pipes over the wide range of flow conditions that are of interest in nuclear safety analysis.

7. Summary and concluding remarks

A new method for the measurement of gas and liquid flow rates in two–phase pipe flow has been developed. The main innovations of this method are the use of the full PDF and PSD of the normalized differential pressure signal as representative features of the flow and the use of Principal Component Analysis and Independent Component Analysis to reduce the dimensions of the inputs to a value that is more suitable for regression algorithms. Each flow was first classified into the appropriate flow regime using the elastic maps method. The PDF and PSD signature was first standardized and then "whitened" using Principal Component Analysis. Finally, the independent features obtained after the application of ICA were used as inputs to dedicated neural networks, which estimated the gas and liquid flow rates in each flow regime.

The PDF and PSD of the differential pressure signal were found to be strong indicators of the phase flow rates. The use of ICA preserved most of the information contained in these two flow properties and enabled their

use without the need to collect an inconveniently large number of calibration measurements. In fact, with the use of linear algebra, one may recover, almost completely, the shapes of the PDF and PSD from six or seven independent features, together with the transformation matrices calculated during pre–processing. Previous authors have attempted to represent the differential pressure signal in a compact form using aggregate statistics, such as the statistical moments or representative values from the PSD. An evaluation of the performance of two feature sets that were based on aggregate statistics of the differential pressure signal proved that these parameters may not be uniquely related to the flow rates, especially in the slug flow regime in bare pipes. As mentioned in the Introduction, this method requires calibration in each experimental setup. However, unlike the cross–correlation method, which would ideally require no calibration, the present method makes accurate flow rate predictions of both gas and liquid flow rates in all flow regimes and for all flow conditions of present interest. This is particularly important, as in most applications, the flow regime in the pipe would not be known beforehand. Moreover, the present method only requires simple, economical and non–intrusive instrumentation and minor modifications to existing piping systems.

The previous discussion has been focused on measurements in vertical upward flows. It seems quite likely, however, that the proposed technique could be applied to flow rate measurements in horizontal air-water pipe flows as well. This assessment is based on the observation of Matsui (1985), who measured the differential pressure between two taps at the top and bottom of the same cross–section in a horizontal air–water pipe flow, and demonstrated that the statistical properties of ΔP^* were indicative of flow regime. Based on this observation, one may postulate that the PDF and the PSD of ΔP^* in horizontal air-water pipe flows would be sensitive to gas and liquid flow rates, in which case it seems evident that the present method would be applicable to horizontal flows. On the other hand, the applicability of this technique to vertical downward flows is not as predictable and needs to be examined carefully.

One of the advantages of this method is that it has been assembled in a modular manner, so that any of its components may be substituted by a different technique, that would be more convenient or accurate under different conditions. In fact, we plan on testing the signal processing algorithm with input signals provided by different types of instruments. Finally, in order to explore whether calibration of the method in one facility would be suitable

for use in other facilities, we intend to test the method in several different experimental set–ups.

Acknowledgements

Financial support for this study was provided by the Natural Sciences and Engineering Research Council of Canada (NSERC), Atomic Energy of Canada Limited (AECL) and the University Network of Excellence in Nuclear Engineering (UNENE).

References

Beg, N., Toral, H., 1993. Off-site calibration of a two-phase pattern recognition flowmeter. Int. J. Multiphase Flow 19, 999–1012.

Cai, S., Toral, H., 1993. Flowrate measurement in air-water horizontal pipeline by neural networks. In: International Joint Conference on Neural Networks. Vol. 2. Nagoya, Japan, 25 - 29 Oct. 1993, pp. 2013–2016.

Dong, F., Xu, Y., Xu, L., Hua, L., Qiao, X., 2005. Application of dual–plane ERT system and cross–correlation technique to measure gas–liquid flow in vertical upward pipe. Flow Meas. Instrum. 16, 191–197.

Falcone, G., Hewitt, G., Alimonti, C., Harrison, B., 2002. Multiphase flow metering: Current trends and future developments. J. Petrol. Technol. Apr 2002, 77–84.

Fan, S., Yan, T., 2013. Two-phase air-water slug flow measurment in horizontal pipe using conductance probes and neural network. IEEE Trans. Instr. Meas., doi: 10.1109/TIM.2013.2280485.

Gorban, A., Zinovyev, A., 2003. *elmap*: C++ package. Available online: http://bioinfo-out.curie.fr/projects/elmap/. Last accessed: 17 November 2013.

Gorban, A., Zinovyev, A., 2005. Elastic principal manifolds and their practical applications. Computing 75, 359–379.

Hastie, T., Tibshirani, R., Friedman, J., 2009. The elements of statistical learning. Springer, New York, USA.

Hyvarinën, A., Oja, E., 2000. Independent component analysis: Algorithms and applications. Neural Networks 13, 411–430.

Jeanmeure, L., Dyakowski, T., Zimmerman, W., Clark, W., 2002. Direct flow–pattern identification using electrical capacitance tomography. Exp. Therm Fluid Sci. 26, 763–773.

Jones, O., Zuber, N., 1975. The interrelation between void fraction fluctuations and flow patterns in two-phase flow. Int. J. Multiphase Flow 2, 273–306.

Julia, J., Liu, Y., Paranjape, S., Ishii, M., 2008. Upward vertical two-phase flow local flow regime identification using neural network techniques. Nucl. Eng. Des. 238, 156–169.

Kowalski, J., Hanna, B., 1989. Studies of two–phase flow distribution in a CANDU–type header/feeder system. In: Fourth International Topical Meeting on Nuclear Reactor Thermalhydraulics (NURETH-4). Karlsruhe, Federal Republic of Germany, 10–13 October, 1989, pp. 28–33.

Lin, Z., 1982. Two–phase flow measurements with sharp–edged orifices. Int. J. Multiphase Flow 8, 683–693.

Liu, T., 1993. Bubble size and entrance length effects on void development in a vertical channel. Int. J. Multiphase Flow 19, 99–113.

Matsui, G., 1984. Identification of flow regimes in vertical gas-liquid two-phase flow using differential pressure fluctuations. Int. J. Multiphase Flow 10, 711–720.

Matsui, G., 1985. Identification of flow patterns in horizontal gas–liquid two–phase flow using diferential pressure fluctuations. In: Proceedings of the International Symposium on Fluid Control and Measurement. Tokyo, Japan, 2–6 September, 1985, pp. 819–824.

Meng, Z., Huang, Z., Wang, B., Ji, H., Li, H., Yan, Y., 5 - 7 May, 2009 2010. Air–water two–phase flow measurement using a Venturi meter and an electrical resistance tomography sensor. Flow Meas. Instrum. 21, 268–276.

Meribout, M., Al-Rawahi, N., Al-Naamany, A., Al-Bimani, A., Al-Busaidi, K., Meribout, A., 2010. Integration of impedance measurements with acoustic measurements for accurate two phase flow metering in case of high water-cut. Flow Meas. Instrum. 21, 8–19.

Mi, Y., Ishii, M., Tsoukalas, L., 1998. Two-phase flow identification using advanced instrumentation and neural networks. Nucl. Eng. Des. 184, 409–420.

Minemura, K., Takeoka, T., Syoda, S., Egasira, K., Ogawa, Y., 1998. Correlative mapping method for measuring individual phase flow rates in air-water two-phase flow based on stochastic features. JSME Int. J. 41, 863–870.

RapidMiner, 2013. RapidMiner 5: Open source data mining and predictive analytics software. Available online: http://www.rapidminer.com. Last accessed: 8 November, 2013.

Scilab Enterprises, 2013. Scilab 5.4: Free and open source software for numerical computation. Available online: http://www.scilab.org. Last accessed: 17 November, 2013.

Shaban, H., Tavoularis, S., 2014a. Identification of flow regime in vertical upward air-water flow using differential pressure signals and elastic maps. Int. J. Multiphase Flow 61, 62–72.

Shaban, H., Tavoularis, S., 2014b. The wire–mesh sensor as a two–phase flow meter. Submitted to Measurement Science and Technology.

Taitel, Y., Bornea, D., Dukler, A., 1980. Modelling flow pattern transitions for steady upward gas-liquid flow in vertical tubes. AIChE J. 26, 345–354.

Tan, C., Dong, F., 2006. Two–phase flow measurement by dual–plane ERT system with drift–flux model and cross correlation technique. In: Proceedings of the Fifth International Conference on Machine Learning and Cybernetics. Dalian, China, 13 - 16 August, 2006, pp. 1443–1448.

Teclemariam, Z., Soliman, H., Sims, G., Kowalski, J., 2003. Experimental investigation of the two-phase flow distribution in the outlets of a horizontal multi-branch header. Nucl. Eng. Des. 222, 29–39.

Thorn, R., Johansen, G., Hjertaker, B., 2013. Three-phase flow measurement in the petroleum industry. Meas. Sci. Technol. 24, doi:10.1088/0957–0233/24/1/0120.

Vince, M., Lahey, R., 1982. On the development of an objective flow regime indicator. Int. J. Multiphase Flow 8, 93–124.

Wang, J., Chang, C.-I., 2006. Independent Component Analysis–based dimensionality reduction with applications in hyperspectral image analysis. IEEE Trans. Geosci. Remote Sensing 44, 1586–1600.

Zabaras, G., Dukler, A., Moalem-Maron, D., 1986. Vertical upward cocurrent gas–liquid annular flow. AIChE J. 32, 829–843.

Zhang, H., Lu, S., Yu, G., 1992. An investigation of two–phase flow measurement with orifices for low–quality mixtures. Int. J. Multiphase Flow 18, 149–155.

Chapter 6

Wire-mesh tomography: areas of application, performance evaluation and measurement uncertainty

In this chapter, the technique of wire–mesh tomography is reviewed and various issues related to its measurement uncertainty are discussed, as a prelude to the use of this technique in subsequent studies. The chapter is presented as the manuscript

> "Shaban, H. and Tavoularis, S. 2015 Wire-mesh tomography: areas of application, performance evaluation and measurement uncertainty. (submitted)"

This manuscript was split into two parts that were submitted to *International Journal of Multiphase Flow* and *Flow Measurement and Instrumentation* in early July 2015.

Wire-mesh tomography: areas of application, performance evaluation and measurement uncertainty

H. Shaban, S. Tavoularis*

Department of Mechanical Engineering, University of Ottawa, 161 Louis Pasteur, Ottawa, ON K1N 6N5, Canada

Abstract

This article presents a comprehensive and critical discussion of available literature on wire–mesh tomography as well as some complementary original analysis. Wire-mesh tomographs were first classified into different categories, depending on their principles of operation, and then the discussion was focused on the most commonly used type, namely, the wire–mesh sensor (WMS). The main applications of WMS were outlined and the properties that can be determined from WMS signals were identified, together with the corresponding procedures. WMS performance and the factors that affect this performance were evaluated in detail using results of previous investigations as well as new analysis and data. The principles of operation and main applications of global wire–mesh tomographs were then described. This article finally presents several examples of wire–mesh tomography applications in multicomponent flows.

Keywords: tomography, wire-mesh sensors, multiphase, multicomponent, image reconstruction

1. Introduction

The properties of flows of fluid mixtures have been studied extensively, both experimentally and analytically, as such flows are encountered in many

engineering applications. Flows of mixtures may be classified into two general classes: multiphase flows, which consist of immiscible fluids with generally distinct velocities and temperatures, and multicomponent ones, in which the constituent fluids are miscible and typically share a common velocity and temperature (Drew and Passman, 2012). Multiphase flows are encountered in many heat exchangers and thermal power generation systems, whereas multicomponent mixtures are present in combustors and chemical reactors.

Available techniques for the measurement of flow properties in multiphase and multicomponent flows may provide either volume–, area– or line–averaged values of a property or local values at discrete locations. Spatially averaged measurements may usually be collected faster and more conveniently than local measurements, and they often include sufficient information for the needs of many applications. On the other hand, the availability of spatially distributed local measurements allows for a more detailed analysis of the flow structure and insight into phenomena and processes that cannot be described by global measurements alone. A number of measurement procedures, commonly referred to as tomographic methods, aim at reconstructing the cross–sectional or volumetric distribution of a flow property from a number of discrete measurements collected simultaneously at many points in the flow. Several tomographic methods have been applied to multiphase and multicomponent flows with the objective of distinguishing the constituents of the mixture.

Multiphase/multicomponent tomographs distinguish between the mixture constituents by detecting differences in electrical properties (impedance, permittivity and conductivity tomographs), radiation attenuation (X–ray and gamma ray tomographs), sound attenuation (ultrasonic tomographs) or light attenuation (optical tomography systems) (Williams and Beck, 1995). Electric tomographs, in particular, comprise a number of electrodes, which are either mounted on the periphery of the flow channel or stretched across its cross–section. In these devices, an electric property is measured in the space between each pair of electrodes and its spatial distribution is reconstructed from these measurements with the use of analytical algorithms.

The subject of the present study is the wire–mesh tomographs (WMT), which measure either the conductivity or the permittivity of the fluid in the vicinity of electrodes stretched across the flow domain (Johnson, 1987; Reinecke et al., 1998; Prasser et al., 1998). Past literature on WMT includes numerous experimental studies, most of which have appeared in the last 15 years. Although some previous publications include reviews of applications

(*e.g.*, Prasser, 2008) and measurement uncertainty (*e.g.*, Beyer et al., 2010) of a specific type of WMT, an all–encompassing review of WMT applications and a critical evaluation of the performance and measurement uncertainty of various WMT devices operating under wide ranges of flow conditions have not yet become available. The present article is meant to fill this gap by addressing these issues. WMT are particularly suitable for measurements in gas–liquid flows, as gases and liquids that are commonly encountered in industrial applications have very different electrical properties. The main focus of the present review is the use of WMT in gas–liquid flows, but the applicability of WMT to the study of multicomponent flows will also be reviewed in a separate section.

In the following sections, we will first describe the different types of WMT, then identify the various flow parameters that may be extracted from WMT signals, overview successful applications of WMT and present an in–depth discussion of the measurement uncertainty of both types of these devices. This information will hopefully be of interest to readers conducting WMT measurements or considering the possible use of WMT in types of systems that are either similar to or different from those of past WMT application.

2. Types of WMT

Wire–mesh tomographs may be broadly classified into two categories, depending on the electrical property that is measured. Conductivity WMT measure a current (or a voltage proportional to this current) that is proportional to the local conductivity of the fluid. Permittivity WMT, sometimes referred to as capacitance WMT, measure the capacitance of a space near the electrodes, which is proportional to the permittivity of the fluid, *i.e.*, its ability to transmit electric fields. For the WMT to function in a mixture, the constituent fluids are required to have distinguishable values of the measured property. Moreover, conductivity WMT require at least one of the constituents to have a relatively large value of electrical conductivity (*e.g.*, greater than 5 S/mm).

WMT may also be classified according to the technique used to reconstruct the cross–sectional phase distribution; different techniques are suitable for different sensor designs, particularly the arrangement of the electrode wires. The most widely used type of WMT comprises two arrays of parallel electrode wires separated by a small axial distance, such that the wires in each array are perpendicular to the wires in the other array (Figure 1a). Thus, the

two arrays may be projected into a mesh with nodes at the projected crossing points of the wires. The output of this sensor is temporally and spatially discrete measurements of conductivity or permittivity, which are nominally assigned to each individual node. Then, provided that the measurable property is sufficiently sensitive to the phase that is present in the vicinity of each node, one may reconstruct the cross–sectional phase distribution from the nodal conductivity or permittivity values. Consequently, one may identify such a device as a nodal WMT (NWMT), however, to avoid possible confusion, we will instead adopt the well–established label, wire–mesh sensor (WMS). The first device that can be classified as a WMS was described in a patent by Johnson (1987) and was intended to measure the volume fraction of water in crude oil. It used a conductivity WMS design with the two wire arrays designated as the transmitter and receiver electrodes, respectively. The author described the design of a multiplexer that could be used to achieve relatively high cross–section sampling rates. Continuous application of DC current to the electrodes would possibly cause electrolysis, which would lead to unreliable measurements and even destruction of the sensor. Therefore, the conductivity measurements were acquired node by node, such that a voltage was applied to a particular transmitter wire for a short time interval. An improved conductivity WMS (Figure 1a) was proposed by Prasser et al. (1997, 1998), and it incorporated some important modifications to the data acquisition procedure (Figure 1b). Most notably, to increase the data acquisition speed, measurements were done row by row, rather than node by node. For each transmitter wire, the current signal from each receiver wire was converted to a voltage by an operational amplifier and then sampled by an individual sample–and–hold circuit. To prevent electrolysis, a square–wave type pulsating voltage was applied to the transmitter wire. These authors achieved sampling rates of up to 1,200 frames/s, which were later increased to 10,000 frames/s by an improvement of the digital components of the data acquisition system (Prasser et al., 2000). A similar device that was based on measurements of capacitance rather than conductivity was proposed by Da Silva et al. (2007) for measurements in non–conducting fluids.

A second type of WMT was developed by Reinecke et al. (1998) to measure the phase distribution in a gas–liquid flow. This device consisted of three arrays of 29 parallel electrode wires (Figure 2), with the wires in each array rotated by an angle of 60° with respect to those in the adjacent array. With the device inserted in a pipe, the cross–section was discretised into 1000 equilateral–triangle–shaped pixels by the wire projections (Figure 2b). This

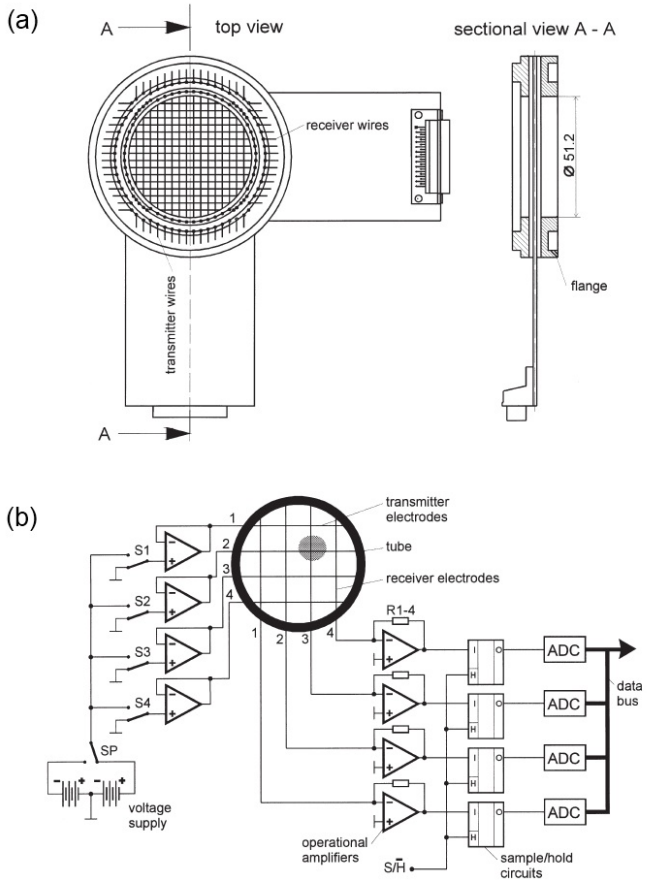

Figure 1: (a) Schematic of wire–mesh sensor (WMS) and (b) its associated data acquisition system (Prasser et al., 1998). (Reproduced with permission from Elsevier)

sensor measured sequentially the conductivity of the fluid between adjacent wires in each array, from which the cross–sectional phase distribution was determined with the use of analytical reconstruction algorithms at a sampling rate of up to 110 frames/s. Unlike WMS, which provide nodal phase measurements, this device reconstructs the cross–sectional phase distribution by processing the measurements of all pairs of wires simultaneously. To distinguish such devices from WMS, we shall refer to them as global wire–mesh tomographs (GWMT). It is noted that, in both WMS and GWMT, individual measurements of conductivity or permittivity are collected sequentially to eliminate electrical interference and/or electrolysis effects on the mea-

surements; this necessarily results in a phase shift between the signals of different nodes in a WMS and those of different wire pairs in a GWMT. The GWMT has been far less popular than the WMS, presumably because of the dependence of the former on time–consuming reconstruction algorithms. The two devices will be discussed separately in the following sections, first with respect to their use in multiphase flows, then with respect to their few applications in multicomponent flows.

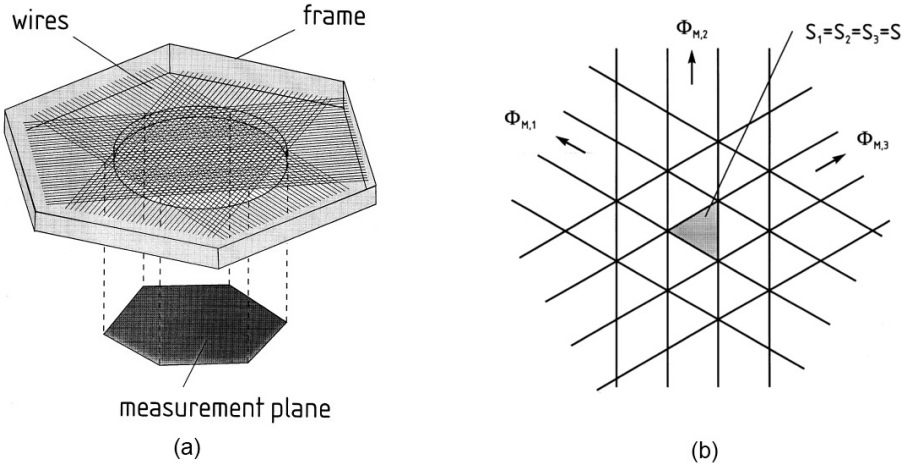

Figure 2: (a) Schematic diagram of a global wire–mesh tomograph and (b) discretization of cross–section into equilateral–triangle–shaped pixels (Reinecke et al., 1998). (Reproduced with permission from Elsevier)

3. Wire–mesh sensors in multiphase flows

3.1. Extraction of flow properties from WMS signals

Wire–mesh sensors provide as output the cross–sectional distribution of conductivity or permittivity. In multiphase flows, one may post–process this output to obtain estimates of the cross–sectional phase distribution, the area–averaged phase fraction and the flow regime. Under certain flow conditions, one may also obtain estimates of the interfacial velocity, the individual bubble diameters and the interfacial area density (namely, the surface area of the interface between the two phases per unit volume).

A sequence of images of an air bubble as it crosses a WMS in water flow and the corresponding instantaneous void fraction maps, determined from

the WMS output, are shown in Figure 3 (Prasser et al., 2001). Each map was largely consistent with the corresponding image of the bubble. Consecutive maps were used to reconstruct an Eulerian side view of the bubble (sometimes referred to as a virtual– or pseudo–side view), by plotting the output of a single WMS row *vs.* an inverted time axis (Figure 3). Although such a representation is useful for visualizing the flow inside channels, it must be noted that an Eulerian side view would not match any actual instantaneous volumetric phase distribution. When a slip velocity between the phases is present, as it is often the case in many multiphase flows, an accurate determination of the streamwise phase distribution would also require the phase velocities, which are not measured by a single WMS. Moreover, reconstruction of the streamwise variations of a property from time histories of the same property, which in turbulence research is known as Taylor's "frozen flow" approximation, requires that the distribution of the property remain "frozen" during the measurement time interval. In turbulent flows, this requirement would only be satisfied when the turbulence intensity were sufficiently low; even then, this approximation would gradually fail, if it were applied to "eddies" with progressively larger length scales. The accuracy of this approximation would be further reduced in gas–liquid flows, in which bubbles get distorted as they approach and cross the WMS. The reconstruction of the spatial phase distribution from WMS measurements is a challenging task that requires further study.

Prasser et al. (2005a) proposed a method for the calibration of the WMS, *i.e.*, the determination of the relationship between the measured nodal conductivity/permittivity and the local phase fraction. A separate issue is the construction of full cross–sectional void fraction maps from the nodal (*i.e.*, discrete) WMS output. A simple approach that has been used in several studies is to assume that each nodal value applies to a corresponding area of influence surrounding the node; the areas of influence of internal nodes would be square, whereas those of nodes adjacent to a circular pipe wall would have irregular shapes. An example of a cross–sectional void fraction map constructed in this way is shown in Figure 4a. Refinements of this approach, which are capable of reconstructing fine–grain interfaces, were proposed by Roitberg et al. (2007) and Prasser (2007); an example is shown in Figure 4b. Prasser et al. (2005a) further calculated an area–averaged phase fraction by weighing the nodal values by the appropriate areas of influence surrounding each node. Two approaches have so far been suggested for identifying the flow regime from WMS measurements: inspection of Eulerian side views

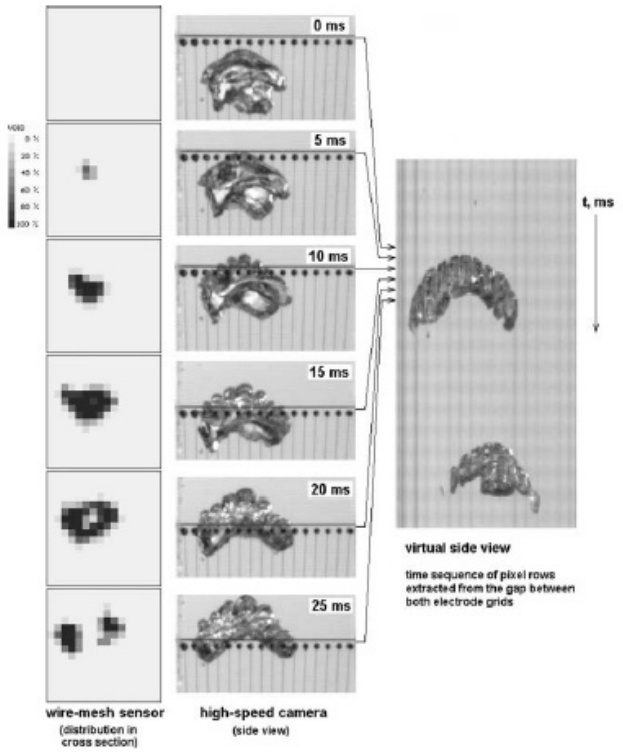

Figure 3: Time sequence of cross–sectional void fraction distributions determined from the output of a WMS (left column), time sequence of flow images (central column) and Eulerian side view of an air bubble transported by water flow (right column) (Prasser et al., 2001). (Reproduced with permission from Elsevier)

of the flow, reconstructed from sequences of instantaneous outputs (Prasser et al., 1998; Pietruske and Prasser, 2007) and statistical analysis of the time history of cross–sectional phase fraction (Shaban and Tavoularis, 2015).

Prasser et al. (2005a) introduced a cross–correlation–based approach to estimate a "gas velocity" in gas–liquid channel flows from the signals of two axially separated WMS. As will be demonstrated in Appendix A, the velocity calculated using the cross–correlation method is an estimate of the time–averaged interfacial velocity, which, under certain conditions, may differ from the true gas velocity. The interfacial velocity has been used as input to algorithms that were developed to estimate the bubble size (Prasser et al., 2001) and the interfacial area density (Prasser, 2007) in bubbly flows. Some authors (Prasser et al., 2005a; Beyer et al., 2010) have further estimated the

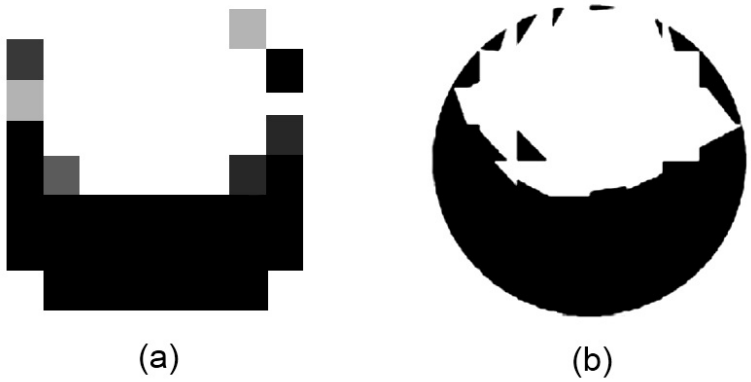

Figure 4: Instantaneous cross–sectional phase distribution in air–water pipe flow from WMS measurements (a) by assigning nodal voltages to areas of influence and (b) using the Piecewise Linear Interface Calculation (PLIC) algorithm (Roitberg et al., 2007). (Reproduced with permission from Elsevier)

gas flow rate in a channel by integrating the product of the local void fraction and the local cross–correlation velocity over the cross–section. The accuracy of the cross–correlation method for estimating the interfacial velocity will be evaluated in Section 4.6, whereas the validity of the integration method to estimate the gas flow rate will be discussed in Section 4.7 and Appendix A.

3.2. Areas of WMS use

Wire–mesh sensors have been used for measurements in multiphase and multicomponent flows occurring in petroleum transport components, nuclear safety research installations, heat exchangers, chemical reactors and other technological systems. A discussion of the applications of the WMS, in particular in relation to the validation of CFD codes, has been presented by Prasser (2008). Some of these applications will be outlined in this section.

Many studies using WMS have been conducted in flows of immiscible fluids in straight pipes. For example, Prasser et al. (2002) and Lucas et al. (2005) measured the bubble size and phase distribution in vertical upward air–water bubbly and slug flows using a conductivity WMS and used these measurements to describe the axial evolutions of these flows. Capacitance WMS were used to study the phase distribution in bubbly flows with one or more non–conducting fluids; examples of such flows are the air–silicone oil flow in a vertical pipe (Szalinski et al., 2010) and a three–phase air–water–

silicone oil flow in a vertical rectangular channel (Da Silva and Hampel, 2013). Shaban and Tavoularis (2015) proposed the use of a machine learning algorithm to identify the flow regime and measure the flow rates of both phases from the output of a conductivity WMS in vertical upward and downward air–water pipe flow.

Studies of flows in channels other than straight pipes have also been reported. Conductivity WMS were used by Al Issa et al. (2007) to study the phase distribution in an air–water flow downstream of a semi–circular obstacle. Hampel et al. (2009) used a miniature conductivity WMS to measure the phase distribution in the mixing chamber of a model atomizer. The effect of bends on the phase distribution and flow pattern in an air–silicone oil flow was studied by Abdulkadir (2011) with the use of a capacitance WMS. Krepper et al. (2007) measured the void fraction and flow patterns in bubble columns using conductivity WMS, whereas Llamas et al. (2008) presented WMS measurements that shed light on the liquid maldistribution in trickle bed reactors. The results of many of these studies are suitable for the development or validation of multiphase CFD models and indeed have been used for such purposes (Lucas et al., 2007; Krepper et al., 2007; Al Issa et al., 2007).

Another class of applications that is of particular interest in the design and analysis of heat exchangers is multiphase flow in pipes with phase change as a result of heat addition or changes in pressure. A conductivity WMS that is suitable for use at temperatures up to 286°C and pressures up to 7 MPa was developed by Pietruske and Prasser (2007) and used for flow visualization in vertical upward steam–water flow at different pressures. Manera et al. (2006) used a conductivity WMS to visualize the flow patterns during the flashing cycles in transient flashing steam–water flows (Figure 5).

4. WMS performance evaluation

4.1. Design considerations

The main geometrical design parameters for the construction of a WMS are the wire diameter, the in–plane wire spacing ("mesh size") and the distance between the wire planes; the main parameter for the construction of the data acquisition system is the sampling rate.

The spatial resolution of a WMS is intimately connected to the in–plane wire spacing (Richter et al., 2002). Typical values of wire spacing for both types of WMS have been in the range from 2 mm to 5 mm, but WMS

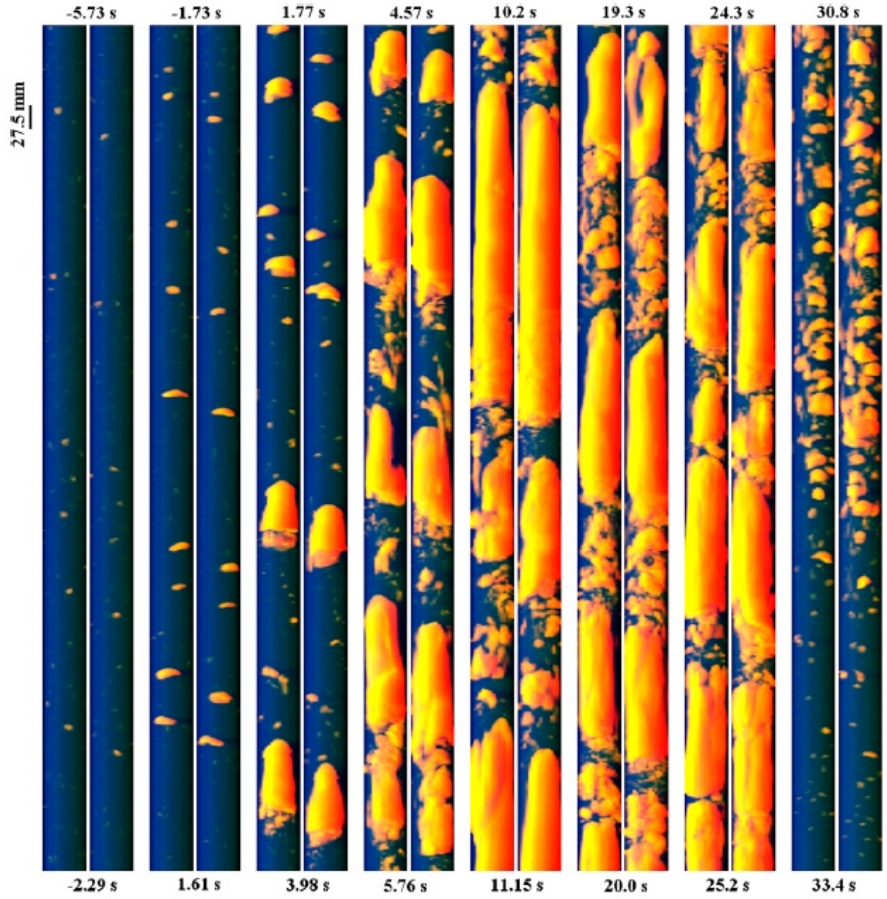

Figure 5: Flow pattern visualization during a transient flashing flow, reconstructed from WMS data. Two successive columns correspond to the measurements extracted from each of two sensors of a dual WMS unit. (Manera et al., 2006). (Reproduced with permission from Elsevier)

with a wire spacing of up to 15 mm have been reported in the literature (Llamas et al., 2008). The spatial resolution that is necessary for a particular application would depend on the flow regime under investigation and the size of the volumes occupied by each phase. It is evident that the accuracy of void fraction measurement in a dispersed flow would be poor, if the size of the individual dispersed bubbles or droplets were significantly smaller than the mesh size; the same would apply to annular flows with a sufficiently small film thickness. On the other hand, there are several factors that effectively

impose a lower bound on the in–plane wire spacing. To achieve a smaller wire spacing, one would necessarily use a larger number of wires; this would result in a larger pressure drop across the sensor, a greater distortion of the flow and a higher possibility of errors due to cross–talk (Section 4.4). The operation of a sensor with a larger number of wires would also require a data acquisition system that can operate at a much larger sampling rate, as the number of measurement nodes would increase quadratically with the number of sensor wires in each array. Among the practical aspects of WMS design that require further research is the determination of the mesh size that would be optimal for each specified combination of channel size and flow regime. The possibility of using WMS with non–uniform wire spacing, such that the node density would be higher at locations with sharper variations of phase fraction (*e.g.*, near solid walls), seems worth exploring.

The WMS wire diameter has to be as small as possible to keep the flow distortion by the device and the associated pressure drop within acceptable limits; a lower bound of this diameter is set by the mechanical strength of individual wires (Prasser et al., 1998). Typically, WMS wires have diameters around 0.1 mm, but thicker wires have been used for applications in which the experimental conditions were particularly hostile. For example, Pietruske and Prasser (2007) designed a WMS with thick (0.25 mm diameter) wires for an application in which both the pressure and the temperature were high. Each wire was mounted on a spring at one end, which regulated its tension and prevented wire contact or breakage in the presence of thermal expansion and contraction caused by temperature fluctuations. The sensor housing was also specifically designed to withstand high pressures. Electrodes in the form of rigid rods have also been proposed as substitutes for wires in applications in which heavy mechanical loads on the sensor elements are expected (Prasser et al., 1998).

Although no specific studies of the optimal axial spacing of the wire planes for accurate WMS measurements are known, it seems evident that this distance should be sufficiently small for changes in the cross–sectional distributions of flow properties from one plane to the other to be negligible. In addition, it is known that a relatively large spacing would exacerbate the problem of cross–talk in conductivity WMS as discussed in Section 4.4.

The temporal resolution of a WMS is connected mainly to its sampling rate. The Nyquist criterion must be met for measuring accurately time histories of phase fraction, but this requirement may be relaxed if one is merely interested in determining the time– and area–averaged phase fraction. For

example, we have recently determined that, in air water flow through a pipe with an ID of 32.5 mm and liquid and gas superficial velocities up to 3 m/s and 20 m/s, respectively, the measured average void fraction was insensitive to the WMS sampling rate, when the latter exceeded 20 samples/s (Shaban, 2015). We have also found that, depending on the flow conditions, the measurement accuracy of interfacial velocity using dual WMS may be sensitive to the sampling rate and the response time of the WMS instrumentation.

4.2. Intrusiveness of the sensor wires

WMS are intrusive devices and their presence necessarily affects the flow parameters that are being measured. A few studies have evaluated the intrusiveness of the WMS wires in gas–liquid flows by examining images from video recordings (Prasser et al., 2001; Wangjiraniran et al., 2003) and X–ray tomographs (Prasser et al., 2005b). The consensus from these studies was that the presence of wires would inevitably lead to fragmentation of gas bubbles, regardless of their size or the flow conditions (Figure 6). For example, a reconstructed view of a single bubble, shown in Figure 3, resembles fairly well the image of the bubble shortly after it crossed the WMS, but other images show that the bubble shape changed visibly during the time considered. Although random bubble deformation is expected to occur at all times in a turbulent flow, the apparent flattening of the bubble may be attributed to its "impact" upon the WMS, whereas the fragmentation of its originally smooth interface contour to a cluster of connected small semi–circles is attributable to the dissection of the bubble by the WMS wires (Figure 6). Prasser et al. (2001) noted that bubble fragments tended to coalesce downstream of the sensor when the liquid flow rate was sufficiently high, but, for low liquid flow rates, the fragments did not coalesce for a relatively large downstream distance. The shape of Taylor bubbles in slug flows with a low liquid flow rate was found to be distorted as they crossed a WMS from bullet–like to mushroom–like (Prasser et al., 2005b). Lessard et al. (2014) found that the signals of the two sensors in a dual WMS unit were measurably different, presumably due mainly to distortion of the bubbles by the upstream sensor. Such distortions would adversely affect the accuracy of the interfacial velocity and bubble size estimates. Lessard et al. (2014) reported that the difference in the area–averaged void fraction measured by the two sensors was up to 0.05 for liquid superficial velocities lower than 0.5 m/s, but this difference became smaller at larger liquid flow rates.

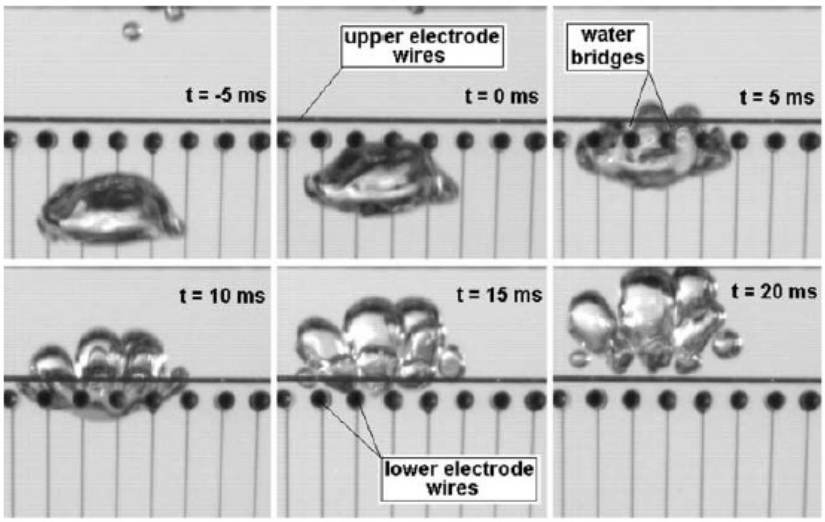

Figure 6: Bubble fragmentation caused by a wire–mesh sensor (Prasser et al., 2001). (Reproduced with permission from Elsevier)

Depending on the wire diameter and spacing, WMS would typically introduce a 4–10 % blockage of the cross–sectional area of the channel. In principle, this blockage would cause a local acceleration of the flow, but, in practice, bubble acceleration in air–water flows has been observed only for relatively large liquid flow rates (Prasser et al., 2001), whereas the liquid velocity in the vicinity of the WMS has not been measured. For very low liquid flow rates ($j_l \leq 0.2$ m/s), Prasser et al. (2001) and Wangjiraniran et al. (2003) observed a deceleration of gas bubbles as they approached the sensor, which they attributed to the increased resistance applied to the bubbles by the wires as a result of an increasing relative strength of surface tension forces. The high pressure induced on the upstream surface of the sensor wires by the flow also possibly contributes to the bubble deceleration.

In summary, it has been demonstrated in the available literature that the wires of wire–mesh sensors cause a significant distortion of gas bubbles in the bubbly and slug flow regimes and that this distortion is more pronounced at lower liquid flow rates. The effect of the wire intrusiveness in flows of fluid pairs with large surface tension coefficients and viscosity ratios has not yet been studied. It seems possible that, in addition to a large wire–induced deceleration effect in low–speed flows, the wires may be wetted by one fluid

and the inertia of the flow may be insufficient to dislodge it from the wires, leading to erroneous measurements. Furthermore, the flow in a channel with an installed WMS has never been compared to an identical flow without WMS, possibly due to the technical difficulty of consistently reproducing the same flow conditions. If such a study were performed, it would clarify the effect of the WMS on the upstream flow and the accuracy of reconstruction of the undisturbed phase distribution from WMS measurements.

4.3. The measurement volume of a WMS

The WMS output consists of an array of phase fraction values at each node. As discussed in section 3.1, the construction of cross–sectional phase maps and the calculation of a cross–sectional phase fraction have commonly been based on the assumption that each nodal value applies uniformly to an appropriate influence area of the cross–section that surrounds the node. This is in turn based on the assumption that the nodal output value represents accurately the average conductivity or permittivity of fluid within a prism that has as base the nodal influence area and as height the distance between the two WMS wire planes. However, measurements performed by Zoeteweij (2007) using a conductivity WMS demonstrated that a bubble crossing the measurement plane affected the measurements at the receiver electrodes that were up to two mesh wires away from the measurement node. In support of this observation, Zoeteweij (2007) cited numerical simulations of the electrostatic field around the wires of a simplified conductivity WMS with 3 transmitter and 3 receiver wires by Smeets (2007); the conclusion of these simulations was that the measurement volume to which a node would be sensitive was not prismatic but tetrahedral, having a side in the direction of the receiver wires that was up to 4 times longer than the wire spacing (Figure 7b). This implies that the nominal volume of measurement of a WMS would include regions within which the conductivity or permittivity would influence the readings of more than one nodes, as well as regions whose conductivity or permittivity would not influence any node. Numerical simulations of the electrostatic field around the wires of a simplified permittivity WMS were performed by Da Silva (2008), who computed the magnitude of the nodal capacitance for different sizes and locations of a permittivity perturbation. These results also confirmed that the nodal capacitance reading would be affected by perturbations outside the nominal prismatic measurement volume.

The available literature has provided sufficient evidence for one to conclude that the shape and size of the volume of influence of a WMS node would

depend on the fluid properties, the sensor geometry and the driving signal. For simplicity, nearly all studies using the WMS have assumed that the nodal measurement volumes are prismatic, non–overlapping and filling the entire space between the two wire arrays. Errors introduced by this assumption, for example the error in calculating a cross–sectional void fraction, have not yet been quantified. Such errors would be difficult to determine experimentally, but it seems possible that CFD analysis, coupled with magnetohydrodynamics and multiphase models, would provide answers to some of the lingering questions.

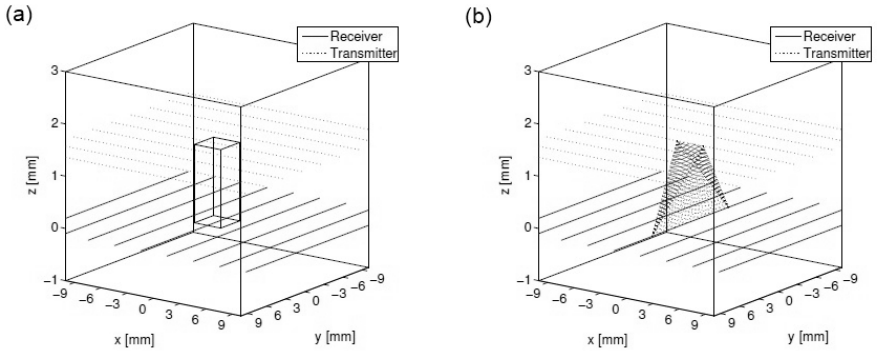

Figure 7: Definitions of WMS measurement volume: (a) nominal prismatic measurement volume *vs.* (b) tetrahedral measurement volume proposed by Smeets (2007) (Zoeteweij, 2007). (Reproduced with permission from M.L. Zoeteweij)

4.4. Cross–talk

In conductivity WMS, even when the measurement volume of a node contains exclusively the non–conductive phase, a non–zero (actually positive) current may flow into the associated receiver wire. This current is a consequence of the existence of multiple electron paths between the transmitter and receiver wires, in addition to the direct straight path, whose projection is the measurement node. One such electron path (Figure 8a) could start at the activated transmitter wire, pass through an adjacent wire in the transmitter or receiver plane, and end at the activated receiver wire, whose current is being sampled; this scenario is more likely to occur when the WMS mesh size is relatively small. To reduce the current flowing through such a path, Prasser et al. (1998) designed a WMS with transmitter and

receiver electronic circuits that had impedances that were much lower than that of the fluid, such that the potentials of all the transmitter and receiver wires, except for the activated transmitter wire, would remain essentially zero. Llamas et al. (2008) documented cross–talk for a conductivity WMS used in annular flows, where the electron path would be much longer than the direct electron path at the measurement node. In this case, the current would flow from the activated transmitter wire to the activated receiver wire, in a circumferential path through the liquid film (Figure 8b). These authors concluded that this type of cross–talk would be exacerbated by the use of a large WMS wire–plane spacing.

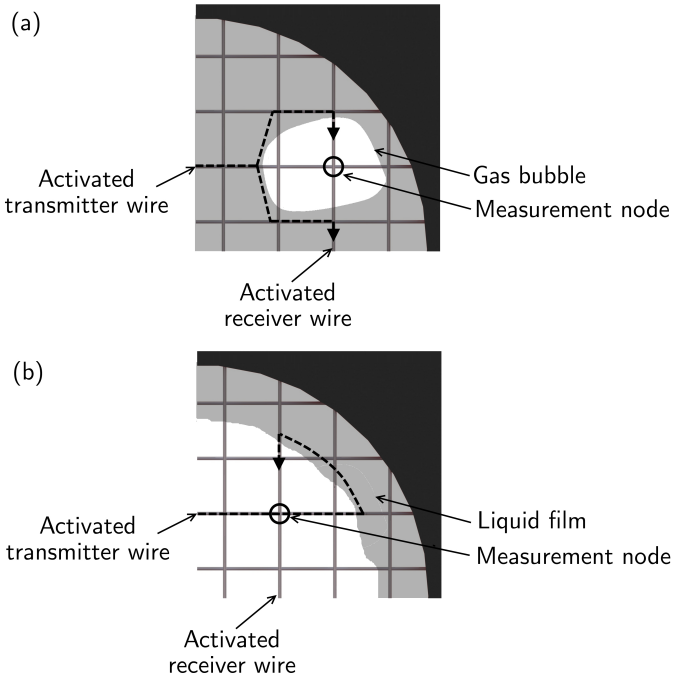

Figure 8: Illustration of alternative electron paths (dashed lines) from a transmitter wire to a receiver wire that lead to cross–talk in a conductivity WMS: (a) path through neighbouring wires and (b) path through the liquid film in annular flow.

4.5. Uncertainty of void fraction measurements

Several studies have compared measurements of void fraction in gas–liquid flows using WMS to those using other methods. A summary of some of these

Table 1: Summary of selected studies comparing WMS measurements of the time– and area–averaged void fraction $\overline{\alpha}$ to reference measurement methods.

Study	Experimental details	Observations
Prasser et al. (2005a)	WMS *vs.* γ–ray densitometer in vertical flow $D = 51.2$ mm $\overline{\alpha} = 0 - 1$	The centre–line–averaged void fraction had an uncertainty of 0.05.
Prasser et al. (2005b)	16×16 WMS *vs.* X–ray tomograph in vertical flow $D = 42$ mm $\overline{\alpha} = 0.05 - 0.45$	$\overline{\alpha}$ had an uncertainty of 0.01 for bubbly flows and a negative bias of -0.04 for slug flows.
Sharaf et al. (2011)	16×16 WMS *vs.* γ–ray densitometer in vertical flow $D = 50$ mm $\overline{\alpha} = 0.05 - 0.5$	Local void fraction measurements were in fair agreement on the pipe axis but had large discrepancies near the wall.
Salve et al. (2012)	16×16 WMS *vs.* quick closing valve method in horizontal flow $D = 19.5$ mm $\overline{\alpha} = 0.02 - 0.9$	The WMS over–estimated low values of $\overline{\alpha}$, under–estimated intermediate values of $\overline{\alpha}$ and estimated accurately large values of $\overline{\alpha}$.
Present (data from Shaban and Tavoularis (2015))	8×8 WMS *vs.* pressure gradient method in vertical flow $D = 32.5$ mm $\overline{\alpha} = 0.02 - 0.95$	The WMS over–estimated low values of $\overline{\alpha}$, introduced a negative bias in slug flow and made fair estimates in churn and annular flows.

studies is given in Table 1. Unless indicated otherwise, such studies were conducted in air–water pipe flows.

The time– and area–averaged void fraction $\overline{\alpha}$, measured by a 16×16 WMS in a horizontal 19.5 mm I.D. pipe was compared by Salve et al. (2012) to the volume–averaged void fraction $\overline{\alpha}_{QCV}$, measured using the quick–closing valve (QCV) method, which often serves as the standard for void fraction measurements. Good agreement was found between the results of the two methods for large void fractions in the annular flow regime ($0.8 < \overline{\alpha}_{QCV}$). However, the WMS systematically over–estimated the void fraction for $\overline{\alpha}_{QCV} < 0.15$ and consistently underestimated it for intermediate void fractions ($0.5 < \overline{\alpha}_{QCV} < 0.8$).

A few studies have compared the void fraction measured using WMS with measurements by radiation attenuation methods. For example, Sharaf et al. (2011) compared the line–averaged void fraction along several chords, measured using a 16 × 16 WMS in vertical–upward air–water flow in a 50 mm I.D. pipe to the corresponding values measured using a γ–ray densitometer that was traversed along the pipe diameter. Fair agreement was found between the two methods near the centre of the pipe, however, large discrepancies were noted near the pipe wall. Prasser et al. (2005b) compared void fraction measurements using a 16 × 16 WMS and an ultra–fast X–ray tomograph in vertical–upward air–water flow in a 42 mm I.D. pipe. The time histories of the area–averaged void fraction revealed that the WMS tended to under–estimate the instantaneous local void fraction within the Taylor bubbles in the slug flow regime, which resulted in an under–estimation of $\overline{\alpha}$ in the slug flow regime. Good agreement was found for void fraction measurements in bubbly flows using the two methods. A more detailed comparison of the void fraction profiles obtained using these two methods was presented by Zhang et al. (2013). Their results show that the WMS consistently over–estimated the void fraction near the pipe wall compared to the X–ray tomograph and it under–estimated the void fraction near the centre of the pipe in the slug flow regime.

The WMS has also been compared to other electrical methods for void fraction measurement. Manera et al. (2009) presented a comparison of void fraction profiles at the centre–line of a 50.8 mm I.D. pipe, measured using a conductivity WMS and a four–tip conductivity needle probe. The WMS was found to over–estimate the void fraction for the bubbly flow cases, whereas it showed no measurable bias for the slug flow measurements. Void fraction measurements using more recent tomographic techniques, for example,

electrical resistance tomograph (ERT) (Olerni et al., 2013) and electrical capacitance tomography (Azzopardi and Abdulkareem, 2010), have also been compared to the WMS; in general WMS measurements were found to be in fair agreement with measurements by these methods.

In a parallel study (Shaban and Tavoularis, 2015), we have recently collected a large database of 1250 WMS measurements in vertical upward air–water flow in a 32.5 mm I.D. pipe using a 8×8 WMS, with air superficial velocity j_g in the range from 0.04 to 20.0 m/s and water superficial velocity j_l in the range from 0.13 to 3.0 m/s. Further processing of these data provided values of $\overline{\alpha}_{WMS}$, which were compared to void fraction $\overline{\alpha}_{PGM}$ values calculated using the pressure gradient method. Upon measuring the total pressure gradient in the test section, the contribution of friction to the total pressure gradient was accounted for with the two–phase friction multiplier ϕ^2_{fo} calculated using the Friedel correlation, as suggested by Collier and Thome (1994), then $\overline{\alpha}_{PGM}$ was calculated from the gravitational contribution to the total pressure gradient. As an accuracy check for the pressure gradient method, ϕ^2_{fo} was calculated for a few representative cases using the pressure gradient equation with the void fraction measured using the QCV method and compared to ϕ^2_{fo} calculated using the Friedel correlation; good agreement was found between the two methods. Figure 9 demonstrates that, in bubbly flows with $\overline{\alpha}_{PGM} < 0.1$, the WMS estimate was systematically higher than that of the pressure gradient method. On the contrary, $\overline{\alpha}_{WMS}$ tended to be smaller than $\overline{\alpha}_{PGM}$ in slug flows with $\overline{\alpha}_{PGM} < 0.6$. Fair agreement was found between the two methods for $0.6 < \overline{\alpha}_{PGM}$.

The previous discussion makes it clear that the accuracy of void fraction measurements by WMS would depend on the phase flow rates, the flow regime and the spatial resolution of the sensor. Even though none of the reference methods used for comparison is free of error and uncertainty, several trends of the WMS performance appear to have been documented in a convincing manner. Overall, the WMS provides fair estimates of the time– and area–averaged void fraction. However, in bubbly flows at very low void fractions, especially in small–diameter pipes, the WMS tends to over–predict the area–averaged void fraction. This is most probably a result of the limited spatial resolution of the sensor, as these flow conditions are expected to correspond to very small bubble sizes. In slug flows, a systematic negative bias in the void fraction measurements by WMS has been noted by several researchers. This could be explained by the persistence of thin liquid bridges (Figure 6) in the wake of the upstream wires during the passage of a gas bubble (Prasser

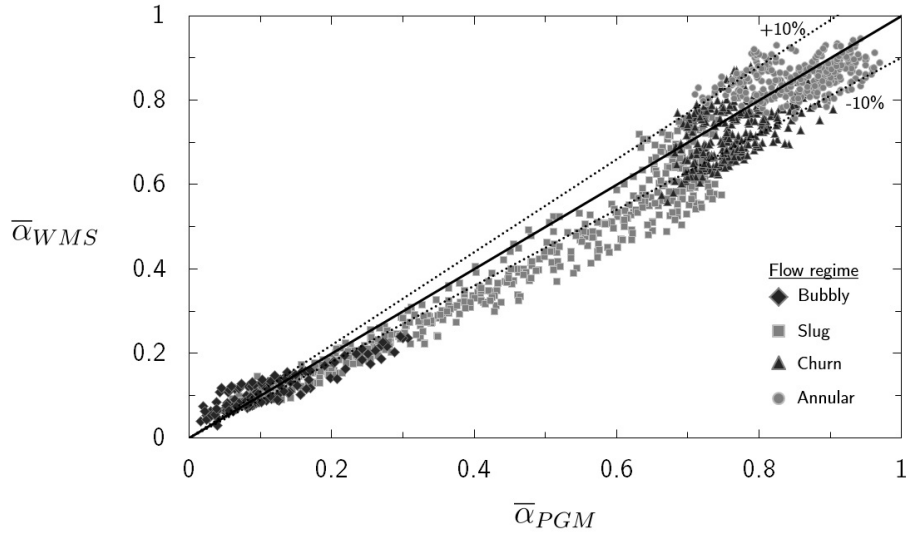

Figure 9: Void fraction measured using a wire–mesh sensor ($\overline{\alpha}_{WMS}$) *vs.* that calculated using the pressure gradient method ($\overline{\alpha}_{PGM}$).

et al., 2005b). Fair agreement between the WMS and other void fraction measurement methods has been observed for upward churn and annular flows in vertical channels and stratified flows in horizontal channels.

4.6. Uncertainty of interfacial velocity measurements

The accuracy of interfacial velocity measurements using WMS has previously been quantified in several studies. For example, Richter et al. (2002) used a signal processing technique to identify the passage of a bubble in the signals of dual WMS separated by a small axial distance. They calculated the velocity indicated by the time of flight of the bubble between the two sensors and found that it agreed well with that obtained using high speed camera for interfacial velocities $U_{int} < 0.5$ m/s. Lessard et al. (2014) also found good agreement of the interfacial velocity calculated using the cross–correlation method from the signals of dual WMS with the bubble velocity obtained from high–speed video recordings in a horizontal air–water flow in the range of interfacial velocity 0.5 m/s $< U_{int} <$ 2 m/s. Ofuchi et al. (2012) presented results that showed good agreement of the interfacial velocity estimates obtained by WMS, high speed video and an ultrasonic velocity measurement technique in the range 0.8 m/s $< U_{int} <$ 2 m/s. However,

these authors found growing discrepancies between the methods in the range 2 m/s $< U_{int} <$ 5 m/s, which they attributed to the presence of small bubbles affecting the accuracy of the cross–correlation technique used with the WMS and the ultrasonic sensors. Finally, Manera et al. (2009) compared the interfacial velocity profiles obtained from the WMS to those obtained by averaging the individual bubble velocities obtained from a four–tip conductivity probe and found small differences in the values measured by the two methods at low interfacial velocities and larger differences at larger interfacial velocities, especially near the centre of the pipe. Thus, it can be concluded that, using the cross–correlation method or other approaches, dual WMS can provide fairly accurate estimates of the interfacial velocity, especially in the lower ranges of interfacial velocity. At larger interfacial velocities, this accuracy would be somewhat diminished, mainly due to the flow distortion between the two WMS.

4.7. Uncertainty of gas flow rate calculated using the cross–correlation method

It has been suggested that an estimate of the time–averaged gas flow rate, or equivalently the time–averaged gas superficial velocity j_{xc}, in a gas–liquid flow could be obtained by integrating the product of void fraction and interfacial velocity over a cross–section (Prasser et al., 2005a, 2007; Lucas et al., 2010; Beyer et al., 2010). Comparisons between j_{xc} and j_g and other relevant discussions have been presented by previous authors. Prasser et al. (2001) suggested the use of the average gas superficial velocity as an estimate of the actual gas velocity for bubble volume calculations in the bubbly regime. These authors stated that this approximation would only be valid if the non–uniformity of gas velocity over the cross–section and the temporal fluctuations of gas velocity were negligible; such assumptions may be appropriate for the bubbly flow regime but would clearly be violated for flows in other regimes. A positive bias in j_{xc} in bubbly flows was observed by Beyer et al. (2010) and Lucas et al. (2010) for low j_g in a 195.3 mm I.D. pipe. With increasing gas flow rate, the bias decreased and j_{xc} approached j_g. Prasser et al. (2005a, 2007) calculated j_{xc} using measurements of a 16×16 WMS in a pipe with an internal diameter of 52.3 mm for gas superficial velocities in the range 0.0025 m/s $< j_g <$1.16 m/s. They found a fair agreement of j_{xc} with j_g for $j_g < 0.3$ m/s, but also observed an increasing tendency for j_{xc} to under–estimate j_g at higher velocities, a discrepancy which they attributed to flow distortion by the sensor wires.

As described in Appendix A, we used data from Shaban and Tavoularis (2015) to establish the ranges of flow conditions under which the velocity j_{xc} calculated by the cross–correlation method would be an acceptable estimate of the gas superficial velocity j_g. This study was conducted using a 8×8 WMS in a pipe with an internal diameter of 32.5 mm for air superficial velocity j_g in the range from 0.04 m/s to 20 m/s and water superficial velocity j_l in the range from 0.13 to 3.0 m/s. In bubbly flows with large bubble sizes, usually corresponding to large gas flow rates (0.5 m/s $< j_g$ in that study), the spatial resolution of the WMS was deemed to be sufficient for accurate gas superficial velocity estimates. In slug flows at low gas flow rates ($j_g < 1.5$ m/s in that study), the interfaces were sufficiently well–defined and j_{xc} was within ±25% of j_g. For all churn and annular flows, the cross–correlation method provided a gas superficial velocity that was systematically much smaller than the measured value.

5. Global wire–mesh tomographs in multiphase flows

The WMS and GWMT follow different procedures for the reconstruction of the phase distribution from discrete conductivity/permittivity measurements. The conductivity/permittivity distribution can be obtained from the output of a GWMT using the image reconstruction techniques described by Reinecke et al. (1998). As mentioned earlier, in the original design of the GWMT, using 29 wires in each wire plane, the flow cross–section was discretized into 1000 equilateral–triangle–shaped pixels. This meant that 84 linearly independent measurements were available for the estimation of the phase fraction at each of the 1000 pixels. Because this system of equations was grossly under–determined, it could not be solved directly to reconstruct the cross–sectional phase distribution. An iterative algorithm was used instead, and some constraints had to be imposed on the solution to reduce the number of unknowns. For example, during the course of the solution, the void fraction was bounded between 0 and 1. Also, if the dimensionless conductivity measurement between a pair of wires corresponded to either liquid or gas, the phase fraction for all the pixels between those two wires were set accordingly. The GWMT provides values of phase fraction at discrete pixels, each of which corresponds to a known fraction of the cross–sectional area and area–averaging can be directly performed using these values. Schmitz and Mewes (2000) compared the area–averaged void fraction measured using a GWMT to the volumetric void fraction $\overline{\alpha}_{LS}$ measured using the level–swell

technique and found deviations up to 25% for $\overline{\alpha}_{LS} < 0.25$. The same authors also compared the time histories of void fraction obtained using the GWMT to those obtained using the pressure gradient method during a rapid de–pressurization of a vessel and found a fair agreement between the two sets of results. The intrusiveness of the GWMT wires has not been discussed in the literature, but it is expected to have similar effects on the flow structure and the measurement uncertainty as for the WMS (Section 4.2).

Although the GWMT has been far less popular than WMS, it has nevertheless been used in some unique multiphase flow applications. The original design of the GWMT was used by Reinecke et al. (1998) to measure the phase distribution and interfacial velocity in horizontal air–water slug flow. This device, adapted to a larger diameter, was subsequently used to measure the phase distribution and to visualize the flow regime in a developing air–water flow in a model of the hot leg of a pressurized water reactor (Petritsch and Mewes, 1999). The two–phase flow during a rapid depressurization of a chemical reactor vessel was studied by Schmitz and Mewes (2000). The use of a GWMT in this study allowed time–resolved measurements of void fraction to be collected during the pressure transient. Finally, Vauth et al. (2004) employed a GWMT for flow regime visualization in a test facility designed to investigate the operational performance of multiphase twin screw pumps, which were designed to pump oil–water–air mixtures.

6. Application of wire–mesh tomography to multicomponent flows

Wire–mesh tomography has been used for studying properties of multicomponent flows, consisting of streams of a reference fluid and a tracer fluid with significantly different conductivities. A popular choice has been to use salt water as a tracer fluid and distilled water as the reference fluid. The cross–sectional component distribution in multicomponent flows may be obtained using similar techniques to those used in reconstructing the phase distribution in multiphase flows. This has been previously used in the study of the mixing of a passive scalar downstream of porous tubular reactors (Häfeli et al., 2013) and T–junctions (Kickhofel et al., 2014). It has also been used to measure the coolant distribution in certain components of a Pressurized Water Reactor (PWR) model after a postulated Loss Of Coolant Accident (LOCA) (Kliem et al., 2008). Recently, Ylönen (2013) used wire–mesh sensors to study scalar mixing in the sub–channels of a simplified 4×4 rod bundle. This author also tested the effect of different grid spacer designs

on the dispersion of the tracer fluid (Figure 10). No available studies have quantified the measurement uncertainty of WMT or the significance of the wire intrusiveness in multicomponent flows.

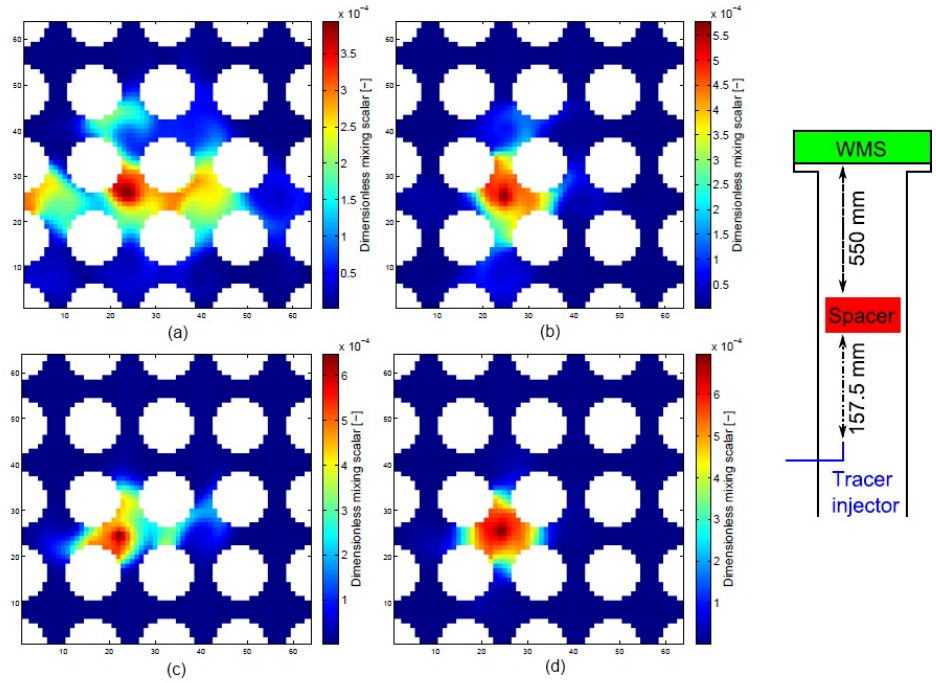

Figure 10: Effect of different spacer designs (a-d) on the dispersion of a conducting tracer fluid in a non–conducting reference fluid (Ylönen, 2013). (Reproduced with permission from A. Ylönen)

7. Summary and concluding remarks

Wire–mesh tomography is a measurement technique that produces cross–sectional phase or component maps in multiphase and multicomponent flows with relatively high spatial and temporal resolutions. Several other important flow properties can be determined by post–processing of WMT output signals. This document has summarised the available literature on various aspects of wire–mesh tomography, and complemented some of this information with additional original analysis. The different types of WMT and their principles of operation have been described. The extraction of various flow properties from wire–mesh sensor signals was briefly explained, followed by

a summary of a number of successful applications of WMS in multiphase flows. The performance of wire–mesh sensors has been evaluated in detail, using new data, as well as results obtained by other authors. This evaluation has shed light on several issues related to WMS design and accuracy, including the sensor intrusiveness, spatial resolution, cross–talk and measurement uncertainty. We have concluded that WMS generally provides fairly accurate estimates of the void fraction and the interfacial velocity, but it is also subjected to systematic errors in certain flow regimes and under certain flow conditions. The prediction of the gas flow rate in gas–liquid flows using the cross–correlation method was found to be accurate only for a very narrow range of flow conditions. The principles and successful applications of global WMT have also been presented. An attempt has been made in this work to identify lingering issues related to wire–mesh tomography and to suggest procedures that may be used for resolving these issues in the future.

Acknowledgements

Financial support for this study was provided by the University Network of Excellence in Nuclear Engineering (UNENE), Atomic Energy of Canada Limited (AECL) and the Natural Sciences and Engineering Research Council of Canada (NSERC).

Appendix A. Estimation of gas superficial velocity with the use of the cross–correlation method

Appendix A.1. Analytical background

The time–averaged gas superficial velocity through a pipe with an inner radius R can be calculated as

$$j_g = \frac{1}{T}\frac{1}{\pi R^2}\int_{t=0}^{T}\int_{r=0}^{R}\int_{\theta=0}^{2\pi} U(r,\theta,t)\;\alpha(r,\theta,t)\;r\;d\theta\;dr\;dt, \tag{A.1}$$

where t denotes time, r and θ are, respectively, the radial and azimuthal coordinates, T is a time interval that is sufficiently long for the time averages to converge, U is the instantaneous local velocity and α is the local void fraction; it is noted that $\alpha = 1$ and $U = U_g$ when the location of concern is occupied by gas, whereas $\alpha = 0$ and $U = U_l$ when this location is occupied by liquid.

Equation A.1 shows that, to determine j_g, one would require the spatial and temporal distributions of the instantaneous local gas velocity U_g and void fraction α. To obtain the spatial distribution of the flow properties, the WMS discretizes the measurement section into a grid, whose spacing is a measure of the spatial resolution of the method. The temporal distribution (namely, the time history) of gas velocity cannot be measured directly by WMS. Instead, by analysing the output of a single WMS, one may identify the passage of the interface between the two phases through each node; by analysing the outputs of a dual WMS unit, one may, in principle, estimate the interfacial velocity. For simplicity, one may assume that the interfacial velocity is equal to the velocity of the liquid and gas in contact with that interface. Note that the interfacial velocity is a discrete function and is only defined at phase interfaces, as opposed to the gas and liquid velocities, which are piecewise continuous functions. Consequently, the interfacial velocity at best represents the gas velocity at certain instants in time and it cannot take into account gas motion in continuous gas structures, such as within bubbles and in the gas core of annular flows.

Let us consider two WMS separated by a distance Δx and let Δt be the time required by an interface to traverse the distance between the two sensors. The velocity of an individual gas–liquid interface, to be denoted as U_{int}, can be estimated as

$$U_{int} = \frac{\Delta x}{\Delta t} \ . \tag{A.2}$$

Ideally, individual interfaces may be identified by comparing the outputs of two WMS in tandem, however, this approach would only be practical for relatively narrow ranges of liquid and gas flow rates, due to the flow distortion caused by the sensor. As a surrogate, several authors (Prasser et al., 2005a; Beyer et al., 2010; Lucas et al., 2010) have suggested the "cross–correlation velocity" U_{xc}, which can be calculated from the cross–correlation function of the signals of corresponding WMS nodes as

$$U_{xc} = \frac{\Delta x}{\Delta t_{CCF_{max}}} \ , \tag{A.3}$$

where $\Delta t_{CCF_{max}}$ is the time lag corresponding to the peak in this cross–correlation function. Unlike U_{int}, which is a discrete function, U_{xc} is a single–valued property, which is equal to the most probable value (mode) of U_{int}, which, depending on the probability density function of U_{int}, may or may not be equal to the average interfacial velocity. To reduce the non–uniformity

of the radial gas velocity profiles, (Prasser et al., 2005a) proposed that the nodal cross–correlation functions be azimuthally averaged to produce the azimuthally averaged cross–correlation velocity $U_{xcr}(r)$.

Following suggestions by the previously mentioned authors, a gas superficial velocity estimate, to be denoted as j_{xc}, was determined as

$$j_{xc} = \frac{1}{\pi R^2} \int_0^R U_{xcr}(r)\ \alpha_r(r)\ 2\pi r\ dr, \tag{A.4}$$

where $\alpha_r(r)$ is the temporally and azimuthally averaged void fraction.

Appendix A.2. Accuracy of the cross–correlation method

Using the experimental database collected in a parallel study (Shaban and Tavoularis, 2015), we evaluated the accuracy of the cross–correlation method for estimating the gas flow rate. This data was collected using an 8×8 WMS in vertical upward air–water flow in a 32.5 mm I.D. tube at near–atmospheric pressure, with air superficial velocity j_g in the range from 0.04 to 20.0 m/s and water superficial velocity j_l in the range from 0.13 to 3.0 m/s. Figure 11 presents the ratio of the estimated gas superficial velocity j_{xc}, calculated from equation A.4, and the experimental value j_g, measured independently by flow meters, over a wide range of conditions and for all flow regimes. This ratio spanned two orders of magnitude and generally decreased with increasing j_g and increased with increasing j_l. Its value depended strongly on both the flow regime and the flow rate. The relative errors of superficial velocity predictions using this method were within $\pm 25\%$ for bubbly flows in the range 0.5 m/s $< j_g$ and for slug flows in the range $j_g < 1.5$ m/s. However, outside these ranges, j_{xc} systematically over–estimated j_g in bubbly flows, with the difference increasing with decreasing j_g and increasing j_l, and j_{xc} systematically under–estimated j_g in slug flows, with the difference increasing as j_g was increased. For all churn and annular flows, this method gave a very inaccurate estimate of gas superficial velocity, namely one that was 200–1000% smaller than the measured value. Separate tests were performed to determine the dependence of j_{xc} on the WMS sampling frequency and they demonstrated that j_{xc} was weakly sensitive to the sampling frequency. Nevertheless, the same trends in the discrepancy between j_{xc} and j_g were noted even for the highest possible sampling frequency of 10,000 samples/s.

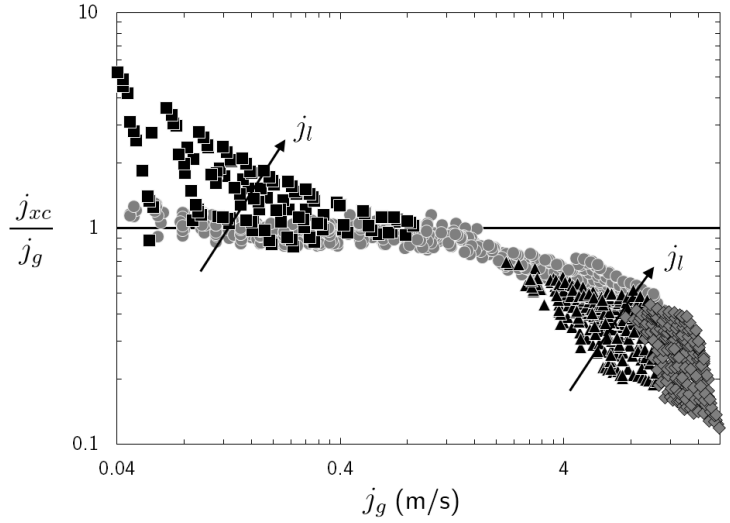

Figure 11: Comparison of the cross–correlation velocity j_{xc} to the measured gas superficial velocity j_g. ■: bubbly flow regime, ●: slug flow regime, ▲: churn flow regime, ◆: annular flow regime.

Appendix A.3. Sources of error

The observed differences between the gas superficial velocity estimates via the cross–correlation method and the measured values may be attributed to several sources of error, the main ones of which may be summarized as follows.

- As explained earlier, the cross–correlation velocity U_{xc} would, in general, be different from the time–average interfacial velocity. In addition, the average interfacial velocity itself would not necessarily be equal to the time–averaged gas velocity.

- Even if one assumed that U_{xc} were an appropriate surrogate of the time–averaged U_g, the use of Equation A.4 would introduce an error because the integrand does not account for temporal fluctuations of void fraction and gas velocity. Replacement of the product of instantaneous values of fluctuating properties in integrands by the product of their averages introduces an error of a type that is well known in the analysis of stochastic processes, as for example in the theory of turbulence. In vertical upward flows at relatively high flow rates, this approximation would generate a negative bias in the estimates of j_g,

as may be observed in Figure 11; this issue will be discussed in more detail in Appendix B.

- An obvious source of error, especially in the bubbly flow regime, is the limited spatial resolution of the WMS. In bubbly flows with bubble diameters smaller than the wire mesh spacing, the estimated void fraction and, consequently, the estimated gas superficial velocity would likely be subjected to large uncertainties.

- Additional errors associated with the use of the cross–correlation approach may be expected to occur under specific two–phase flow conditions. For example, in the churn and annular flow regimes, even when a WMS node is exclusively immersed in the gas phase during the sampling interval, its output would be fluctuating, due to the presence of noise. The interfacial velocity output for that node would be erroneous, as there would be no interface to contribute to a strong peak in the cross–correlation function. In the churn flow regime at low liquid flow rates, backflow would occur over some of the WMS nodes, which would tend to widen the peak in the cross–correlation function due to the presence of both negative and positive velocities. Moreover, at high mixture flow rates, the void fraction may change drastically as the mixture traverses the space between the two sensors, due to the increased turbulence of the flow and distortion of the phases by the upstream sensor; this effect would also lead to a distortion of the cross–correlation function.

Appendix A.4. Significance of errors in each flow regime

In the present study, it was found that the different types of error that were discussed in the previous section are not equally significant in all flow regimes. For improved clarity, the importance of these errors in each flow regime will be discussed separately in this section.

In bubbly flow, the dominant error was found to be the positive bias due to the limited spatial resolution of the sensor. The bubbles were injected through 100 micron pores, which is much smaller than the wire spacing of approximately 3.8 mm. It was observed that j_{xc} tended to exceed the gas superficial velocity value measured by the flow meter. The discrepancy became more pronounced with increasing liquid superficial velocity or decreasing gas superficial velocity (Figure 11). This can be explained by considering that

these changes in the phase flow rates would result in bubbles with a smaller average size, and consequently a greater bias related to spatial resolution.

Figure 11 shows that j_{xc} closely matched j_g at relatively low gas superficial velocities in the slug flow regime, but, at larger gas superficial velocities, j_{xc} under–estimated j_g, with the difference becoming more prominent with increasing gas flow rates. The discrepancy between j_{xc} and j_g was within $\pm 25\%$ in the range $j_g < 1.5$ m/s. The WMS spatial resolution was deemed to be adequate in this range of flow rates and the gas–liquid interfaces are expected to be large and well–defined. Also, the temporal fluctuations of gas velocity and void fraction are expected to be small. However, at larger gas flow rates, the negative bias introduced by neglecting the spatial and temporal fluctuations of void fraction and gas velocity could be significant and it grows with increasing gas flow rate.

In the entire ranges of conditions corresponding to the churn and annular flow regimes, j_{xc} was found to be much lower than the measured gas superficial velocity j_g. Negative bias was introduced in the procedure by the neglecting of temporal and spatial fluctuations of void fraction and gas velocity in the cross–correlation analysis. The primary source of error, however, is deemed to be the miscalculation of U_{xc} because of the extensive exposure of most of the nodes of the sensor to single–phase air. In this study, we found that the peak in the normalized cross–correlation function for these nodes had a magnitude that was about half of that of a typical peak for a node exposed to both phases. The time lag at the peak of the cross–correlation function always corresponded to a very low value of interfacial velocity, which introduced a consistently negative bias in the calculation of j_{xc}.

Appendix B. Effect of void fraction and gas velocity fluctuations on the cross–correlation velocity

Starting from Equation A.1, one may apply a modified Reynolds decomposition to decompose the instantaneous local fluid velocity and void fraction into mean and fluctuating parts as

$$U(r,\theta,t) = \overline{U}_r(r) + U'(r,\theta,t) \tag{B.1}$$

and

$$\alpha(r,\theta,t) = \overline{\alpha}_r(r) + \alpha'(r,\theta,t), \tag{B.2}$$

where the temporally and azimuthally averaged fluid velocity and void fraction are defined as, respectively,

$$\overline{U}_r(r) = \frac{1}{T}\frac{1}{2\pi}\int_{t=0}^{T}\int_{\theta=0}^{2\pi} U(r,\theta,t)\; d\theta\; dt \tag{B.3}$$

and

$$\overline{\alpha}_r(r) = \frac{1}{T}\frac{1}{2\pi}\int_{t=0}^{T}\int_{\theta=0}^{2\pi} \alpha(r,\theta,t)\; d\theta\; dt\;, \tag{B.4}$$

and primes indicate fluctuations. Substituting equations B.1 and B.2 into equation A.1, one gets

$$j_g = \frac{1}{T}\frac{1}{\pi R^2}\int_{t=0}^{T}\int_{r=0}^{R}\int_{\theta=0}^{2\pi} [\overline{U}_r(r)\;\overline{\alpha}_r(r) + U'(r,\theta,t)\;\alpha'(r,\theta,t) + \overline{U}_r(r)\;\alpha'(r,\theta,t) + \overline{\alpha}_r(r)\;U'(r,\theta,t)]\; r\; d\theta\; dr\; dt. \tag{B.5}$$

The integrals that contain the last two integrands on the right–hand side of the previous equation would vanish, because each contains a time integral of the fluctuating part of a variable, which would, by definition, have a zero average. For example,

$$\int_{t=0}^{T}\int_{r=0}^{R}\int_{\theta=0}^{2\pi} \overline{U}_r(r)\;\alpha'(r,\theta,t)\; r\; d\theta\; dr\; dt = \int_{r=0}^{R} \overline{U}_r(r)\; r \left(\int_{\theta=0}^{2\pi}\int_{t=0}^{T} \alpha'(r,\theta,t)\; dt\; d\theta\right)\; dr = 0. \tag{B.6}$$

In this process, it was possible to change the order of integration because $\alpha'(r,\theta,t)$ is bounded between -1 and 1 in the integration domain, thus satisfying the conditions for the application of Fubini's theorem. In consequence,

equation B.5 may be reduced to

$$j_g = \frac{1}{\pi R^2} \int_0^R \overline{U}_r(r)\, \overline{\alpha}_r(r)\, 2\pi r\, dr + \frac{1}{T} \frac{1}{\pi R^2} \int_{t=0}^{T} \int_{r=0}^{R} \int_{\theta=0}^{2\pi} U'(r,\theta,t)\, \alpha'(r,\theta,t)\, r\, d\theta\, dr\, dt \tag{B.7}$$

Equation A.4 may be used if the mean velocity $\overline{U}_r$ were assumed to be equal to the cross–correlation velocity $\overline{U}_{xcr}$. This assumption may be valid for the bubbly regime, at least when the bubble size is relatively small for internal gas motions to be negligible, but it is expected to introduce significant errors in other regimes. In any case, even if this assumption were valid, equation B.5 would be reduced to equation A.4 only if the second term on its right–hand side were negligible. This would be true only if the instantaneous local interfacial velocity were statistically independent of the instantaneous local void fraction or if spatial and temporal variations in these two variables were negligible. Unfortunately, neither of these two conditions is valid for the majority of the present tests. The sign of the second term on the right–hand side of equation B.7 could, in principle, be positive or negative. In vertical upward flow, this correction would be negligible at low gas flow rates for which the fluctuations of void fraction and fluid velocity would be very small. At higher gas flow rates, the gas velocity would always be greater than the liquid velocity because the gas, being lighter than the liquid, would tend to rise faster. High values of both the void fraction (*i.e.*, 1) and the fluid velocity would always occupy the same time intervals, so that the product of their fluctuations during these intervals would be positive. During the remaining time, the void fraction would be zero and the fluid velocity would be equal to the local liquid velocity; in this case the fluctuations of void fraction and fluid velocity would both be negative, but their product would be positive.

In conclusion, the product $U'(t)\,\alpha'(t)$ would always be non–negative in vertical upward flow, and so the covariance $\overline{U'\,\alpha'}$ would be positive. The previous discussion demonstrates that the term that is being neglected in the calculation of j_{xc} by equation A.4 would always be positive in vertical upward flow. Moreover, the relative magnitude of this term would increase with in-

creasing j_g, as a result of increases in both the gas velocity fluctuations and their correlation coefficient with the void fraction. These conclusions explain, at least qualitatively, the trends that were observed in Figure 11, namely that j_{xc} under–estimates j_g and that the difference between the corresponding values becomes larger with increasing j_g. The error due to neglecting the temporal fluctuations of void fraction and gas velocity is the dominant source of error in j_{xc} in the slug flow regime. Although it is also expected to contribute to the errors in the churn and annular regimes, the exposure of some WMS nodes exclusively to single phase gas during the measurement interval would be a more significant source of error in these regimes.

References

Abdulkadir, M., 2011. Experimental and computational fluid dynamics (CFD) studies of gas-liquid flow in bends. Ph.D. thesis. University of Nottingham. Nottingham, United Kingdom.

Al Issa, S., Beyer, M., Prasser, H.M., Frank, T., 2007. Reconstruction of the 3D velocity field of the two-phase bubbly flow around a half moon obstacle using wire-mesh sensor data, in: Sixth International Conference on Multiphase Flow, Leipzig, Germany, July 9-13, 2007.

Azzopardi, B., Abdulkareem, L., 2010. Comparison between electrical capacitance tomography and wire mesh sensor output for air/silicone oil flow in a vertical pipe. Ind. Eng. Chem. Res. 49, 8805–8811.

Beyer, M., Lucas, D., Kussin, J., 2010. Quality check of wire-mesh sensor measurements in a vertical air/water flow. Flow Meas. Instrum. 21, 511–520.

Collier, J.G., Thome, J.R., 1994. Convective Boiling and Condensation. Clarendon Press, Oxford.

Da Silva, M.J., 2008. Impedance sensors for fast multiphase flow measurement and imaging. Ph.D. thesis. Technischen Universität Dresden. Dresden, Germany.

Da Silva, M.J., Hampel, U., 2013. Capacitance wire-mesh sensor applied for the visualization of three-phase gas-liquid-liquid flows. Flow Meas. Instrum. 34, 113–117.

Da Silva, M.J., Schleicher, E., Hampel, U., 2007. Capacitance wire-mesh sensor for fast measurement of phase fraction distributions. Meas. Sci. Technol. 18, 2245–2251.

Drew, D., Passman, S., 2012. Theory of Multicomponent Fluids. Springer New York.

Häfeli, R., Hutter, C., Damsohn, M., Prasser, H.M., Rudolf von Rohr, P., 2013. Dispersion in fully developed flow through regular porous structures: Experiments with wire-mesh sensors. Chem. Eng. Process. 69, 104–111.

Hampel, U., Otahal, J., Boden, S., Beyer, M., Schleicher, E., Zimmermann, W., Jicha, M., 2009. Miniature conductivity wire-mesh sensor for gas-liquid two-phase flow measurement. Flow Meas. Instrum. 20, 15–21.

Johnson, I.D., 1987. Method and apparatus for measuring water in crude oil. US Patent No. 4644263 A.

Kickhofel, J., Valori, V., Prasser, H.M., 2014. Turbulent penetration in T-junction branch lines with leakage flow. Nucl. Eng. Des. 276, 43–53.

Kliem, S., Prasser, H.M., Sühnel, T., Weiss, F.P., Hansen, A., 2008. Experimental determination of the boron concentration distribution in the primary circuit of a PWR after a postulated cold leg small break loss-of-coolant-accident with cold leg safety injection. Nucl. Eng. Des. 238, 1788–1801.

Krepper, E., Reddy Vanga, B.N., Zaruba, A., Prasser, H.M., Lopez de Bertodano, M.A., 2007. Experimental and numerical studies of void fraction distribution in rectangular bubble columns. Nucl. Eng. Des. 237, 399–408.

Lessard, E., Shaban, H., Tavoularis, S., 2014. Measurements in horizontal air-water pipe flows using wire-mesh sensors, in: 2014 Canada-China Conference on Advanced Reactor Development, Niagara Falls, Canada, April 27-30, 2014.

Llamas, J.D., Pérat, C., Lesage, F., Weber, M., D'Ortona, U., Wild, G., 2008. Wire mesh tomography applied to trickle beds: A new way to study liquid maldistribution. Chem. Eng. Process. 47, 1765–1770.

Lucas, D., Beyer, M., Kussin, J., Schütz, P., 2010. Benchmark database on the evolution of two-phase flows in a vertical pipe. Nucl. Eng. Des. 240, 2338–2346.

Lucas, D., Krepper, E., Prasser, H.M., 2005. Development of co-current air-water flow in a vertical pipe. Int. J. Multiphase Flow 31, 1304–1328.

Lucas, D., Krepper, E., Prasser, H.M., 2007. Use of models for lift, wall and turbulent dispersion forces acting on bubbles for poly-disperse flows. Chem. Eng. Sci. 62, 4146–4157.

Manera, A., Ozar, B., Paranjape, S., Ishii, M., Prasser, H.M., 2009. Comparison between wire-mesh sensors and conductive needle-probes for measurements of two-phase flow parameters. Nucl. Eng. Des. 239, 1718–1724.

Manera, A., Prasser, H.M., Lucas, D., van der Hagen, T., 2006. Three-dimensional flow pattern visualization and bubble size distributions in stationary and transient upward flashing flow. Int. J. Multiphase Flow 32, 996–1016.

Ofuchi, C.Y., Morales, R.E.M., Arruda, L.V.R., Neves Jr., F., Dorini, L., do Amaral, C.E.F., da Silva, M.J., 2012. Wire-mesh sensor, ultrasound and high-speed videometry applied for the characterization of horizontal gas-liquid slug flow, in: Seventh International Symposium on Measurement Techniques for Multiphase Flows, Tianjin, China, 17-19 September 2011.

Olerni, C., Jia, J., Wang, M., 2013. Measurement of air distribution and void fraction of an upwards airwater flow using electrical resistance tomography and a wire-mesh sensor. Meas. Sci. Technol. 24, 035403 (9 pp.).

Petritsch, G., Mewes, D., 1999. Experimental investigations of the flow patterns in the hot leg of a pressurized water reactor. Nucl. Eng. Des. 188, 75–84.

Pietruske, H., Prasser, H.M., 2007. Wire-mesh sensors for high-resolving two-phase flow studies at high pressures and temperatures. Flow Meas. Instrum. 18, 87–94.

Prasser, H.M., 2007. Evolution of interfacial area concentration in a vertical air-water flow measured by wire-mesh sensors. Nucl. Eng. Des. 237, 1608–1617.

Prasser, H.M., 2008. Novel experimental measuring techniques required to provide data for CFD validation. Nucl. Eng. Des. 238, 744–770.

Prasser, H.M., Beyer, M., Böttger, A., Carl, H., Lucas, D., Schaffrath, A., Schutz, P., Weiss, F.P., Zschau, J., 2005a. Influence of the pipe diameter on the structure of the gas-liquid interface in a vertical two-phase pipe flow. Nucl. Technol. 152, 3–22.

Prasser, H.M., Beyer, M., Carl, H., Manera, A., Pietruske, H., Schütz, P., 2007. Experiments on upwards gas/liquid flow in vertical pipes. Technical Report FZD-482. Institute of Safety Research, Dresden, Germany.

Prasser, H.M., Böttger, A., Zschau, J., 1997. A new electrode-mesh tomograph for gas-liquid fiows. Annual Report 1996 (FZR-190). Institute of Safety Research. Dresden, Germany.

Prasser, H.M., Böttger, A., Zschau, J., 1998. A new electrode-mesh tomograph for gas-liquid flows. Flow Meas. Instrum. 9, 111–119.

Prasser, H.M., Krepper, E., Lucas, D., 2002. Evolution of the two-phase flow in a vertical tube-decomposition of gas fraction profiles according to bubble size classes using wire-mesh sensors. Int. J. Therm. Sci. 41, 17–28.

Prasser, H.M., Misawa, M., Tiseanu, I., 2005b. Comparison between wire-mesh sensor and ultra-fast X-ray tomograph for an air-water flow in a vertical pipe. Flow Meas. Instrum. 16, 73–83.

Prasser, H.M., Scholz, D., Zippe, C., 2001. Bubble size measurement using wire-mesh sensors. Flow Meas. Instrum. 12, 299–312.

Prasser, H.M., Zschau, J., Peters, D., Pietzsch, G., Taubert, W., Trepte, M., 2000. Wire-mesh sensor-now 10,000 frames per second. Annual Report 1999 (FZR-284). Institute of Safety Research. Dresden, Germany.

Reinecke, N., Petritsch, G., Boddem, M., Mewes, D., 1998. Tomographic imaging of the phase distribution in two-phase slug flow. Int. J. Multiphase Flow 24, 617–634.

Richter, S., Aritomi, M., Prasser, H.M., Hampel, R., 2002. Approach towards spatial phase reconstruction in transient bubbly flow using a wire-mesh sensor. Int. J. Heat Mass Transfer 45, 1063–1075.

Roitberg, E., Shemer, L., Barnea, D., 2007. Measurements of cross-sectional instantaneous phase distribution in gas-liquid pipe flow. Exp. Therm Fluid Sci. 31, 867–875.

Salve, M.D., Monni, G., Panella, B., 2012. Horizontal Air-Water Flow Analysis with Wire Mesh Sensor. J. Phys: Conf. Ser. 395, 012179 (8 pp.).

Schmitz, D., Mewes, D., 2000. Tomographic imaging of transient multiphase flow in bubble columns. Chem. Eng. J. 77, 99–104.

Shaban, H., 2015. Experimental investigations of internal air-water flows. Ph.D. thesis. University of Ottawa, Ottawa, Canada.

Shaban, H., Tavoularis, S., 2015. The wire-mesh sensor as a two-phase flow meter. Meas. Sci. Technol. 26, 015306 (16 pp.).

Sharaf, S., Da Silva, M., Hampel, U., Zippe, C., Beyer, M., Azzopardi, B., 2011. Comparison between wire mesh sensor and gamma densitometry void measurements in two-phase flows. Meas. Sci. Technol. 22, 104019 (13 pp.).

Szalinski, L., Abdulkareem, L., Da Silva, M., Thiele, S., Beyer, M., Lucas, D., Hernandez Perez, V., Hampel, U., Azzopardi, B., 2010. Comparative study of gas-oil and gas-water two-phase flow in a vertical pipe. Chem. Eng. Sci. 65, 3836–3848.

Vauth, T., Rausch, T., Mewes, D., 2004. Test facility for multiphase pumps in serial and parallel operation, in: Proceedings of the 2004 ASME International Mechanical Engineering Congress and Exposition (IMECE2004), Anaheim, USA, November 13-19, 2004.

Wangjiraniran, W., Motegi, Y., Richter, S., Kikura, H., Aritomi, M., Yamamoto, K., 2003. Intrusive effect of wire mesh tomography on gas-liquid flow measurement. J. Nucl. Sci. Technol. 40, 932–940.

Williams, R., Beck, M. (Eds.), 1995. Process Tomography: Principles, Techniques and Applications. Butterworth-Heinemann, Oxford.

Ylönen, A., 2013. High-resolution flow structure measurements in a rod bundle. Ph.D. Thesis. ETH Zurich, Zürich, Switzerland.

Zhang, Z., Bieberle, M., Barthel, F., Szalinski, L., Hampel, U., 2013. Investigation of upward cocurrent gas-liquid pipe flow using ultrafast X-ray tomography and wire-mesh sensor. Flow Meas. Instrum. 32, 111–118.

Zoeteweij, M.L., 2007. Long liquid slugs in horizontal tubes. Ph.D. Thesis. Delft University of Technology, Delft, The Netherlands.

Chapter 7

The wire–mesh sensor as a two–phase flow meter

In this chapter, machine–learning methods are applied to the area–averaged void fraction signal measured using wire–mesh sensors to identify the flow regime as well as measure the gas and liquid flow rates in vertical upward and downward two–phase flow. The chapter is presented as the article

> "Shaban, H. and Tavoularis, S. 2015 The wire–mesh sensor as a two–phase flow meter. *Meas. Sci. Tech.* **26**, 015306 (16 pp.)"

which was submitted to *Measurement Science and Technology* on 25 August 2014 and accepted for publication on 20 November 2014. This is an author-created, un-copyedited version of an article accepted for publication in *Measurement Science and Technology*. The publisher is not responsible for any errors or omissions in this version of the manuscript or any version derived from it. The Version of Record is available online at `http://dx.doi.org/10.1088/0957-0233/26/1/015306`.

The wire–mesh sensor as a two–phase flow meter

H. Shaban, S. Tavoularis*

Department of Mechanical Engineering, University of Ottawa,
161 Louis Pasteur, Ottawa, ON K1N 6N5, Canada

Abstract

A novel gas and liquid flow rate measurement method is proposed for use in vertical upward and downward gas–liquid pipe flows. This method is based on the analysis of the time history of area–averaged void fraction that is measured using a conductivity wire–mesh sensor (WMS). WMS measurements were collected in vertical upward and downward air–water flows in a pipe with an internal diameter of 32.5 mm at nearly atmospheric pressure. The relative frequencies and the power spectral density of area–averaged void fraction were calculated and used as representative properties. Independent features, extracted from these properties using Principal Component Analysis and Independent Component Analysis, were used as inputs to artificial neural networks, which were trained to give the gas and liquid flow rates as outputs. The present method was shown to be accurate for all four encountered flow regimes and for a wide range of flow conditions. Besides providing accurate predictions for steady flows, the method was also tested successfully in three flows with transient liquid flow rates. The method was augmented by the use of the cross–correlation function of area–averaged void fraction determined from the output of a dual WMS unit as an additional representative property, which was found to improve the accuracy of flow rate prediction.

Keywords: two-phase, wire-mesh sensor, flow rates, elastic maps, independent component analysis, cross–correlation

1. Introduction

The accurate measurement of the flow rates of both phases in gas–liquid pipe flows is important in several industries. In the petroleum industry, gas–liquid pipe flow may be encountered during various stages of petroleum extraction and transport. In particular, gases dissolved in liquid petroleum at large depths below the earth's surface are released in the liquid as the mixture gets extracted towards the ground level. Gas-liquid flows in the oil well and pipelines are also deliberately generated during some petroleum extraction methods, such as the gas–lift method in which gas is injected into an oil well to reduce the density of the oil column. In nuclear reactor safety analysis, which is the application area of interest in this work, water-steam flows would be encountered in the fuel channels of a nuclear reactor during certain postulated accident scenarios; accurate measurement or prediction of the liquid flow rate under these conditions would be essential to ensure adequate cooling of the nuclear fuel rods.

A classical method of two–phase flow rate measurement is the separation of the phases into individual streams, followed by separate metering of each phase using single–phase flow meters. Although this method is considered to be accurate and reliable, it requires expensive and bulky phase separators and its use in many situations may not be convenient, or even possible. Measurement of gas-liquid flow rates has also been accomplished with the use of methods that require partial or no separation of the phases; these are generally known as multiphase flow metering (MFM) methods. Reviews of MFM methods have been presented by Falcone et al. (2002) and, more recently, by Thorn et al. (2013). A number of MFM methods employ machine–learning algorithms to correlate the phase flow rates to certain features of a measured signal. Earlier examples of such techniques include ones that used machine learning algorithms with measurements of differential pressure across orifices (Beg and Toral, 1993) or Venturi tubes (Minemura et al., 1998). The signals from other sensors, such as turbine flowmeters (Minemura et al., 1996), electrical resistance tomographs (Meng et al., 2010) and conductance probes (Fan and Yan, 2013), have also been used as inputs to machine learning algorithms for the measurement of the phase flow rates.

We have recently introduced an MFM method based on differential pressure measurement in bare tubes. Details of this method have been presented in two articles (Shaban and Tavoularis, 2014a,b), to be referred as ST1 and ST2, respectively. In ST1, the elastic maps algorithm was successfully ap-

plied to differential pressure measurements in a bare tube, in order to identify the flow regime in vertical upward air–water flow. In ST2, the flow regime was first identified using the ST1 algorithm; then, independent features were extracted from the time histories of differential pressure and were used to train flow–regime dependent artificial neural networks; finally, these trained neural networks were used to predict the gas and liquid flow rates. The ST2 method has several advantages over previous approaches. Most importantly, it was found to be fairly accurate in all flow regimes and it used simple, relatively inexpensive instrumentation. Its range of application is, however, limited by the temporal response of the differential pressure transducer that is a necessary component of the instrumentation. In the ST2 tests, the response time of the differential pressure sensing assembly (transducer and tubing), defined as the time required for the output of the sensor to rise to within 1% of its final value when exposed to a step change in the input, was 0.05 s; consequently, this method could only be applied to flows with liquid superficial velocities that were lower than 0.4 m/s. To extend the range of applicability of this method, we would require a pressure transducer with a much lower response time (*e.g.*, lower than 0.005 s), while also being capable of measuring accurately differential pressures in the range 0–500 Pa and having material compatibility with both air and water. Unfortunately, we were not able to find a commercially available differential pressure transducer that satisfied all these requirements. Although the ST2 method relied on differential pressure signals, it may be adapted for use with different types of sensors, thus widening the range of commercial instruments that may be suitable for two–phase flow rate measurement. Among various possibilities considered, the present work presents an adaptation of the ST1/ST2 method that is based on the conductivity wire–mesh sensor (WMS).

The WMS used in this study was first described by Prasser et al. (1998). It consists of two perpendicular arrays of electrodes that form a grid of conductivity–sensing nodes, which allow the measurement of gas–liquid phase distribution in a cross–section of the flow, provided that the liquid has a much higher electrical conductivity than the gas. Such sensors have been used previously for flow pattern visualization and for the measurement of void fraction, interfacial velocity and bubble size distribution (Prasser et al., 2007). Devices that can be operated at a sampling frequency of up to 10,000 cross–sectional frames/s are available. A variant of this device, called the capacitance wire–mesh sensor, was developed to estimate the phase distribution by measuring the relative permittivity of the fluids, rather than their

conductivity (Da Silva et al., 2007). This sensor can, therefore, be used in gas–liquid flows in which both phases are non–conductive, such as in oil–gas flows.

The objective of this research is to develop an MFM method that is capable of estimating accurately and at a fast rate the gas and liquid flow rates in air-water mixtures, based exclusively on WMS signals. Previous authors (Prasser et al., 2005, 2007; Beyer et al., 2008, 2010; Lucas et al., 2010) have proposed a method for estimating the gas flow rate by cross-correlating the signals of two WMS in tandem. In combination with a simple empirical model, such as the one–dimensional drift–flux model, and void fraction measurements provided by the WMS, this approach could, in principle, be used to estimate the liquid flow rate. A detailed analysis of this method, which will be presented in a separate manuscript, revealed that its range of applicability would at best be very limited, so that it would not be suitable for use under the flow conditions of present interest. Nevertheless, one may further exploit the wealth of information about the two–phase flow structure and dynamics contained in the WMS signal to develop an MFM method for using the WMS as a two–phase flow meter. Two such methods are described in the present article. The first one uses the output of a single WMS, whereas the second one uses the outputs of two WMS in tandem to achieve improved accuracy. Both methods have been tested for measuring air and water flow rates in vertical upward and downward pipe flows.

2. Experimental setup and procedure

2.1. Air–water flow facility

The measurements used in the present study were collected in the air–water pipe flow facility at the University of Ottawa (ST1, ST2). The flow loop (Figure 1) consisted primarily of 32.5 mm I.D. clear polyvinyl chloride (PVC) tubing, which allowed visual observation of the flow. Filtered tap water was pumped from a main tank into a settling tank before entering the loop. The loop had a horizontal branch, a vertical upward flow branch and a vertical downward flow branch, each of which was equipped with a separate valve connected to a regulated compressed air line. Air could be injected in the desired branch through a porous stainless steel injector, available commercially for use as a muffler (ALWITCO Model 0579038, North Royalton, Ohio, USA, 100 μm pore size). For the work presented in this article, air was injected near the inlet of the vertical upward flow branch. The water flow rate

was measured using a calibrated ultrasonic transit–time flow meter (Omega FDT-30, Laval, Quebec, Canada), while the air flow rate was measured by a rotameter, selected from an array of seven rotameters with different operating ranges (King Instruments Series 7510, Garden Grove, California, USA). The temperatures and gauge pressures were monitored in the air supply line and just upstream of the test section.

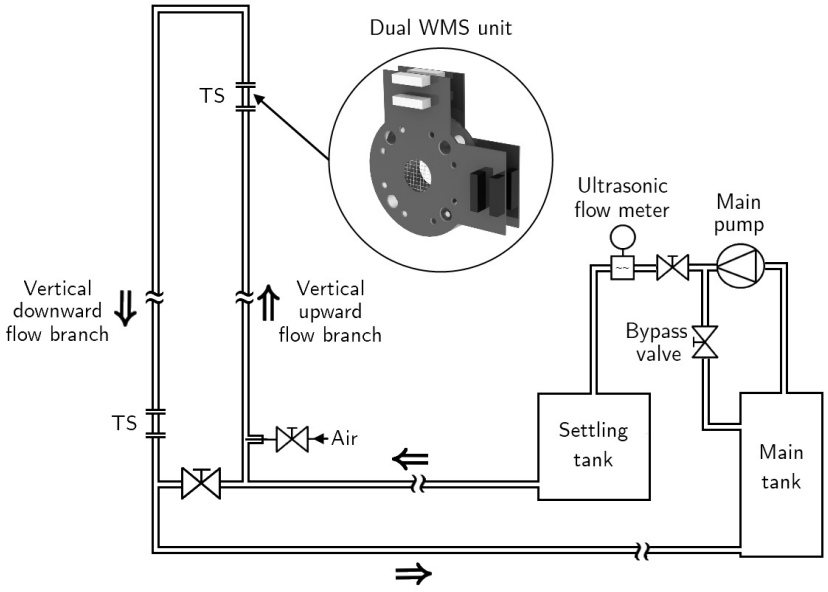

Figure 1: Schematic diagram of the air–water flow loop.

2.2. The wire–mesh sensors

The main instrument used in the present study was a dual 8×8 wire-mesh sensor (WMS) unit, model WMS200, manufactured by Teletronic Rossendorf, Radeberg, Germany. Each WMS consisted of two mutually perpendicular arrays of eight parallel wires that were separated in the streamwise direction by a distance of 2 mm, centre-to-centre. Among the 64 nodes at the crossing points of the two wire arrays, only 52 were within the wet area of the pipe cross–section. This device measures the instantaneous conductivity of the flowing mixture within a measurement volume around each node. An electronic control circuit applies sequentially voltage pulses to the electrodes of

the upstream array. The current flowing through each of the receiver array wires is converted to a voltage, which is then recorded by a data acquisition system. When some or all of the measurement volume around a node is occupied by air, the corresponding voltage would be lower than the voltage when this node is surrounded by water. The dual WMS unit consisted of a pair of identical sensors, separated by a 20 mm thick spacer ring. Combined operation of the two sensors was meant to permit the measurement of the velocity of the interface between the two phases. Two dual WMS units were installed in the facility; the first in the vertical upward test section at an axial distance of 2.44 m (namely, 75 pipe diameters) downstream of the air injection location and the second one in the vertical downward test section at a distance of 2.44 m from the top of the pipe. The following analysis is presented for the WMS unit in the vertical upward section. The results for downward flow are briefly discussed in Section 8.

2.3. Experimental procedure

For each series of tests, the water flow rate through the loop was adjusted to the desired value using a butterfly valve. One calibration measurement was collected using the WMS in single phase water flow at this water flow rate. Then, the air flow was increased by opening an air control needle valve and several test measurements were collected at different air flow rates, with the same setting of the water control valve. The flow regime, assumed to be one of four vertical upward flow regime choices, *i.e.*, bubbly, slug, churn or annular flow regime (see ST1 for a detailed description of the appearance of the flows in these regimes), was identified by one of two procedures. For liquid superficial velocities less than 1 m/s, this was accomplished by visual observation of the flow through the transparent pipe wall. At larger liquid superficial velocities, however, visual identification of the flow regime was not possible and the flow regime was identified by examining the cross–sectional voltage maps displayed by the data acquisition program provided by the WMS manufacturer. The flow regime, the air flow rate measured by the rotameter and the temperatures in the air supply line and in the test section were noted down. The water flow rate and the gauge pressures in the air supply line and in the test section were recorded at a rate of 200 samples/s over an interval of 75 s, using a 12-bit data acquisition system (Omega Engineering OM–USB–1208FS, Stamford, USA). During the same time interval, the output of the dual WMS unit was recorded at a sampling rate of 1000 cross–sectional frames/s using the WMS manufacturer's data acquisition system.

Preliminary tests revealed that this sampling frequency was sufficient for the convergence of the statistical properties of area–averaged void fraction in the ranges of flow rates used in the present tests.

2.4. Data pre–processing

The recorded data were pre-processed using the open–source computational package, SCILAB 5.4 (Scilab Enterprises, 2013). First, the gas and liquid superficial velocities j_g and j_l, respectively, at the measurement location were calculated from the corresponding measured volumetric flow rates, following correction of the air flow rate for density changes. It may be noted here that, whereas the liquid superficial velocity, or equivalently its volumetric flow rate, may be considered to be constant along the test section, the values of the gas superficial velocity and volumetric flow rate depend on the local air pressure, which varies in the streamwise direction. The gas volumetric flow rates and superficial velocities reported in this article were calculated for a pressure measured just upstream of the WMS. For each set of measurements, corresponding to specified air and water flow rates, the recorded WMS signals consisted of a three-dimensional matrix with a height I=8, a width J=8 and a depth K=75000. The height and width corresponded to the number of wires on each array of the sensor, and the depth corresponded to the number of recorded frames. The time history of the WMS voltage output for a node i,j is denoted as V_{ijk}, where $k = t/f_s$ with t and f_s denoting the time and sampling frequency, respectively. Calibration of the WMS for a series of measurements was performed by recording the WMS output over an interval of 75 s in single–phase water flow, as described in the previous section. The calibration data were time–averaged for each node and recorded as nodal calibration values $\overline{V}_{cal,ij}$. Following the recommendations of Prasser et al. (2002), each WMS voltage output value was then converted to an instantaneous local void fraction as

$$\alpha_{ijk} = 1 - \frac{V_{ijk}}{\overline{V}_{cal,ij}} \ . \tag{1}$$

Measurements of α_{ijk} that were greater than 1 or lower than 0 were reset to 1 and 0, respectively. The instantaneous area–averaged void fraction was subsequently calculated as

$$\alpha_k = \sum_{i=1}^{I} \sum_{j=1}^{J} a_{ij} \alpha_{ijk} \ , \tag{2}$$

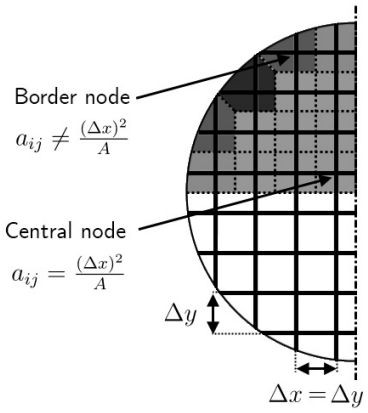

Figure 2: Definition of area weight coefficients for area–averaging of void fraction; thick solid lines denote the WMS wires, whereas thinner dotted lines denote the boundaries of areas used to calculate these coefficients.

where a_{ij} is the area weight coefficient of a node i,j representing the ratio of the projected area of the nodal measurement volume and the total cross–sectional area A of the sensor. For all central nodes, this projected area was taken to be that of a square with sides equal to the wire spacing, while for border nodes, namely nodes which were adjacent to the pipe wall, irregular projected areas were considered, as shown in Figure 2.

Finally, the time– and area–averaged void fraction was calculated as

$$\overline{\alpha} = \frac{1}{K} \sum_{k=1}^{K} \alpha_k. \tag{3}$$

The time histories of the area–averaged void fraction α_k were processed further with the use of built–in functions in SCILAB 5.4 (Scilab Enterprises, 2013). The relative frequencies RF of α_k were calculated for 40 void fraction bins between 0 and 1. The power spectral density PSD of α_k was determined using Welch's average periodogram method; it consisted of 40 values for frequencies f between 0.5 and 20 Hz at 0.5 Hz intervals. In addition, when signals provided by a dual WMS unit were used, the cross–correlation function CCF between the area–averaged void fraction signals of the upstream and downstream WMS was determined as

$$\mathrm{CCF}_{\Delta k} = \frac{\sum_{k=1}^{K-\Delta k} (\alpha_k - \overline{\alpha})_U \, (\alpha_{k+\Delta k} - \overline{\alpha})_D}{\sqrt{\sum_{k=1}^{K} (\alpha_k - \overline{\alpha})_U^2} \sqrt{\sum_{k=1}^{K} (\alpha_k - \overline{\alpha})_D^2}}, \tag{4}$$

where the subscripts U and D denote values corresponding to the upstream and downstream sensor, respectively. This function was calculated for Δk= 0, 1, 2, ..., 49, corresponding to 50 time lags between 0 and 0.049 s.

3. Experimental database

In total, 1250 sets of measurements were collected in flows with air superficial velocity j_g in the range from 0.04 to 20.0 m/s and water superficial velocity j_l in the range from 0.13 to 3.0 m/s. The ranges of gas and liquid flow rates in the present experiments were sufficiently wide for all the flow regimes of interest in vertical upward air–water pipe flow to be encountered. Table 1 shows the number of measurement sets recorded in each flow regime. Relatively few measurements were collected in the bubbly flow regime, because this regime occurred only for high liquid superficial velocities in the present test section.

Table 1: Number of measurement sets in each flow regime.

Flow regime	Number of measurement sets
Bubbly	125
Slug	525
Churn	290
Annular	310
Total	1250

A flow regime map for the present measurements, plotted on j_l and j_g axes, is presented in Figure 3. The present flow regime transition boundaries, as well as their locations estimated with the use of the Mishima and Ishii (1984) model are also shown in this figure. This model comprises correlations for four transition boundaries, namely, the bubbly to slug, slug to churn, slug to annular and churn to annular boundaries. The correlations were derived based on mechanistic arguments for the flow regime transitions. The four correlations were presented in terms of the fluid properties and void fraction and the authors suggested the calculation of void fraction using a one–dimensional drift–flux model. With the exception of the bubbly to slug transition, these correlations also included the pipe diameter as an independent parameter. In the present study, the Mishima and Ishii model

was applied in its original form, using the properties of air and water at atmospheric pressure and the drift flux parameters suggested by the authors. This model's prediction of the transition to annular flow is in fair agreement with our observations. In contrast, the model's prediction of the transition boundary from slug to churn flow is quite poor, being shifted towards higher gas superficial velocities than those in the present map. Moreover, unlike the observations that show successive transitions from slug to churn and then from churn to annular flow regimes for all values of j_l considered, the model predicts a direct transition for slug to annular regime for a range of j_l; in this respect, it is noted that Mishima and Ishii's slug to churn flow transition criterion does not take into account the effect of axial location of the measurement, which is known to affect this boundary (Taitel et al., 1980). Finally, the model's prediction of the bubbly to slug flow transition boundary was at lower j_l than the observed boundary. This difference may be attributed to the effect of pipe diameter on this transition boundary. The present observation is consistent with the suggestion by Taitel et al. (1980) that the bubbly flow regime may be absent at relatively low liquid flow rates in pipes with diameter less than 50 mm for air–water flow at atmospheric pressure. In contrast, the bubbly to slug transition correlation in the Mishima and Ishii model is independent of pipe diameter and predicts the existence of bubbly flow for all liquid flow rates.

4. Measurement of two–phase flow rates with a single WMS

A flowchart outlining the main steps of the proposed flow rate measurement method using a single WMS is shown in Figure 4. This method consists of two distinct algorithms: (i) an algorithm that identifies the flow regime using the elastic maps method, which has been described in ST1, and (ii) an algorithm that estimates the gas and liquid flow rates using a modified version of the machine learning method described in ST2. The same figure also contains the relevant terminology that will be used in the following presentation. Before application of the proposed method, the experimental database was divided at random to two parts, the neural network training database, consisting of 80 % of the measurement sets, and the testing database, consisting of the remaining 20% of the measurement sets.

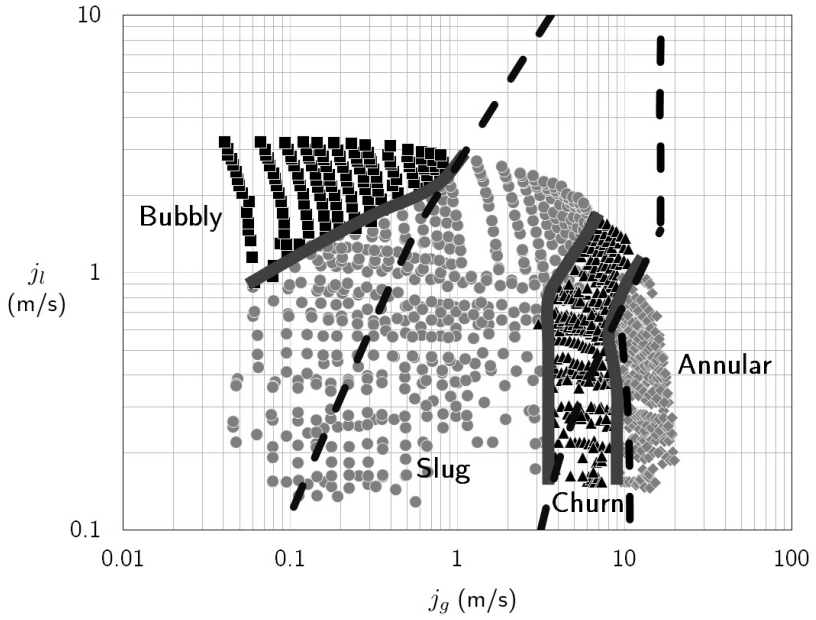

Figure 3: Flow regime map indicating the flow rates of the present measurement sets. ■: bubbly flow regime, ●: slug flow regime, ▲: churn flow regime, ◆: annular flow regime. Solid bands denote approximately the presently found flow regime transition boundaries. Dashed lines denote the flow regime transition boundaries obtained from the Mishima and Ishii (1984) model.

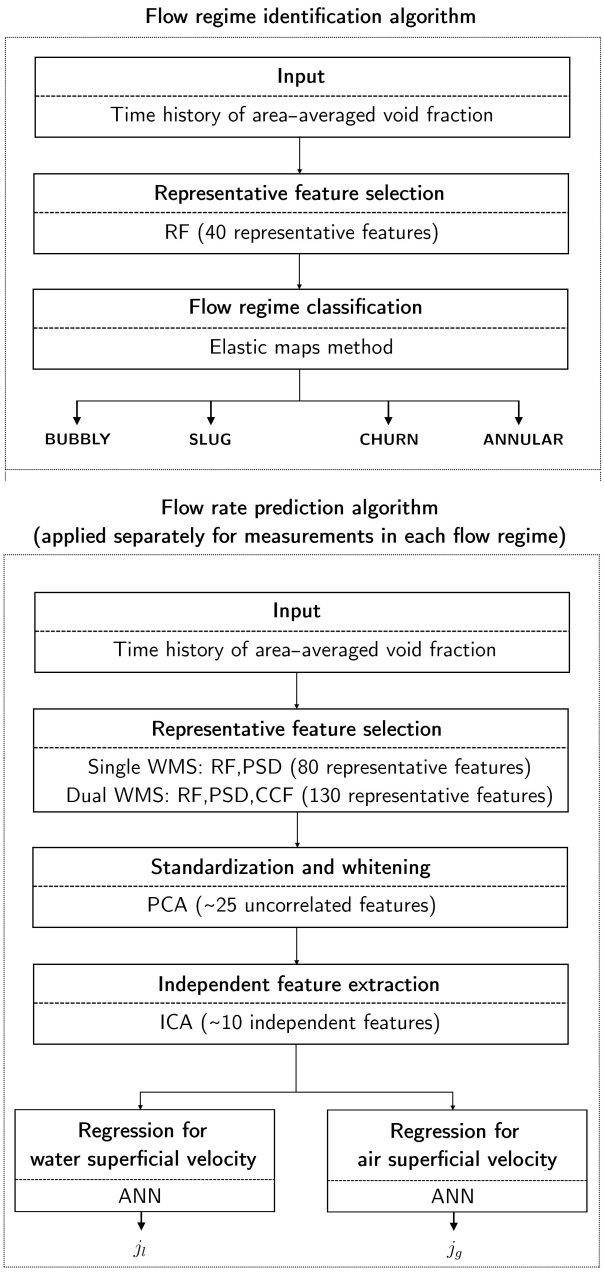

Figure 4: Flowchart of the proposed method.

4.1. Flow regime identification

Figure 5 shows representative examples of the relative frequencies of area–averaged void fraction $\mathrm{RF}(\alpha_k)$ obtained using the WMS in flows in different flow regimes. This figure clearly demonstrates that the appearance of $\mathrm{RF}(\alpha_k)$ depends strongly on the flow regime. In single phase water flow, $\mathrm{RF}(\alpha_k)$ has a sharp peak at $\alpha_k = 0$ (Figure 5a), whereas in single phase air flow, a sharp peak occurs at $\alpha_k = 1$ (Figure 5b). In the bubbly flow regime, $\mathrm{RF}(\alpha_k)$ has a single large–amplitude peak at small α_k (Figure 5c). In slug flow, $\mathrm{RF}(\alpha_k)$ is double-peaked, with one of the peaks located at relatively small α_k and the other one at relatively large α_k (Figure 5d). In churn flow, $\mathrm{RF}(\alpha_k)$ is broad and negatively skewed, with a peak at large α_k (Figure 5e). Finally, in annular flow, $\mathrm{RF}(\alpha_k)$ has a large–amplitude peak at α_k close to 1 (Figure 5f).

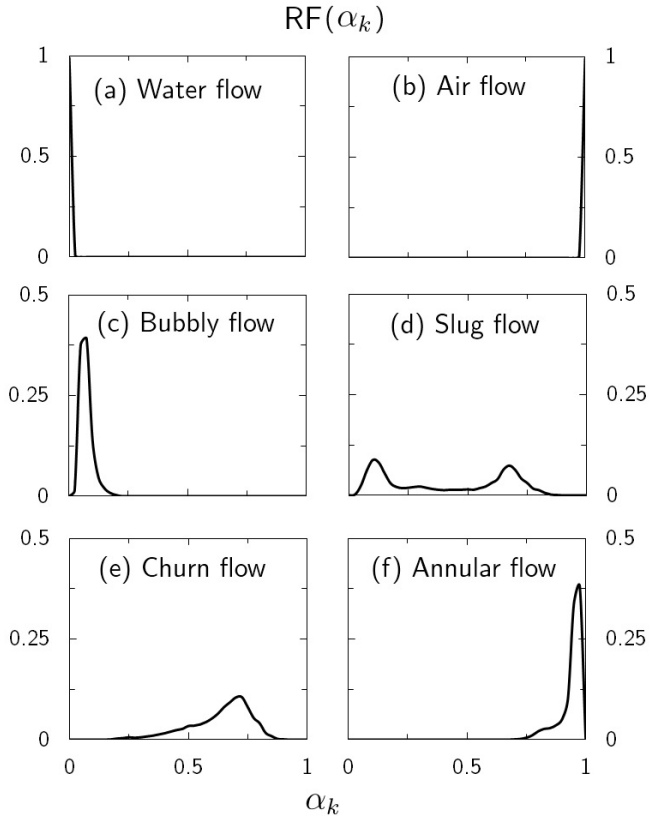

Figure 5: Relative frequencies of area–averaged void fraction in different flow regimes.

The elastic maps algorithm (Gorban and Zinovyev, 2005), as implemented in the C++ package *elmap* (Gorban and Zinovyev, 2003), was used to reduce RF(α_k) of each measurement in the training dataset, which consisted of 40 features, to a two–dimensional elastic map. This map is shown in Figure 6, in which each point represents the two–dimensional projection of RF(α_k) of a single measurement. The different flow regimes are denoted by different symbols and the flow regime map zones are denoted by solid lines, which were demarcated manually following a procedure explained in ST1. Using this elastic map, one may identify the flow regime of any WMS measurement that was not used for the construction of the map by locating the map zone in which the corresponding RF(α_k) was projected. This approach was fully validated, as all data in the testing database were classified by this algorithm in the same flow regime as the one noted down during the experiments (Section 2.3).

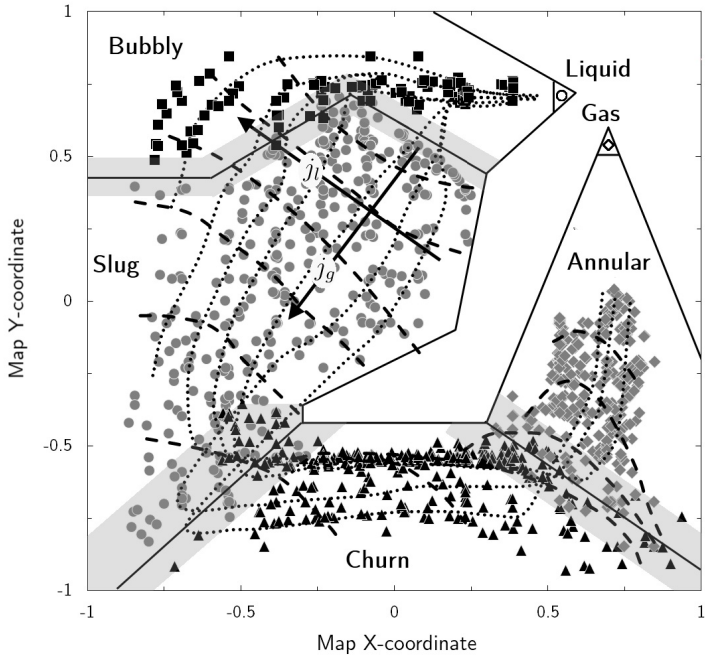

Figure 6: Elastic map calibrated to the present experimental database showing the flow regime transition boundaries (solid lines), iso–lines of j_l (dotted lines) and iso–lines of j_g (dashed lines). Symbols denote the flow regime to which each measurement was classified. Shading indicates zones of flow regime transition. ■: bubbly flow regime, ●: slug flow regime, ▲: churn flow regime, ◆: annular flow regime.

The availability of a large training database allowed us to examine parametric trends on the elastic map by constructing the iso–lines of gas and liquid superficial velocities. The iso–lines of gas superficial velocity form families that mesh with the iso–lines of liquid superficial velocity. In general, RF projections with different gas and liquid flow rates are separated fairly well. Thus, in addition to identifying the flow regime, the location of an RF projection of a measurement on the elastic map also gives a rough indication of the corresponding gas and liquid flow rates.

4.2. Dependence of void fraction properties on the phase flow rates

The second algorithm of the proposed method, used for flow rate prediction, was applied using two properties of the area–averaged void fraction α_k from the upstream WMS, namely, the relative frequencies RF and the power spectral density PSD. In this section, the effects of gas and liquid flow rates on these properties is discussed.

4.2.1. Bubbly flow

In bubbly flow (Figure 7), bubbles cause very small fluctuations in the area–averaged void fraction and as a result, the PSD at all frequencies was very small, being 2–3 orders of magnitude smaller than values in other flow regimes. The value of the PSD at all frequencies was found to generally increase with decreasing liquid flow rate or increasing gas flow rate. RF(α_k) was found to have a single peak that decreased in amplitude and shifted to larger α_k with increasing gas flow rate.

With increasing liquid flow rate, the peak in RF(α_k) also shifted towards larger α_k, contrary to the expectation that the void fraction would decrease with increasing liquid flow rate. In an effort to explain this counter–intuitive trend, we assessed that the calibration relationships might be inapplicable to flows with temperatures that are substantially different from the temperature during the calibration tests and flows in which the deformation of the WMS wires during the calibration tests and the main experiments would be significantly different, as a result of differences in liquid velocity. To minimize such effects, we recalibrated the sensor before each series of test measurements under closely matched conditions of liquid flow rate and flow temperature. It must be emphasized, however, that, even if the void fraction were calculated erroneously, this error would have no effect at all on the accuracy of the present flow rate measurements, because the output of the WMS was correlated to the gas and liquid flow rates indicated by the flow meters without

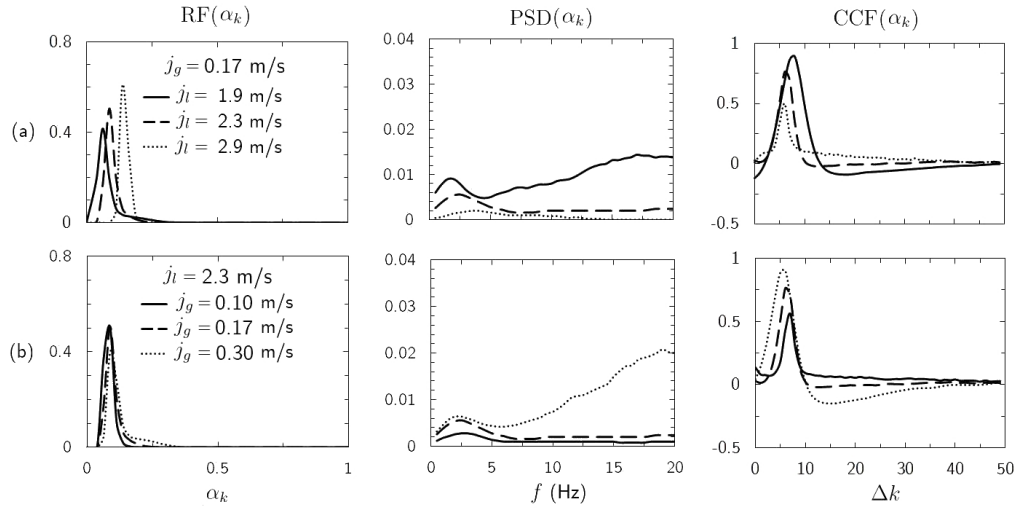

Figure 7: Effects of (a) liquid flow rate and (b) gas flow rate on the properties of area–averaged void fraction in the bubbly flow regime.

any consideration given to the void fraction measurement. Although a possible error in void fraction measurement is of no consequence to the present work, it deserves the attention of researchers using WMS for other purposes.

4.2.2. Slug flow

In slug flow (Figure 8), RF(α_k) was found to be double–peaked, with one peak at small α_k, which corresponds to the residence time of liquid slugs, and another peak at large α_k, which corresponds to the residence time of Taylor bubbles. With increasing liquid flow rate, the amplitude of the large α_k peak decreased, while that of the small α_k peak increased. However, when the gas flow rate was increased, the opposite trend was observed in the peaks of RF(α_k) and, in addition, the location of the small–α_k peak moved to higher void fractions, indicating that the gas content in the liquid slugs increased. With increasing liquid flow rate, the amplitude of the peak in PSD(α_k) decreased and moved to higher frequencies, whereas, for increasing gas flow rate, the amplitude of the peak in PSD(α_k) increased and moved to lower frequencies.

4.2.3. Churn flow

In churn flow (Figure 9), RF(α_k) was single-peaked and negatively skewed. The liquid flow rate had a small effect on the amplitude of the peak in RF(α_k),

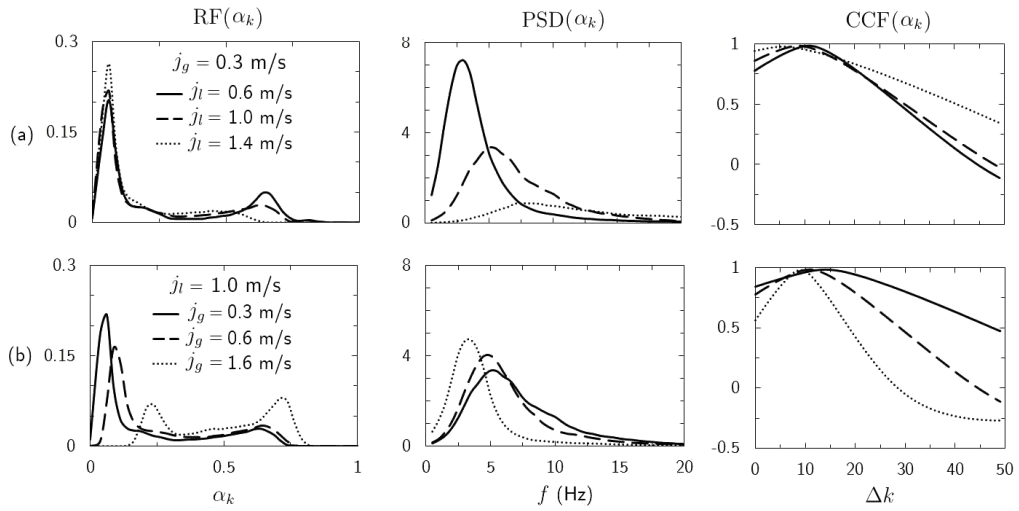

Figure 8: Effects of (a) liquid flow rate and (b) gas flow rate on the properties of area–averaged void fraction in the slug flow regime.

while the gas flow rate tended to shift the peak towards larger α_k, without affecting significantly its amplitude. Increasing the liquid flow rate shifted the peak in PSD(α_k) towards higher frequencies. On the other hand, increasing the gas flow rate had almost no effect on the peak frequency of PSD(α_k), but tended to increase the value of the PSD.

4.2.4. Annular flow

In annular flow (Figure 10), RF(α_k) appeared to have a single peak at α_k close to 1. Increasing gas flow rate or decreasing liquid flow rate shifted RF(α_k) towards larger α_k. The power density decreased with increasing gas flow rate or decreasing liquid flow rate, which implies that the fluctuations of α_k were decreasing.

4.3. Neural network training

Artificial neural networks (ANN) were trained to predict the gas or liquid flow rate in each of the flow regimes. The method used was the same as the one described in ST2, but in the present study the input to the algorithm was the time history of the area–averaged void fraction obtained from the WMS instead of the time history of dimensionless differential pressure that was used in ST2. This procedure was carried out using the freely available

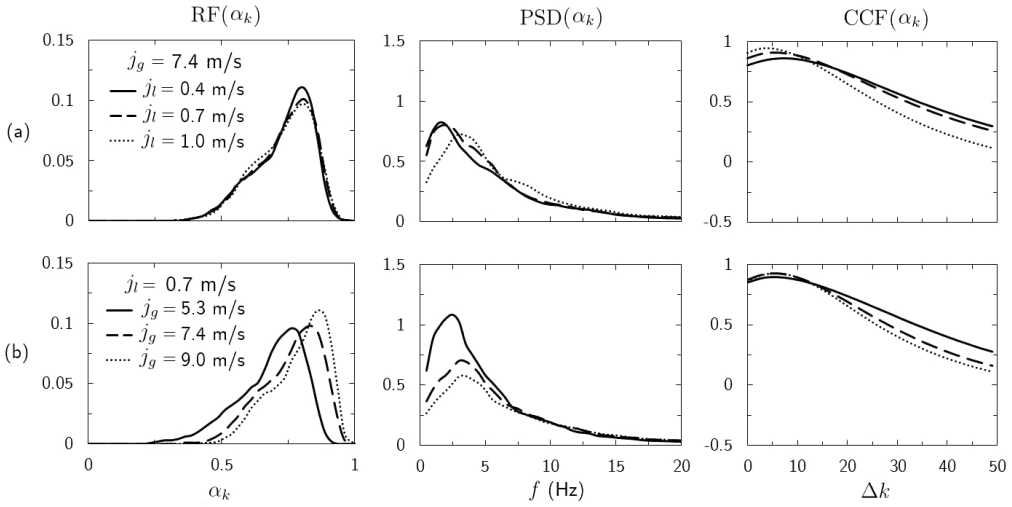

Figure 9: Effects of (a) liquid flow rate and (b) gas flow rate on the properties of area–averaged void fraction in the churn flow regime.

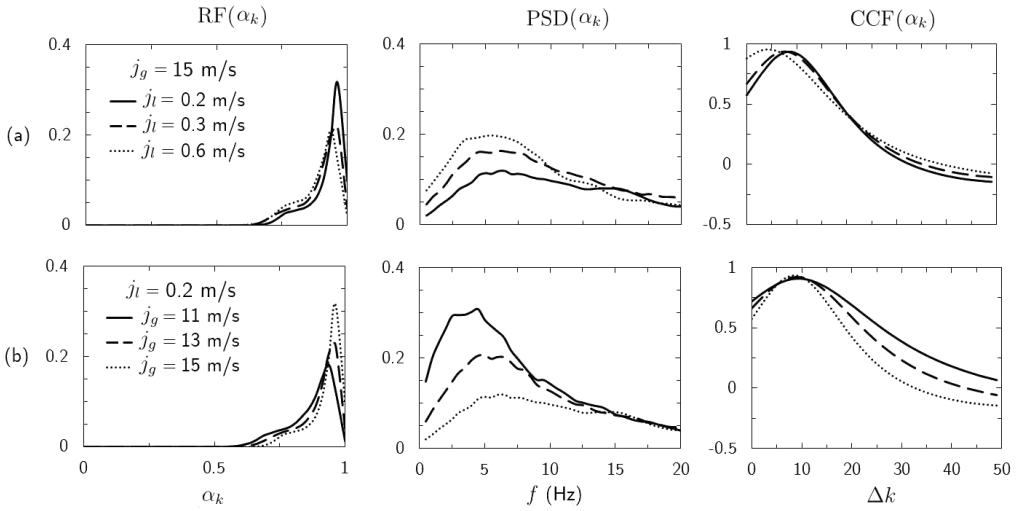

Figure 10: Effects of (a) liquid flow rate and (b) gas flow rate on the properties of area–averaged void fraction in the annular flow regime.

software RapidMiner 5 (RapidMiner, 2013) and consisted of the following steps.

1. Eighty representative features (40 values of RF(α_k) and 40 values of PSD(α_k)) were selected. Each feature was standardized by subtracting its mean and dividing by its standard deviation over the set of all representative examples.
2. Principal Component Analysis (PCA) was used to transform the representative features to uncorrelated features. This is called *whitening* of the dataset.
3. Independent Component Analysis (ICA) was performed on the uncorrelated features using the FastICA algorithm by Hyvarinën and Oja (2000). This reduced the dataset to examples consisting of 12–13 independent features each.
4. The independent features were used as inputs to train ANN using the backpropagation algorithm with momentum. In total, eight ANN were trained to estimate the gas and liquid superficial velocities in each of the four flow regimes.

4.4. Neural network testing

The trained neural networks were tested for flow rate prediction of results in the testing database according to the following procedure.

1. The representative features, namely, RF(α_k) and PSD(α_k), were calculated from each measured time history of area–averaged void fraction.
2. RF(α_k) was used to identify the flow regime.
3. Each representative feature was standardized by using the mean and standard deviation that were calculated for that feature during the training phase.
4. The dataset was whitened, then independent features were extracted using, respectively, the PCA and ICA transformation matrices calculated during the training phase.
5. The independent features were used as inputs to the appropriate trained ANN and the appropriate flow rate was calculated.
6. The flow rate predictions were compared to the ones measured with flow meters and an error analysis was performed. The results will be presented in the following subsection.

4.5. Accuracy of volumetric flow rate predictions

The relative prediction error for each measurement of superficial gas velocity is defined as

$$\epsilon = \frac{j_{gp} - j_g}{j_g} \times 100\% \ , \tag{5}$$

where j_g is the value of gas superficial velocity measured using a flow meter and j_{gp} is the corresponding value predicted by the present method. A similar definition can be made for the relative prediction error of the liquid superficial velocity j_l. The prediction accuracy of the flow rate prediction method will be quantified by the percentages of predictions with $|\epsilon| < 10\%$, to be denoted as ϵ_{10}, and $|\epsilon| < 20\%$, to be denoted as ϵ_{20}. The performance metrics ϵ_{10} and ϵ_{20} are presented in Table 2 for each flow regime.

Figure 11a presents the ratio of predicted and measured liquid superficial velocities for flows in the testing database. The predictions of liquid superficial velocity were found to be within $\pm 10\%$ of the measured values for more than 70% of the tested cases and within $\pm 20\%$ for more than 90% of these cases. The largest relative errors occurred at the lowest liquid flow rates. Figure 11b shows the ratio of predicted and measured gas superficial velocities for flows in the testing database. The performance of the present method was very good, with $\epsilon_{10} = 83\%$ and $\epsilon_{20} = 91\%$. The largest relative errors occurred in the range of very low gas superficial velocities ($j_g < 0.2$ m/s), where the absolute errors were actually quite small. Thus, the present method may be used to predict liquid superficial velocities in the range $j_l > 1.25$ m/s, if a maximum relative error of about 10% can be tolerated, and in the range $j_l > 0.5$ m/s, if a maximum relative error of about 20% can be tolerated. In addition, this method may be used to predict gas superficial velocities in the range $j_g > 1.5$ m/s, if a maximum relative error of about 10% can be tolerated, and in the range $j_g > 0.3$ m/s, if a maximum relative error of about 20% can be tolerated.

5. Measurement of two-phase flow rates with a dual WMS unit

When, in addition to the single WMS considered in the previous section, a second, axially displaced, WMS is installed in the pipe, one may take advantage of the information contained in the second WMS output to improve the accuracy of the MFM procedure. This was the case of the present loop, which was equipped with a dual WMS unit providing separate outputs for each of the two sensors. Following consideration of various alternatives, we

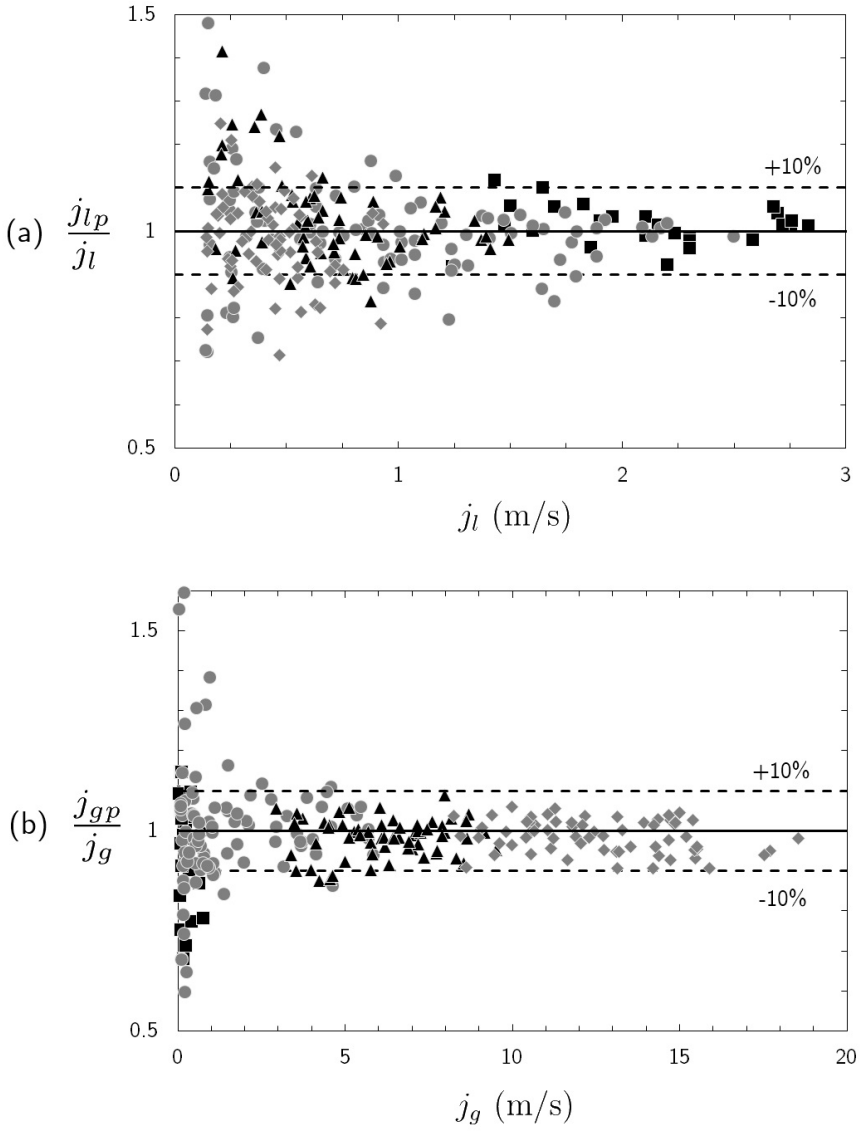

Figure 11: Ratios of predicted (using single WMS) and measured (using flow meters) superficial velocities of (a) liquid and (b) gas for measurements in the testing database. ■: bubbly flow regime, ●: slug flow regime, ▲: churn flow regime, ◆: annular flow regime.

Table 2: Accuracy of the predictions of gas and liquid superficial velocities using the present method with a single WMS and a dual WMS unit; results for the ST2 method, which uses a differential pressure sensor, are also shown for comparison. ϵ_x: Percentage of flow rate predictions in the range from $-x\%$ to $x\%$ of the value measured using flow meters.

Flow regime	Flow variable	Single WMS		Dual WMS unit		ST2 method	
		ϵ_{10}	ϵ_{20}	ϵ_{10}	ϵ_{20}	ϵ_{10}	ϵ_{20}
Bubbly	j_l	93	100	100	100	-	-
	j_g	59	74	78	89	-	-
Slug	j_l	69	87	91	99	72	92
	j_g	71	83	73	88	48	75
Churn	j_l	75	92	84	100	77	96
	j_g	94	100	94	100	85	99
Annular	j_l	71	92	94	100	81	98
	j_g	100	100	100	100	80	98
All	j_l	74	91	91	100	77	95
	j_g	83	91	86	94	70	90

decided to include the cross-correlation function CCF(α_k) (see equation 4) among the representative properties of the MFM analysis.

To verify that CCF(α_k) was appropriate as a representative property of the WMS outputs, we confirmed that it was sensitive to both phase flow rates and that its dependence on each of them was well defined. Evidence for this verification for each flow regime is provided in Figures 7 to 10. In bubbly flows, the value of CCF(α_k) at its peak was relatively small at low gas flow rates or large liquid flow rates and it increased with increasing gas flow rate or decreasing liquid flow rate. In both bubbly and slug flows, the location of the peak in CCF(α_k) was shifted to smaller lags with increasing gas or liquid flow rates. In slug flows, CCF(α_k) became broader with increasing liquid flow rate or decreasing gas flow rate. In churn and annular flows, the location of the peak of CCF(α_k) was found to be fairly insensitive to gas flow rate, however it moved to smaller lags with increasing liquid flow rate. The shape of CCF(α_k) was broadened as the gas flow rate increased and narrowed as the liquid flow rate increased.

Performance indicators of the present method using a dual WMS unit are shown in Table 2, together with those obtained using a single WMS. In general, the use of dual WMS led to a significant improvement in the

prediction accuracy of liquid flow rate. Some improvement in the prediction accuracy of gas flow rate was also achieved, especially in the bubbly flow regime. The average absolute value of relative error in the predictions of liquid and gas superficial velocities, was reduced from, respectively, 8.3% and 9.3% using a single WMS to 4.1% and 5.8% using a dual WMS, which correspond to error reductions of 51% and 37%, respectively. Consequently, if a dual WMS unit, or equivalent instrumentation, is available, it would be advantageous to use the cross–correlation function as a representative feature, in addition to the relative frequency and power spectral density of the void fraction measured by a single WMS.

6. A comparison with MFM analysis using differential pressure signals

In addition to the performance indicators of the present method using single and dual WMS, Table 2 shows the performance indicators using the differential pressure method presented in ST2. The measurements in that study were collected in the same facility and under the same conditions as in the present one, with the exception that, for accurate differential pressure measurements, the liquid superficial velocity was restricted to the range below 0.4 m/s. Consequently the comparison does not extend to bubbly flows, because this regime was not encountered during the differential pressure tests.

It is clear that the dual-WMS method has a higher accuracy than either the single-WMS method or the ST2 method, for both gas and liquid superficial velocities in all flow regimes. The accuracies of liquid superficial velocity predictions of the single-WMS method and the ST2 method are comparable in the slug and churn flow regimes, while the ST2 method outperforms the single-WMS method in the annular flow regime. Both of these methods have comparable ϵ_{20} for predictions of gas superficial velocity, but the single-WMS method has a significantly larger ϵ_{10} in all flow regimes, indicating that it is more precise than the ST2 method for gas flow rate measurements. In conclusion, the ST2 method and the single-WMS method have roughly equal accuracies for the liquid superficial velocity predictions, whereas the former achieves more accurate gas flow rate measurements. The dual-WMS method is clearly the best choice in terms of accuracy in predicting both phase flow rates in all flow regimes.

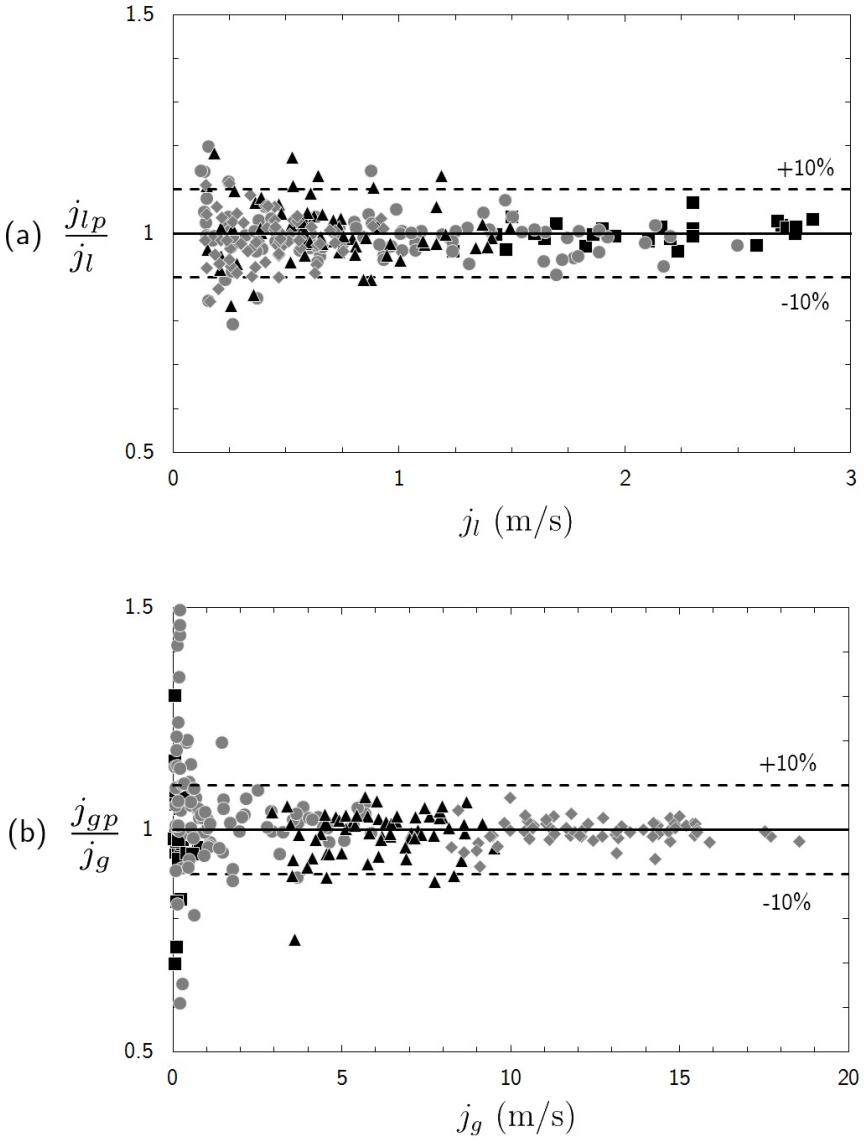

Figure 12: Ratios of predicted (using dual WMS) and measured (using flow meters) superficial velocities of (a) liquid and (b) gas for measurements in the testing database. ■: bubbly flow regime, ●: slug flow regime, ▲: churn flow regime, ◆: annular flow regime.

7. Measurement of liquid flow rate transients

The present method has so far been validated for steady flow conditions. However, it is also of interest, particularly in nuclear safety analysis, to measure flow rate under unsteady conditions, similar to those that occur in many practical applications. In this section, we report results of tests of the present method for three representative types of flows with a time-dependent liquid flow rate in the test section. Variation of the liquid flow rate was effected by manual changing of the opening of a valve installed on a bypass line, as illustrated in Figure 1. The time history of the "actual" liquid superficial velocity was obtained from the readings of the ultrasonic flow meter, which had a response time of 0.3 s. The present method was applied to 5 s long segments of α_k measured by the WMS to estimate the "instantaneous" j_l. We found this sample duration to be the minimum required for convergence of the statistical properties of the area–averaged void fraction. To allow more frequent updates of the current j_l, each segment overlapped by 80% with each of the two neighbouring segments. It should be noted that the calculations done in this section were performed after the measurements were completed, and the symbols in Figures 13–15 were placed at the mid-point of the time segments for which they were calculated; in contrast, if this method were used for online monitoring of flow rates, the superficial velocity would be updated at the end of each time segment. The time history of the gas superficial velocity could not be monitored accurately with the available rotameters, so only the initial value of j_g will be reported. The performance of the present method during these three transient tests will be described in the remainder of this section.

Gradual increase of liquid flow rate: This flow condition was generated by a gradual closing of the bypass valve. The superficial gas velocity at the start of the measurement was set as $j_g = 0.8$ m/s and the flow regime was identified as slug flow for the entire duration of the measurements. Figure 13 shows that the predictions of the present method followed fairly closely the measurements of the ultrasonic flow meter.

Sudden stop of liquid flow: This flow condition was created by shutting off the power to the main pump, although, as a result of the inertia of the water, its flow rate did not vanish abruptly but gradually (Figure 14). Initially, the flow rates were set as $j_l = 1.62$ m/s and $j_g = 0.8$ m/s, so that the flow was in the slug flow regime. Following pump shut down, the flow transitioned to the churn flow regime, then to the annular flow regime and

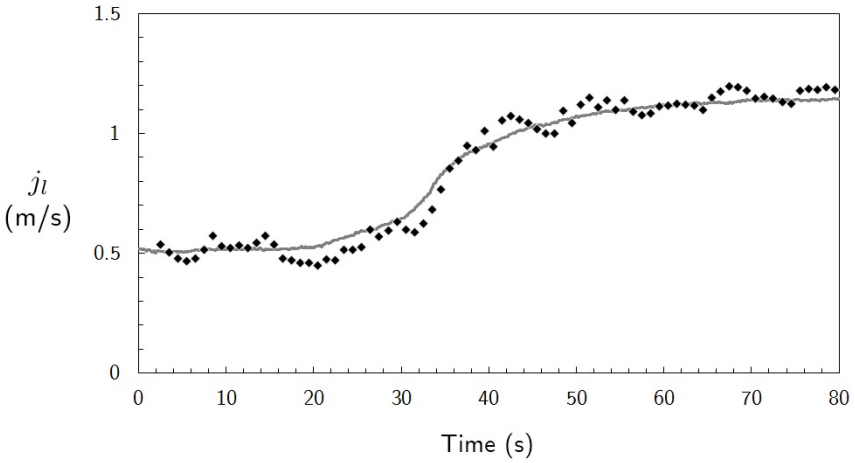

Figure 13: Predictions of j_l by the present method (symbols) and measurements of j_l by an ultrasonic flow meter (solid line) in a flow with a gradually increasing liquid flow rate.

finally to a single phase gas flow. The liquid superficial velocity predicted by the present method during the transient lagged behind the measured j_l.

Oscillatory liquid flow rate: This flow condition was generated by opening and closing the bypass valve at a frequency of 0.08 Hz. The average flow rates were $j_l = 0.9$ m/s and $j_g = 1$ m/s and the flow remained in the slug flow regime at all times. As Figure 15 shows, the predictions of the present method were very close to the measurements during flow acceleration, but lagged somewhat behind the measurements during flow deceleration.

Although it has so far been shown that the present method is able to follow accurately slow transients, the WMS appears to have a delayed response to decreasing flow rates. This observation does not necessarily prove that the WMS was in error, because a close examination of the loop operation indicated that the liquid flow rates at the water flowmeter and the WMS may have been somewhat different during periods of sharply decreasing liquid velocities. As shown in Figure 1, the water flow control valve was positioned just upstream of the water flow meter, which was, in turn, located approximately 6 m upstream of the WMS (3.5 m along the horizontal branch and 2.44 m along the vertical branch). The air injection port was located far downstream of the ultrasonic flow meter and well upstream of the WMS; in consequence, the flow meter was always immersed in single–phase water, whereas the WMS could be exposed to water, air or two–phase flows. As

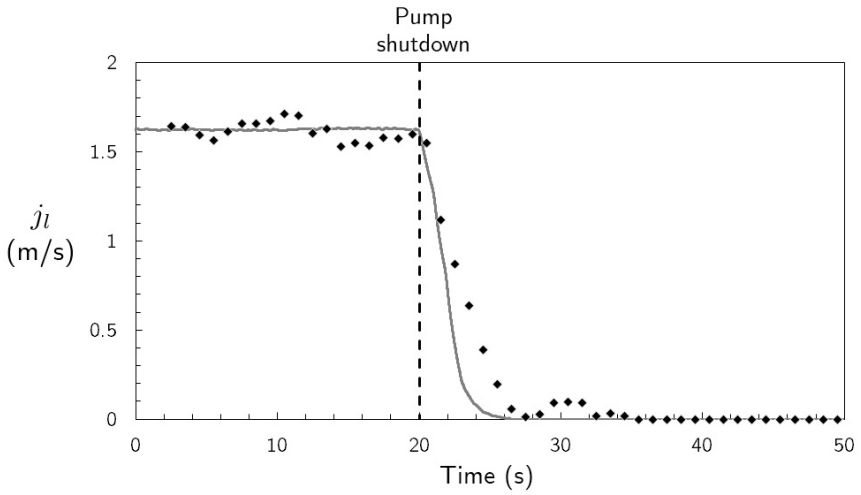

Figure 14: Predictions of j_l by the present method (symbols) and measurements of j_l by an ultrasonic flow meter (solid line) in a flow with a sudden stop of liquid flow.

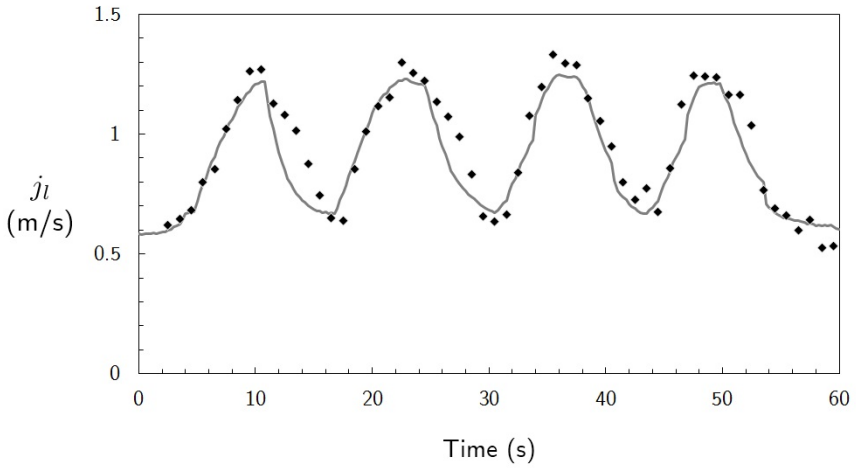

Figure 15: Predictions of j_l by the present method (symbols) and measurements of j_l by an ultrasonic flow meter (solid line) in a flow with oscillations of j_l.

the result of incompressibility of water, a decrease in the liquid flow rate during closing of the valve would be imposed instantaneously on the flow meter, and so an error in its output could only be caused by an inadequate frequency response, which was not the case for the present instrument. On the other hand, air would flow at a constant mass flow rate past the WMS before, during and after valve closing. Therefore, some water would continue to flow for a short time past the WMS, because of the inertia of the fluid in the vertical upward branch, combined with the compressibility of the gas phase. In addition, some of the water that remained in the vertical upward flow branch would be lifted by the flowing air past the WMS section, until enough water would be depleted so that the liquid level would drop below the air injection port. These arguments support our assessment that the apparent delay in WMS response corresponded, to a large portion or its entirety, to residual water flow through the WMS and so it was not necessarily a measurement error. Besides the previous explanation, we also examined the possibility that WMS signal averaging (over 5 s) would somehow introduce a delay during water flow deceleration. It is evident that the ratio of the average and the value at mid-interval would depend on the waveform of the flow rate transient. At the start of a drop in flow rate, when the output signal would be convex, averaging would lead to under–estimation of the flow rate, whereas at times past the inflection point of the signal, when it would be concave, averaging would lead to over–estimation of the flow rate; this observation makes averaging an implausible cause of delayed WMS response, regardless of the waveform of the flow rate transient. In summary, we believe that the apparent delay in the flow rate output of the WMS is related to the specific experimental configuration used in the present study, rather than to inaccuracies of the WMS or the data processing procedure.

8. Flow rate measurement in vertical downward flow

The method described previously for measuring gas and liquid flow rates in vertical upward pipe flows was also tested in vertical downward flows. In fact, the flow loop was designed to permit simultaneous measurements in both upward and downward flows with two separate dual WMS units. Separate sensor calibrations were performed, as it is well-known that the flow regimes in downward flows differ from those in upward ones. In fact, in downward flows in the range of conditions of present interest, only three flow regimes were encountered, in agreement with the observations of Barnea

et al. (1982); these regimes are the bubbly, slug and annular flow regimes. In the present experiments, the flow regime in the pipe was found to depend mainly on the liquid flow rate (Figure 16). At low liquid flow rates, the flow was annular with the liquid flowing as a film on the wall and the gas flowing in the core. At intermediate liquid flow rates, slug flow was observed, whereby the liquid would occasionally bridge the gas core forming liquid slugs. In this regime, at larger liquid flow rates, distinct Taylor bubbles could be noticed, having noses pointing upwards, *i.e.*, opposite to the direction of water flow. At the largest liquid flow rates, the flow was bubbly, resembling bubbly flow in vertical upward air–water flow. The presently observed flow regime transition boundaries were qualitatively similar to those reported by other researchers. For example, as illustrated in Figure 16, transition from the slug to the bubbly regime found by Barnea et al. (1982) was almost identical to the one determined in the present experiments, while their transition from the annular to the slug regime occurred at slightly larger liquid flow rates than that in the present study.

The proposed flow rate measurement method was applied using the area–averaged void fraction measured by single and dual WMS following the procedure presented in Section 4.3. An elastic map was trained to identify the flow regime based on $\mathrm{RF}(\alpha_k)$, then six separate neural networks were trained to estimate the gas and liquid superficial velocity in the three flow regimes. The accuracy of this method was found to be very similar to the results presented in Section 4.5 and thus we concluded that the proposed method is applicable to vertical downward as well as vertical upward gas–liquid flows.

9. Summary and concluding remarks

A novel flow rate measurement method has been proposed that utilizes machine–learning algorithms to process the area–averaged void fraction signals measured by a single wire–mesh sensor in vertical upward air–water flow. The flow regime is first identified from the relative frequencies of the area–averaged void fraction using the elastic maps method, which we presented in a previous article (Shaban and Tavoularis, 2014a). The relative frequencies and the power spectral density of α_k are selected as representative properties of the flow and independent features are then extracted from them using Principal Component Analysis and Independent Component Analysis. The resulting features are used as inputs to separate artificial neural networks for each flow regime, which are trained to give the gas and

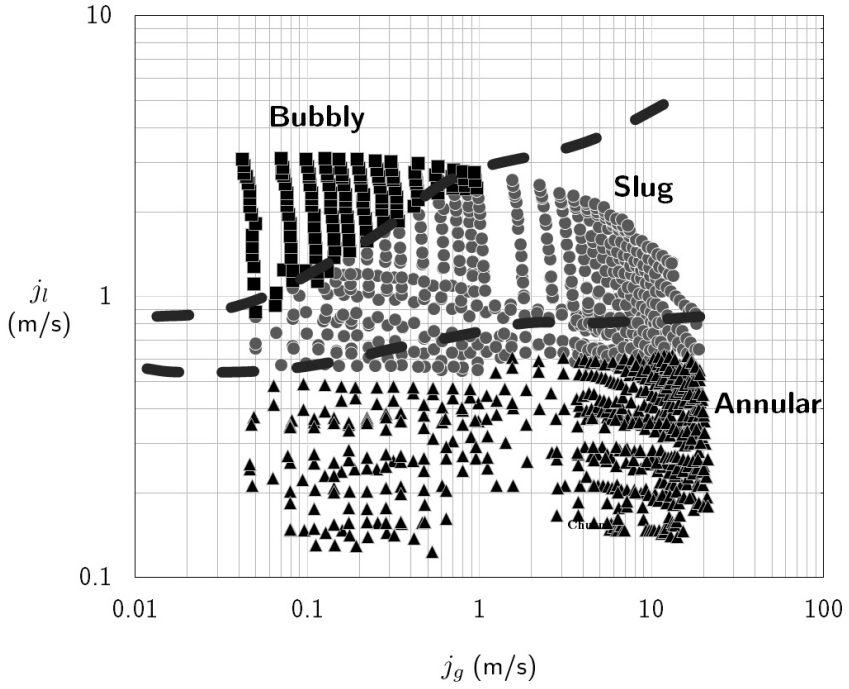

Figure 16: Flow regime map in vertical downwards flow indicating the flow rates of the present measurement sets. ■: bubbly flow regime, ●: slug flow regime, ▲: annular flow regime. Dashed lines denote the flow regime transition boundaries reported by Barnea et al. (1982) for a 51 mm pipe.

liquid flow rates as outputs. The method has also been applied using the signals from a dual WMS unit, in which case the cross–correlation function of void fraction measurements from the upstream and downstream sensors is used as an additional representative property in the algorithm. It was found that using the cross–correlation function led to significant improvement in the overall accuracy of the flow rate predictions, especially that of the liquid flow rate. The average absolute value of the relative error of liquid and gas superficial velocity predictions was found to be, respectively, 8.3% and 9.3% using a single WMS and 4.1% and 5.8% using a dual WMS unit. The same method has also been applied successfully to three simple transient flows and to vertical downward air–water flows.

Although the proposed method cannot be used in single phase flows, it offers several advantages in the measurement of two–phase flow rates. Firstly, it does not require separation of the two phases and the required sensors can be installed in existing piping systems with only small modifications. WMS measure the instantaneous void fraction distribution, which is an important parameter in two–phase flow analysis. Unlike the cross–correlation method, which has been suggested previously as suitable for measuring gas flow rate using dual WMS, the present method is accurate for all flow regimes and all flow conditions of interest. However, the present method can only be reliably used with the same working fluids and under the same thermodynamic conditions as those used for training. The cross–correlation method does not depend on calibration under specific flow conditions, which makes it a more robust approach within its range of applicability. Although the WMS is more intrusive than differential pressure sensors, used in our previous study (Shaban and Tavoularis, 2014b), the faster temporal response of the WMS allows flow rate measurements to be made for a much wider range of gas and liquid flow rates. Finally, an additional advantage of the proposed method is that all of the data processing tasks and machine learning algorithms were implemented using free or open–source software, thus eliminating accessibility problems and licensing costs.

Acknowledgements

Financial support for this study was provided by the University Network of Excellence in Nuclear Engineering (UNENE), Atomic Energy of Canada Limited (AECL) and the Natural Sciences and Engineering Research Council

of Canada (NSERC). The wire-mesh sensor instrumentation used in this work was on loan from AECL.

References

Barnea, D., Shoham, O., Taitel, Y., 1982. Flow pattern transition for vertical downward two phase flow. Chem. Eng. Sci. 37, 741–744.

Beg, N., Toral, H., 1993. Off-site calibration of a two-phase pattern recognition flowmeter. Int. J. Multiphase Flow 19, 999–1012.

Beyer, M., Lucas, D., Kussin, J., 2010. Quality check of wire-mesh sensor measurements in a vertical air/water flow. Flow Meas. Instrum. 21, 511–520.

Beyer, M., Lucas, D., Kussin, J., Schutz, P., 2008. Air-water experiments in a vertical DN200 pipe. Tech. Rep. FZD-505, Forschungszentrum Dresden-Rossendorf e.V., Radeberg, Germany.

Da Silva, M. J., Schleicher, E., Hampel, U., 2007. Capacitance wire-mesh sensor for fast measurement of phase fraction distributions. Meas. Sci. Technol. 18, 2245–2251.

Falcone, G., Hewitt, G., Alimonti, C., Harrison, B., 2002. Multiphase flow metering: Current trends and future developments. J. Petrol. Technol. Apr 2002, 77–84.

Fan, S., Yan, T., 2013. Two-phase air-water slug flow measurment in horizontal pipe using conductance probes and neural network. IEEE Trans. Instr. Meas., doi: 10.1109/TIM.2013.2280485.

Gorban, A., Zinovyev, A., 2003. *elmap*: C++ package. Available online: http://bioinfo-out.curie.fr/projects/elmap/. Last accessed: 17 November 2013.

Gorban, A., Zinovyev, A., 2005. Elastic principal manifolds and their practical applications. Computing 75, 359–379.

Hyvarinën, A., Oja, E., 2000. Independent component analysis: Algorithms and applications. Neural Networks 13, 411–430.

Lucas, D., Beyer, M., Kussin, J., Schütz, P., 2010. Benchmark database on the evolution of two-phase flows in a vertical pipe. Nucl. Eng. Des. 240, 2338–2346.

Meng, Z., Huang, Z., Wang, B., Ji, H., Li, H., Yan, Y., 2010. Air-water two-phase flow measurement using a Venturi meter and an electrical resistance tomography sensor. Flow Meas. Instrum. 21, 268–276.

Minemura, K., Egashira, K., Ihara, K., Yamamoto, K., 1996. Simultaneous Measuring Method for Both Volumetric Flow Rates of Air-Water Mixture Using a Turbine Flowmeter. J. Energy Resour. Technol. 118, 29–35.

Minemura, K., Takeoka, T., Syoda, S., Egasira, K., Ogawa, Y., 1998. Correlative mapping method for measuring individual phase flow rates in air-water two-phase flow based on stochastic features. JSME Int. J. 41, 863–870.

Mishima, K., Ishii, M., 1984. Flow regime transition criteria for upward two–phase flow in vertical tubes. Int. J. Heat Mass Transfer 27, 723–737.

Prasser, H.-M., Beyer, M., Böttger, A., Carl, H., Lucas, D., Schaffrath, A., Schütz, P., Weiss, F.-P., Zschau, J., 2005. Influence of the pipe diameter on the structure of the gas-liquid interface in a vertical two-phase pipe flow. Nucl. Technol. 152, 3–22.

Prasser, H.-M., Beyer, M., Carl, H., Manera, A., Pietruske, H., Schutz, P., 2007. Experiments on upward gas/liquid flow in vertical pipes. Tech. Rep. FZD-482, Forschungszentrum Dresden-Rossendorf e.V., Radeberg, Germany.

Prasser, H.-M., Böttger, A., Zschau, J., 1998. A new electrode–mesh tomograph for gas–liquid flows. Flow Meas. Instrum. 9, 111–119.

Prasser, H.-M., Krepper, E., Lucas, D., 2002. Evolution of the two–phase flow in a vertical tube – decomposition of gas fraction profiles according to bubble size classes using wire-mesh sensors. Int. J. Therm. Sci. 41, 17–28.

RapidMiner, 2013. RapidMiner 5: Open source data mining and predictive analytics software. Available online: http://www.rapidminer.com. Last accessed: 8 November, 2013.

Scilab Enterprises, 2013. Scilab 5.4: Free and open source software for numerical computation. Available online: http://www.scilab.org. Last accessed: 17 November, 2013.

Shaban, H., Tavoularis, S., 2014a. Identification of flow regime in vertical upward air–water pipe flow using differential pressure signals and elastic maps. Int. J. Multiphase Flow 61, 62–72.

Shaban, H., Tavoularis, S., 2014b. Measurement of gas and liquid flow rates in two-phase pipe flows by the application of machine learning techniques to differential pressure signals. Int. J. Multiphase Flow 67, 106–117.

Taitel, Y., Bornea, D., Dukler, A., 1980. Modelling flow pattern transitions for steady upward gas-liquid flow in vertical tubes. AIChE J. 26, 345–354.

Thorn, R., Johansen, G., Hjertaker, B., 2013. Three-phase flow measurement in the petroleum industry. Meas. Sci. Technol. 24, doi:10.1088/0957–0233/24/1/0120.

Chapter 8

Distribution of downward air–water flow in vertical tubes connected to a horizontal cylindrical header

In this chapter, the flow rate distribution in vertical feeders connected to a horizontal header is experimentally studied using a flow rate measurement method based on machine learning. The flow distribution is described in relation to the flow patterns in the header and the pressure distribution. The chapter is presented as the manuscript

> "Shaban, H. and Tavoularis, S. 2015 Distribution of downward air–water flow in vertical tubes connected to a horizontal cylindrical header. *Nuc. Eng. Des* **291**, 90-100."

which was submitted to *Nuclear Engineering and Design* on 5 January 2015 and accepted for publication on 18 May 2015.

Distribution of downward air–water flow in vertical tubes connected to a horizontal cylindrical header

H. Shaban, S. Tavoularis*

Department of Mechanical Engineering, University of Ottawa,
161 Louis Pasteur, Ottawa, ON K1N 6N5, Canada

Abstract

The distribution of downward air–water flow in vertical 32.5 mm feeder tubes connected to a horizontal 203 mm cylindrical header was studied experimentally in a modular header facility operating at near–atmospheric pressure. Several experimental configurations with different combinations of two or four feeders were used. A large database of mass flow rate measurements was compiled using a flow rate measurement method based on machine learning. The collected data allowed the effects of inlet flow rates and feeder location on the gas and liquid flow distribution to be studied. The feeder mass flow rates were also qualitatively correlated to the observed flow patterns in the header, including the inlet gas–liquid jet, the free surface level and the cross–flow velocity over the feeders. Three potential approaches for correlating the wall pressures measured at different locations to the flow rate distribution were tested. Although under certain conditions a measurable pressure was found to be correlated with the flow distribution, it was concluded that none of these methods was capable of estimating consistently and accurately the flow distribution in a header–feeder system.

Keywords: two–phase, header, feeders, maldistribution, CANDU

1. Introduction

Piping networks supplied by a *manifold* or *header* are encountered in many industrial systems. The headers used in the primary heat transport system of a CANDU (CANada Deuterium Uranium) reactor are horizontal cylindrical tanks connected to the fuel channels of the reactor by pipes called *feeders*. During normal reactor operation, headers ensure a steady flow of single–phase heavy water coolant through all of the fuel channels. In an inlet header, liquid heavy water coolant enters from the coolant pump through one or more inlet *turrets* and is distributed among the fuel channels by different feeders. After being heated in the fuel channels, the coolant is collected into an outlet header, and from there it flows to the steam generator through one or more outlet turrets. In case of a Loss Of Coolant Accident (LOCA), the reactor is shut down and the Emergency Coolant Injection System (ECIS) is activated. This system injects light water at high pressure into the inlet headers to enhance the cooling of the reactor core. Boiling is expected to occur in this case, and the flow in the headers would change from a single–phase water flow to a two–phase steam–water flow. Nuclear safety analyses are concerned with the possibly non–uniform distribution, or *maldistribution*, of the two phases among the different feeders which may cause the supply of little or no liquid coolant to some of the fuel channels; this would introduce the possibility of fuel element overheat. Nuclear safety analysts are required to devise methods that ensure that the coolant distribution in the feeders can be measured or predicted accurately, allowing them to improve the accuracy of the header–feeder models used in thermalhydraulics system codes for modeling postulated accident scenarios.

Due to the importance of this type of flow in nuclear safety analysis, many studies have been performed, using both simple and complicated geometries, to provide insight into the causes of two–phase flow maldistribution in header–feeder systems. A literature review of several experimental investigations of two–phase flow distribution in header–feeder systems was presented recently by Dario et al. (2013). These authors concluded that the flow distribution was primarily affected by the geometrical configuration, the flow conditions and the fluid properties. For a given geometry, the flow distribution was found to depend mainly on the inertial and gravitational forces, represented by the gas and liquid Froude numbers, which, in turn, depend on the gas and liquid flow rates. The relationship between the gas and liquid flow rates in the feeders and the phenomena of gas and liquid

entrainment into the feeders have been investigated by several authors (Hassan et al., 1997; Ahmad and Hassan, 2006; Bartley et al., 2008; Bowden and Hassan, 2008). Smoglie and Reimann (1986) identified two patterns of flow into vertical downward feeders, namely, *vortex–induced* flow and *vortex–free* flow, whereas Bowden and Hassan (2007) used Particle Image Velocimetry (PIV) to demonstrate the existence of strong radial velocities while liquid was discharging from a single vertical downward feeder in vortex–free flow. The strong effect of cross–flow on the flow pattern into the feeders has been demonstrated by Reimann and Khan (1984) and Schrock et al. (1986). Other work relevant to header–feeder geometries includes PIV studies of the flow into feeders inclined at different angles (Bowden and Hassan, 2008; Saleh et al., 2010, 2011), as well as attempts at modeling header–feeder flows using potential flow theory (Saleh et al., 2009; Bowden and Hassan, 2009).

Kowalski et al. (1989) conducted an experimental investigation of two–phase steam–water flow in the Full–Scale Header Test Facility at Stern Laboratories Inc., in a half–length model of the CANDU header–feeder system consisting of an inlet and an outlet header connected by 30 feeders at different orientations. These experiments were conducted with single and double–turret injection and for pressures ranging from 1 to 5 MPa. These authors found that there was clear flow stratification in the header, even at relatively low inlet gas flow rates and proposed that the momentum of the impinging inlet jet was the dominating effect on liquid distribution. They measured water level in the header by using a combination of conductivity probes and differential pressure rakes and noted that the shape of the interface between the two phases depended on the type of injection (single/double turret) as well as the injection quality. In a separate study,Teclemariam et al. (2003) documented the two–phase flow patterns in a scaled–down version of the header test facility used by Kowalski et al. (1989). They presented visual observations of the flow patterns in the header, as well as flow rate measurements in all of the feeders, obtained with the use of a gas–liquid separation technique. These authors found a wide variation in the flow rates out of the different feeders and proposed that the inlet gas and liquid flow rates had a significant effect on the flow distribution in the feeders.

From the above discussion, it may be concluded that two important parameters affecting the two–phase flow distribution in header–feeder systems are (i) the geometrical configuration, including the location and angle of the feeders and the location and number of inlet turrets and (ii) the inlet gas and liquid flow rates, which affect the flow pattern in the header. The objective of

the present work is to complement the available knowledge on this problem, by isolating two effects, namely, the effect of feeder axial location and the effect of inlet gas and liquid flow rates on the two–phase flow distribution. To this end, the present experiments were conducted in a modular horizontal header facility with different combinations of up to four vertical feeders in downward flow. Extensive measurements of the two–phase flow rates in the feeders were collected using a machine–learning technique, which offered significant savings in terms of cost and time. In addition to establishing the trends in the two–phase flow distribution for different feeder axial locations and inlet flow rates, the present data may be used to validate existing and future header–feeder models in thermalhydraulics system codes, as well as multiphase computational fluid dynamics (CFD) simulations of these flows.

2. Experimental facility and instrumentation

2.1. Modular header facility

The present experiments were performed at the Modular Header Facility at the University of Ottawa. The main component of the facility is a 203 mm I.D. horizontal cylindrical header made of black–anodized aluminium (Figure 1). The header has two inlet turrets, with inner diameters of 32.5 mm and 154 mm, respectively. In the present experiments, air–water mixtures were supplied to the header through the smaller turret, while the larger one was capped with a clear acrylic cover, thus permitting visual observation of the header interior. Two additional observation ports made of clear acrylic were installed at either end of the header. Twenty feeder ports with end flanges were arranged in axially equidistant groups of four *banks* and, in each bank, the feeder ports leave the header at three angles of inclination, namely, horizontal, inclined at 45° below horizontal and vertical downward. The header is described as *modular* as it is possible to use only a few feeder ports, connected to the *active feeders*, during an experiment, with the remaining ports plugged up to the inside diameter of the header body, using specially machined plugs made of polyvinyl chloride (PVC). The feeders, which were attached to the feeder ports using standard flanges, were tubes made of clear PVC with an inside diameter of 32.5 mm. As presented later in this section, a number of different configurations of the vertical downward feeders were used in the present study, using one, two or four feeders at a time.

Beside the header, the facility comprised a stainless steel water tank, a centrifugal pump and a 32.5 mm I.D. clear PVC inlet line (Figure 2). The

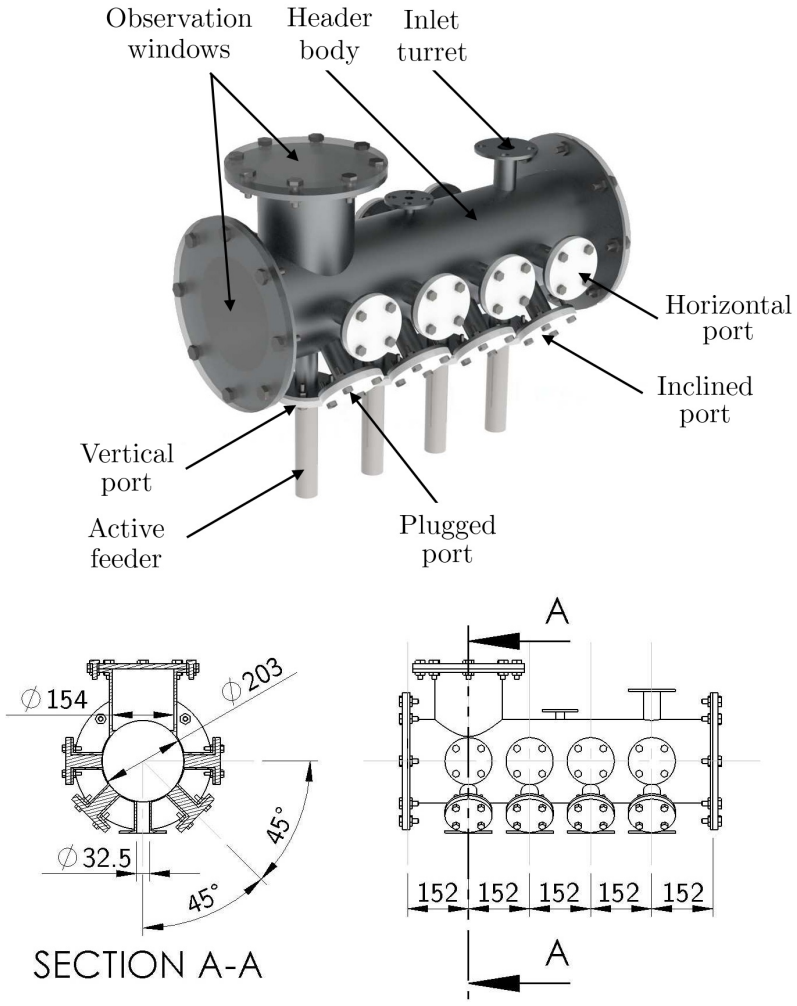

Figure 1: Three–dimensional (top), cross–sectional (bottom left) and side (bottom right) views of the modular header. All dimensions are in mm.

water tank was 1830 mm long, 610 mm wide and 1220 mm high. During each experiment, water was pumped from the water tank to the header through the inlet line, while air was supplied by a regulated compressed air line. All of the tests were performed with the regulator gauge pressure P_R set at 103.5 kPa. The water and air flow rates were controlled using gate and needle valves, respectively. The free surface level in the water tank was maintained at 600 mm from the bottom. It was ensured that no air released

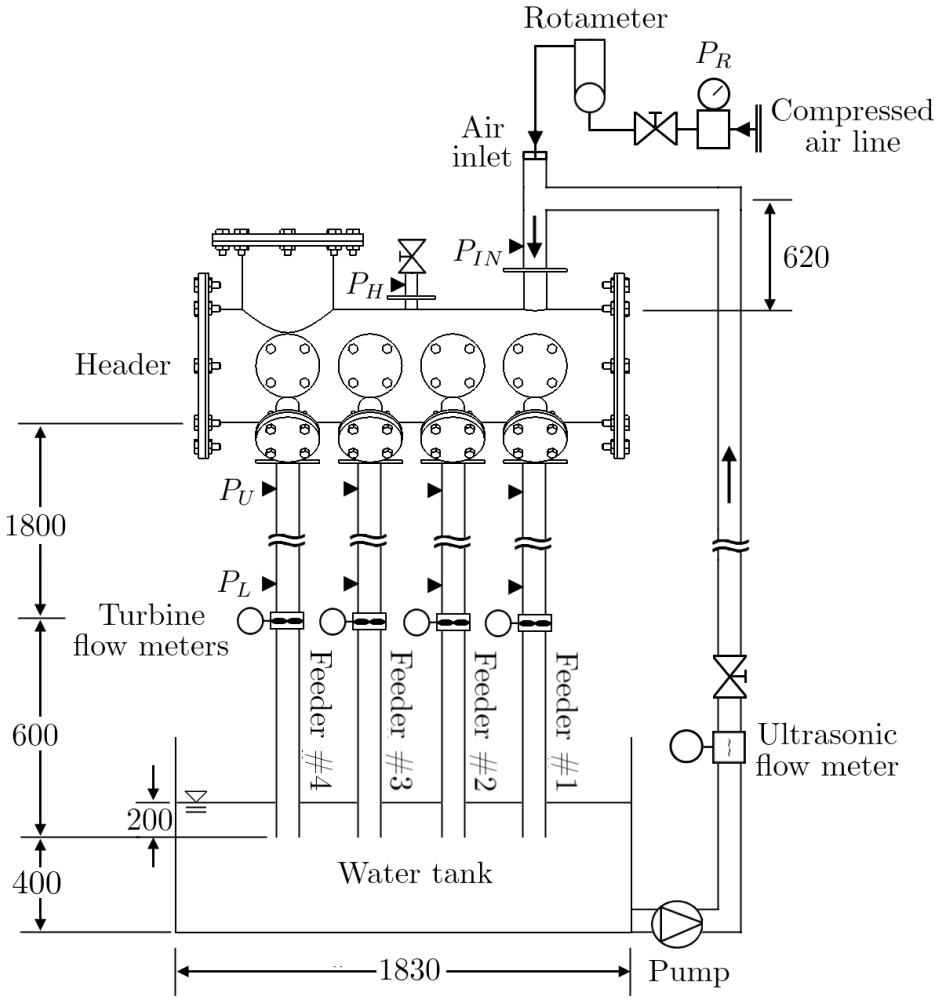

Figure 2: Schematic diagram of the modular header facility. All dimensions are in mm.

into the tank entered the pumps. The two fluids were mixed in a T–junction, 620 mm upstream of the header inlet. After passing through the header, the air–water mixture was distributed among a number of active feeder tubes and flowed back to the water tank. Each feeder had an inner diameter of 32.5 mm and a length of 2.4 m. The feeders were numbered according to their distance from the inlet turret, with feeder #1 being directly below the inlet turret and feeder #4 being the farthest away from it. Turbine flow meters (Shenzen FD Electronic LWGB–32, Zhejiang, China) were installed

1.8 m from the bottom of the header as part of the flow rate measurement scheme explained later. The inlet air flow rate was measured using a set of three rotameters (King Instruments Series 7510, Garden Grove, USA), having different ranges, while the water flow rate was monitored using a transit–time ultrasonic flow meter (Omega FDT–30, Laval, Canada). The gauge pressures P_{IN} at the header inlet and P_H at the top of the header body, as well as the pressure in the air supply line were monitored during all tests. The gauge pressures P_U, near the top of each feeder (200 mm from the bottom of the header), and P_L, just upstream of the turbine flow meter in each feeder, were also monitored. The outlets of the feeders were submerged in 200 mm of water in the water tank, whose top was open to the atmosphere. The outputs of all instruments were sampled at a rate of 1000 samples/s for a time period of 30 s. The visually observed flow patterns in the header and feeders were also recorded. Post–processing was performed using the open–source computational software SCILAB 5.4 (Scilab Enterprises, 2013); this software package has been successfully validated by other authors and was found to produce results that were identical to those produced by established computational packages, including MATLAB and Octave (Sharma and Gobbert, 2010). The inlet water mass flow rate $\dot{m}_l$ and the inlet air mass flow rate $\dot{m}_g$ were calculated from the corresponding measured volumetric flow rates, using appropriate density corrections for the air flow rate. The time–averaged voltage output of the turbine flow meters V_{TM} and the time–averaged pressure difference in each feeder $\Delta P_F = P_U - P_L$ were also calculated; these were required for the application of the feeder mass flow rate measurement method, to be discussed in Section 2.3.

2.2. Experimental conditions

Three types of tests were performed in the present study: single feeder tests, two–feeder tests and four–feeder tests; in these tests all feeders were connected to the vertical downward ports. A summary of the feeder configurations and experimental conditions is given in Table 1. The name of each test series indicates which feeders were active; for example, V12 indicates that feeders connected to vertical ports #1 and #2 were active. The single feeder tests were used for calibration of the feeder mass flow rate measurement method, while the two–feeder test were performed to study the interaction between different pairs of feeders located at different axial locations. The four–feeder experiments were meant to be representative of a more complex

header–feeder system. Additional tests using feeders connected to one or more vertical, inclined and/or horizontal ports are delegated to the future.

Table 1: Test matrix used in present study. n is the number of cases examined in each test series.

Test series	$\dot{m}_l$ (kg/s)	$\dot{m}_g$ ($\times 10^3$ kg/s)	n
V1, V2, V3, V4	0 – 1.6	0 – 4.5	150
V12, V13, V14, V24, V34	0.57 – 2	0.85 – 8.1	56
V1234	1.15 – 2.9	1.8 – 17	59

2.3. Mass flow rate measurement in the feeders

The study of the two–phase flow distribution in header–feeder systems requires the measurement of the mass flow rates of both phases in a large number of feeders. Although many two–phase flow rate measurement methods are available (see Thorn et al. (2013) for a review), none of them were considered feasible for a system with many tubes, such as the present one, due to excessive equipment cost and/or required measurement time. For example, Teclemariam et al. (2003) separated the two phases and metered each phase separately using single–phase flow meters. They used a single gas–liquid separator for all 30 feeders in their experimental setup, to which each feeder was connected consecutively. For the measurement in a single feeder, the flow had to be rerouted and required about 25 min to reach a steady state by adjusting the flow rates out of the separator. The collection of a large number of two–phase mass flow rate measurements in several feeders using this technique was deemed not feasible due to the excessive time requirement. Instead, we decided to adopt an alternative flow rate measurement approach, which follows our previous successful applications of machine learning techniques for the measurement of the gas and liquid flow rates using the signals of differential pressure sensors (Shaban and Tavoularis, 2014) and wire–mesh sensors (Shaban and Tavoularis, 2015). In this work, we have implemented a different machine learning approach for gas–liquid flow rate measurements using the signals of turbine flow meters and pressure transducers.

This method is based on the training of a neural network model that takes several input variables and gives the gas and liquid flow rates as output (Figure 3). The freely available software RapidMiner 5 (RapidMiner, 2013) was

used for this purpose. The neural network algorithm implemented in RapidMiner has been previously tested using benchmark datasets, and its accuracy was found to be comparable to those of other academic and commercial codes (Borges et al., 2013). Our choice of input variables was based on past literature and preliminary tests in the present setup. Minemura et al. (1996) demonstrated that a non–linear relationship existed between the phase flow rates and two features: (i) the time–averaged output of a turbine flow meter V_{TM} and (ii) the pressure drop across the turbine flow meter. In the present approach, V_{TM} was used as the first input variable, whereas the pressure drop $\Delta P_{TM} = P_L - P_{atm}$, which is proportional to the pressure drop across the turbine meter, was used as the second variable. The pressure drop in the feeders, which is also non–linearly correlated to the phase flow rates (Collier and Thome, 1994), it was used as the third variable. Calibration of this method was performed separately for each feeder by recording the values of the three input variables with only one feeder connected to the header (test series V1, V2, V3 and V4). At steady state, the inlet flow rates were equal to the liquid and gas flow rates in feeder $\#i$, *i.e.*, the output variables $\dot{m}_{l,i}$ and $\dot{m}_{g,i}$ of the neural network. The set of measurements was split into a training subset and a test subset. Two neural networks, one each for the gas and liquid flow rate, were then trained using the backpropagation algorithm, with the neural network parameters identified using cross–validation. The trained neural networks were tested using the measurements in the test subset to quantify the accuracy of the method.

For the single feeder tests, the average absolute relative errors of liquid and gas flow rate predictions using the present method were calculated as 6.2% and 11.7%, respectively. For the multiple feeder tests, a mass balance error ϵ_m was calculated as,

$$\epsilon_m = \frac{\text{total outlet flow rate} - \text{inlet flow rate}}{\text{inlet flow rate}} \times 100 \tag{1}$$

The average absolute value of ϵ_m was 2% and 3.3% for the liquid and gas flow rates, respectively. The maximum values of ϵ_m were found to be 8.6% and 16.3% for the liquid and gas flow rates, respectively. The present method was only slightly less accurate than the phase separation method used by Teclemariam et al. (2003), who reported corresponding maximum errors of 5.2% and 15.3%, and allowed a single measurement with four active feeders to be performed in 30 s, rather than the estimated time of 2 hrs that would be required if we used the phase separation method with a single gas–liquid

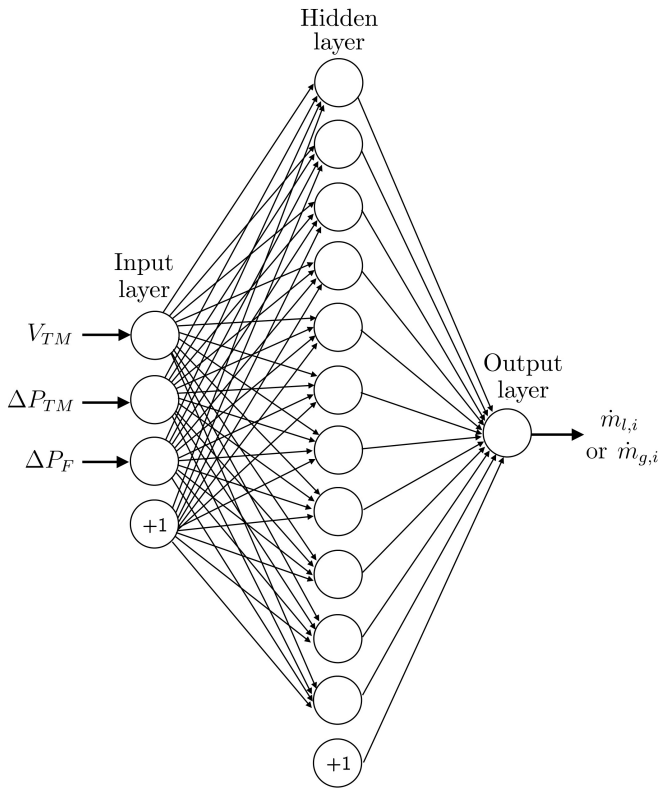

Figure 3: Schematic diagram of neural network used for liquid and gas mass flow rate measurements in a feeder.

separator.

3. Results and discussion

3.1. Flow in the header

For all of the present tests, the flow in the header was clearly stratified with the gas collecting near the top. A general representation of the flow patterns in the header for relatively high gas and liquid inlet flow rates ($\dot{m}_l >$ 2 kg/s and $\dot{m}_g > 0.01$ kg/s for four–feeder tests) is shown in Figure 4. In these flow ranges, it was possible to observe concurrently several different flow patterns in the header. The air–water mixture entered the header through the inlet turret as a jet and impinged on the free surface in a manner which has been referred to as a *plunging jet* by Bonetto and Lahey Jr. (1993). The

free surface of the water was very perturbed close to the inlet turret and became more calm and smooth away from it. At relatively high gas and liquid flow rates, the free surface level was relatively low in the middle of the header and higher near the two ends. On the contrary, at low gas and liquid flow rates ($\dot{m}_l < 1.2$ kg/s and $\dot{m}_g < 0.003$ kg/s for four–feeder tests), the free surface level was low and nearly constant along the entire header. The shape of the free surface in the header did not appear to be affected by the number or locations of the active feeders. The jet expansion angle increased with increasing inlet gas flow rate and, to a lesser extent, with increasing inlet liquid flow rate. Close to the area of impingement of the jet on the free surface, small bubbles were continuously entrained into the flow by the plunging jet, thus confirming the presence of a phenomenon called *air carryunder* (Bonetto and Lahey Jr., 1993). At low liquid flow rates, these bubbles tended to rise quickly to the surface, however, at high liquid flow rates, the bubbles were trapped below the surface by the oncoming liquid and mostly flowed into the feeders. This bubble transport mechanism was very weak by comparison to other mechanisms of gas flow into the feeders, which will be discussed next.

In all present tests, all vertical feeder ports were immersed in liquid and so liquid was drained readily through all these ports into the corresponding feeders. The mechanism of gas transport through each feeder, however, depended strongly on the location of the feeder, the free surface elevation and the flow pattern in the header. When port #1, which was positioned directly below the inlet turret, was active, it received directly a portion of the incoming gas–liquid mixture. All other ports received gas from the upper region of the header, which was entrained into the liquid entering the feeders forming one of two distinct patterns, collectively referred to in the literature as *gas pull–through* or *gas entrainment*. Smoglie and Reimann (1986) identified these two patterns as *vortex–induced* flow and *vortex–free* flow. The observed vortex–induced flow was characterized by strong swirl and the formation of a continuous or intermittent gas core that extended from the free surface to the port and allowed the gas phase to enter the feeder (Figure 5a). Vortex–free flow, on the other hand, appeared to be swirl–free and was characterized by an extensive gas core, whose diameter was close to the diameter of the feeder pipe, thus restricting the liquid flow to an annular region (Figure 5b). Vortex–free and vortex–induced flow were the primary mechanisms of flow through the vertical ports #2, #3, #4. During the single–feeder tests, it was observed that vortex–induced flow occurred at relatively high liquid flow

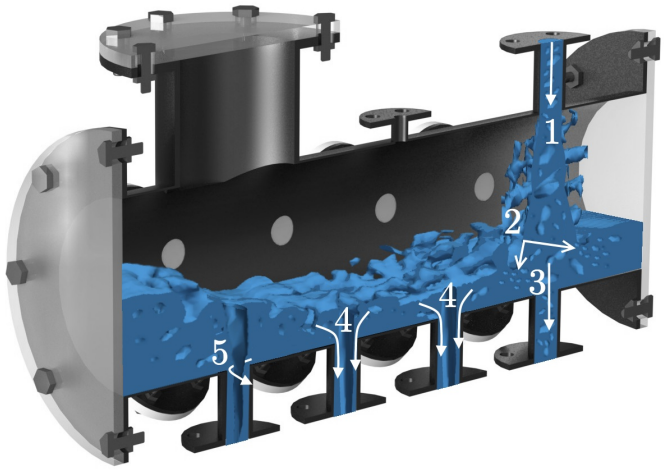

1 - Inlet gas-liquid jet
2 - Small bubbles formed due to plunging jet
3 - Direct flow
4 - Vortex-free flow
5 - Vortex-induced flow

Figure 4: Artistic representation of flow patterns in the header for test series V1234 with $\dot{m}_l = 2$ kg/s and $\dot{m}_g = 0.01$ kg/s – composite figure incorporating results of numerical simulations with the Volume of Fluid (VOF) method.

rates and relatively low gas flow rates (Figure 5c), when the free surface level was far from the ports. Conversely, vortex–free flow was observed when the inlet liquid and gas flow rates were such that the free surface level was close to the ports. For some intermediate flow conditions, hysteresis was noted, whereby the observed feeder flow pattern depended on the initial conditions of the test, and the flow pattern was unstable, intermittently switching between vortex–free and vortex–induced flow.

3.2. Two–phase flow distributions in two–feeder tests

The measured values of inlet and feeder mass flow rates and the header pressure for the two–feeder tests are presented in a table linked to the present document. Three two–feeder tests (V12, V13 and V14) were carried out by activating only feeder #1 and one of feeders #2, #3 or #4. The measured liquid $\dot{m}_{l,i}, i = 1, 2, ..., 4$ and gas $\dot{m}_{g,i}, i = 1, 2, ..., 4$ flow rates were used to

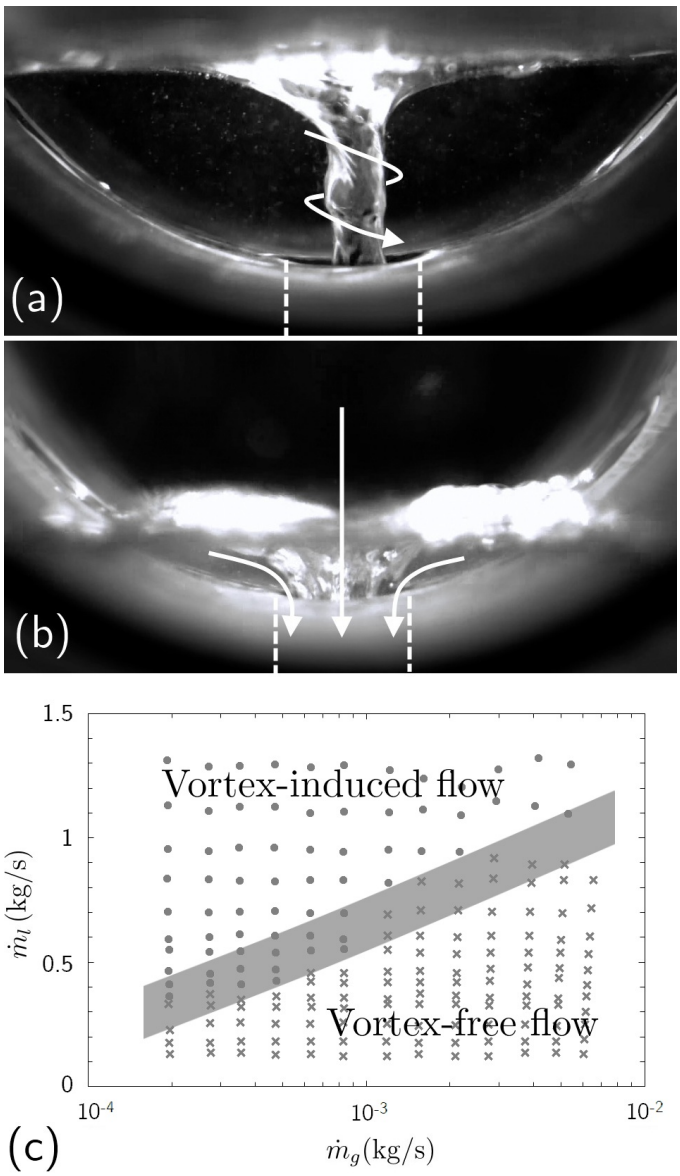

Figure 5: Annotated photographs showing (a) vortex–induced flow, (b) vortex–free flow, and (c) flow pattern map for test series V2, V3 and V4; a grey band marks the unstable flow pattern region.

calculate the corresponding flow rate portions through each feeder #i as

$$R_{l,i} = \frac{\dot{m}_{l,i}}{\Sigma \dot{m}_{l,i}} \approx \frac{\dot{m}_{l,i}}{\dot{m}_l} \tag{2}$$

and

$$R_{g,i} = \frac{\dot{m}_{h,i}}{\Sigma \dot{m}_{h,i}} \approx \frac{\dot{m}_{g,i}}{\dot{m}_g}. \tag{3}$$

Contours of the ratios $R_{l,1}$ and $R_{g,1}$, manually fitted to the measurements for test series V12, V13 and V14 with different combinations of total liquid and gas flow rates, are presented in Figure 6. At very low inlet liquid and gas flow rates, most of the incoming gas–liquid mixture flowed into feeder #1 for all feeder combinations considered. For any fixed $\dot{m}_l$, $R_{l,1}$ seemed to decrease monotonically with increasing $\dot{m}_g$, as the liquid flows through the two feeders tended to become more even. This is partially attributed to the increasing spreading angle of the incoming gas–liquid jet with increasing $\dot{m}_g$. For small fixed $\dot{m}_g$, $R_{l,1}$ seemed also to decrease monotonically with increasing $\dot{m}_l$, however, for some intermediate $\dot{m}_g$ (*e.g.*, $\dot{m}_g \approx 0.002$ kg/s for the V12 case), $R_{l,1}$ was insensitive to the value of $\dot{m}_l$ within the range considered. For fixed $\dot{m}_g$ larger than this value, $R_{l,1}$ increased monotonically with increasing $\dot{m}_l$. The dependence of $R_{g,1}$ on liquid and gas mass flow rates was more complex. For any fixed $\dot{m}_g$, $R_{g,1}$ seemed to decrease monotonically with increasing $\dot{m}_l$, but, for fixed $\dot{m}_l$ that exceeded a certain value (*e.g.*, $\dot{m}_l > 1$ kg/s for the V12 case), $R_{g,1}$ first increased up to a local maximum value and then decreased again as $\dot{m}_g$ was increased. At the conditions corresponding to this local maximum, we observed a transition in the flow regime in feeder #1 from annular flow to slug flow and flooding of the feeder entrance with liquid, which restricted the continuous flow of gas into the feeder.

Contours of the ratios $R_{l,4}$ and $R_{g,4}$ from the two–feeder test series V14, V24 and V34, during all of which feeder #4 was active, are shown in Figure 7. It is immediately evident that the flow distribution pattern for test series V14, which was discussed previously, was quite different from those for test series V24 and V34, which were qualitatively similar to each other. At inlet gas and liquid flow rates that were much lower than the range of presented measurements, it was visually observed that a large proportion of the incoming liquid flowed into the active feeder closest to the inlet, *i.e.*, feeder #4 received the least amount of liquid under these conditions. This can be explained by considering the *cross–flow velocity* of the liquid, *i.e.*, the velocity

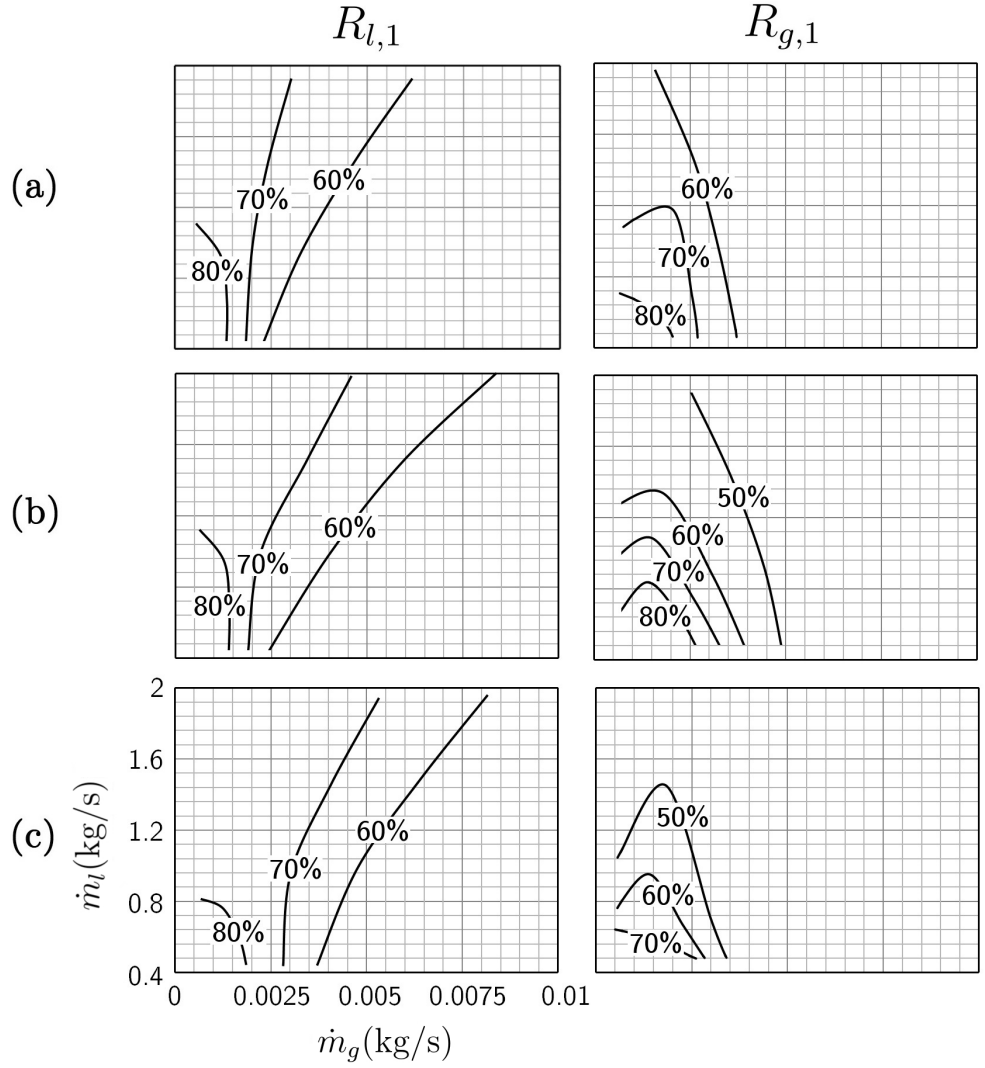

Figure 6: Contour maps of the ratios $R_{l,1}$ and $R_{g,1}$ of liquid and gas mass flow rates measured in feeder #1 to the inlet liquid and gas flow rates $\dot{m}_l$ and $\dot{m}_g$, respectively, in test series (a) V12, (b) V13, and (c) V14 shown on axes of $\dot{m}_g$ *vs.* $\dot{m}_l$. The axes of the bottom left plot apply to all other plots as well.

of liquid over the feeder openings, in the direction of the axis of the header. The flow of liquid into feeders #2, #3 and #4 required a sharp 90° change in the local flow direction, namely, from horizontal to vertical downwards. The low cross–flow velocity associated with low inlet flow rate conditions allowed the gas–liquid mixture to be drained preferentially through the first feeder that it encountered. As $\dot{m}_l$ increased, the free surface above feeder #4 moved upwards and away from the feeder inlet and the proportion of liquid entering feeder #4 in V24 and V34 also increased. This rise in the free surface level near the end of the header is attributed to the impingement of the flow on the end–wall of the header and the resulting recirculation (Figure 4). The actual liquid mass flow rate into feeders #2 or #3, increased very slightly but their share of the incoming liquid decreased drastically. This is possibly a consequence of the larger cross–flow velocity associated with large $\dot{m}_l$, which makes it more difficult for the flow to be diverted into these intermediate feeders. An increase in $\dot{m}_g$, which was found to increase the spreading angle of the incoming jet, did not affect significantly the liquid distribution in tests V24 and V34, in contrast to the previous observation that it led to a more uniform liquid distribution in V14. In general, in tests V24 and V34, the proportion of the inlet gas flow rate entering feeder #4 tended to decrease with increasing gas and liquid flow rates.

In summary, it was demonstrated that, at very low inlet gas and liquid flow rates, the incoming fluid would be drained preferentially through the active feeder that was closest to the inlet turret and that the flow distribution would change drastically as the inlet gas and liquid flow rates increased. The width and momentum of the incoming gas–liquid jet played important roles in the flow distribution when an active feeder was directly below the inlet: at larger gas flow rates, which were associated with an increased spreading angle of the incoming jet, the flow distribution in the feeders tended to become more uniform, whereas, at larger inlet liquid flow rates, which led to an increased momentum of the incoming jet, the direct flow of liquid into feeder #1 tended to increase. When the feeder underneath the inlet turret was inactive, the inlet gas flow rate had a very weak effect on the liquid distribution. In such cases, an increase in inlet liquid flow rate resulted in an increase in the relative liquid flow rate through the feeder that was closest to the end of the header.

3.3. Two–phase flow distributions in four–feeder tests

Contour maps of the two–phase flow distribution through each of the feeders for test series V1234, during which all four feeders were active, are

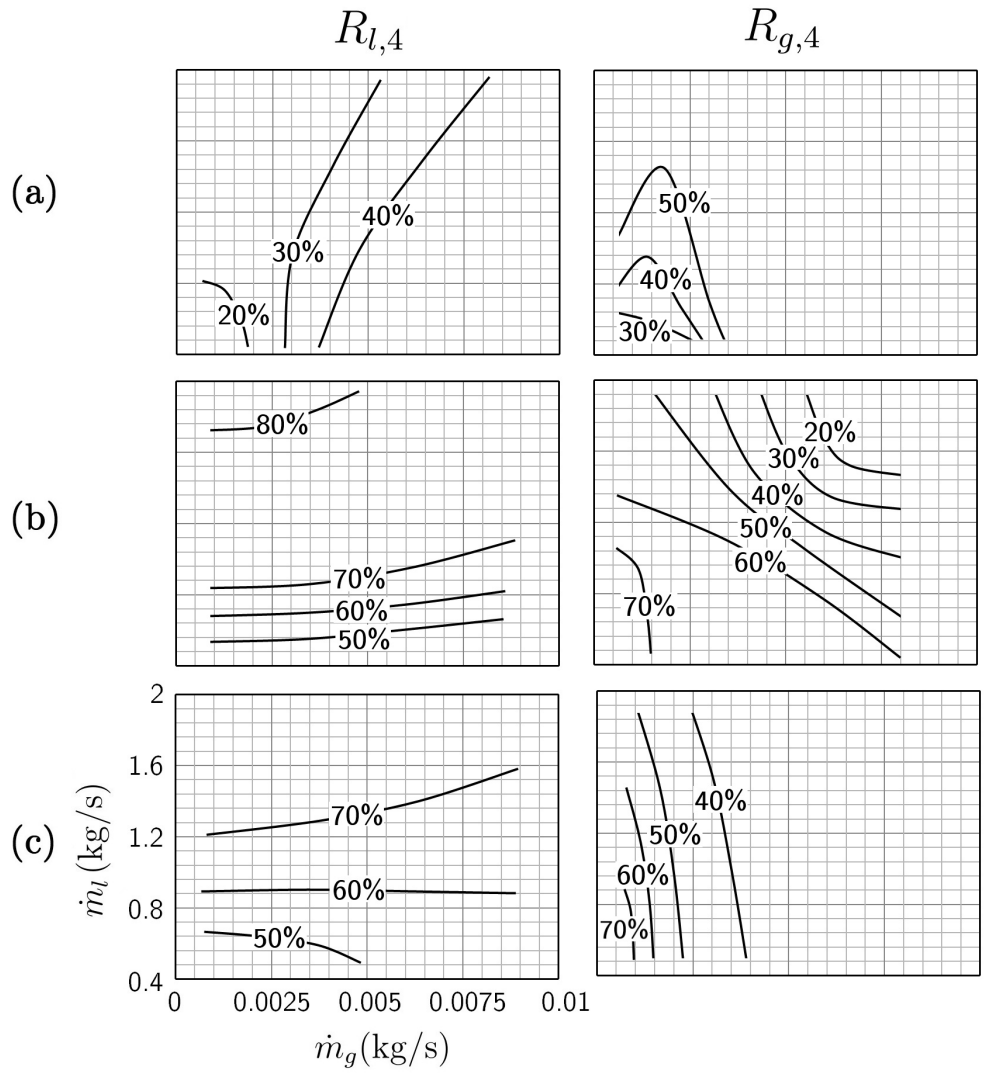

Figure 7: Contour maps of the ratios $R_{l,4}$ and $R_{g,4}$ of liquid and gas mass flow rates measured in feeder #4 to the inlet liquid and gas flow rates $\dot{m}_l$ and $\dot{m}_g$, respectively, in test series (a) V14, (b) V24, and (c) V34 shown on axes of $\dot{m}_g$ *vs.* $\dot{m}_l$. The axes of the bottom left plot apply to all other plots as well.

shown in Figure 8. These results are also presented in the linked table. The patterns that may be observed in these results were fairly complex, although they are also fairly consistent with the patterns in the two–feeder tests.

At the lowest tested inlet gas and liquid flow rates ($\dot{m}_l < 1.25$ kg/s, $\dot{m}_g < 0.0025$ kg/s), most of the gas–liquid mixture flowed into the feeder #1, while feeder #2 received a much smaller proportion of fluid and feeders #3 and #4 received even less (less than 10% of both liquid and gas each). The proportion of the incoming liquid entering feeder #1 gradually decreased with increasing $\dot{m}_l$ at low gas flow rates but increased with increasing $\dot{m}_l$ at large gas flow rates; it is also noted that the actual liquid flow rate into that feeder always increased with increasing $\dot{m}_l$. For fixed $\dot{m}_l$, $R_{l,1}$ decreased monotonically with increasing $\dot{m}_g$ for $\dot{m}_g < 0.007$ kg/s, as a consequence of the growing spreading angle of the incoming gas–liquid jet, which allowed part of the incoming liquid to be diverted away from the inlet of feeder #1. However, for larger $\dot{m}_g$, $R_{l,1}$ became nearly independent of $\dot{m}_g$, which possibly indicates that the jet spreading angle reached an upper bound. Feeder #2 received progressively smaller proportions of the incoming liquid at larger $\dot{m}_l$; this effect is attributed to the increasing liquid cross–flow velocity. We also observed that, for a fixed $\dot{m}_g$, $R_{l,3}$ increased with increasing $\dot{m}_l$; this may be explained by the observed elevation of the free surface, which allowed a larger proportion of the incoming liquid to reach feeder #3. At a certain $\dot{m}_l$, $R_{l,3}$ reached a maximum, then decreased with a further increase in $\dot{m}_l$, as the cross–flow became stronger and more liquid tended to flow towards the end of the header rather than draining through feeder #3. As in the two–feeder tests, feeder #4 consistently received a larger share of the incoming liquid with increasing $\dot{m}_l$. In general, and for all feeders, the gas distribution was very sensitive to $\dot{m}_g$ but relatively insensitive to $\dot{m}_l$. The proportion of the incoming gas entering feeder #1 tended to decrease with increasing $\dot{m}_g$ and the opposite trend was noted for feeders #2 and #3, whose share of the incoming gas increased with increasing $\dot{m}_g$. At a fixed $\dot{m}_l$, the ratio $R_{g,4}$ in feeder #4 increased with increasing $\dot{m}_g$, reached a local maximum at around $\dot{m}_g \approx 0.004$ kg/s, then decreased with further increases in $\dot{m}_g$. Visual observation indicated that, at conditions close to those corresponding to the maximum $R_{g,4}$, the free surface in the header ceased to be nearly horizontal and started resembling the one shown in Figure 4. Because the free surface level near the end of the header was higher than elsewhere and flow into feeder #4 was vortex–induced, gas was met with strong resistance against entering this feeder.

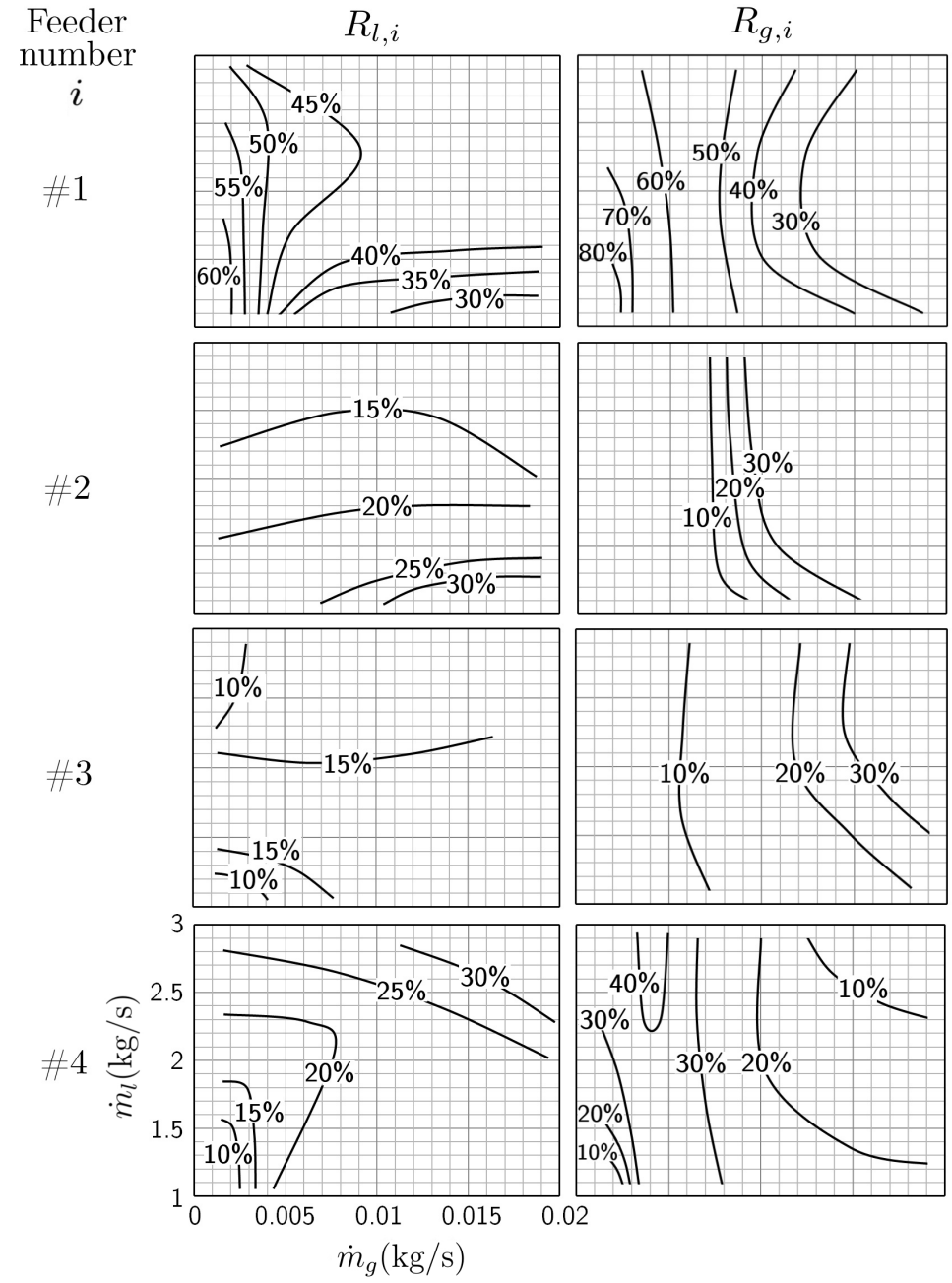

Figure 8: Contour maps of the ratios $R_{l,i}$ and $R_{g,i}$ of liquid and gas mass flow rates measured in feeder $\#i$ to the inlet liquid and gas flow rates $\dot{m}_l$ and $\dot{m}_g$, respectively, in test series V1234 shown on axes of $\dot{m}_g$ *vs.* $\dot{m}_l$. The axes of the bottom left plot apply to all other plots as well.

3.4. Relationship between the header pressure and the mass flow rate distribution

The flow rate in any fluid channel is intimately related to the pressure variation within it. This section discusses attempts to identify any possible relationship between the flow rate in each feeder and the pressures measured at different locations in the header–feeder system. One objective of this effort is to gain insight into flow distribution in the headers by analysis of wall pressure measurements, which are non–intrusive and relatively easy to obtain. An equally important objective is to highlight the general inapplicability of concepts from single–phase flow analysis to two–phase header–feeder flows and to dispel certain design misconceptions regarding flow distribution in header–like systems. As explained in section 2.1, the static pressure was monitored continuously near the exit of the inlet turret (P_{IN}), at the top of the header body (P_H), which was always above the free surface in all present tests, and in each active feeder ($P_{U,i}$), at a distance of $6.2D$ from its inlet. The pressure P_{OUT} at the outlets of all feeders was approximately equal to the hydrostatic pressure at the depth of the outlets. All pressures in this discussion are deemed to be gauge pressures. It is important to emphasize that the only pressures that were controlled independently were the compressed air line regulator pressure P_R, which was set to a constant value manually, and the feeder outlet pressure P_{OUT}, which was set by the tank free surface elevation. All other pressures attained values that depended on P_R, P_{OUT} and the independently regulated overall mass flow rates $\dot{m}_g$ and $\dot{m}_l$.

On intuitive grounds, one may speculate that the non–uniformity of the flow distribution among the active feeders would tend to decrease as the header pressure were increased. If this hypothesis were verified by the observations, then it would be worthwhile to seek some quantitative relationship between the header pressure and some indicator of feeder two–phase flow distribution. It is noted that the header pressure P_H was always smaller than the inlet pressure P_{IN} and the difference increased with increasing gas and liquid flow rates.

Contour plots of the header pressure P_H during the two–feeder and four–feeder tests are shown in Figures 9a and 9b, respectively. The two–feeder contour plots were found to be insensitive to the choice of active feeders, however, the header pressure contours changed drastically when the number of active feeders was changed from two to four. A comparison between Figures 9a and 6 reveals that, in tests V12, V13 and V14, except at the lowest gas flow rates, the header pressure was correlated with the uniformity of the gas flow

rate distribution among the feeders: as the header pressure became higher, the gas flow tended to be more uniformly distributed between the feeders. In these three tests, feeder #1 was always active and received directly much of the gas that was entrapped in the inlet jet. As $\dot{m}_g$ was increased, more gas escaped the jet and accumulated on the top of the header, from which it escaped through feeders other than #1, while also increasing the header pressure. In tests V24 and V34 (Figure 7), the proportion of gas entering feeder #4 decreased with increasing header pressure. The flow pattern in the header associated with a large header pressure resembled that shown in Figure 4. Inlet conditions that led to an increasing header pressure also resulted in elevating the free surface over feeder #4, thus restricting the flow of gas into this feeder. No clear correlation could be observed between the header pressure and the liquid flow rate distribution in the feeders for tests V24 and V34. Figure 9b shows contours of the header pressure during the four–feeder tests. The header pressure changed very little with $\dot{m}_l$, however, there was a clear monotonic increase of P_H with increased $\dot{m}_g$. Again, there appeared to be no clear correlation between the header pressure and the liquid flow rate distribution. However, as in the two–feeder tests, an increased header pressure was associated with a more even gas flow distribution among feeders #1, #2 and #3, and a lower gas flow rate through feeder #4. In conclusion, the previous analysis demonstrated that while measurements of header pressure could qualitatively indicate the gas flow distribution, it would not provide a consistent and reliable indication of liquid flow distribution among the feeders.

A second plausible hypothesis was whether the pressure difference $P_{U,i} - P_{OUT}$ across each feeder can be used as an indicator of the corresponding two–phase flow rates, and in particular of the liquid flow rate. In single–phase flow, the pressure drop in a channel increases monotonically with flow rate, however, this is not necessarily true in two–phase flows. An analysis of pressure change in a feeder can be performed by applying the momentum equation in a control volume bounded by the inlet, outlet and walls of the feeder. By converting all terms to equivalent pressures, one may write this equation in the form

$$P_{U,i} - P_{OUT} = \Delta P_{f,i} - \Delta P_{g,i} + \Delta P_{a,i} \ . \tag{4}$$

In Eq. 4, $\Delta P_{f,i}$ represents the frictional forces in the feeder and the turbine flow meter; $\Delta P_{g,i}$ represents the weight of the fluid column in the feeder; and $\Delta P_{a,i}$ represents the rate of change of fluid mixture momentum from inlet to

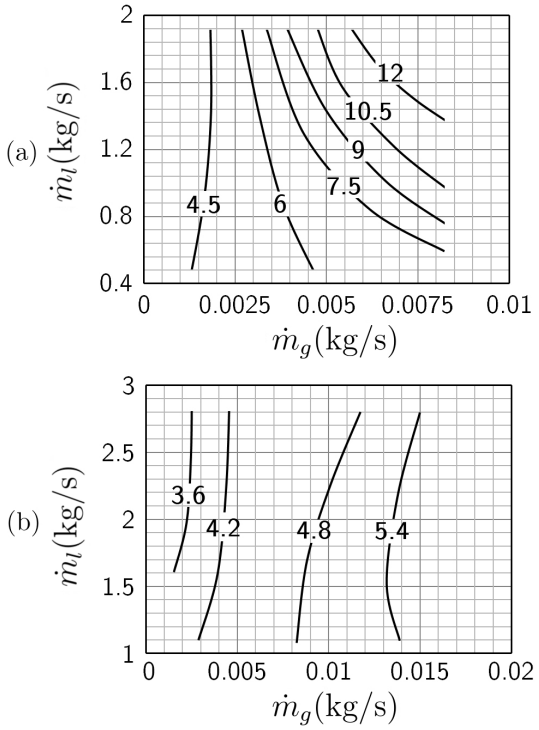

Figure 9: Contour maps of the header gauge pressure P_H (kPa) in the (a) two–feeder tests and (b) four–feeder tests, shown on axes of $\dot{m}_g$ *vs.* $\dot{m}_l$.

outlet. Assuming that the flow was adiabatic and that air density changes along the feeder were negligible, one may neglect $\Delta P_{a,i}$. The mass quality in the present tests did not exceed 1.5%, and, within this range, it can be shown that an increase in either the gas or liquid flow rate would lead to an increase in $\Delta P_{f,i}$. On the other hand, $\Delta P_{g,i}$, which would be inversely proportional to the void fraction, would increase with increasing liquid flow rate and decrease with increasing gas flow rate. Consequently, $P_{U,i} - P_{OUT}$ would not be a monotonic function of the feeder liquid and gas flow rates, and the possibility arises that there may be more than one combinations of $\dot{m}_l$ and $\dot{m}_g$ pairs that correspond to a single value of $P_{U,i} - P_{OUT}$. Indeed, an examination of the experimental data identified several cases that affirmed this possibility. For example, the pressure difference value $P_{U,1} - P_{OUT} = 4.6 \pm 0.1$ kPa was measured in three different tests, namely, V1234_06, V1234_15 and V1234_23 (see linked table); the corresponding flow rates were $\dot{m}_{l,1} = 0.42, 0.62, 0.87$ kg/s and $\dot{m}_{g,1} = 0.00386, 0.00328, 0.00235$ kg/s. One may therefore conclude

with confidence that neither the liquid nor the gas flow rate in a feeder can be determined solely from pressure difference measurements along the feeder.

A third hypothesis that seemed worth testing because of its practical implications was whether a comparison of simultaneous measurements of pressure $P_{U,i}$ at the inlets of different feeders could indicate, at least qualitatively, the flow rate distribution among these feeders. To test this hypothesis, feeder pressure measurements $P_{U,i}$ for two representative examples were examined and compared to the corresponding gas and liquid flow rate distributions. The ratio $(P_{U,i} - P_{IN})/P_{IN}$ and the corresponding flow rate distributions for the first case (V1234_51, $\dot{m}_l = 2.90$ kg/s, $\dot{m}_g = 0.0019$ kg/s) are shown in Figure 10a. The flow rate distribution that satisfied this pressure field corresponded to large gas and liquid flow rates in feeder #1, moderate flow rates in feeder #4 and very low (actually negligible for the liquid) flow rates in the intermediate feeders. Both the gas and liquid flow rate distributions seem to be closely correlated to the measurements of $P_{U,i}$.

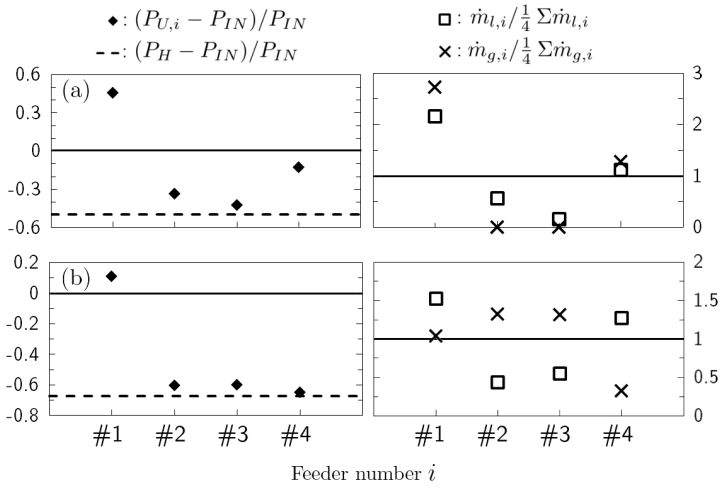

Figure 10: The pressure ratio $(P_{U,i} - P_{IN})/P_{IN}$ and the gas and liquid flow rate ratios $\dot{m}_{g,i}/\frac{1}{4}\Sigma\dot{m}_{g,i}$ and $\dot{m}_{l,i}/\frac{1}{4}\Sigma\dot{m}_{l,i}$ for tests (a) V1234_51 ($\dot{m}_l = 2.9$ kg/s, $\dot{m}_g = 0.0019$ kg/s, $P_{IN} = 4.0$ kPa) and (b) V1234_59 ($\dot{m}_l = 2.74$ kg/s, $\dot{m}_g = 0.016$ kg/s, $P_{IN} = 16$ kPa).

The second case (V1234_59, $\dot{m}_l = 2.74$ kg/s, $\dot{m}_g = 0.016$ kg/s) was selected such that it had an overall liquid flow rate that was comparable to that for the first case, but an overall gas flow rate that was larger, by one order of magnitude, than that for the first case. As shown in Figure 10b, the flow rates in feeders #2 and #3 were very different from those in feeder #4, even

though these three feeders had comparable values of $P_{U,i}$. These examples demonstrate that one should, in general, avoid even a rough assessment of feeder flow distribution levels by comparing feeder inlet pressures. Moreover, at least for feeders with vertical downward flow, designing and operating a header under conditions that would equalise the pressures at the feeder inlets would not necessarily lead to a more even distribution of gas and liquid flows through all feeders.

3.5. Discussion of scaling effects

For an evaluation of scaling effects on the flow patterns in header–feeder systems, we will compare the present results to those of two previous experiments by Teclemariam et al. (2003) and Kowalski et al. (1989); these experiments were performed in header facilities with geometries that were similar in shape to the one used in the present study, albeit with different sizes and aspect ratios of the header. The facility in the Kowalski et al. experiments was larger than the present one; it had a header with an I.D. of 325 mm and a length of 4200 mm, feeders with 50 mm I.D. and operated with steam–water mixtures. The Teclemariam et al. facility was smaller than the present one, having a header with an I.D. of 38.1 mm and a length of 485 mm; its feeders had an I.D. of 6.4 mm and it operated with air–water mixtures. Both of these studies had vertical, horizontal and inclined active feeders. The flow patterns observed in the present header (for example, the ones shown in Figure 4) were qualitatively the same as those reported in the two previous studies, despite the differences in geometry, pressure and working fluids. In addition, flow rate measurements in the vertical downward feeders by Teclemariam et al. displayed the same trends as the ones noted in the present study, despite the fact that horizontal and inclined feeders were also active in the previous study. These observations lead us to speculate that, even in large headers with hundreds of feeders, like the ones used in power plants, the liquid coolant flow rate would tend to be largest in the vertical downward feeders that are closest to the inlet turret and in the vertical downward feeders that are near the header end wall that is away from the active turret, whereas the intermediate feeders would receive a much smaller proportion of the incoming liquid coolant flow. The present study also demonstrated that, in the range of very small inlet flow rates, the proportion of liquid flowing into a feeder would increase with proximity to the inlet turret.

4. Summary and concluding remarks

An experimental investigation of the gas and liquid flow distributions through vertical feeder tubes supplied by a horizontal header tank has been performed in the modular header/feeder facility at the University of Ottawa. The liquid and gas mass flow rates in each feeder were determined with the use of a machine learning algorithm, applied to the outputs of turbine flow meters and pressure transducers. The flow patterns in the header and near the feeder inlets were observed visually and were found to depend on the overall gas and liquid flow rates as well as the number and locations of active feeders. The two–phase flow distributions in the feeders were also found to be correlated with the flow patterns in the header. In particular, when an active feeder was located across the inlet turret, it carried most of the liquid and gas, especially at low overall gas flow rates. At relatively large inlet gas and liquid flow rates, the feeder that was farthest away from the turret and near the header wall carried a larger amount of liquid than intermediate feeders, whose inlets were exposed to strong cross–flows over them.

In view of the relative ease of obtaining wall pressure measurements, we tested three plausible hypotheses for using such measurements to estimate, at least qualitatively, two–phase flow distributions to the feeders. Firstly, we demonstrated that, although the header pressure was correlated positively with the proportion of gas that passed through the intermediate feeders and negatively with the gas proportion that passed through the end feeders, the header pressure appeared to have no significant correlation to the liquid flow rate distribution. Secondly, we proved that the pressure change along a feeder could not serve as an indicator of either the liquid or the gas flow rates through the feeder, as multiple pairs of flow rate values could produce the same pressure difference value. Thirdly, and despite the fact that liquid and gas seemed to flow at relatively high proportions though a feeder whose inlet pressure was much higher than those of the others, we found that the relative magnitudes of feeder inlet pressures do not correspond consistently to flow distribution patterns. In summary, we found no acceptable means of estimating feeder flow distribution in a header–feeder system by exclusively using pressure measurements.

The present measurements could be useful for designing future header–feeder systems. For example, it seems worthwhile to evaluate the use of baffles to reduce the cross–flow liquid velocity, which may enforce a more uniform liquid distribution among the different feeders. In addition, all mea-

surements collected in this study have been compiled into a large experimental database, which has been linked to this document. This database could be used for the validation of multiphase CFD and thermalhydraulics system codes. Future experiments planned to be performed in the same facility include measurements of gas–liquid flow distributions in active feeders connected to various combinations of vertical, horizontal and inclined ports. Another future study will be concerned with the two–phase flow distribution in partially obstructed feeders, which could be of interest in the analysis of specific nuclear accident scenarios.

Acknowledgements

Financial support for this study was provided by the University Network of Excellence in Nuclear Engineering (UNENE), Atomic Energy of Canada Limited (AECL) and the Natural Sciences and Engineering Research Council of Canada (NSERC).

References

Ahmad, T., Hassan, I., 2006. Experimental investigation on the onset of gas entrainment from a stratified two-phase region through multiple branches mounted on a curved surface. J. Fluids Eng. 128, 726–733.

Bartley, J., Soliman, H., Sims, G., 2008. Experimental investigation of the onsets of gas and liquid entrainment from a small branch mounted on an inclined wall. Int. J. Multiphase Flow 34, 905–915.

Bonetto, F., Lahey Jr., R., 1993. An experimental study on air carryunder due to a plunging liquid jet. Int. J. Multiphase Flow 19, 281–294.

Borges, L., Marques, V., Bernardino, J., 2013. Comparison of data mining techniques and tools for data classification. In: Proceedings of the Sixth International C* Conference on Computer Science and Software Engineering (C3S2E '13), 10-12 July 2013, Porto, Portugal. pp. 113–116.

Bowden, R., Hassan, I., 2007. Flow field characterization at the onset of gas entrainment in a single downward discharge using particle image velocimetry. J. Fluids Eng. 129, 1565–1576.

Bowden, R., Hassan, I., 2008. Incipience of liquid entrainment from a stratified gas-liquid region in multiple discharging branches. J. Fluids Eng. 130, 011301.

Bowden, R., Hassan, I., 2009. Modeling the onset of gas entrainment in a single downward discharge from a stratified gas-liquid region with liquid crossflow. J. Fluids Eng. 131, 031304.

Collier, J., Thome, J., 1994. Convective boiling and condensation. Oxford, UK: Clarendon Press.

Dario, E., Tadrist, L., Passos, J., 2013. Review on two-phase flow distribution in parallel channels with macro and micro hydraulic diameters: Main results, analyses, trends. Appl. Therm. Eng. 59, 316–335.

Hassan, I., Soliman, H., Sims, G., Kowalski, J., 1997. Single and multiple discharge from a stratified two-phase region through small branches. Nucl. Eng. Des. 176, 233–245.

Kowalski, J., Hanna, B., Shim, S., 1989. Studies of two-phase flow distribution in a CANDU-type header/feeder system. In: Proceedings of the Fourth International Topical Meeting on Nuclear Reactor Thermalhydraulics (NURETH-4), October 10 -13, 1989, Karlsruhe, Federal Republic of Germany. pp. 28–33.

Minemura, K., Egashira, K., Ihara, K., Yamamoto, K., 1996. Simultaneous measuring method for both volumetric flow rates of air-water mixture using a turbine flowmeter. J. Energy Resour. Technol. 118, 29–35.

RapidMiner, 2013. RapidMiner 5: Open source data mining and predictive analytics software. Available online: http://www.rapidminer.com. Last accessed: 8 November, 2013.

Reimann, J., Khan, M., 1984. Flow through a small break at the bottom of a large pipe with stratified flow. Nucl. Sci. Eng. 88, 297–310.

Saleh, W., Bowden, R., Hassan, I., Kadem, L., 2009. A hybrid model to predict the onset of gas entrainment with surface tension effects. J. Fluids Eng. 131, 011305.

Saleh, W., Bowden, R., Hassan, I., Kadem, L., 2010. Two-phase flow structure in dual discharges stereo piv measurements. Exp. Therm Fluid Sci. 34, 1016–1028.

Saleh, W., Bowden, R., Hassan, I., Kadem, L., 2011. Techniques of piv in stratified two-phase headers. Exp. Therm Fluid Sci. 35, 82–95.

Schrock, V., Revankar, S., Mannheimer, R., Wang, C., Jia, D., 1986. Steam water critical flow through small pipes from stratified upstream regions. In: Proceedings of the Eighth International Heat Transfer Conference, 17-22 August, 1986, San Francisco, USA. pp. 2307–2311.

Scilab Enterprises, 2013. Scilab 5.4: Free and open source software for numerical computation. Available online: http://www.scilab.org. Last accessed: 17 November, 2013.

Shaban, H., Tavoularis, S., 2014. Measurement of gas and liquid flow rates in two-phase pipe flows by the application of machine learning techniques to differential pressure signals. Int. J. Multiphase Flow 67, 106–117.

Shaban, H., Tavoularis, S., 2015. The wire-mesh sensor as a two-phase flow meter. Meas. Sci. Technol. 26, 015306 (16 pp.).

Sharma, N., Gobbert, m., 2010. A comparative evaluation of MATLAB, Octave, Freemat, and Scilab for research and teaching. Tech. Rep. HPCF-2010-7, University of Maryland, Baltimore, USA.

Smoglie, C., Reimann, J., 1986. Two-phase flow through small branches in a horizontal pipe with stratified flow. Int. J. Multiphase Flow 12, 609–625.

Teclemariam, Z., Soliman, H., Sims, G., Kowalski, J., 2003. Experimental investigation of the two-phase flow distribution in the outlets of a horizontal multi-branch header. Nucl. Eng. Des. 222, 29–39.

Thorn, R., Johansen, G., Hjertaker, B., 2013. Three-phase flow measurement in the petroleum industry. Meas. Sci. Technol. 24, 012003 (17 pp.).

Chapter 9

Conclusion

9.1 Summary

In this work novel experimental and signal analysis methods were proposed for the identification of flow regime and measurement of the gas and liquid flow rates in air–water pipe flows. The effects of flow regime and the phase flow rates on the signals of differential pressure sensors and wire–mesh sensors were documented in detail. In addition, the effects of the inlet flow rates and feeder position were investigated in a modular header–feeder facility.

Firstly, measurements of differential pressure were collected in vertical upwards air–water pipe flow. The PDF of the dimensionless differential pressure parameter ΔP^* was found to strongly depend on the prevalent flow regime. The elastic maps algorithm was used to correlate the PDF of ΔP^* to the flow regime in the pipe. This method had high identification accuracy and non–intrusiveness, while also not requiring transparent pipe walls and expensive sensors for measurement.

The gas and liquid flow rates in the pipe were also found to affect the PDF and PSD of ΔP^*. These properties were correlated to the gas and liquid flow rates using artificial neural networks. Principal Component Analysis and Independent Component Analysis were used to reduce the dimension of the input dataset, making the calibration of the neural networks less time–consuming. The resulting flow rate measurement method was found to be fairly accurate and did not require separation of the gas–liquid mixture into separate streams.

A large database of wire–mesh sensor measurements of phase distribution, void fraction and flow regime was compiled in vertical upwards and downwards air–water flow. These

measurements were analyzed and, along with a comprehensive review of literature, were used to evaluate the performance of wire–mesh sensors in gas–liquid pipe flow over a wide range of flow conditions. The elastic maps method and the flow rate measurement method proposed earlier were adapted to enable the prediction of the flow regime and gas and liquid flow rates from wire–mesh sensor measurements.

Lastly, a simplified modular header–feeder facility was designed, constructed and instrumented. This facility was then used to investigate the problem of non–uniform distribution in header–feeder systems. A machine–learning approach was used to correlate the signals of turbine flow meters and pressure transducers to the gas and liquid flow rates in the feeders. An extensive database of flow rate measurements in the feeders was compiled for several experimental configurations and under a wide range of inlet flow rates. The non–uniformity in the flow distribution in the feeders was explained using physical arguments related to the flow patterns that were observed in the header.

9.2 Main contributions

The main contributions of the present work can be summarized as follows.

- We confirmed the relationship of the PDF of the dimensionless differential pressure parameter ΔP^* with the flow regime in vertical upward air–water flow.

- We demonstrated that the elastic maps algorithm was an accurate method of correlating the PDF of ΔP^* to the flow regime, with good accuracy in pipes of different sizes and under different system pressures.

- We documented the trends in the PDF and PSD of ΔP^* with varying gas and liquid flow rates.

- We proposed a novel machine learning approach to the prediction of gas and liquid flow rates from the PDF and PSD of ΔP^*, which did not require separation of the phases.

- We collected a large database of void fraction measurements in vertical upwards and downwards air–water pipe flow using wire–mesh sensors (Shaban & Tavoularis, 2014*a*). This database is suitable for the development of simple one–dimensional models for the void fraction, for example, drift–flux models (Zuber & Findlay, 1965).

- We performed a detailed evaluation of the performance and measurement uncertainty of wire–mesh sensors in air–water pipe flow. This provides a guide for future users of wire–mesh sensors, especially regarding the accuracy and applicability of these devices under different flow conditions.

- We adapted the elastic maps method and the flow measurement algorithm to enable their use with single and dual wire–mesh sensors in vertical upwards and downwards air–water flows.

- We proposed a machine learning method using turbine flow meter signals and differential pressure for the measurement of gas and liquid flow rates in vertical downwards air–water flow.

- We compiled an experimental database of gas and liquid flow distribution in the vertical downward branches of a horizontal header and presented mechanistic arguments for the non–uniform flow distribution based on the flow patterns in the header (Shaban & Tavoularis, 2015*a*). This database will enable the validation of thermalhydraulics codes or multiphase CFD simulations of these flows.

At the time of this thesis submission (September 2015), there is accumulating evidence that demonstrates that this work has so far been disseminated extensively and that it is on its way to make an impact in the field. Evidence available at this time includes the following facts.

- The article presented in Chapter 4 (Shaban & Tavoularis, 2014*b*) was featured on the list of the most downloaded *International Journal of Multiphase Flow* articles for several months. It has been downloaded or viewed more than 1000 times.

- The article presented in Chapter 5 (Shaban & Tavoularis, 2014*c*) was also featured on the list of the most downloaded *International Journal of Multiphase Flow* articles for several month and has been downloaded or viewe more than 850 times.

- Overviews of the two articles presented in Chapters 4 and 5 have been included in a Wikipedia article (`http://en.wikipedia.org/wiki/Elastic_map`) as examples of practical applications of the Elastic Maps algorithm.

- The article presented in Chapter 7 (Shaban & Tavoularis, 2015*b*) was designated by the editor of *Measurement Science and Technology* as 'IOPSelect', a designation given to articles that "bring substantial advances or significant breakthroughs", "demonstrate a high degree of novelty" and "are expected to exert a significant impact and influence on future research". As such, the article will be made available on an open access basis, without any fees on the Institute Of Physics (IOP) website for a period of one year (`http://iopscience.iop.org/0957-0233/26/1/015306`).

9.3 Future work

The proposed methods have been developed by calibration in a specific experimental setup using air and water as the working fluids. Although this is sufficient for most engineering applications, which take place under controlled flow conditions, future work could assess the potential of using the calibration performed under specific conditions with different working fluids or under different thermodynamic conditions. The present work provides methods for future two–phase flow researchers to efficiently collect measurements of flow rates and flow regime, in a cost–effective manner. These methods could be further applied to study the two–phase flows occurring in heat exchangers found in refrigeration applications, solar thermal power generation and in the safety analysis of nuclear power plants, in addition to the manifolds found in the petroleum processing industry. The experimental database of WMS measurements in air–water pipe flow can be used to validate one–dimensional drift–flux models. Moreover, the availability of detailed cross–sectional void fraction distributions from these measurements would allow the validation and development of multiphase computational fluid dynamics codes.

Additional research may be targeted at evaluating the use of these methods in vapour-liquid flows, where evaporation and condensation introduce additional measurement complexities. The use of more advanced machine learning algorithms in lieu of neural networks (for example, radial basis functions) may be found to be more suitable for processing the signals produced in certain flow regimes. Moreover, it may be possible to use machine learning models of the flow in feeders in order to carry out optimization, which would lead to drastic time savings compared to alternative numerical and computational methods. The modular header facility, constructed as part of this study, may be used for additional investigations of the gas–liquid flow distribution in header–feeder systems. For example, the two-phase flow distribution in feeders leaving the header at different orientations may be measured for the purpose of improving our understanding of the phenomena of gas and liquid entrainment in feeders whose openings may be below or above the free surface level. The availability of a second inlet turret introduces the possibility of studying the effect of inlet turret size or the simultaneous use of two inlet turrets on the flow distribution in the header. Finally, the flow distribution in partially obstructed feeders may also be investigated, as this would be of interest in the analysis of specific nuclear accident scenarios.

Appendices

Appendix A

Selection of WMS data record time and sampling frequency

The time interval T over which WMS measurements were recorded, to be referred to as the record time, was selected such as to allow convergence of time averages, while at the same time avoiding the recording of unnecessarily long time histories, which would occupy excessive data storage space. The sampling frequency f of WMS measurements was selected such as to provide sufficient temporal resolution of the signals, while also avoiding the recording of excessively large quantities of data. To determine suitable values for these two experimental settings, four sets of measurements were collected at conditions corresponding to the corners of the test matrix, namely at the following flow conditions.

- LLLG – lowest measurable liquid and gas flow rates; $j_l = 0.1$ m/s and $j_g = 0.04$ m/s.
- LLHG – lowest measurable liquid flow rate and highest possible gas flow rate; $j_l = 0.1$ m/s and $j_g = 20$ m/s.
- HLHG – highest possible liquid and gas flow rates; $j_l = 1.4$ m/s and $j_g = 9.6$ m/s.
- HLLG – highest possible liquid flow rate and lowest measurable gas flow rate; $j_l = 3$ m/ and $j_g = 0.04$ m/s.

All of these measurements were made at the maximum possible sampling frequency $f_{max} = 10000$ samples/s and for a record time $T_{max} = 120$ s.

First, the time–and–area–averaged void fraction α_T was calculated from the same measurement file for different data record times in the range $1 \text{ s} \leq T \leq 120$ s. Figure A.1 shows

that the ratio $\alpha_T/\alpha_{T_{max}}$ converges relatively quickly towards 1. The difference between α_T and $\alpha_{T_{max}}$ would be lower than 2% for $T \geq 30$ s and lower than 1% for $T \geq 75$ s for all flow conditions in this facility.

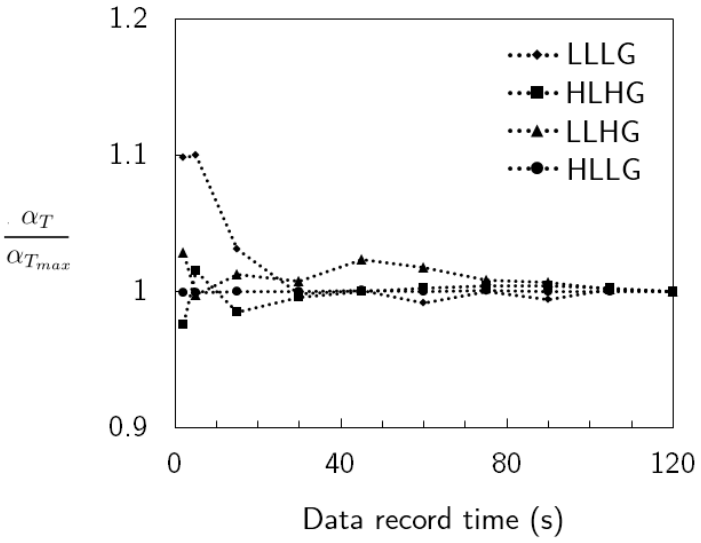

Figure A.1: Effect of data record time on the time–and–area–averaged void fraction.

The effect of sampling frequency on α was also tested in a similar fashion in the range 1 sample/s $\leq f \leq$ 10000 samples/s. Figure A.2 shows that the ratio $\alpha_f/\alpha_{f_{max}}$ converges very quickly to 1 and would become approximately 1 for 20 samples/s $\leq f$ for all flow conditions in our facility.

Separate tests were performed to determine the dependence of the cross–correlation–based superficial velocity j_{xc} on the sampling frequency. Representative results are shown in Figure A.3, which demonstrates that j_{xc} was sensitive to f. Nevertheless, it was subject to the same biases discussed in Chapter 6, even for the highest possible sampling frequency of 10000 samples/s, as it was observed that $j_g < j_{xc}$ in the bubbly flow regime and $j_{xc} < j_g$ in the other flow regimes.

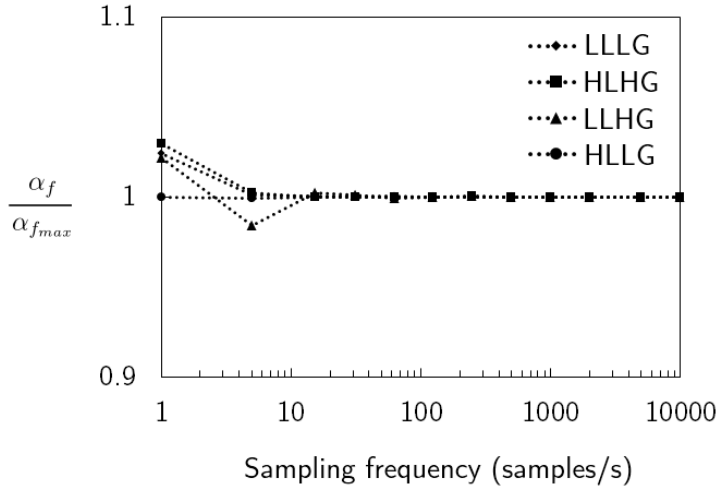

Figure A.2: Effect of sampling frequency on the time–and–area–averaged void fraction.

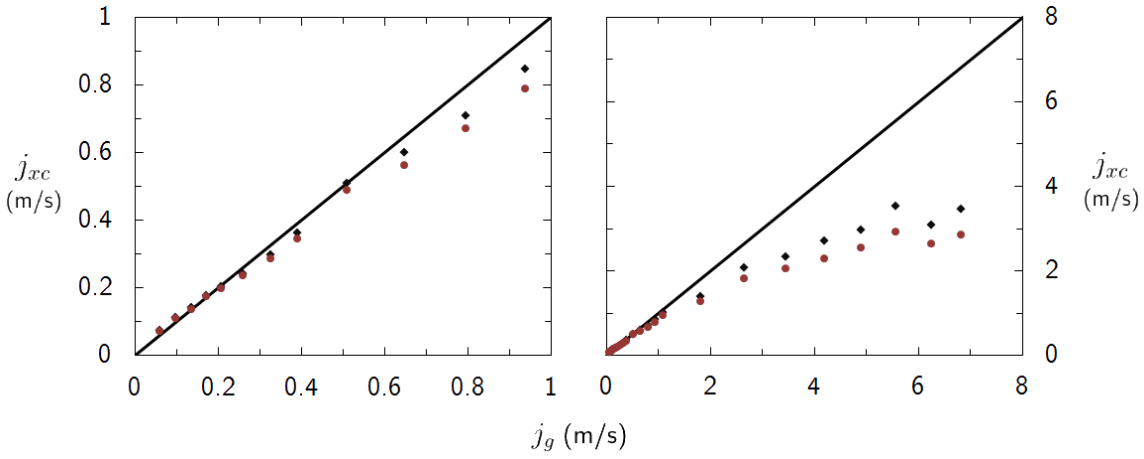

Figure A.3: Effect of sampling frequency on the cross–correlation superficial velocity j_{xc} for $j_l = 0.8$ m/s; $f = 1000$ (•) or 10000 (◆) samples/s.

References

Abdulkadir, M. 2011 Experimental and computational fluid dynamics (CFD) studies of gas-liquid flow in bends. Ph.D. thesis, University of Nottingham, Nottingham, United Kingdom.

Ahmad, T. & Hassan, I. 2006 Experimental investigation on the Onset of Gas Entrainment from a stratified two-phase region through multiple branches mounted on a curved surface. *J. Fluids Eng.* **128**, 726–733.

Al Issa, S., Beyer, M., Prasser, H.-M. & Frank, Th. 2007 Reconstruction of the 3D velocity field of the two-phase bubbly flow around a half moon obstacle using wire-mesh sensor data. In *Sixth International Conference on Multiphase Flow, Leipzig, Germany, July 9-13, 2007*.

Al-Masry, W.A., Ali, E.M. & Aqeel, Y.M. 2005 Determination of bubble characteristics in bubble columns using statistical analysis of acoustic sound measurements. *Chem. Eng. Res. Des.* **83**, 1196–1207.

Albrecht, R.W., Crowe, R.D., Dailey, D.J., Damborg, M.J. & Kosaly, G. 1982 Measurement of two phase flow properties using the nuclear reactor instrument. *Prog. Nucl. Energy* **9**, 37–50.

Azzopardi, B. & Abdulkareem, L. 2010 Comparison between electrical capacitance tomography and wire mesh sensor output for air/silicone oil flow in a vertical pipe. *Ind. Eng. Chem. Res.* **49**, 8805–8811.

Balachandar, S. & Eaton, J.K. 2010 Turbulent dispersed multiphase flow. *Annu. Rev. Fluid Mech.* **42**, 111–133.

Barnea, D., Shoham, O. & Taitel, Y. 1982 Flow pattern transition for vertical downward two phase flow. *Chem. Eng. Sci.* **37**, 741–744.

Bartley, J.T., Soliman, H.M. & Sims, G.E. 2008 Experimental investigation of the onsets of gas and liquid entrainment from a small branch mounted on an inclined wall. *Int. J. Multiphase Flow* **34**, 905–915.

Beg, N.A. & Toral, H. 1993 Off-site calibration of a two-phase pattern recognition flowmeter. *Int. J. Multiphase Flow* **19**, 999–1012.

Beyer, M., Lucas, D. & Kussin, J. 2010 Quality check of wire-mesh sensor measurements in a vertical air/water flow. *Flow Meas. Instrum.* **21**, 511–520.

Bonetto, F. & Lahey Jr., R.T. 1993 An experimental study on air carryunder due to a plunging liquid jet. *Int. J. Multiphase Flow* **19**, 281–294.

Brown, R.A.S., Sullivan, G.A. & Govier, G.W. 1960 The upward vertical flow of air-water mixtures III: Effect of gas phase density on flow pattern, holdup and pressure drop. *Can. J. Chem. Eng.* **38**, 62–66.

Cai, S. & Toral, H. 1993 Flowrate measurement in air-water horizontal pipeline by neural networks. In *International Joint Conference on Neural Networks, Nagoya, Japan, 25 - 29 October 1993*, pp. 2013–2016.

Chen, R.C., Reese, J. & Fan, L.-S. 1994 Flow structure in a three-dimensional bubble column and three-phase fluidized bed. *AIChE J.* **40**, 1093–1104.

Collier, J G & Thome, J R 1994 *Convective Boiling and Condensation*. Clarendon Press, Oxford.

Da Silva, M.J., Schleicher, E. & Hampel, U. 2007 Capacitance wire-mesh sensor for fast measurement of phase fraction distributions. *Meas. Sci. Technol.* **18**, 2245–2251.

Da Silva, M J 2008 Impedance sensors for fast multiphase flow measurement and imaging. Ph.D. thesis, Technischen Universität Dresden, Dresden, Germany.

Da Silva, M J & Hampel, U 2013 Capacitance wire-mesh sensor applied for the visualization of three-phase gas-liquid-liquid flows. *Flow Meas. Instrum.* **34**, 113–117.

Dario, E.R., Tadrist, L. & Passos, J.C. 2013 Review on two-phase flow distribution in parallel channels with macro and micro hydraulic diameters: Main results, analyses, trends. *Appl. Therm. Eng.* **59**, 316–335.

De Salve, M., Monni, G. & Panella, B. 2012 Horizontal Air-Water Flow Analysis with Wire Mesh Sensor. *J. Phys: Conf. Ser.* **395**, 012179 (8 pp.).

Dergachev, V.A., Gorban, A.N., Rossiev, A.A., Karimova, L.M., Kuandykov, E.B., Makarenko, N.G. & Steier, P. 2001 The filling of gaps in geophysical time series by artificial neural networks. *Radiocarbon* **43**, 365–371.

Dong, F., Xu, Y.B., Xu, L.J., Hua, L. & Qiao, X.T. 2005 Application of dual–plane ERT system and cross–correlation technique to measure gas–liquid flow in vertical upward pipe. *Flow Meas. Instrum.* **16**, 191–197.

Drew, D. & Passman, S. 2012 *Theory of Multicomponent Fluids*. Springer New York.

Falcone, G., Hewitt, G.F., Alimonti, C. & Harrison, B. 2002 Multiphase flow metering: Current trends and future developments. *J. Petrol. Technol.* **Apr 2002**, 77–84.

Fan, S. & Yan, T. 2014 Two-phase air-water slug flow measurment in horizontal pipe using conductance probes and neural network. *IEEE Trans. Instr. Meas.* **63**, 456–466.

Gorban, A.N. & Zinovyev, A.Y. 2001 Visualization of data by method of elastic maps and its applications in genomics, economics and sociology. Preprint of Institut des Hautes Etudes Scientifiques M/01/36.

Gorban, A.N. & Zinovyev, A.Y. 2003 *elmap*: C++ package. Available online: http://bioinfo-out.curie.fr/projects/elmap/. Last accessed: 17 November 2013.

Gorban, A.N. & Zinovyev, A.Y. 2005 Elastic principal manifolds and their practical applications. *Computing* **75**, 359–379.

Gorban, A.N. & Zinovyev, A.Y. 2007 *Principal Manifolds for Data Visualisation and Dimension Reduction*, chap. Elastic Maps and Nets for Approximating Principal Manifolds and Their Application to Microarray Data Visualization, pp. 97–131. Springer: Berlin-Heidelberg-New York.

Gorban, A.N. & Zinovyev, A.Y. 2009 *Handbook of Research on Machine Learning Applications and Trends: Algorithms, Methods and Techniques*, chap. Principal Graphs and Manifolds, pp. 28–59. IGI Global: Hershey, USA.

Häfeli, R., Hutter, C., Damsohn, M., Prasser, H.-M. & Rudolf von Rohr, Ph. 2013 Dispersion in fully developed flow through regular porous structures: Experiments with wire-mesh sensors. *Chem. Eng. Process.* **69**, 104–111.

Hampel, U., Otahal, J., Boden, S., Beyer, M., Schleicher, E., Zimmermann, W. & Jicha, M. 2009 Miniature conductivity wire-mesh sensor for gas-liquid two-phase flow measurement. *Flow Meas. Instrum.* **20**, 15–21.

Hassan, I.G, Soliman, H.M, Sims, G.E & Kowalski, J.E 1997 Single and multiple discharge from a stratified two-phase region through small branches. *Nucl. Eng. Des.* **176**, 233–245.

Hastie, T., Tibshirani, R. & Friedman, J. 2009 *The elements of statistical learning*. Springer, New York, USA.

Hibiki, T. & Ishii, M. 2003 One-dimensional drift-flux model for two-phase flow in a large diameter pipe. *Int. J. Heat Mass Tran.* **46**, 1773–1790.

Horiki, S., Nakamura, T. & Osakabe, M. 2004 Thin flow header to distribute feed water for compact heat exchanger. *Exp. Therm Fluid Sci.* **28**, 201–207.

Hyvarinën, A. & Oja, E. 2000 Independent component analysis: Algorithms and applications. *Neural Networks* **13**, 411–430.

Jeanmeure, L., Dyakowski, T., Zimmerman, W. & Clark, W. 2002 Direct flow–pattern identification using electrical capacitance tomography. *Exp. Therm Fluid Sci.* **26**, 763–773.

Johnson, I.D. 1987 Method and apparatus for measuring water in crude oil. US Patent No. 4644263 A.

Jones, O.C. 1983 *Two-phase flow measurement techniques in gas-liquid systems*, pp. 479–558. Hemisphere Publishing Corporation, Washington D.C.

Jones, O.C. & Zuber, N. 1975 The interrelation between void fraction fluctuations and flow patterns in two-phase flow. *Int. J. Multiphase Flow* **2**, 273–306.

Julia, J., Liu, Y., Paranjape, S. & Ishii, M. 2008 Upward vertical two-phase flow local flow regime identification using neural network techniques. *Nucl. Eng. Des.* **238**, 156–169.

Kickhofel, J., Valori, V. & Prasser, H.-M. 2014 Turbulent penetration in T-junction branch lines with leakage flow. *Nucl. Eng. Des.* **276**, 43–53.

Kliem, S., Prasser, H.-M., Sühnel, T., Weiss, F.-P. & Hansen, A. 2008 Experimental determination of the boron concentration distribution in the primary circuit of a PWR after a postulated cold leg small break loss-of-coolant-accident with cold leg safety injection. *Nucl. Eng. Des.* **238**, 1788–1801.

Kowalski, J.E., Hanna, B.N. & Shim, S.Y. 1989 Studies of two-phase flow distribution in a CANDU-type header/feeder system. In *Proceedings of the Fourth International Topical Meeting on Nuclear Reactor Thermalhydraulics (NURETH-4), October 10-13, 1989, Karlsruhe, Federal Republic of Germany.*, pp. 28–33.

Krepper, E., Reddy Vanga, B.N., Zaruba, A., Prasser, H.-M. & Lopez de Bertodano, M.A. 2007 Experimental and numerical studies of void fraction distribution in rectangular bubble columns. *Nucl. Eng. Des.* **237**, 399–408.

Lessard, E. 2013 Measurements in horizontal air-water pipe flows using wire-mesh sensors. Master's thesis, University of Ottawa, Ottawa, Canada.

Lessard, E, Shaban, H. & Tavoularis, S. 2014 Measurements in horizontal air-water pipe flows using wire-mesh sensors. In *2014 Canada-China Conference on Advanced Reactor Development, Niagara Falls, Canada, 27-30 April, 2014*.

Lin, T.-J., Reese, J., Hong, T. & Fan, L.-S. 1996 Quantitative analysis and computation of two-dimensional bubble columns. *AIChE J.* **42**, 301–318.

Lin, Z.H. 1982 Two–phase flow measurements with sharp–edged orifices. *Int. J. Multiphase Flow* **8**, 683–693.

Liu, T.J. 1993 Bubble size and entrance length effects on void development in a vertical channel. *Int. J. Multiphase Flow* **19**, 99–113.

Llamas, J.-D., Pérat, C., Lesage, F., Weber, M., D'Ortona, U. & Wild, G. 2008 Wire mesh tomography applied to trickle beds: A new way to study liquid maldistribution. *Chem. Eng. Process.* **47**, 1765–1770.

Lucas, D., Beyer, M., Kussin, J. & Schütz, P. 2010 Benchmark database on the evolution of two-phase flows in a vertical pipe. *Nucl. Eng. Des.* **240**, 2338–2346.

Lucas, D., Krepper, E. & Prasser, H.-M. 2005 Development of co-current air-water flow in a vertical pipe. *Int. J. Multiphase Flow* **31**, 1304–1328.

Lucas, D., Krepper, E. & Prasser, H.-M. 2007 Use of models for lift, wall and turbulent dispersion forces acting on bubbles for poly-disperse flows. *Chem. Eng. Sci.* **62**, 4146–4157.

Manera, A. 2003 Experimental and analytical investigations on flashing-induced instabilities in natural circulation two-phase systems - applications to the startup of Boiling Water Reactors. PhD thesis, Delft University of Technology, Delft, The Netherlands.

Manera, A., Ozar, B., Paranjape, S., Ishii, M. & Prasser, H.-M. 2009 Comparison between wire-mesh sensors and conductive needle-probes for measurements of two-phase flow parameters. *Nucl. Eng. Des.* **239**, 1718–1724.

Manera, A., Prasser, H.-M., Lucas, D. & van der Hagen, T.H.J.J. 2006 Three-dimensional flow pattern visualization and bubble size distributions in stationary and transient upward flashing flow. *Int. J. Multiphase Flow* **32**, 996–1016.

Marchitto, A., Fossa, M. & Guglielmini, G. 2009 Distribution of air-water mixtures in parallel vertical channels as an effect of the header geometry. *Exp. Therm Fluid Sci.* **33**, 895–902.

Matsui, G. 1984 Identification of flow regimes in vertical gas-liquid two-phase flow using differential pressure fluctuations. *Int. J. Multiphase Flow* **10**, 711–720.

Matsui, G. 1985 Identification of flow patterns in horizontal gas–liquid two–phase flow using diferential pressure fluctuations. In *Proceedings of the International Symposium on Fluid Control and Measurement*, pp. 819–824. Tokyo, Japan, 2–6 September, 1985.

Meng, Z., Huang, Z., Wang, B., Ji, Haifeng, Li, H. & Yan, Y. 2010 Air-water two-phase flow measurement using a Venturi meter and an electrical resistance tomography sensor. *Flow Meas. Instrum.* **21**, 268–276.

Meribout, M., Al-Rawahi, N., Al-Naamany, A., Al-Bimani, A., Al-Busaidi, K. & Meribout, A. 2010 Integration of impedance measurements with acoustic measurements for accurate two phase flow metering in case of high water-cut. *Flow Meas. Instrum.* **21**, 8–19.

Mi, Y., Ishii, M. & Tsoukalas, L.H. 1998 Two-phase flow identification using advanced instrumentation and neural networks. *Nucl. Eng. Des.* **184**, 409–420.

Mi, Y., Ishii, M. & Tsoukalas, L.H. 2001 Flow regime identification methodology with neural networks and two-phase flow models. *Nucl. Eng. Des.* **204**, 87–100.

Minemura, K., Egashira, K., Ihara, K. & Yamamoto, K. 1996 Simultaneous Measuring Method for Both Volumetric Flow Rates of Air-Water Mixture Using a Turbine Flowmeter. *J. Energy Resour. Technol.* **118**, 29–35.

Minemura, K., Takeoka, T., Syoda, S., Egasira, K. & Ogawa, Y. 1998 Correlative mapping method for measuring individual phase flow rates in air-water two-phase flow based on stochastic features. *JSME Int. J.* **41**, 863–870.

Mishima, K. & Ishii, M. 1984 Flow regime transition criteria for upward two–phase flow in vertical tubes. *Int. J. Heat Mass Transfer* **27**, 723–737.

Nishikawa, K., Segokuchi, K. & Fukano, T. 1969 On the pulsation phenomena in gas-liquid two-phase flow. *B. JSME* **12**, 1410–1416.

Oddie, G. & Pearson, J.R.A. 2004 Flow rate measurement in two–phase flow. *Annu. Rev. Fluid Mech.* **36**, 149–172.

Ofuchi, C. Y., Morales, R. E. M., Arruda, L. V. R., Neves Jr., F., Dorini, L., do Amaral, C. E. F. & da Silva, M. J. 2012 Wire-mesh sensor, ultrasound and high-speed videometry applied for the characterization of horizontal gas-liquid slug flow. In *Seventh International Symposium on Measurement Techniques for Multiphase Flows, Tianjin, China, 17-19 September 2011*.

Olerni, Claudio, Jia, Jiabin & Wang, Mi 2013 Measurement of air distribution and void fraction of an upwards airwater flow using electrical resistance tomography and a wire-mesh sensor. *Meas. Sci. Technol.* **24**, 035403 (9 pp.).

Olmos, E., Gentric, C., Poncin, S. & Midoux, N. 2003 Description of flow regime transitions in bubble columns via laser Doppler anemometry signals processing. *Chem. Eng. Sci.* **58**, 1731–1742.

Petritsch, G. & Mewes, D. 1999 Experimental investigations of the flow patterns in the hot leg of a pressurized water reactor. *Nucl. Eng. Des.* **188**, 75–84.

Pietruske, H. & Prasser, H.-M. 2007 Wire-mesh sensors for high-resolving two-phase flow studies at high pressures and temperatures. *Flow Meas. Instrum.* **18**, 87–94.

Prasser, Horst-Michael 2007 Evolution of interfacial area concentration in a vertical air-water flow measured by wire-mesh sensors. *Nucl. Eng. Des.* **237**, 1608–1617.

Prasser, H.-M. 2008 Novel experimental measuring techniques required to provide data for CFD validation. *Nucl. Eng. Des.* **238**, 744–770.

Prasser, H.-M., Beyer, M., Böttger, A., Carl, H., Lucas, D., Schaffrath, A., Schutz, P., Weiss, F.-P. & Zschau, J. 2005*a* Influence of the pipe diameter on the structure of the gas-liquid interface in a vertical two-phase pipe flow. *Nucl. Technol.* **152**, 3–22.

Prasser, H.-M., Beyer, M., Carl, H., Gregor, S., Lucas, D., Pietruske, H., Schütz, P. & Weiss, F.-P. 2007*a* Evolution of the structure of a gas-liquid two-phase flow in a large vertical pipe. *Nucl. Eng. Des.* **237**, 1848–1861.

Prasser, H.-M., Beyer, M., Carl, H., Manera, A., Pietruske, H. & Schütz, P. 2007*b* Experiments on upwards gas/liquid flow in vertical pipes. *Tech. Rep.* FZD-482. Institute of Safety Research, Dresden, Germany.

Prasser, H.-M., Böttger, A. & Zschau, J. 1997 A new electrode-mesh tomograph for gas-liquid fiows. Annual Report 1996 (FZR-190). Institute of Safety Research, Dresden, Germany.

Prasser, H.-M., Böttger, A & Zschau, J 1998 A new electrode-mesh tomograph for gas-liquid flows. *Flow Meas. Instrum.* **9**, 111–119.

Prasser, Horst-Michael, Krepper, Eckhard & Lucas, Dirk 2002 Evolution of the two-phase flow in a vertical tube-decomposition of gas fraction profiles according to bubble size classes using wire-mesh sensors. *Int. J. Therm. Sci.* **41**, 17–28.

Prasser, H.-M., Misawa, M. & Tiseanu, I. 2005*b* Comparison between wire-mesh sensor and ultra-fast X-ray tomograph for an air-water flow in a vertical pipe. *Flow Meas. Instrum.* **16**, 73–83.

Prasser, H.-M., Scholz, D. & Zippe, C. 2001 Bubble size measurement using wire-mesh sensors. *Flow Meas. Instrum.* **12**, 299–312.

Prasser, H.-M., Zschau, J., Peters, D., Pietzsch, G., Taubert, W. & Trepte, M. 2000 Wire-mesh sensor-now 10,000 frames per second. Annual Report 1999 (FZR-284). Institute of Safety Research, Dresden, Germany.

Qi, F.S., Yeoh, G.H., Cheung, S.C.P., Tu, J.Y., Krepper, E. & Lucas, D. 2012 Classification of bubbles in vertical gasliquid flow: Part 1 An analysis of experimental data. *Int. J. Multiphase Flow* **39**, 121–134.

Rahman, M.A., Heidrick, T. & Fleck, B.A. 2009 A critical review of advanced experimental techniques to measure two-phase gas/liquid flow. *Open Fuel. Energ. Sci. J.* **2**, 54–70.

RapidMiner 2013 RapidMiner 5: Open source data mining and predictive analytics software. Available online: http://www.rapidminer.com. Last accessed: 8 November, 2013.

Reinecke, N., Petritsch, G., Boddem, M. & Mewes, D. 1998 Tomographic imaging of the phase distribution in two-phase slug flow. *Int. J. Multiphase Flow* **24**, 617–634.

Resta, M. 2007 Portfolio optimization through elastic maps: Some evidence from the italian stock exchange. *Lect. Notes Comput. Sci.* **4693**, 635–641.

Richter, S, Aritomi, M, Prasser, H.-M. & Hampel, R 2002 Approach towards spatial phase reconstruction in transient bubbly flow using a wire-mesh sensor. *Int. J. Heat Mass Transfer* **45**, 1063–1075.

Roitberg, E., Shemer, L. & Barnea, D. 2007 Measurements of cross-sectional instantaneous phase distribution in gas-liquid pipe flow. *Exp. Therm Fluid Sci.* **31**, 867–875.

Rouhani, S.Z. & Sohal, M.S. 1983 Two phase flow patterns: A review of research results. *Prog. Nucl. Energy* **11**, 219–259.

Saba, N. & Lahey Jr., R.T. 1983 The analysis of phase separation phenomena in branching conduits. *Int. J. Multiphase Flow* **10**, 1–20.

Schmitz, D & Mewes, D 2000 Tomographic imaging of transient multiphase flow in bubble columns. *Chem. Eng. J.* **77**, 99–104.

Scilab Enterprises 2013 Scilab 5.4: Free and open source software for numerical computation. Available online: http://www.scilab.org. Last accessed: 17 November, 2013.

Shaban, H. 2015 Experimental investigations of internal air-water flows. PhD thesis, University of Ottawa, Ottawa, Canada.

Shaban, H. & Tavoularis, S. 2014*a* Development of drift-flux models for evaluating two-phase mass flow rates in a header facility. *Tech. Rep.* UO-MCG-DFM-2014-01. University of Ottawa, Ottawa, Canada.

Shaban, H. & Tavoularis, S. 2014*b* Identification of flow regime in vertical upward air–water pipe flow using differential pressure signals and elastic maps. *Int. J. Multiphase Flow* **61**, 62–72.

Shaban, H. & Tavoularis, S. 2014*c* Measurement of gas and liquid flow rates in two-phase pipe flows by the application of machine learning techniques to differential pressure signals. *Int. J. Multiphase Flow* **67**, 106–117.

Shaban, H. & Tavoularis, S. 2015*a* Distribution of downward air-water flow in vertical tubes connected to a horizontal cylindrical header. (submitted).

Shaban, H. & Tavoularis, S. 2015*b* The wire-mesh sensor as a two-phase flow meter. *Meas. Sci. Technol.* **26**, 015306 (16 pp.).

Shaban, H. & Tavoularis, S. 2015*c* Wire-mesh tomography: areas of application, performance evaluation and measurement uncertainty. (submitted).

Shaikh, A. & Al-Dahhan, M. 2005 Characterization of the hydrodynamic flow regime in bubble columns via computed tomography. *Flow Meas. Instrum.* **16**, 91–98.

Shaikh, A. & Al-Dahhan, M. 2007 A review on flow regime transition in bubble columns. *Int. J. Chem. Reactor Eng.* **5**, 1–68.

Sharaf, S., Da Silva, M., Hampel, U., Zippe, C., Beyer, M. & Azzopardi, B. 2011 Comparison between wire mesh sensor and gamma densitometry void measurements in two-phase flows. *Meas. Sci. Technol.* **22**, doi:10.1088/0957–0233/22/10/104019.

Shearer, C.J. & Nedderman, R.M. 1965 Pressure gradient and liquid film thickness in co-current uupward flow of gas/liquid mixtures: Application to film-cooler design. *Chem. Eng. Sci.* **20**, 671–683.

Shoukri, M., Hassan, I. & Peng, F. 2002 Steam-water stratified flow in t-junctions-experiments and modeling. *Trans. CSME* **26**, 241–259.

Simpson, H.C. 1975 Flow patterns in two-phase flow, Parts 1 and 2. *Tech. Rep.* AERE-R 8120 and AERE-R 9197. Heat Transfer and Fluid Flow Service, Harwell, UK.

Smoglie, C. & Reimann, J. 1986 Two-phase flow through small branches in a horizontal pipe with stratified flow. *Int. J. Multiphase Flow* **12**, 609–625.

Spedding, P.L., Woods, G.S., Ragunathan, R.S. & Watterson, J.K. 1998 Vertical two-phase flow, Part I: Flow regimes. *Trans. IChemE* **76**, 612–619.

Sun, Z. & Zhang, H. 2008 Neural networks approach for prediction of gas-liquid two-phase flow pattern based on frequency domain analysis of vortex flowmeter signals. *Meas. Sci. Tech.* **19**, doi:10.1088/0957–0233/19/1/015401.

Szalinski, L., Abdulkareem, L.A., Da Silva, M.J., Thiele, S., Beyer, M., Lucas, D., Hernandez Perez, V., Hampel, U. & Azzopardi, B.J. 2010 Comparative study of gas-oil and gas-water two-phase flow in a vertical pipe. *Chem. Eng. Sci.* **65**, 3836–3848.

Taitel, Y., Bornea, D. & Dukler, A.E. 1980 Modelling flow pattern transitions for steady upward gas-liquid flow in vertical tubes. *AIChE J.* **26**, 345–354.

Tambouratzis, T. & Pazsit, I. 2009 Non-invasive on-line two-phase flow regime identification employing artificial neural networks. *Ann. Nucl. Energy* **36**, 464–469.

Tan, C. & Dong, F. 2006 Two–phase flow measurement by dual–plane ERT system with drift–flux model and cross correlation technique. In *Proceedings of the Fifth International Conference on Machine Learning and Cybernetics, Dalian, China, 13 - 16 August, 2006*, pp. 1443–1448.

Tavoularis, S. 2005 *Measurement in Fluid Mechanics*. Cambridge, UK: Cambridge University Press.

Teclemariam, Z., Soliman, H.M., Sims, G.E. & Kowalski, J.E. 2003 Experimental investigation of the two-phase flow distribution in the outlets of a horizontal multi-branch header. *Nucl. Eng. Des.* **222**, 29–39.

Thimmapuram, P.R., Rao, N.S. & Saxena, S.C. 1992 Characterization of hydrodynamic regimes in a bubble column. *Chem. Eng. Sci.* **47**, 3335–3362.

Thorn, R., Johansen, G. & Hjertaker, B. 2013 Three-phase flow measurement in the petroleum industry. *Meas. Sci. Technol.* **24**, 012003 (17 pp.).

Trafalis, T., Oladunni, O. & Papavassiliou, D. 2005 Two-phase flow regime identification with a multiclassification support vector machine (SVM) model. *Ind. Eng. Chem. Res.* **44**, 4414–4426.

Vauth, T., Rausch, T. & Mewes, D. 2004 Test facility for multiphase pumps in serial and parallel operation. In *Proceedings of the 2004 ASME International Mechanical Engineering Congress and Exposition (IMECE2004), Anaheim, USA, November 13-19, 2004*.

Vince, M.A. & Lahey, R.T. 1982 On the development of an objective flow regime indicator. *Int. J. Multiphase Flow* **8**, 93–124.

Wang, H. & Zhang, L. 2009 Identification of two-phase flow regimes based on support vector machine and electrical capacitance tomography. *Meas. Sci. Tech.* **20**, 114007 (8 pp.).

Wang, J. & Chang, C.-I. 2006 Independent Component Analysis–based dimensionality reduction with applications in hyperspectral image analysis. *IEEE Trans. Geosci. Remote Sensing* **44**, 1586–1600.

Wangjiraniran, W., Aritomi, M., Kikura, H., Motegi, Y. & Prasser, H.-M. 2005 A study of non-symmetric air water flow using wire mesh sensor. *Exp. Therm Fluid Sci.* **29**, 315–322.

Wangjiraniran, W., Motegi, Y., Richter, S., Kikura, H., Aritomi, M. & Yamamoto, K. 2003 Intrusive effect of wire mesh tomography on gas-liquid flow measurement. *J. Nucl. Sci. Technol.* **40**, 932–940.

Williams, R.A. & Beck, M.S., ed. 1995 *Process Tomography: Principles, Techniques and Applications*. Butterworth-Heinemann, Oxford.

Yang, J. 2013 AECL header test facility. Private communication.

Ylönen, Arto 2013 High-resolution flow structure measurements in a rod bundle. Ph.D. Thesis, ETH Zurich, Zürich, Switzerland.

Ylönen, A., Bissels, W.-M. & Prasser, H.-M. 2011 Single-phase cross-mixing measurements in a 4 × 4 rod bundle. *Nucl. Eng. Des.* **241**, 2484–2493.

Zabaras, G., Dukler, A.E. & Moalem-Maron, D. 1986 Vertical upward cocurrent gas–liquid annular flow. *AIChE J.* **32**, 829–843.

Zhang, H.J., Lu, S.J. & Yu, G.Z. 1992 An investigation of two–phase flow measurement with orifices for low–quality mixtures. *Int. J. Multiphase Flow* **18**, 149–155.

Zhang, J.-P., Grace, J.R., Epstein, N. & Lim, K.S. 1997 Flow regime identification in gas-liquid flow and three-phase fluidized beds. *Chem. Eng. Sci.* **52**, 3979–3992.

Zhang, Zhiqiang, Bieberle, Martina, Barthel, Frank, Szalinski, Lutz & Hampel, Uwe 2013 Investigation of upward cocurrent gas-liquid pipe flow using ultrafast X-ray tomography and wire-mesh sensor. *Flow Meas. Instrum.* **32**, 111–118.

Zinovyev, A.Y. & Gorban, A.N. 2003 Self-organizing approach for automated gene identification. *Open Syst. Inf. Dyn.* **10**, 321–333.

Zoeteweij, Marco Leendert 2007 Long liquid slugs in horizontal tubes. Ph.D. Thesis, Delft University of Technology, Delft, The Netherlands.

Zuber, N. & Findlay, J.A. 1965 Average volumetric concentration in two-phase flow systems. *J. Heat Transfer* **87**, 453–468.